Design of gas sensors using carbon nanotubes

By

Shams B. A. Al-Atraqchi

A thesis submitted in partial fulfilment of the requirements of the degree of Doctor of Philosophy

School of Natural and Environmental Sciences
University of Newcastle Upon Tyne
Newcastle Upon Tyne, United Kingdom

2019

Abstract

This thesis is concerned with the structural, chemical and physical properties of carbon nanotubes (CNTs) and composites of CNTs with conductive polymers and DNA. The application of these composites in electronic sensors for volatile organic compounds VOCs, carbon monoxide and ozone gas was also investigated. CNTs are promising materials for a gas sensor because of their unique properties; small size, large specific surface area and high aspect ratio. However, the conductance of bare CNTs gives a small response to many analytes and therefore the formation of CNT composites with other polymeric materials to enhance the sensing performance was explored.

The first part of the study is based on coating CNTs by polypyrrole and using these composites to detect volatile organic compounds (VOCs: methanol, ethanol, acetone and chloroform). Polypyrrole (Ppy)-coated CNTs were prepared by an *in situ* oxidative polymerization method with $FeCl_3$:$6H_2O$ as the oxidant. TEM and AFM images showed a significant change in the diameter of the nanotubes upon polymerization from the mean value of 10 nm for multi walled carbon nanotubes (MWCNTs) to 60 nm after coating and from 5 nm to 50 nm for single-walled carbon nanotubes (SWCNTs). FTIR and Raman spectra indicated successful coupling between CNTs and polypyrrole. In addition, I-V characterization of two terminal nanotube devices and impedance spectroscopy demonstrated the change in the electrical properties of drop-cast CNT films after coating with polymer. The electrical current decreased after coating for both MWCNTs and SWCNTs (8 mA to 0.027 μA) and (10 mA to 88 μA) at an applied voltage of 2 V. Uncoated CNTs had a small analytical sensitivity (S), where S is defined as the percentage change in resistance upon exposure to analyte. For 12.9 kPa of methanol vapour, typically S < 1% for bare CNTs, while the sensitivity of the nanocomposites was typically S > 50% for 12.9 kPa of MeOH at room temperature. The sensing mechanism was found to be reversible and the temperature dependence could be analyzed using a simple extension of the Van't Hoff equation. This suggests that the temperature dependence of the sensitivity is controlled by the enthalpy of adsorption on the composite.

The second part of this study used CNTs/boron nitride nanotube (BNNTs) composites as an ozone gas sensor. Ozone is a powerful oxidant and polymer additives are not sufficiently robust for this application. CNT/BNNT films were prepared by drop-casting from equimolar solutions of BNNTs/methanol and CNTs/methanol. The electrical properties of drop-cast CNTs were changed after adding the insulating BNNTs; the electrical current decreased from 8 mA to 1 mA at applied voltage of 2 V. The sensitivity was improved from 18% to 50% for 80 ppm of ozone. However, the problem with the CNT ozone sensor was a long recovery time which can be 25 min or more, depending on the gas concentration. For CNTs/BNNTs the recovery time was shorter, but still lies between (2-17) min at room temperature.

The third part of the study was related to detection of CO gas by CNTs/Ppy at room temperature. It has been shown that the sensitivity of CNTs is enhanced after polypyrrole coating: S > 20% for SWCNTs/Ppy and S < 2% for SWCNTs at 1923 ppm CO in air. Again, the sensitivity of these nanotube composites decreased with increased temperature according to an adsorption equilibrium model.

The last part of this study evaluated DNA@CNT composites as a VOCs sensor. Three samples of CNTs/DNA were prepared with three different amounts of -DNA 2μL, 5 μL and 10 μL of (500 μg mL^{-1}) which were added to 50μL (0.001 mg mL^{-1}) of an aqueous dispersion of CNTs. DNA@CNT Films were drop cast across microelectrodes and from I-V measurements, it was found that the current (at a bias of 2 V) decreased after coating with increasing amounts of DNA from 8 mA (bare CNTs) to 4.5 mA to 2 mA and finally to 1 mA for the 50:10 sample. AFM and TEM images showed the DNA coats the CNTs and this suggests that tunnel junctions are introduced between CNTs which account for the drop in conductance. These junctions are also suggested to be the origin of the improved sensing response: DNA@CNT composites have good sensitivity for VOCs (MeOH, EtOH, C_3H_6O and $CHCl_3$) and are more sensitive to methanol vapour than other VOCs. Further, DNA/CNTs films show a larger response to chloroform vapour at 21.08 kPa than CNTs/Ppy films at room temperature. Interestingly, the sensitivity of CNTs/DNA films increased as the temperature was raised; this suggests that another mechanism apart from adsorption/desorption is involved in their response.

Although CNTs have been suggested as transducers in various gas sensors, they show a poor sensitivity (fractional change in resistance upon exposure to analyte). However by preparing composites of CNTs and less conductive materials, the analytical sensitivity can be greatly increased even though the conductivity of the composite is usually much less than of the bare CNTs.

Acknowledgments

I would like to express my sincere gratitude to my first supervisor ***Dr. Benjamin R. Horrocks*** for all his support, assistance and advice without I would have not been begin writing my thesis. Also many thanks to my second supervisor prof. ***Andrew Houlton*** for his supports and encouragement. I would like to thank the University of Newcastle upon Tyne for the opportunity to carry out my study, and the group of chemical nanoscience laboratories (CNL) staff and PhD students in the School of Environmental and Natural Sciences for all their help. I would like to thank Iraqi ministry of higher education for the funding and the scholarship and also I would like to thank my university (the university of Technology/ Baghdad-Iraq) for all the support and my school in Baghdad, Laser and Electronic Engineering for all the support. I would like to thank Dr. Osama El-Zubir in the school of School of Environmental and Natural Sciences at Newcastle University for all his help in AFM and XPS analysis. And I should never forget to thank Dr Kathryn White and Mrs. Tracey for their help in TEM experiments. I would like to thank Dr Jose Portoles in NEXUS, School of Engineering for his supports in X-Ray Photoelectron Spectroscopy (XPS) analysis. And many thanks to Miss Robyn Hare (Glass Blower) in the Glassblowing Workshop and Gary Day, John Corner in the Mechanical Workshop and My gratitude and thanks to Chris Burrow and Geoff Reah in the Electronic Workshop at the School of Environmental and Natural Sciences for their help to set up the system of gas sensor. My appreciation to Dr Budhika Mendis, department of physics, Durham University for his

help in the high resolution TEM analysis. Finally, I would like to thank my family for their support and motivation me In spite of the far distance between us.

Dedication

To my Family

Abbreviations

CNTs	Carbon nanotubes
SWCNTs	Single walled carbon nanotubes
MWCNTs	Multi walled carbon nanotubes
DWCNTs	Double walled carbon nanotubes
Ch	Chiral vector
EAD	Electrical are discharge
LA	Laser ablation
CVD	Chemical vapour deposition
Eg	Energy gap
CPs	Conductive polymers
Py	Pyrrole
Ppy	Polypyrrole
MO	Metal oxide
PID	photoionization detector
AMGS	Amperometric gas sensor
BNNTs	Boron nitride nanotubes
e.V	Electron volt
VRH	Variable range hopping
ICP	Inductively couple plasma
S-SWCNTs	Semiconducting-single walled carbon nanotubes
QCM	Quartz crystal microbalances
SAWs	Surface acoustics wave
DEP	Dielectrophoresis
VOCs	Volatile organic compounds
W	Watt
H_z	Hertz
AFM	Atomic force microscope
TEM	Transmission electron microscope
BE	Binding energy

FTIR	Fourier transform infrared spectroscopy
IS	impedance spectroscopy
I-V	Current-Voltage
Ω	Ohm
K	Kelvin
ΔH^{θ}	Standard enthalpy of reaction
T	Temperature
XPS	X-ray photoelectron spectroscopy
EDX	Energy Dispersive X-Ray Analysis
q	Electron charge =1.6x10^{-19} C
S	Sensitivity
m	Electron mass = 9x10^{-31} Kg
G	Conductance in S
R_c	Contact resistance in Ω
R_b	Film resistance in Ω
i_{ss}	Current steady state in A
SEM	Scanning electron microscope
nm	Nanometer
J	Joule
R	Gas constant 8.314 J/mol
E_a	Activation energy
V	Volt
λ	Wavelength
μL	Microliter
E	Energy
P	Power in watt
P*	saturated vapour pressure
DMFC	Digital mass flow control
DMM	Digital Multimeters
mL	Millilitre
M	Molar
I	Current in Ampere

mol	Mole
f	Force in Newton (N)
^{o}C	Celsius
C	Capacitance
Z``	impedance for capacitance/ imaginary part in Ω
Z`	Real electrical resistance in Ω
w	angular frequency = $2\pi f$ in Hertz
Γ	Surface excess of the analyte
Γ_m	Monolayer coverage

Table of Contents

List of figures

List of tables

Chapter one: carbon nanotubes, properties and applications

In recent years, there has been an increasing interest in nanoscience, whose aim is to understand the behavior of structures of size in the range 1-10 nm. While many nano structures are currently under investigation, the area of carbon nanotubes is one of the most active[1]. Carbon is an atom that contains six electrons, two of them are core and the four remaining valence electrons are available to form bonds with other atoms. The most common allotropes of carbon are graphite and diamond. The high strength of diamond is due to covalent bonding of all the carbon atoms. On the other hand, in graphite there is a layered structure with a hexagonal arrangement of carbon atoms in each layer held together by strong covalent bonds, but also weak inter-layer bonding.

Figure (1-1) shows the new relatively recent discovery of a type of carbon[2] known as C_{60} which represents the first fullerene or “Buckyball” or “Buckminsterfullerene” and was discovered by H. Kroto, R. Smalley and R.F. Curl in 1985[3]. In 1991, using electron microscopy Iijima could analyse the carbon material (soot) and observed long and thin fibers known as carbon nanotubes[4].

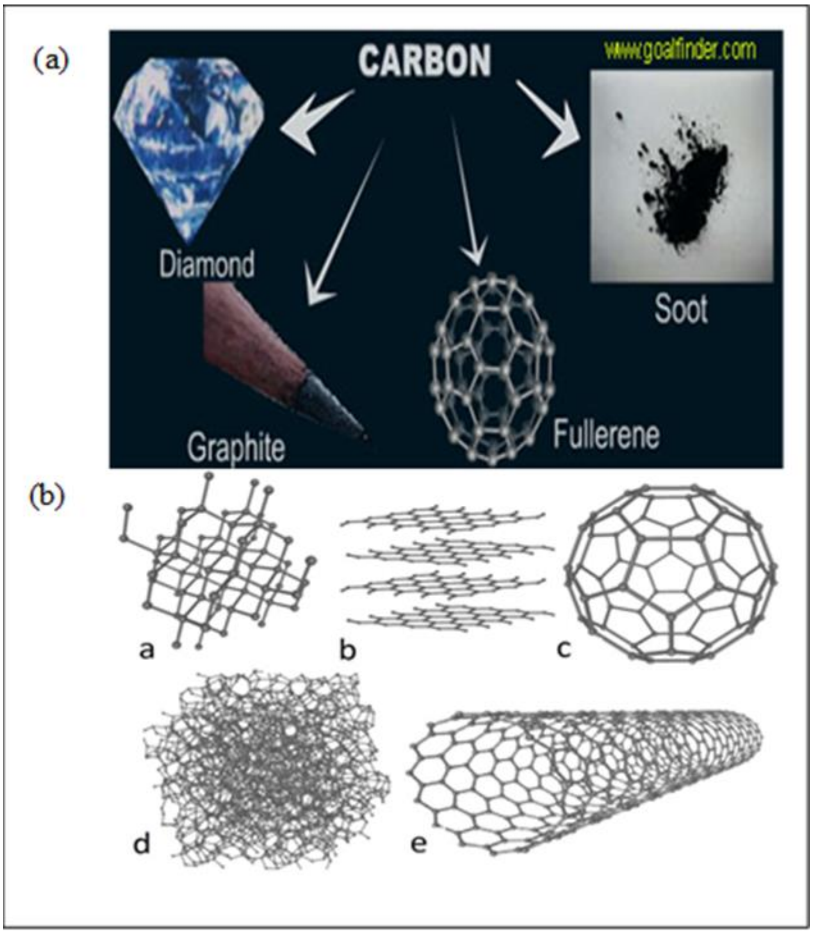

Figure 1-1 (a)types of carbon (b) five allotropes of carbon: a) diamond, b) graphite, c)C60 buckminsterfullerene, d) amorphous carbon, and e) single-walled carbon nanotube[1].

1.1. Carbon nanotubes

Carbon nanotubes may be considered as sheets of graphite rolled up into cylinders and can be capped; they are essentially hollow nanowires[1, 5]. In general, there are three types of CNTs, two major types and the other is a sub-type: Single Wall Carbon Nanotubes SWCNTs, Multiwall Carbon Nanotubes MWCNTs and Double Wall Carbon Nanotubes DWCNTs[6].

1.1.1. Multi walled carbon nanotubes MWCNTs

MWCNTs were discovered in 1991 by Iijima[6-8], figure (1-2) displays the first TEM images of MWCNTs by Iijima after his experiment with the arc discharge[9].

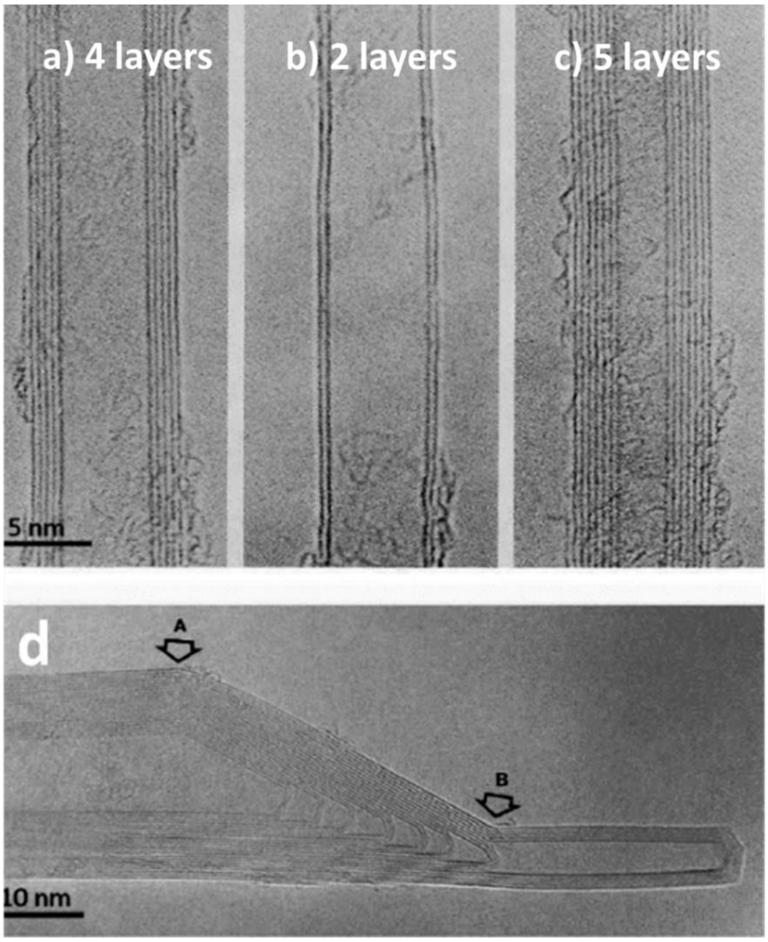

Figure 1-2 The first HRTEM image of MWCNTs-Russian doll with different number of walls, a)4 layers; b)two layers and c) five layers ; d) bamboo of CNTs[10].

MWCNTs have different numbers of graphite layers and form in two different shapes parchment/Swiss roll and Russian doll[11], as shown in figure (1-3 a&b). Their diameter can be between 10-20 nm with a separation distance 0.34 nm between the layers[5, 12]. They may have either open or closed ends according to high resolution TEM (HRTEM). MWCNTs can also have a bamboo shape as shown in figure (1-4)[11]. However, Russian doll CNTs can describe sheets of graphite arranged in concentric cylinders, for example (0,5) SWCNTs within a larger (0,12) SWCNTs, as shown in figure (1-4a). Parchment-type CNTs are a single sheet of graphite rolled in around itself as a newspaper is rolled, as demonstrated in figure (1-4b). The external layer of MWCNTs can protect the internal layers from chemical reactions.

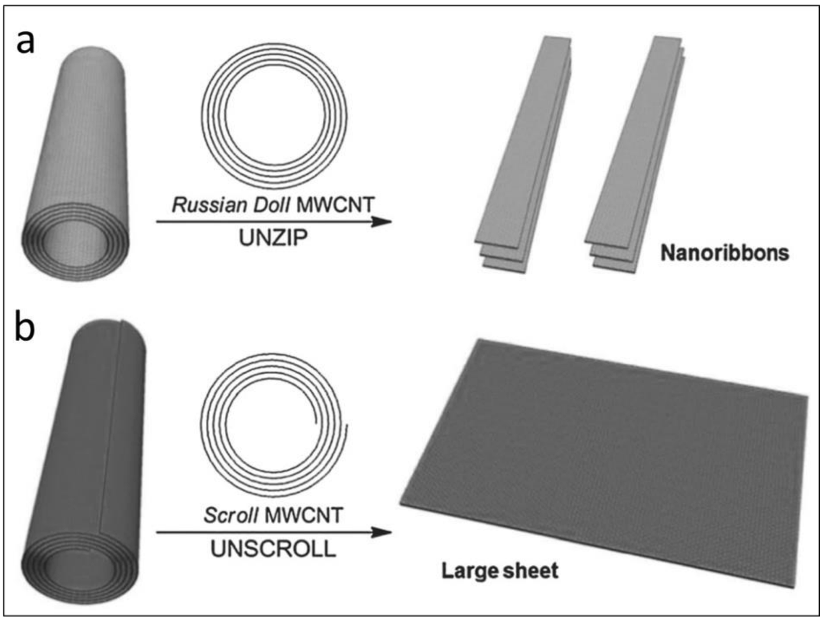

Figure 1-3 a) One bamboo stick (plant); (b&c) HRTEM images of CNTs as a bamboo structure[9, 13]

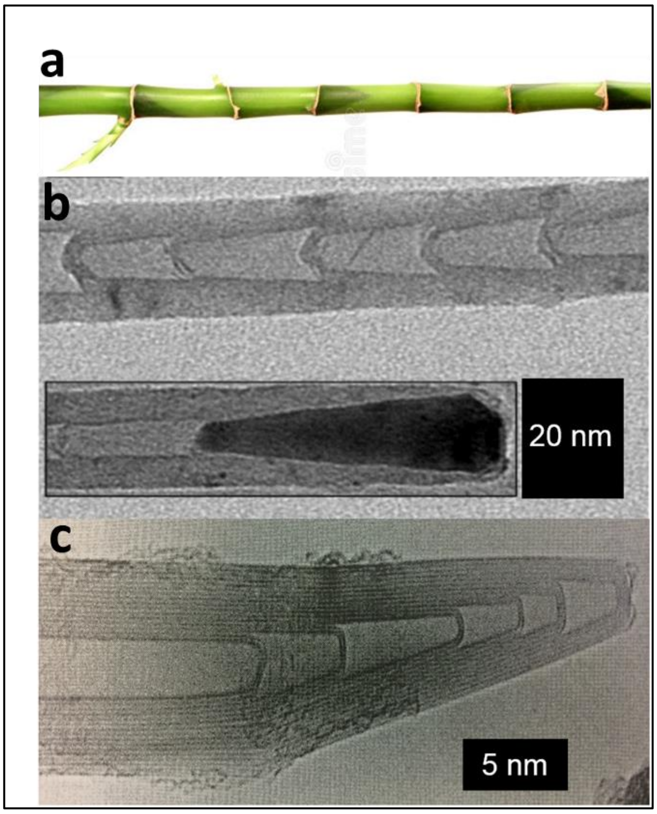

Figure 1-4 Two models for multiwall carbon nanotubes a) Russian doll consisting of a number of nanoribbons, b) structure parchment model from large sheet of graphite[14].

1.1.2. Single walled carbon nanotubes SWCNTs

SWCNTs were discovered in 1993, two years after the discovery of MWCNTs, by Iijima's group and Bethune et al.[4]. Figure (1-5) shows the first TEM of SWCNTs taken by Iijima [9, 10].

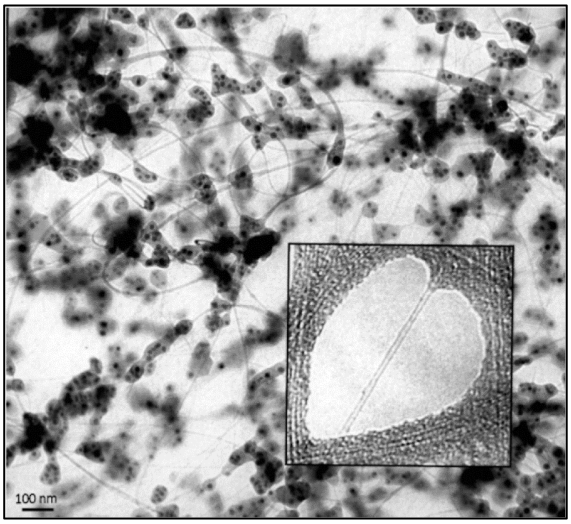

Figure 1-5 The first HRTEM image of SWCNTs was published in Nature journal[10]

The TEM image shows many curves and loops of SWNTs with small particles (black dots), which are impurity particles. The diameter of SWCNTs is (0.5-1.3) nm and the tube length can reach the micrometre range. However, there are three types of SWCNTs depending on the wrapped direction of the graphene sheet: zigzag, chiral and armchair[6, 15-17]. The ‘‘chiral vector’’ is a linear combination of $\overrightarrow{a_1}$ and $\overrightarrow{a_2}$ vectors[18], and is defined in figure (1-6).

$$Ch = (n,m) \Rightarrow n\overrightarrow{a_1} + m\overrightarrow{a_2} \qquad (1-1)$$

Where $\overline{a_1}$ and $\overline{a_2}$ are the lattice vectors in the 2D hexagonal lattice of a graphite sheet and n, m are integers. According to the CNT maps as seen in figure (1-6), θ is the angle between Ch and the zigzag direction. For zigzag nanotubes $\theta = zero\ (n, 0)$, for chiral nanotubes $0 \leq \theta \leq 30^o\ (n,m)$ and $\theta = 30^o$ for armchair nanotubes (n=m)[1, 9, 18, 19]. The diameter of SWCNTs depends [4, 20] on n and m.

$$d = \frac{a}{\pi}\sqrt{n^2 + nm + m^2} \qquad (1-2)$$

Where a=0.246 nm.

The electrical properties of CNTs depend on the roll direction of the graphene sheet, for example, armchair CNTs (n, n) are metallic nanotubes, while the zigzag (n, 0) and chiral (n, m) conductivity depends on n and m values. If $n - m = i3$, chiral CNTs are metallic nanotubes, but if $n - m \neq 3i$, CNTs are semiconductors and in the case of zigzag $n = 3i$, CNTs are metallic and if not, they are semiconducting nanotubes. Any change in the roll direction can therefore affect the electrical properties of carbon nanotubes.

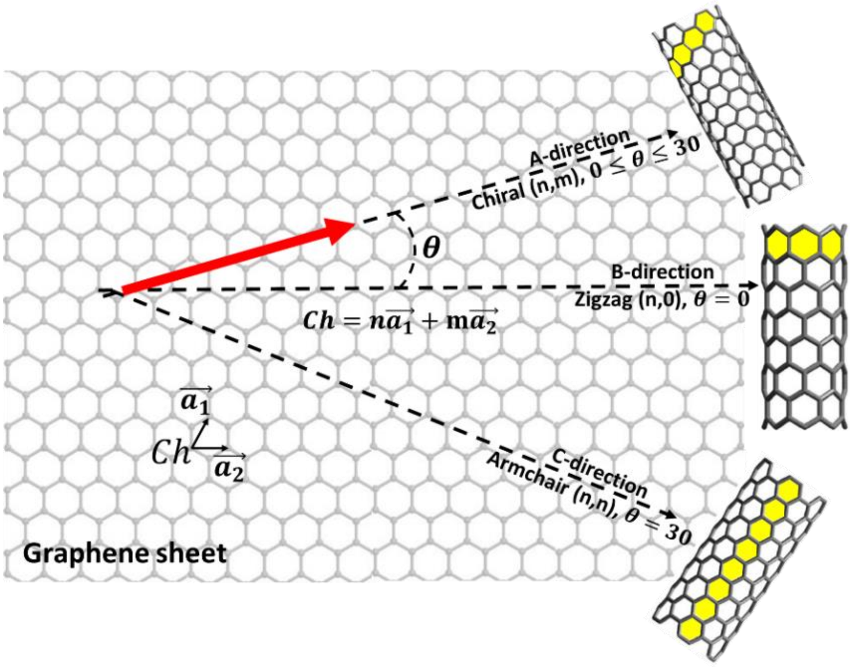

Figure 1-6 Map of SWCNTs on which is shown the three types of SWCNTs according to the roll direction.

1.1.3. Double walled carbon nanotubes DWCNTs

DWCNTs are a sub-class of MWCNTs with 0.34 nm as a distance between the two layers. DWCNTs have the similar structures to MWCNTs and the same physical properties as SWCNTs. This combination of properties encourages researchers to use DWNTs, in biosensors, biological applications and chemical sensors[21]. During preparation of DWCNTs, either SWCNTs or MWCNTs can be produced, therefore ultracentrifugation is used to separate the tubes[22].

1.2. The production of carbon nanotubes

There are many methods used to obtain carbon nanotubes, but the three most important are: *Electrical arc discharge (ECD), Laser ablation (LA) and Chemical vapor deposition (CVD).*

1.2.1. Electrical arc discharge EAD

EAD is the first method was used to produce MW-carbon nanotubes by Iijima in 1991[1]. The discharge happens between two electrodes: the cathode and the anode, which are made from graphite. In the case of SWCNTs, the chamber contains metal particles, for example, Ni, Co and Fe[23-25]. The typical distance between the electrodes is ~ 1mm, typical diameters are in the range 5–20 mm and the applied voltage 10-35 V with a current of 60-100 A. Because of the high temperature, the anode almost sublimes and the soot (carbon) is collected from the chamber walls and the cathode surface[26], figure (1-7) shows a diagram of the arc discharge approach. The advantage of this method is a large production of carbon, but the disadvantage is loss of control of the alignment of the nanotubes[25].

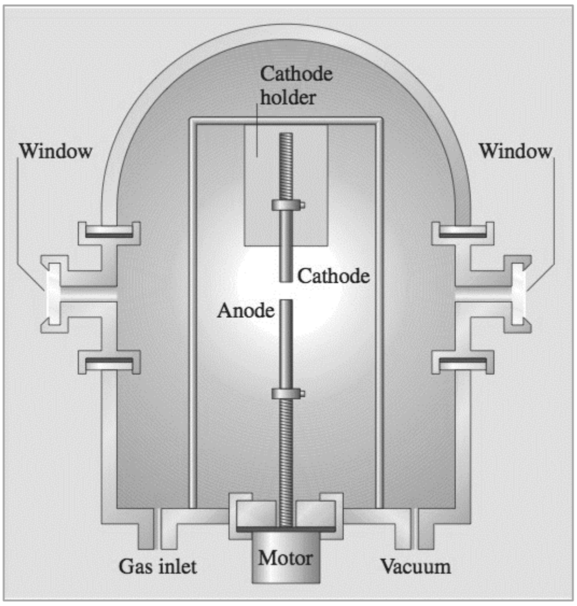

Figure 1-7 EAD method to fabricate CNTs[27]

1.2.2. Laser ablation LA

In this technique, a graphite target is settled on quartz tube and placed in an oven with temperature controller. A pulsed Nd:YAG laser (λ=1064 nm) is used with second harmonic generation (S.H.G) (λ=532 nm) or a CO_2 laser (continuous wave) with a wavelength 10.6 μm can be used to ablate the target and produce CNTs, as shown in figure (1-8). The CNT-containing soot is collected inside the instrument[11, 28]. Generally, the main advantage of the LA method is that it can produce a higher purity of nanotubes than CVD and EAD methods (absence of deliberately added metal particles), but smaller quantities of CNTs are produced compared to CVD and EAD.

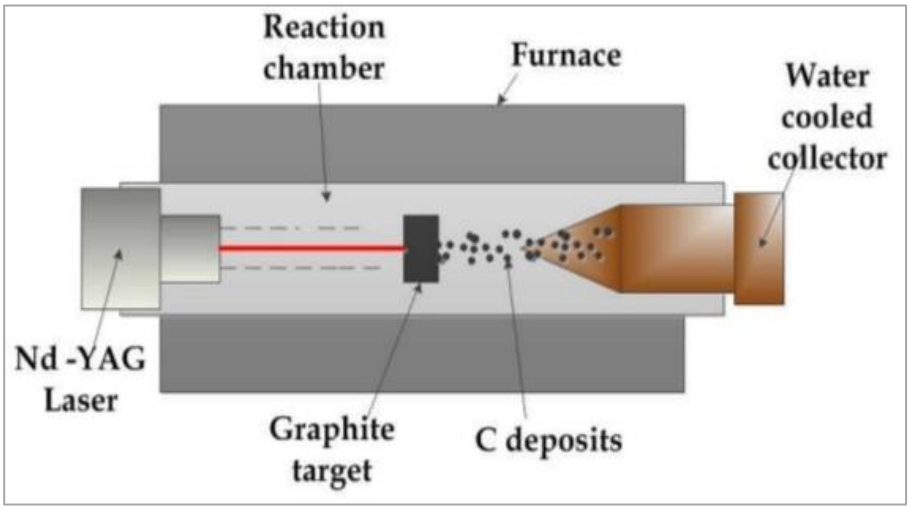

Figure 1-8 Schematic demonstrating the laser ablation method to produce CNTs using an Nd:YAG laser[29].

1.2.3. Chemical vapour deposition CVD

The CVD process depends on the thermal decomposition of gas molecules with high carbon content at a high temperature under the action of a catalyst[30]. The concept of this method is entrenching metallic particles such as Fe in the alignment holes in the Si, which is the substrate as shown in figure (1-9A). Furthermore, the nanotubes' diameters depend on the diameter of the metal seed. Pyrolysis of CO or hydrocarbons including butane, hexane, propane, benzene toluene and methane provides the carbon source. The synthetic process is performed at high temperature; (600-800) °C for MWCNTs and (900-1000) °C for SWCNTs[31]. The advantage of the CVD technique is that it produces large quantities of CNTs with high alignment of tubes. However, shrinking, cracking and curvature can be noticed on these tubes[11]. Figure (1-10) demonstrates the CVD technique to fabricate CNTs. According to the supplier information from Thomas Swan company https://thomas-swan.co.uk/, SWCNTs and

MWCNTs which were used in this thesis were produced by a CVD method. TEM images and EDX spectra indicate some Fe particles associated with nanotubes, as shown in chapter three figures (3-9) and (3-10). By weight, the sample purity was 70% for MWCNTs and 90% for SWCNTs.

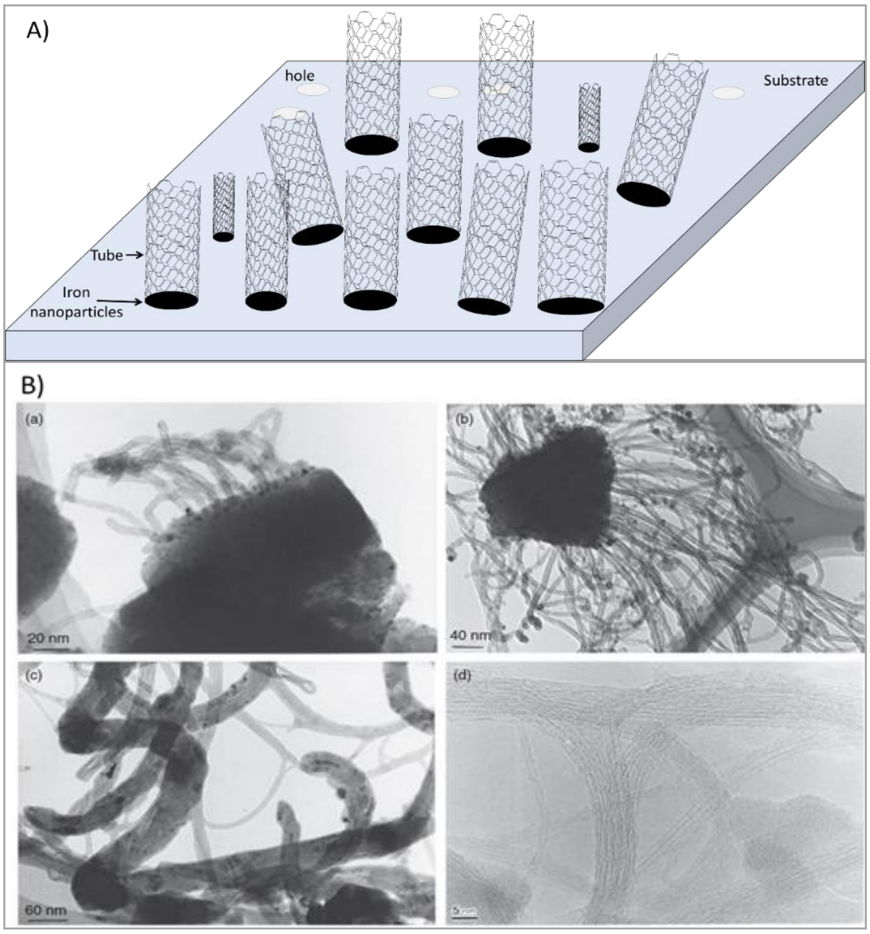

Figure 1-9 A) Scheme of growth of CNTs by the CVD method, nanotubes have different diameters which are depended on a metal diameter. B) TEM images of CNTs have been grown at different , temperature under the atmospheric pressure: (a,b and c) are MWCNTs were grown at 550C, 600C and 900C respectively; d) SWCNTs grown at 900C[32]*. (c and d) have good growth of the MW and SW nanotubes at a high temperature <550C.*

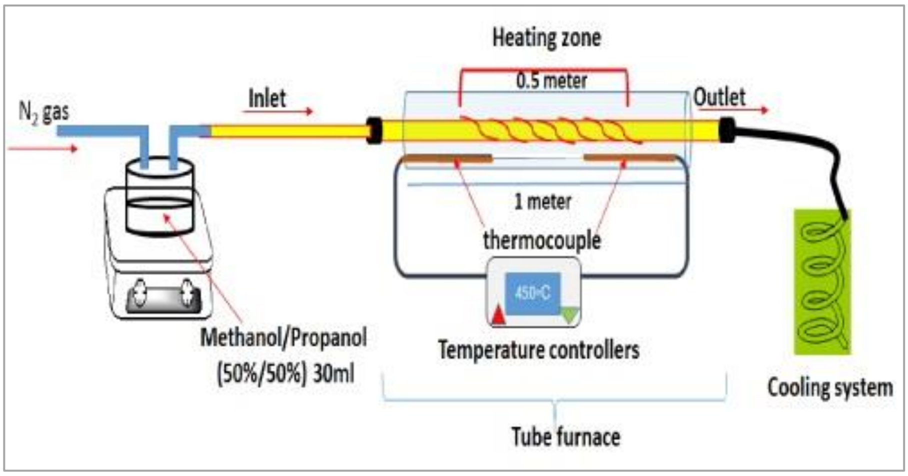

Figure 1-10 Schematic drawing of an CVD system to produce CNTs[33].

Table (1-1) shows the comparison of these techniques to produce CNTs.

Table 1-1 A comparison between the three methods to produce carbon nanotubes[34, 35]

Method	Arc discharge	CVD	Laser ablation
Who	Iijima, 1991	Endo, 1993	Smalley, 1995
MWCNTs	Diameter: inter (1-3) nm and (10 nm) outer diameter and short tubes	Diameter: (10-240) nm with long tubes	Diameter: 100 to 200 nm
SWCNTs	Diameter: (0.6-1.4) nm with short tubes	Diameter: (0.6-4) nm with long tubes	Diameter : ~ (1-2) nm. Length (5-20) µm.
Production	SWCNTs and MWCNTs, with some defects in the SWCNTs	SWCNTs and MWCNTs,	SWCNTs are more common than MWCNTs
Advantage	Cheap, large quantities of CNTs	Large quantities of CNTs with some control of the tube diameter	Higher purity compared to other methods
Disadvantage	Short tubes with a wide range of different sizes	More defects for MWCNTs than SWCNTs	Expensive because it depends on laser (CO_2 or Nd:YAG)

1.3. Properties of carbon nanotubes

Carbon nanotubes have a variety of remarkable physical properties. high aspect ratio and a high specific surface area make CNTs promising materials for applications requiring small conductive elements. Many researchers have attempted to use them in a range of applications, for example in sensors, transistors, super capacitors, water filtration and composite materials[4, 9, 35]. CNTs also have notable mechanical properties; they are a stronger material than steel. Table (1-2) shows some of the mechanical properties of CNTs and a comparison to other materials. They are one of the strongest materials discovered; this is because of the short, strong sp^2 bonds between the sp^2 carbon atoms[1] . However, the hollow structure of CNTs means the tubes can lose their strength under compression[36].

Table 1-2 Young's modulus and tensile strength of CNTs compared to other materials[24]

CNTs	Young's Modulus (GPa)	Tensile Strength (GPa)
MWCNTs	1200	150
SWCNTs	1054	150
Steel	208	0.4
wood	16	0.008

Singh and coauthors reported that CNTs have excellent thermal conductivity, higher than copper. They can transmit ≥6000 $W\ K^{-1}\ m^{-1}$ compared to copper ~ 385 $W\ K^{-1}\ m^{-1}$. They showed stable thermal conductivity at 750 °C under air and at 2800 °C in vacuum[37, 38]. CNTs can support a higher current density than copper ~ 10^{13} A cm^{-2} while 10^5 A cm^{-2} is the typical limit for Cu[36, 39] . It has also been found that under certain conditions, the charge transport in the nanotubes can be ballistic; this happens when the mean free path of the electrons between scattering events exceeds the tube length[40]. These unique properties of CNTs open the door for many researchers to use them in a wide range of applications in different fields. In particular, SWCNTs and MWCNTs are promising materials in sensing applications[25, 41]. A change in the tube's diameter or chiral angle affects the electrical properties of CNTs[42]. The CVD growth of CNTs proceeds from nanoparticle seeds such as Fe. These nanoparticles may undergo agglomeration because of the high temperatures in the growth of CNTs and the control of the nucleation and growth process is very important for the electrical properties of the nanotubes[43, 44]

CNTs can be either semiconducting or metallic and it has been reported that the energy gap of semiconducting tubes is related to their chirality[45, 46] and proportional to the inverse of their diameters[47] . In general, SWCNTs are grouped in bundles and the interactions between them are dominated by Van der Waals' forces. In these bundles, a few CNTs are metallic. Photoluminescence from the recombination of electron-hole pairs across the band gap is expected[19], but the metallic CNTs may provide a non-radiative channel. The luminescence of the bundles of semiconducting CNTs may therefore be quenched because of the interaction between metallic and semiconducting NTs. In order to observe the photoluminescence, the bundles should be separated as individual tubes. The most common technique to separate the nanotubes is the sonication process[45, 48].

The electronic structure of CNTs includes an extensive π-electron system, figure (1-11). The density of states shows Van Hove Singularities (VHSs) of the form typical for a one-dimensional system.

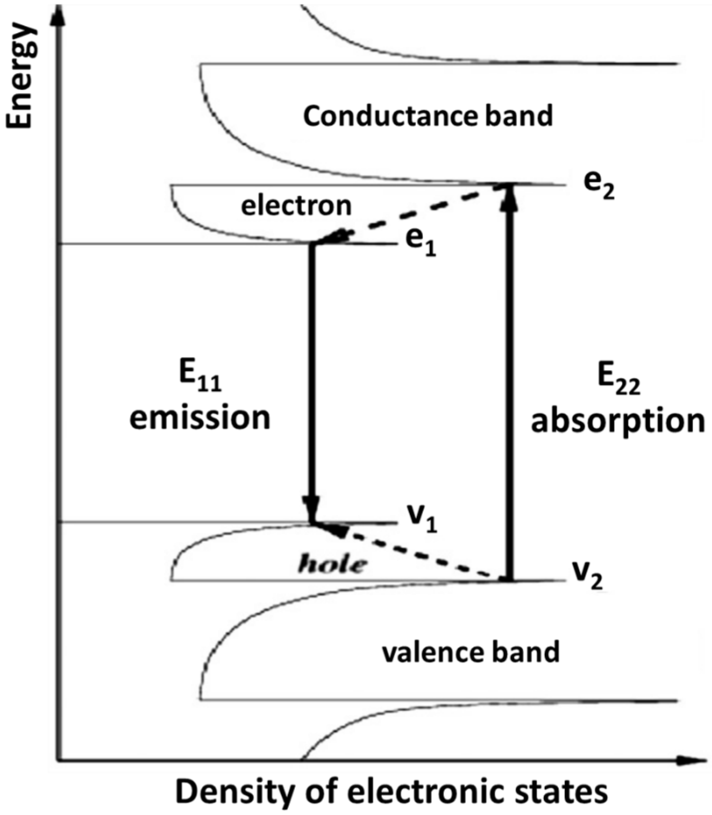

Figure 1-11 scheme of photoluminescence excitation for semiconducting SWCNTs. The conductance and valence Van Hove Singularities (VHSs) are categorized with the sub-band index. The dashed lines demonstrate non-radiative transitions for holes and electrons. Optical transitions E_{11} *and* E_{22} *are also clarified*[19].

The optical spectroscopy of the semiconducting nanotubes corresponds to transitions between the corresponding VHSs in the conductance and valence band DOS[49] which are denoted E_{11} and E_{22} in figure (1-11). The photoluminescence emission is the (E_{11}) transition. The energy of VHS maxima is dependent on the diameter of CNTs[50]., consequently, different *n* and *m* of SWCNTs will demonstrate various distinct E_{xx} transitions and show different wavelengths[51]. As a result, the diameters and the geometries could be obtained by an analysis of the photoluminescence spectra, however, the data also seems to be sensitive to the purity and to the presence of chemical defects[45]. Van Hove Singularities (VHSs) in the density of states can have a profound effect on the electrical and structural properties of solids[52]. The quantization of electronic states of small diameter nanostructures also influences the chemical and physical properties. Recently, many studies of pairing mechanisms at VHSs in carbon nanotubes and graphene predict superconductivity with a transition temperature[61-64] >10 K. Figure (1-12) shows the density of states of semiconducting nanotubes with sharp VHSs at the onset of sub-bands with ΔE_{VHS} as an energy spacing between the sub-band 1 and 2 as shown in the figure (1-12). The energy is determined by the CNTs diameter[65-68]. For each sub-band, the electron energy level spacing is set by the length of the nanotubes and is almost constant in the linear part of the sub-band. The level spacing becomes smaller at the onset of the sub-band, as demonstrated by ΔE_1 and ΔE_2 for the 1 and 2 sub-bands. Generally, Van Hove Singularities affect interfacial models of the electronic wave functions in CNTs and can be identified in the transport measurements in single CNTs.

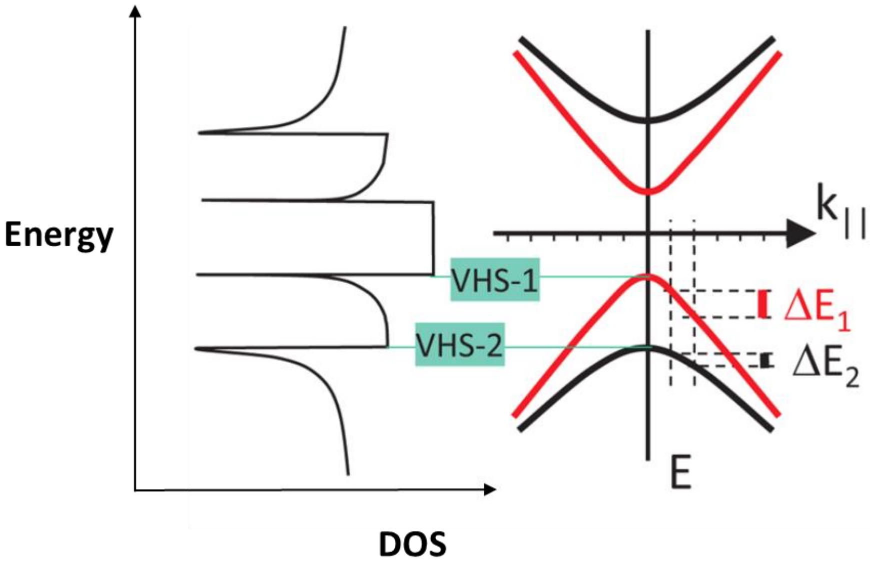

Figure 1-12 Schematic of the electronic band structure (right) and the density of states (left) of a semiconducting carbon nanotube. The energy level spacing near the onset of a new sub-band, ΔE_2 (black vertical bar) is smaller than the energy level spacing ΔE_1 in the linear part of the dispersion relation (red vertical bar)[52].

Charge transport in a network of semiconducting nanotubes can be modelled as a random- resistor network with resistors at the CNT-CNT junctions. The charge transport is facile inside CNTs, but more resistance is encountered at the junction points as shown in figure (1-13). At the junctions, the charge transport involves variable range hopping VRH and each junction is represented as a resistance. It has been reported that the conductivity measurements and temperature-dependent mobility in dense CNT networks clearly demonstrate thermally activated transport, which is described by variable, range hopping VRH or fluctuation induced tunneling[36, 37]. However, in this thesis we observe that networks of CNTs may also show metallic behaviour (resistance increasing with increasing temperature). The electrical properties of networks of MWCNTs and SWCNTs will be described in chapter three.

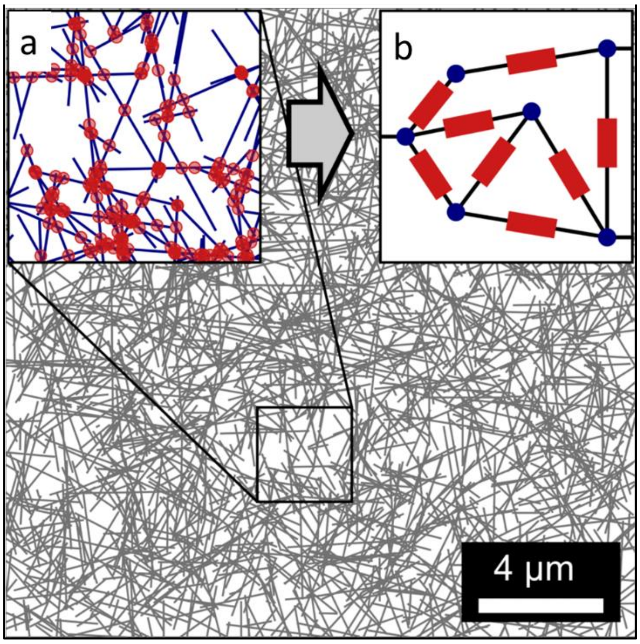

Figure 1-13 2-dimensional network of 1D sticks as a geometric pattern for SWCNTs (grey network),(a) illustrates the junctions (red points) between SWCNTs (blue lines) and their conversion into a random resistor network as shown in (b) with the junctions acting as resistors and SWCNTs as nodes[69].

1.4. Conductive polymers

Conductive polymers such as polypyrrole, polyaniline and polythiophene are promising materials because of their electrical properties and have many applications, for example, as sensors and electrical supercapacitors[38, 39]. In addition, conductive polymers have reasonable strength, low density and simple processing (polymerization)[5]. Pyrrole is one of the class of aromatic organic heterocycles. It is a colourless liquid at room temperature, but easily oxidized and gradually becomes yellow upon exposure to air[40]. Before using pyrrole, it is recommended to distill it to remove the yellow oxidation products. Polypyrrole has the structure shown in figure (1-14)[41].

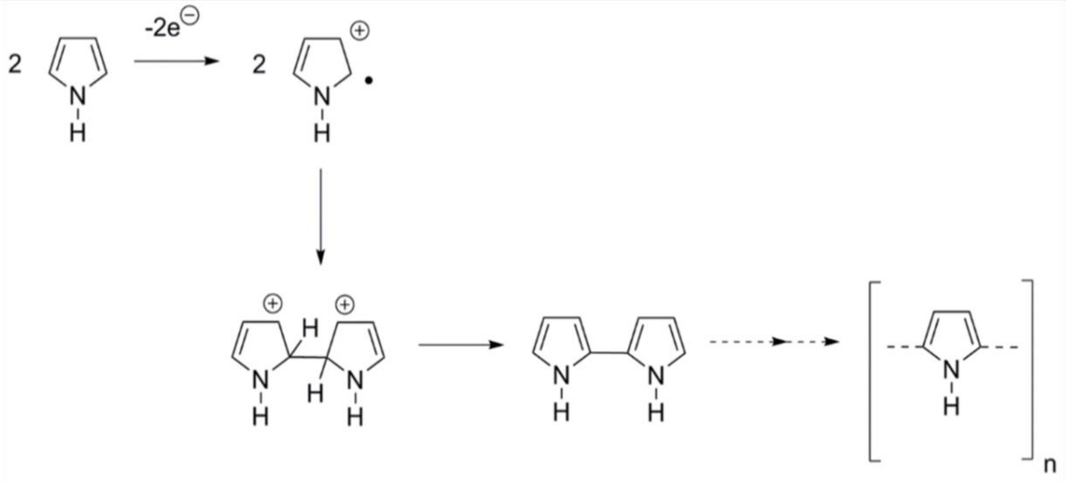

The first step is the oxidation of pyrrole to form a cation radical. When two of these are produced, they can couple via the C2 position and subsequently lose $2H^+$ to form the pyrrole dimer. The pyrrole dimer has more extended conjugation and is oxidized at lower electrode potential, so will be rapidly oxidized under the experimental conditions. The dimer radical cation can couple with another pyrrole radical cation to form a trimer and the process can continue.

Figure 1-14 mechanism of the oxidative polymerization of pyrrole.

There are two common methods to polymerize CPs: electrical and chemical polymerization. Chemical polymerization is convenient to prepare bulk samples of material and also dispersions, while electrochemical polymerization would be preferred to produce a thin layer of polymer on a conductive substrate[42]. In our case, CP/CNT composites were desired and because these were later drop-cast onto substrates which were not uniformly conductive (lithographically defined microelectrodes with insulating gaps on SiO_2), the chemical polymerization method was preferred. The oxidation process leads to long chains of pyrrole monomers by the action of iron(III) chloride ($FeCl_3$) and the polymerization process happens via the formation and oligomerization of the pi-radical cation $C_4H_4NH^{+\bullet}$.

$$2[C_4N_5H] + 2FeCl_3 \rightarrow [C_4H_4N]_2 + 2FeCl_2 + 2HCl$$

The spin density on the radical cation is predominantly at the C2 position and therefore the radical cations tend to dimerize by the formation of s-bond via C2 carbons on each pyrrole unit. This leads to a linear polymer as shown in figure 1-14. As prepared, the polymer is in an oxidized, polycationic, conductive state.

The coupling between CNTs and polypyrrole produces a composite material with good electrochemical charge storage properties[43]. Electrochemical capacitors have attracted attention in high power-energy storage devices and there have been many attempts to use conducting polymers, such as polypyrrole (Ppy) and polyaniline (PANI) in these applications[44]. Polypyrrole is a promising material in many applications because it is insoluble, infusible, has high adhesion to iron or steel treated with nitric acid, higher conductivity, easy synthesis and low cost compared with other polymers[45, 46]. The main applications of polypyrrole are in electronic devices and chemical sensors. Carbon nanotubes can be coated with Ppy to alter their electrical properties in sensing applications. In general, CNT/CPs as nanocomposite materials can show different mechanical, electric, optical, electrochemical, catalytic, and structural properties to those of each individual component. It has been shown that many specific properties of the composite exceed the sum of the values for individual components[47]. CNTs/Ppy films are significant materials, especially in sensing applications. Polypyrrole-carbon nanotube composites have a core/shell structure in which the polymer coats the nanotubes as shown in figure (2-3) and more TEM images in the appendix S2 and S3. There is a strong interaction between the nanotubes and the polypyrrole matrix[48-50]. Although CPs are generally much less conductive than metallic CNTs, the Ppy/CNT composite has advantages in sensing because the conductance of the composite is more responsive than that of the bare CNTs (Chapter 3). Generally, the change in the conductivity of CPs upon exposure to various vapours has been attributed to two mechanisms[5] : (i) structural changes related to polymer swelling and (ii) electron transfer between the vapour and the polymer leading to changes in the density of carriers in the polymer. In addition, the change in the configuration of the nanotubes after coating can affect the charge transport in networks where the conductance depends on the pathway by which the carriers move through the network. Generally, variable range hopping (VRH) is the main theoretical model for charge transport in these nanomaterials [51].

1.5. Boron nitride nanotubes BNNTs

BNNTs have a similar structure to CNTs[52]. A hexagonal arrangement of alternating B and N atoms is isoelectronic to graphite on a simple electron-counting argument. In 1995, arc discharge was the main method used to produce BNNTs. Later researchers used laser ablation and CVD to fabricate BNNTs[53]. Recently, ICP technology ‘‘inductively coupled plasma’’ was used to create these nanotubes[54, 55]. Although, BNNTs have a similar structure to CNTs, BNNTs have a different electrical behaviour. They are insulating nanotubes with a wide band gap[56] (5.5 – 6) e.V. BNNTs are stable thermally and chemically at 800°C with a good thermal conductivity [56]

~ 600 W K^{-1} m^{-1}. Figure (1-15) shows the differences and similarities between CNTs and BNNTs. BNNTs also have a yarn structure in two types single walled or multi walled (2-5) walls[57], the coupling between CNTs and BNNTs (CNBNNTs) produces a promising sensor to detect ozone gas (Chapter 4), in fact there are no deep studies on this specific subject and in our study we will present the effect of CNTs-BNNTs thin films on ozone detection.

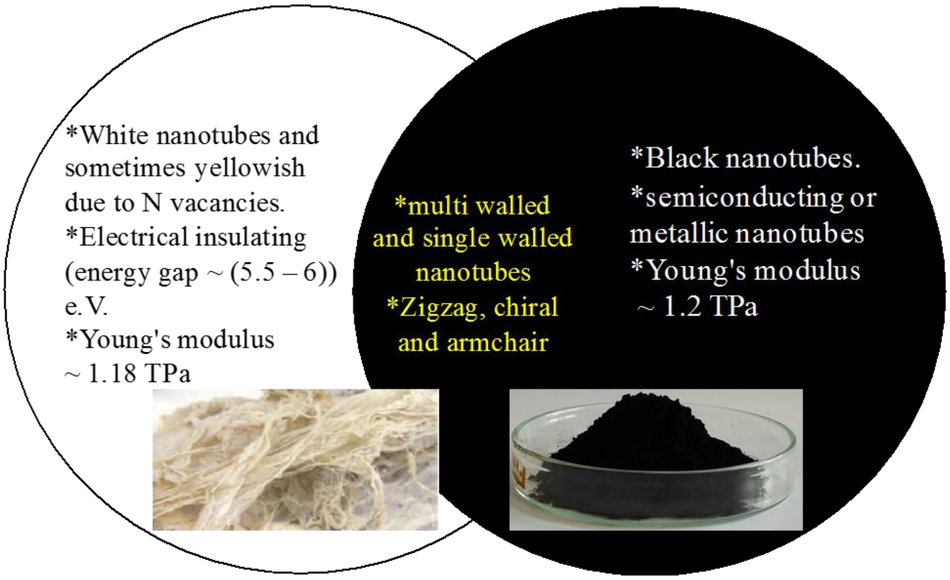

Figure 1-15 Comparison between CNTs and BNNTs[24, 57]

1.6. Carbon nanotubes as gas sensors

The development of nanotechnology has created the potential to build highly sensitive, portable sensors, which are low-cost and consume little power. Gas sensors have a wide range of applications in medical, agriculture, industry and environmental situations, especially with the increasing concern surrounding air quality and global warming[58]. An excellent gas sensor should be sensitive, reliable, low-cost and responsive;

therefore, it was necessary to search for new sensing technology and materials[59, 60]. CNTs have been developed as gas sensors because of their unique properties, for example their small size, hollow centre, nanometre size, large surface area and the ability to change their electrical resistance when exposed to gases at room temperature[61, 62]. In addition, CNTs have a good thermal conductivity, encouraging researchers to consider applications for carbon nanotubes in high temperature gas sensors[16]. Figure (1-16) shows the histogram of numbers of papers about CNTs from Web of Science in different topics from (properties and their applications) between 2001 to May 2018.

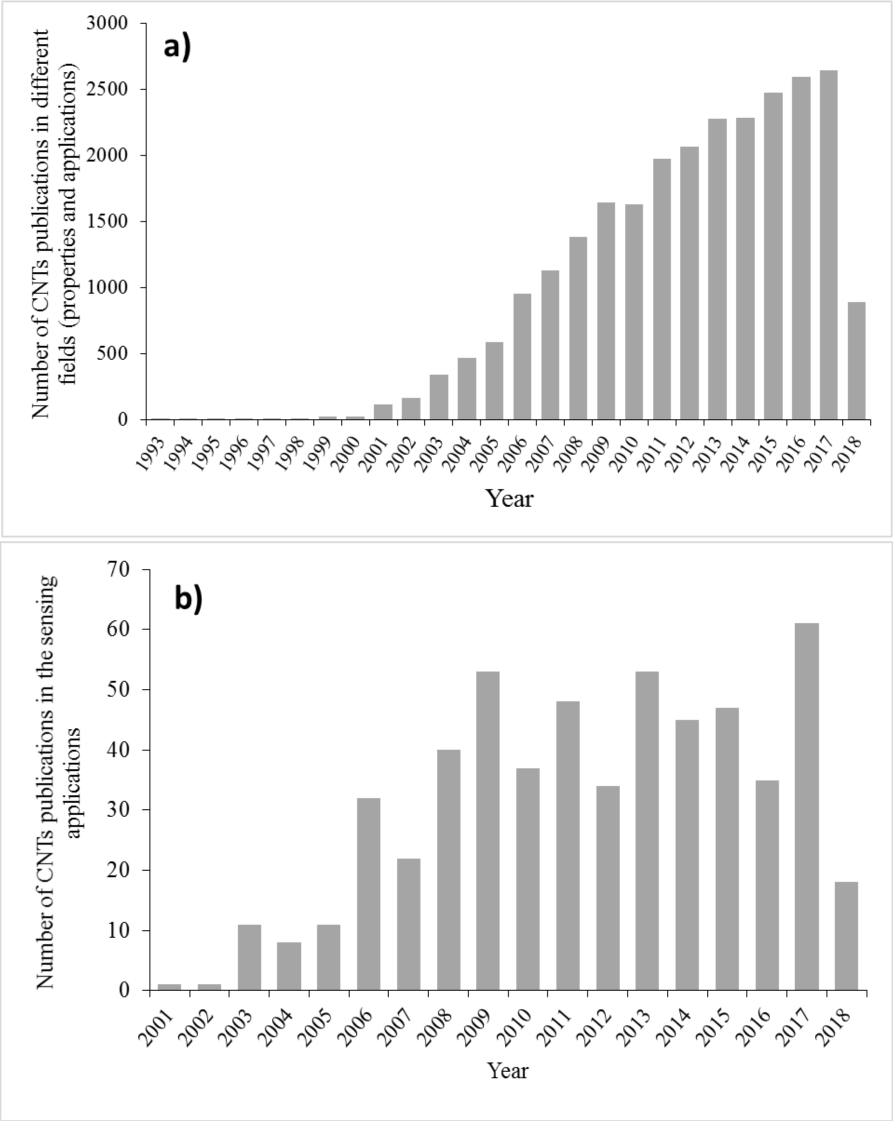

Figure 1-16 The histogram of a) the numbers of CNTs publications in different subjects (properties and applications); (b) numbers of CNTs publications as a gas sensor. All the data was taken from Web of Science http://wok.mimas.ac.uk/. May 2018.

Generally, there are three types of common commercial gas sensors: metal oxide (MO), photoionization detector PID and amperometric[63-65]. Metal oxide: there are two types of MO gas sensors, n-type and p-type. Each depends on the resistance change caused by injection of electrons from the analyte into the semiconducting metal oxide. N-type devices are simple to manufacture and operate at a low temperature, but these sensors have three problems: sensitivity to humidity, negative response and baseline drift. In contrast, p-type devices have a low sensitivity to humidity and a positive gas response (resistance *increases* in the presence of analyte) and a stable baseline. MO sensors have been widely used in industrial safety applications, e.g., to detect H_2S gas at temperatures upon > 120^oC (for oil and gas applications), VOCs for low cost IAQ[1] applications and carbon monoxide for humid environments or extreme temperatures. MO n-type devices have used to detect organic compounds in the range between 10 to 50 ppb[65] and p-type devices to detect high concentrations of VOCs[65]. In general, MO sensors have a nonlinear relationship between the gas concentration and sensor resistance, although a linear relationship has been found for H_2S at < 20 ppm and < 50 ppm for CO gas. MO gas sensors are used to detect the CO, VOCs, H_2S gas in both harsh and benign environments with working temperatures between 20 to 120 ^oC. However, the operating principle of MO devices requires high temperatures for the MO film, typically of the order of 400 ^oC. The MO sensor depends on the redox reaction between the gas and the MO film of the device and the high temperature of the MO film is necessary to drive the reaction. Electron transfer to/from the gas changes the electrical resistance of the sensitive layer, which is printed on a chip that includes co-planar interdigitated electrodes and an integrated heater[65].

---

[1] IAQ: Indoor air quality.

Photoionization detectors (PID) show a good response for VOCs. One of the major manufacturers, Alphasense Ltd., sells two models of PID: PID-AH2 (Photoionization detector (ppb)) and PID-A12 (Photoionization detector (ppm))[65]. PID-A12 has a linear range of 50 ppb to 6,000 ppm and 1 ppb to 50 ppm for PID-AH2. The working temperature is between -40 to 55 ^{o}C for PID-AH2 and PID-A12. When the gas enters the top of the film filter of the PID cell (figure 1-17c), it diffuses into the chamber formed by the filter, walls and UV-lamp. The UV-lamp emits photons at high energy and when the gas molecules absorb such a photon two ions are generated positive X^+ and negative Y^-. The electrical field between two electrodes (anode and cathode) causes a current to flow depending on the amount of ionized gas. From the current measured, the gas concentration is determined. In this type of gas sensor, a fence electrode was added to avoid any significant contributions from water in the chamber[65]. The lifetime of the sensors is typically five years with about 5000 hours for the lifetime of the UV-lamp. PID detectors have a fast response time, typically ~ 3 s. Since PIDs are not purely electrical devices, they have practical disadvantages associated with the power consumed by the UV lamp.

Amperometric gas sensors (AMGS) require very little power to operate and have a linear sensitivity, but a slightly longer response time < 50 s. This type of the sensor is classified as an electrochemical sensor and is used to detect carbon monoxide, oxygen, NO_x, SO_x, hydrogen and any gas that may be oxidized or reduced with a linear calibration of the device current against the volume fraction of the analyte. It has been shown that AMGS are suitable for higher gas concentrations than the other sensor types described above. The typical structure of an AMGS consists of a stack of several layers corresponding to the three electrodes required. At the top is the sensing (working) electrode, covered with a gas-permeable membrane, next is the reference electrode and finally the counter electrode layer. A potentiostat controls the sensing-reference potential and records the current flowing between the sensing and counter electrodes. This applied potential is chosen so that the oxidation/reduction of the analyte at the sensing electrode proceeds at the mass-transport limited rate. Under this condition, the current is directly proportional to the concentration of analyte and is insensitive to small fluctuations of the potential because the mass-transport rate is potential independent. In order to allow permeation of electrolyte through the stack and to increase the surface area of the electro catalysts, metal nanoparticle beds are usually used as the electrode layers. Pt and Pt-group metals are typical working electrode electro catalysts. Power consumption in AMGS is low because almost no current flows in the absence of analyte. The main disadvantages of AMGS relate to the electrolyte: evaporation of the electrolyte or absorption of ambient humidity can degrade the sensor performance over time and typical warranted lifetimes are about 2 years[65]. Figure (1-17) shows the MO, PID and AMGS sensors.

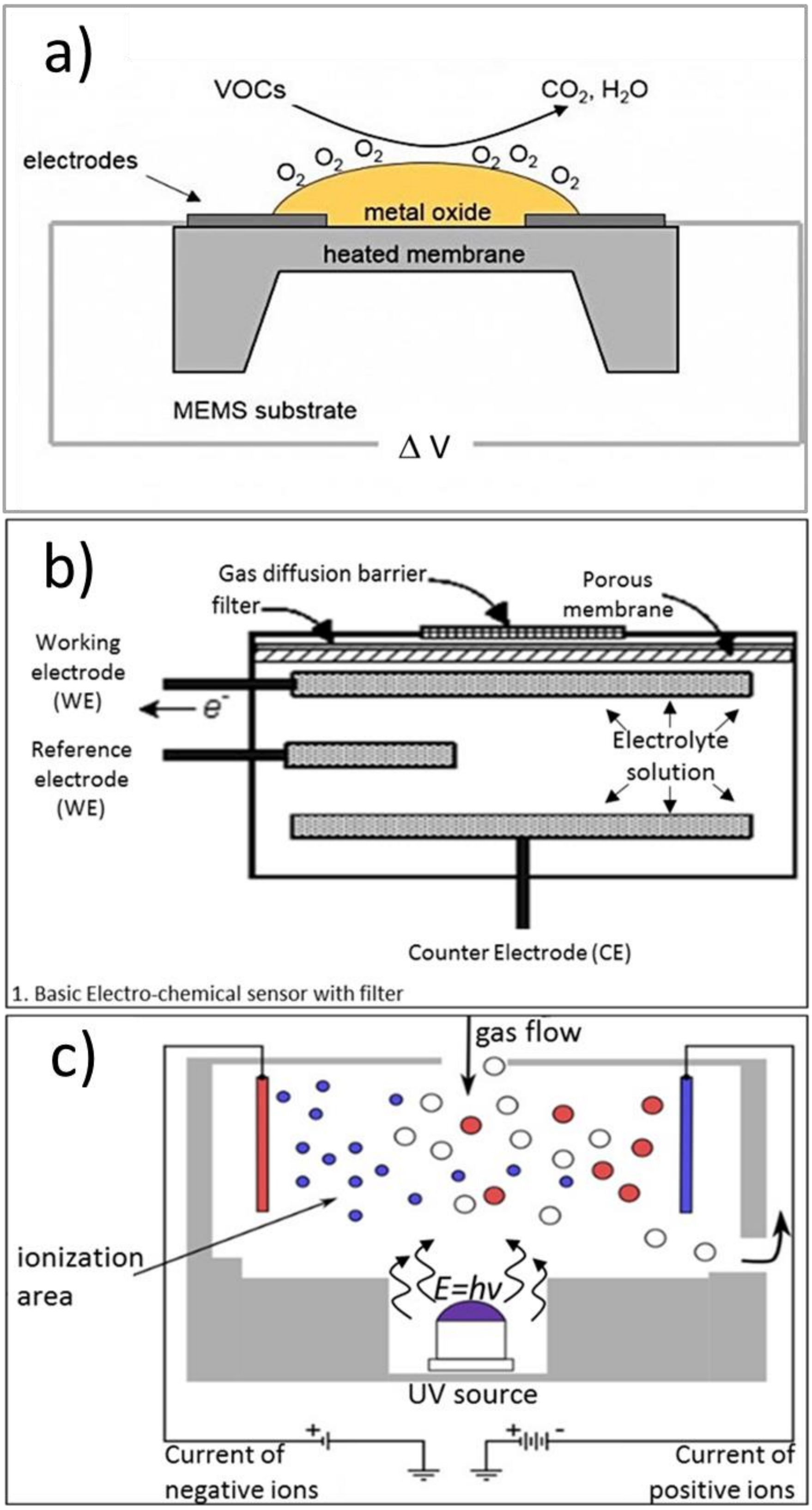

Figure 1-17 Shows a) Metal Oxide gas sensor b) Amperometric gas sensor and c) Photoionization detector[65, 66].

Since 2000, CNTs have become important materials in the sensing field. CNTs are used as bare nanotubes and as components of composites to alter the sensitivity of the devices. CNTs may be combined with nanoparticles, such Au, Ag, Pt, Ti or biopolymers (DNA, RNA) or conductive polymers or chemically altered by thermal treatment[67-71]. The devices generally operate using the change in conductance of CNTs in the presence of the analyte as the signal. The conductance may decrease or increase depending on the nature of the gaseous analyte (oxidant/reductant). The device signal may also originate from changes in the Schottky barrier at the CNTs/metal contact if the contact resistance is significant compared to the bulk resistance. Zhao et al[72] demonstrated that bare CNTs have a weak response for VOCs, NH_3 and NO_2. The adsorption of the gas molecules was suggested to either withdraw or donate electrons from/to CNTs and to produce a small change in the electrical properties of CNTs upon VOC/gas exposure[72]. However, it is not clear if this mechanism can explain the sensitivity to $NH_{3,}$ which is not easily oxidized or reduced under ambient conditions. Many studies have been reported[73] to use conductive polymers, Au, Ag ,Pt to enhance the sensitivity of carbon nanotubes to VOCs, NH_3, NO_2, O_3 and CO. Wang et al[73] investigated the sensitivity of SWCNTs/hexafluoroisopropanol (HFIP-PT) functionalized polythiophene (P3HT) for dimethyl methyl phosphonate (DMMP). They found that the sensitivity of hybrid CNTs increased after coating, which they attributed to strong H-bonding interactions with the analyte (DMMP) and they reported that DMMP changed the Schottky barrier of the

SWCNTs/HFIP-PT/Au contact. Young and Lin[74] investigated the effect of Au nanoparticles to enhance the sensitivity of CNTs for detection of ethanol vapour in the range (50 m Torr to 800 m Torr). Upon injection of different amounts of ethanol into a chamber containing the CNTs/Au sensor, they observed reversible changes to ethanol. The nanocomposite shows semiconducting behaviour and an increased resistance in the presence of ethanol. Nevertheless, the sensitivity of the CNTs/Au composite was slightly greater than for bare CNTs with a maximum response (percentage change in resistance) at 800 m Torr of 5.3% for the composite and 2% for the bare CNTs. Sanchez et al[75] investigated a sensing element comprising CNTs entrenched in a sol–gel TiO_2 matrix with the aim of detecting NH_3 and acetone vapour. They explained the acetone response by the creation of negatively charged ions at the TiO_2 clusters, but they indicated more investigation was required to propose a mechanism for the response to NH_3.

A variety of polymer/CNT composites have been studied, below the responses of the devices are discussed and the attempts to explain the mechanism of the response are considered. CNTs coated with poly(ethylene glycol) (PEG), CNTs/PEG showed higher sensitivity to isopropanol, acetone and ethanol than pristine nanotubes. The coating also improved the detection limit-LDL- of the sensor ~ 9 ppm. The response was reversible with a response time of 110-115 s and a recovery time 152-155s. Santhanama et al[76] studied the sensitivity of CNTs/poly(3-methylthiophene) to VOCs, CNTs were coated by in situ chemical polymerization process, they reported that CNTs/poly (3-methylthiophene) have a higher sensitivity to the chloromethane than acetone, MeOH, EtOH, THF and acetaldehyde. Santhanama et al explained the response of this nanocomposite film in terms of adsorption of the VOC and ionization $\mathrm{XA} + \mathrm{B} \rightarrow \mathrm{AX}^{+}\mathrm{B}^{-}$, where XA refers to $CHCl_3$, CCl_4, CH_2Cl_3 or CH_4 and B indicates the nanocomposite material. However, the charge transfer from such inert molecules as CH_4 seems unlikely at ambient temperature. In another study of CNTs and conductive polymer - based VOC sensors, Verma et al[77] showed that the sensitivity of MWCNTs/Poly(m-aminophenol)(PmAP) for MeOH, EtOH (aliphatic alcohols) increased compared to the pure PmAP at room temperature. Generally, conductive polymers coat CNTs by in situ chemical polymerization process. The adsorption of VOCs changed the electrical resistance of the nanocomposite film and MeOH showed a higher response compared to EtOH, which was attributed to greater film permeation by the smaller MeOH molecules and lower permeation by EtOH. Such an effect can be useful to control the selectivity towards various analytes, but it does not in itself explain the mechanism of the sensing response.

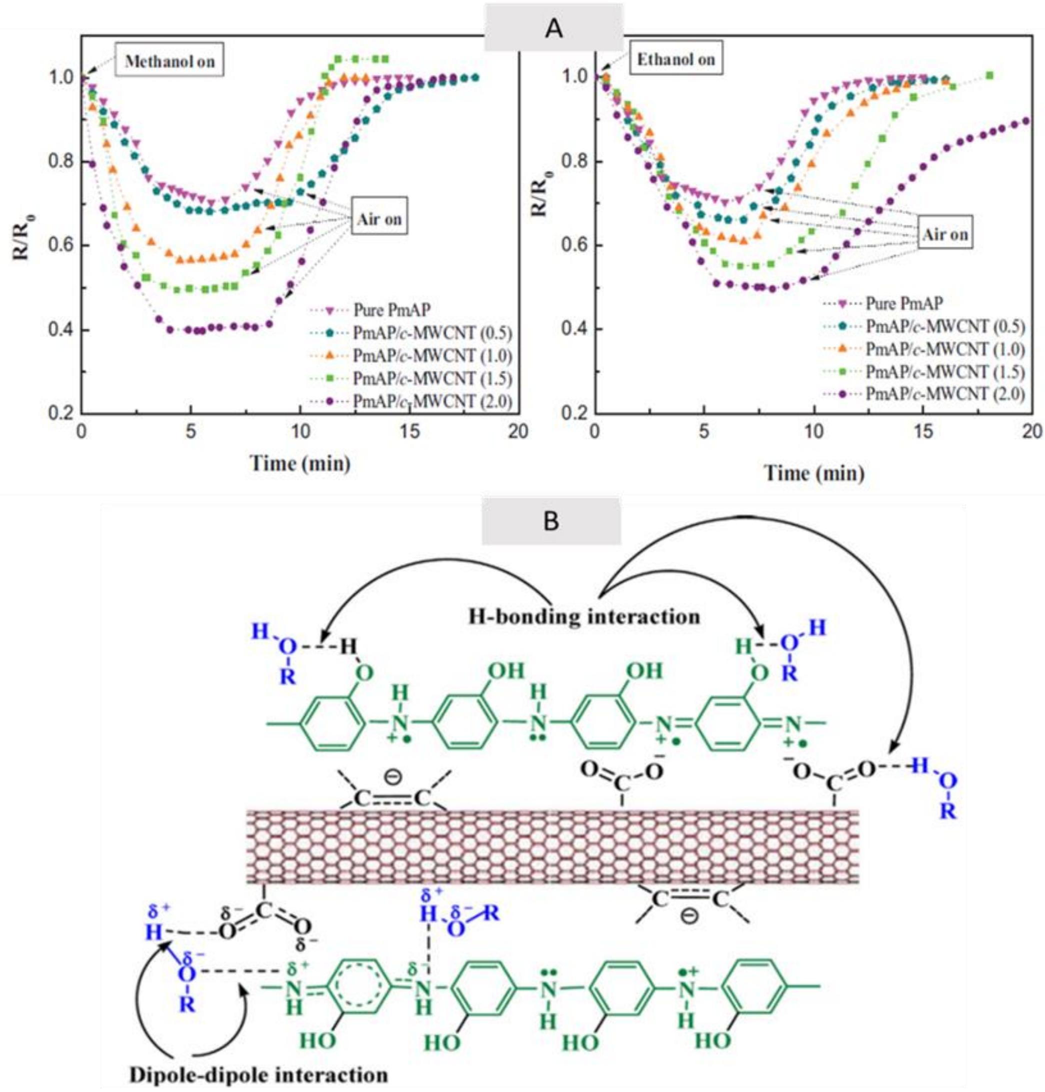

Scheme shows the electron delocalization and charge transport through the polymer chain and consequently decrease the resistance of the exposed nanocomposite sensor.

Figure 1-18 Proposed electrical responses of PmAP/c-MWCNT (2 wt%) nanocomposite sensor upon exposure of (a) methanol and (b) ethanol vapor at different concentration, i.e., 90 ppm (Δ), 140 ppm (•), 190 ppm (o) and 240 ppm (⌂). B) Scheme of the Interactions of MeOH vapour molecules with nanocomposites[77].

The decrease in the electrical resistance was attributed to an interaction between PmAP and alcohols via H-bonding as shown in figure (1-18b). Although such interactions can clearly lead to changes in the polymer conformation and perhaps their conductivity, it remains unclear how the CNTs are involved in the device response. In another study of CNTs decorated by polymer (Poly-methyl methacrylate)-microbands (PMMAµB) to detect VOCs, the coating process depended on spraying layer by layer. Feller et al[78] reported this method as an attempt to obtained a more reproducible and quantitative response to detect MeOH, EtOH, $CHCl_3$ and toluene. However, during VOC exposure, the electrical resistance increased in an irreversible manner. MeOH gave the highest response compared with other VOCs and the CNTs/(PMMAµB) is selective for MeOH over EtOH, $CHCl_3$ and toluene. EtOH, $CHCl_3$ and toluene showed approximately the same response. Feller et al found that pure PMMAµB did not function as well and that the selectivity and sensitivity of CNTs/(PMMAµB) were superior to bare CNTs. In general, the mechanism of operation of many CP/CNT devices is unclear, although many papers have shown good analytical performance. Mechanisms have been suggested involving swelling of the CP by the analyte or charge transfer between the analyte and the CP, but the role of the CNTs is unclear and the contribution of each component to the overall conductance of the device is often not known.

Collins et al[79] studied the sensitivity of SWCNTs as an oxygen gas sensor; the nanotubes were treated by heating to 700°C to remove microcrystalline and amorphous carbon. In this study, the electrical resistance increased during oxygen exposure and upon application of a vacuum, the resistance decreased. The sensor showed reversible behaviour under the conditions applied. Star and Kauffman found that the adsorption of oxygen at room temperature was slow with a long recovery time. However by heating under vacuum the reversal of the response is made much more rapid[80]. Derycke et al[81] investigated the sensitivity of bare CNTs as an oxygen sensor and found that the response of oxygen gas originates from the interaction between CNTs-and the metal contact: oxygen apparently modifies the Schottky barrier. Another study gave evidence that oxygen adsorbs and affects the electrical structure of CNTs[81-83]. From theoretical studies, it has been found that the oxygen adsorption can lead to charge transfer[72, 84, 85]. The mechanism of operation of these devices therefore appears more soundly based than the CP/CNT VOC sensors.

In 2004, Cho et.al prepared SWCNTs-EC (SWCNT/polymer (Ethyl Cellulose)) to detect benzene in (gas phase), it was found that the film's resistance increased during gas exposure[86] as shown in figure (1-19).

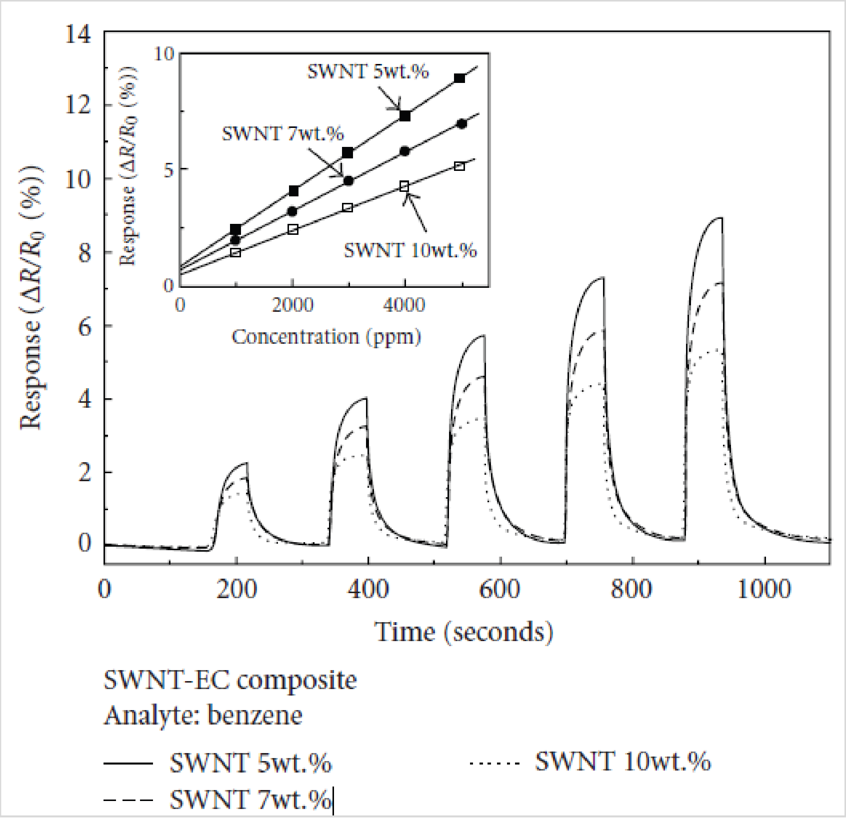

Figure 1-19 The response size of the SWCNTs/polymer as benzene sensor[58]

Philip et.al designed a nanocomposite film by coating MWCNTs with Poly(methyl methacrylate) PMMA to detect chloroform, acetone and dichloromethane and it has been shown that dichloromethane has the largest response compared with acetone and chloroform as seen in figure (1-20) with a short recovery time and fast response time. The film resistance increased in the presence of the gas and returned to the baseline when the gas was removed.[87]

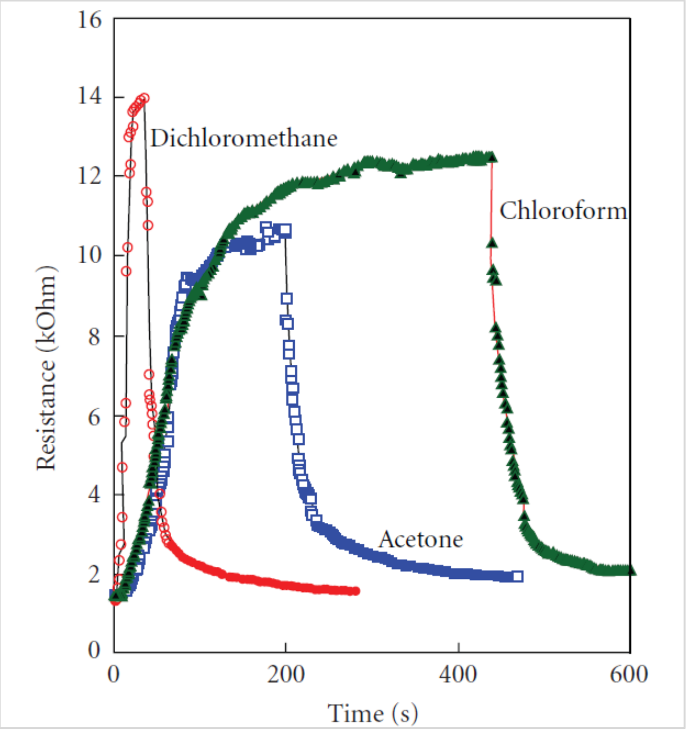

Figure 1-20 The change in the electrical resistance of CNTs/PMMA film[58]

On the other hand, another attempt was made by An to study the sensitivity of SWCNTs as bare and hybrid nanotubes to sense NO_2 gas [88]. SWCNTs were coated by polypyrrole and according to SEM images the ppy coated completely SWCNTs as shown in figure (1-21a). The sensitivity, defined as the fractional change in resistance, and the sensitivity (*S*), of CNTs was increased after the coating treatment. For pristine CNTs S = 20% and after coating S increased to 90% at 3000 ppm of NO_2 gas with fast response time and acceptable recovery time as shown in figure (1-21b).

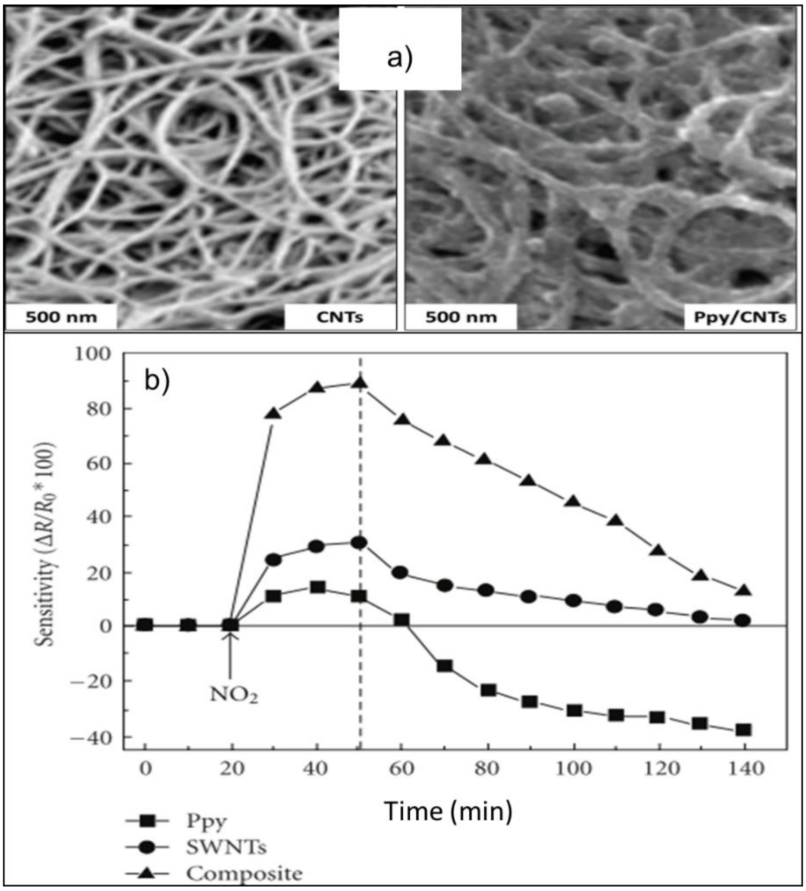

Figure 1-21 a) SEM images of bare and hybrid CNTs[88]*, b) the sensitivity of CNTs after and before coating by polypyrrole to enhance the sensitivity of the films to* NO_2 *3x10*^{3} *ppm*[88]*.*

Interestingly, the response of the composites may even change sign as a function of target analyte concentration; this suggests that a simple mechanism based on swelling and its effect on the percolation behaviour of CNTs in the polypyrrole matrix is not sufficient, nor is the mechanism solely due to charge transfer between CP and analyte. Young and Lin designed gas sensors based on bare MWCNTs deposited on a Si substrate to detect ethanol in the gas phase at room temperature and found that the sensitivity was very weak for pristine nanotubes[89] $S < 2\%$. Zhang et al used an SWCNT/CuCl film to detect carbon monoxide in different concentrations between 20 ppm- 100 ppm at room temperature and found that the sensitivity of the nanocomposite film increased over bare SWCNTs as shown in figure (1-20). The film sensitivity increased more than 100% after the coating process[90].

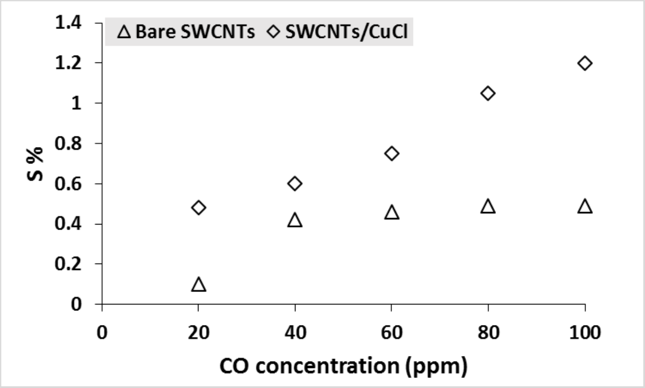

Figure 1-22 The sensitivity of bare and hybrid carbon nanotubes for CO gas at room temperature.[90]*.*

In 2018, Gautam et.al used SWCNTs/Au films to detect the toxic gases NO_2 and NH_3 and noted that CNTs/Au have a better sensitivity for NH_3 and NO_2 than pristine SWCNTs [91], as shown in (1-23 a&b).

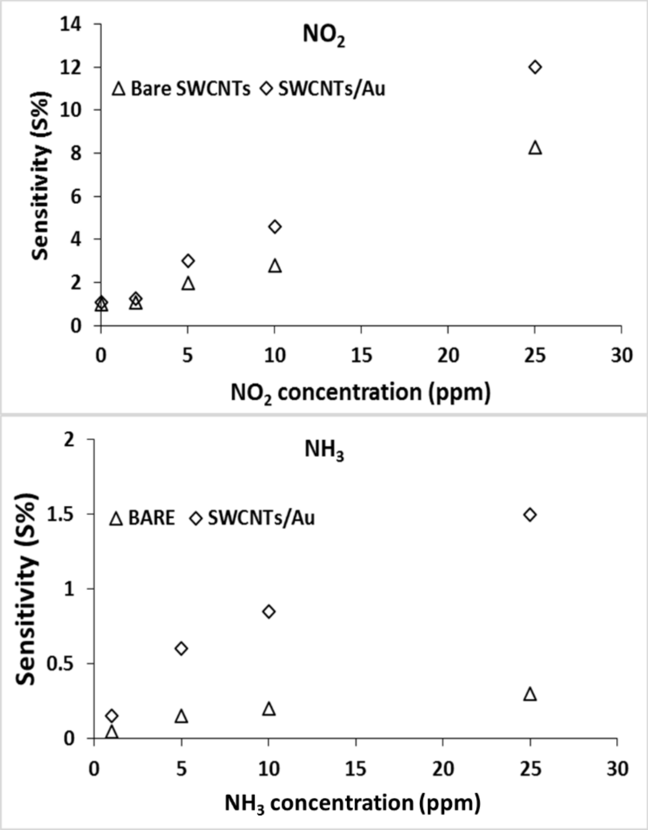

Figure 1-23 The sensitivity of bare CNTs, Au coated CNTs and carboxylated for nitrogen dioxide and ammonia. The figure was re-plotted for clarification from the original copy[91]*.*

The big challenges in design of the any gas sensor are to achieve low cost, reliability, high sensitivity, selectivity and fast response with a short recovery time. These factors have pushed many researchers to develop new materials and CNTs have proved to be a useful component. This thesis describes the design of hybrid nanotube (SWCNTs and MWCNTs) materials as thin films to detect VOCs, CO and ozone gas. In order to improve sensitivity CNTs were decorated by conductive polymer (polypyrrole), BNNTs or DNA. Laser treatment of the CNTs was also applied.

In this thesis, carbon nanotubes are used as the basis of several types of gas sensor. There are many methods reported for the fabrication of CNT gas sensors, e.g., drop-casting or printing electrodes on the CNT film [58], however in this study, the CNTs were drop cast onto Pt microelectrodes for simplicity. CNT devices are somewhat similar to the metal oxide gas sensors in that they are based on changes in electrical resistance, but they do not employ on-chip heaters, which further simplifies the device design.

Bare CNTs were found to have a weak response toward many different gases. However, the response increased significantly after coating by polypyrrole and DNA (VOC sensors) or mixing with boron nitride nanotubes (ozone sensor). As noted in the survey of the literature, this effect is known, but its mechanism remains unclear. The sensitivity of CNT conductance to adsorbed molecules has been explained on the basis of the curvature in the graphene sheet of a nanotube. The π-electron system of the nanotube is distorted and there is an asymmetry in the electron distribution outside and inside tubes[4]. These effects have been suggested to make CNTs active materials in which adsorption of molecular species disturbs the π-electron system. Electron withdrawing/donating molecules, such as O_3, NO_2 and H_2 may lead to withdrawal of electrons from, or injection of electrons into, the nanotubes with increased or decreased the conductivity of the nanotubes[4].

$$\mathrm{CNT} + \mathrm{Gas} \rightarrow CNT^{\delta e}\, Gas^{\delta +} or\ CNT^{\delta +}\, Gas^{\delta e}$$

Where δ is the number of charges transferred. However, such a mechanism seems unlikely under ambient conditions of temperature and pressure for less reactive species such as stable organic molecules. Other mechanisms that may operate include swelling of the CNT/CP network by the analyte or changes in the interfacial barrier at junctions between CNTs and CPs or between two CNTs or at the contact electrodes. This thesis is concerned with attempts to prepare and characterize CNT composite gas sensors and to understand more about the mechanism of the operation. In general, we find that materials which reduce the overall conductance of the CNTs have a beneficial effect on their sensing behaviour. A variety of different composites have been prepared in this thesis with CNT / conductive polymer composites studied in Chapters 3 and 5, CNT/BNNT (boron nitride nanotube) mixtures in Chapter 4 and DNA/CNT composites in Chapter 6. The motivation for these choices is described in the relevant chapter.

Chapter two: Experimental part

This chapter will outline the main materials, which were used to prepare the nanocomposites films and introduce all the techniques, which were used to study the chemical and physical characteristics of the samples, for instance, their structure and electrical properties.

2.1. Materials

Two types of carbon nanotubes were used in this thesis: single walled carbon nanotubes (SWCNTs) (1-2) nm in diameter with purity 90% (by mass) and multi-walled carbon nanotubes MWCNTs (10-12) nm diameter and 70% purity. These impurities include metallic (Fe) nanoparticles used as seeds for the growth of CNTs in the CVD process and carbonaceous impurities such as amorphous carbon. Our samples of SWCNTs contain 1.36% Fe (by mass) and the MWCNTs contain 3.61% Fe (by mass) estimated from EDX spectra, as shown in chapter three section (3.1.2.). Both types of CNTs were purchased from Thomas Swan Company, UK, (Elicarb^{TM}). For other chemical materials such as pyrrole 98%, iron (III) chloride hexahydrate $FeCl_3.6H_2O$ (98-102) % and chloroform 99.9% were purchased from Sigma Aldrich Ltd. Acetone, methanol and ethanol were obtained from Fisher Scientific Ltd. In addition, boron nitride nanotubes (1-10) nm, purity >50%, BNNTs were a gift from (LLC Builds Nanotube Factory, Virginia, USA). For all atomic force microscope (AFM) experiments silicon wafers, dopant boron <111> oriented, p-type, resistivity 0.09-0.12 Ohm.cm and wafer diameter 100±0.3 mm, were purchased from Pi-KEM Ltd, UK. For transmission electron microscopy (TEM) the samples were examined on holey carbon grids (HC300 Cu 50) which were obtained from EM Resolutions Ltd. The deionized water used in this thesis was supplied from a NanoPure Diamond Life Science ultrapure water system equipped with a Diamond RO reverse Osmosis System (Barnstead International). Additionally, silicon wafers were cleaned with sulfuric acid H_2SO_4 99.99% and hydrogen peroxide solution 30% (4:1), purchased from Sigma Aldrich Ltd.

2.2. Preparation the solution of carbon nanotubes

In this thesis, both methanol and chloroform were used to disperse carbon nanotubes. 0.0001 g CNTs were added to 10 mL of methanol or chloroform depending on the oxidizing agent as shown in table (2-1). To disperse the nanotubes and break down agglomerates, the mixture was treated ultrasonically (750W, 20 kHz, amplitude 20%, 230 Volt, ultrasonic processor) for 3h as shown in fig (2-1 & 2) then the solution was ready to use to prepare the nanocomposite films.

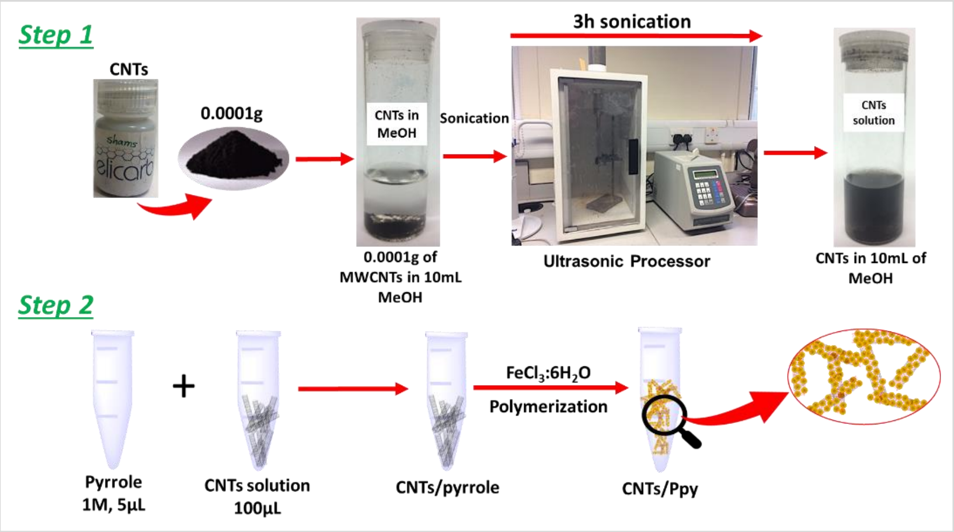

Figure 2-1 Schematic of dispersion CNTs by ultrasonic in 3 hours.

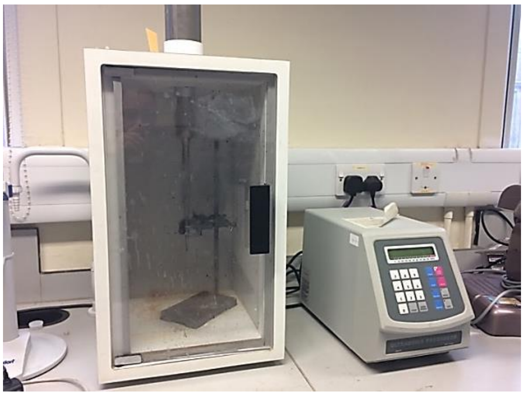

Figure 2-2 Ultrasonic process to disperse carbon nanotubes.

2.3. Templating polypyrrole on carbon nanotubes/ synthesis of CNTs/polypyrrole:

The nanocomposite films were prepared by an in situ chemical oxidative polymerization method. This method is the main approach to coat CNTs because it is easy, inexpensive and polypyrrole coats CNTs directly, as shown in section 1.4. In this study iron(III) chloride hexahydrate ($FeCl_3.6H_2O$) was used to polymerize the conducting polymer (pyrrole) as the oxidant. To template the conductive polymer on the CNTs, there are two steps: first step depended on adding (1M 5µL) pyrrole to CNTs (100 µL of 100 µg mL^{-1}). The second step was the addition (1M 5µL) of the oxidizing agent to the CNTs/pyrrole combination and then the sample was left for 3h before examining it. Polypyrrole coated CNTs as a thick shell as demonstrated in figure (2-3).

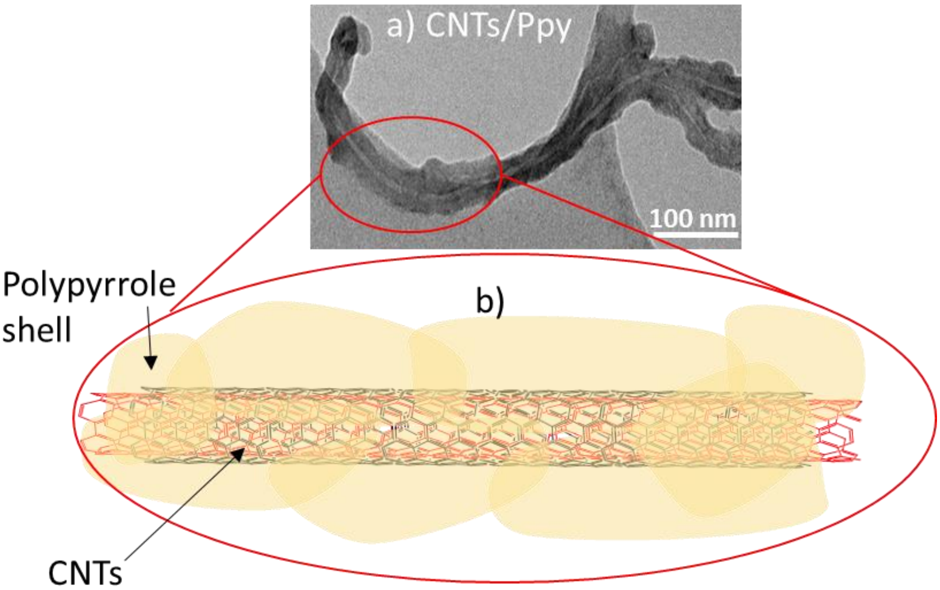

Figure 2-3 a) TEM image of CNTs/Ppy, b) scheme presents the thick polypyrrole shells around the nanotubes.

Table 2-1 The chemical materials were used to prepare CNTs/polypyrrole.

Carbon nanotubes /g	Solvent	Pyrrole	Oxidising agent
0.0001	Methanol 10 mL	5 µL,1 M	$FeCl_3.6H_2O$: 5 µL,1 M
0.0001	Methanol 10 mL	5 µL,0.5 M	$FeCl_3.6H_2O$: 5 µL,1 M

2.4. Synthesis of the hybrid CNTs/BNNTs (CNTs) films

Single wall carbon nanotubes and multiwall carbon nanotubes were used to prepare the hybrid nanotubes CBNNTs. The same amount of carbon nanotubes and boron nitride nanotubes were used about ~10^{-4} g, and added to 10mL of Methanol. Methanol was used to disperse the nanotubes because it has been shown that organic solvents are effective. CNTs/methanol were treated ultrasonically (750W, 20 KHz, amplitude 20%, 230 V, ultrasonic processor) for 3 h, while 1 h at a lower intensity (300 W, 40 Hz, Langford ultrasonic) was sufficient for BNNTs/methanol, to breakdown agglomerates and disperse the nanotubes. After the ultrasonic process, 100 µL was taken and from each dispersion and BNNTs/MeOH and CNTs/MeOH were mixed in 1:1 ratio to obtain 200 µL CNBNNTs. 2-3 µL was taken from the mixed solution and drop cast as a thin film on the microband electrodes for I-V characterisation and impedance spectroscopy. The mixture was also drop cast on Si chips for FTIR and Raman measurements. The film of CNBNNTs was dried at room temperature. Many techniques were used to study the structures, electrical properties of carbon nanotubes and the nanocomposites films for example AFM, TEM, FTIR, SEM, I-V characterizations and impedance spectroscopy IS. The main part of the study was an investigation of their performance in gas and vapour sensing.

2.4.1. Atomic force microscope AFM

The atomic force microscope AFM is a kind of scanning probe microscope (SPM) with established resolution on the order of a nanometer, more than 100 times better than the diffraction limit for visible light. In this study the images were obtained via a multimode 8 scanning probe microscope (SPM) (Bruker), as shown in figure (2-4). The operation system was ScanAsyst Mode, NanoScope, and Version 9.1. Additionally, the cantilever was made from silicon nitride with 0.4 N/m as a spring constant and 70 kHz resonant frequency which was supplied from Bruker. Additionally to reduce the vibration noise the isolation table was used from Bruker, UK. The image information is collected by touching the surface by the mechanical probe. The map of surface (topography) is drawn as a false colour image using the height obtained from the cantilever defection. The height of the tip is related to the force on the tip and stiffness of the cantilever by Hooke's law, equation(1)[92]

$$F = Zk \qquad (2-1)$$

Where: Z is a height of the tip or the amount of displacement observed, k is a spring constant. Generally, there are three AFM modes: *Contact, Non-Contact and tapping mode*. In this thesis, tapping mode and ScanAsyst were used to study the morphology of the samples.

2.4.1.1. ScanAsyst system

ScanAsyst is an first automatic image improvement technology for AFM, which uses algorithms to automatically monitor and adjust the quality of the image and by controlling the imaging parameters directly to obtain high resolution image for example set point, scan rate and gain. ScanAsyst is simpler to use compared to conventional tapping mode systems where these parameters must be tuned by the operator[92].

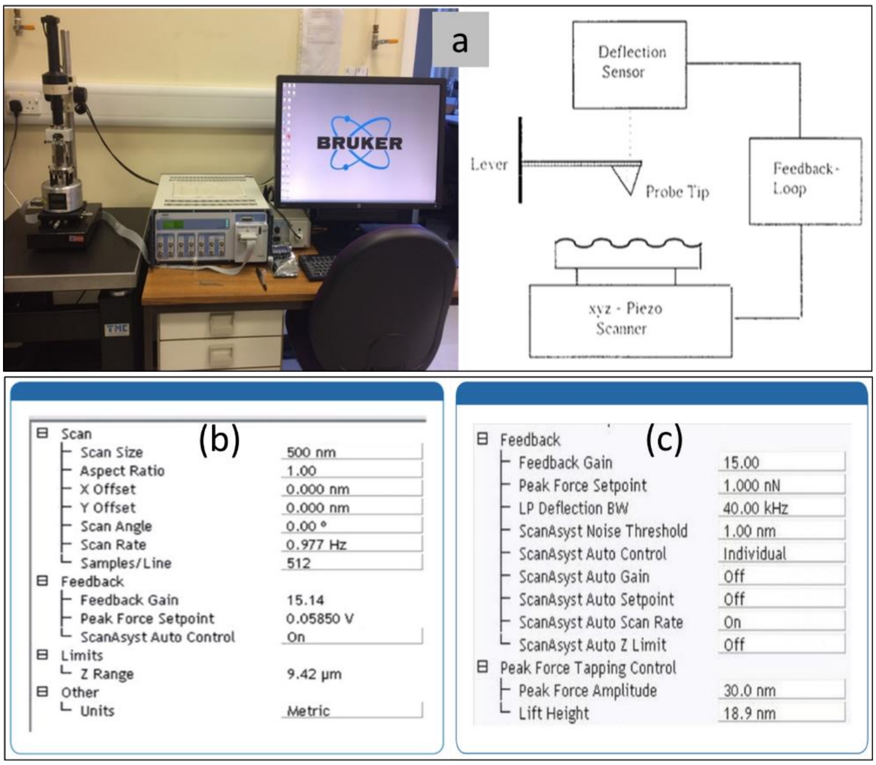

- Scan
  - Scan Size: 500 nm
  - Aspect Ratio: 1.00
  - X Offset: 0.000 nm
  - Y Offset: 0.000 nm
  - Scan Angle: 0.00 °
  - Scan Rate: 0.977 Hz
  - Samples/Line: 512
- Feedback
  - Feedback Gain: 15.14
  - Peak Force Setpoint: 0.05850 V
  - ScanAsyst Auto Control: On
- Limits
  - Z Range: 9.42 µm
- Other
  - Units: Metric

- Feedback
  - Feedback Gain: 15.00
  - Peak Force Setpoint: 1.000 nN
  - LP Deflection BW: 40.00 kHz
  - ScanAsyst Noise Threshold: 1.00 nm
  - ScanAsyst Auto Control: Individual
  - ScanAsyst Auto Gain: Off
  - ScanAsyst Auto Setpoint: Off
  - ScanAsyst Auto Scan Rate: On
  - ScanAsyst Auto Z Limit: Off
- Peak Force Tapping Control
  - Peak Force Amplitude: 30.0 nm
  - Lift Height: 18.9 nm

Figure 2-4 a) Schematic diagram of Atomic Force microscope ScanAsyst , b)ScanAsyst interface, all the setting of the feedback and the scan rate were calculated automatically by AFM. c) Manual change

2.4.1.2. Contact, non-contact and tapping mode

Contact mode (CM) represents the basic mode for AFM. The principle of CM is that the cantilever bends according to the tip/sample force. The feedback system adjusts the sample height to keep the force on the tip constant. The force is proportional to the deflection of the cantilever with a proportionality constant called the spring constant. As the tip rasters over the sample, the computer collects the deflection data in (nm) and X-Y position and assembles an image map on sample height in grayscale or false colour[93]. The major disadvantage of CM is the high tip/sample force which can damage either tip or sample. It is therefore best for studies of hard inorganic samples or where other data, such as tip/sample friction is required as well as topography[94]. *In non-contact mode or dynamic force microscopy (DFM)* the tip oscillates close to the sample surface without touching. As a result the probe has a long lifetime and there is a low force on the surface, therefore the probability to damage the sample surface is very small. DFM has a lower resolution in comparison with contact mode because of the greater average tip/sample distance. *Tapping mode or intermittent contact mode.* Figure (2-5) shows the tapping mode system and figure (2-6) shows the force curve. In this mode the probe lightly taps on the surface during the scanning process and by preserving a regular oscillation amplitude a steady tip-sample integration is maintained and it is easy to obtain the image of the surface. This technique permits high resolution imaging with less sample damage than contact mode. This mode represents the intermediate case between non-contact and contact mode[95]. In this type of mode, the cantilever-tip are oscillated at a resonant frequency. The sample surface is struck by the tip once during each oscillation[95]. The sampled is imaged whilst there is no change in the value of

tapping amplitude[96] . The amplitude of the oscillation usually in a few tens of angstroms in order to keep the tip from sticking on the sample surface. One of the advantages of this mode is the probability of tip damage is small because the average force is decreased[92].

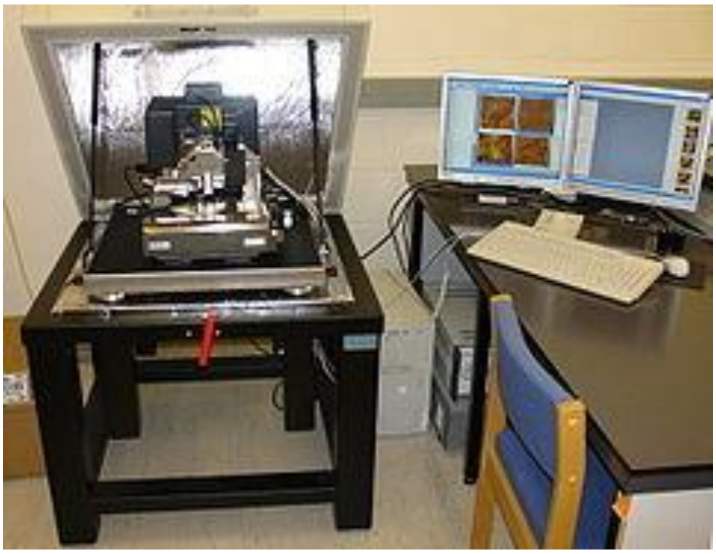

Figure 2-5 Tapping mode AFM system

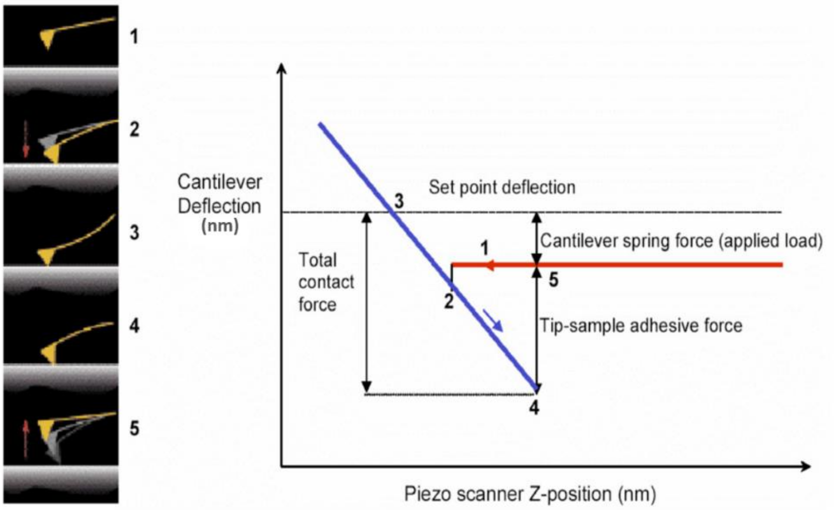

Figure 2-6 Force curve. The method (red) and (blue) withdraw curves are presented on the right. Generally, the total contact force depends on the adhesion in addition to the applied load.

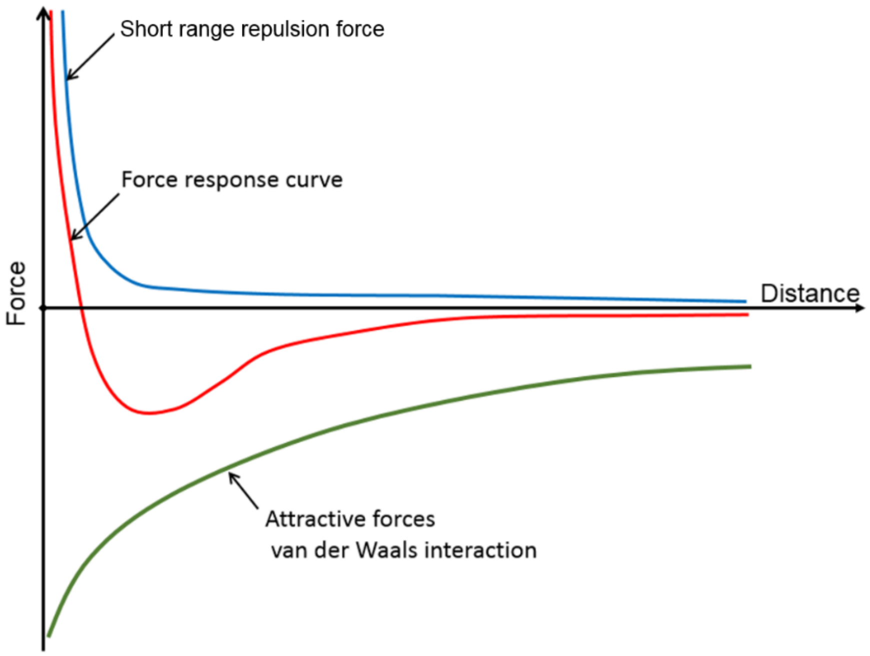

Figure 2-7 Plot of the force against the distance

A piezoelectric scanner monitors the accurate position of a probe in the relation to the surface. X-Y are by convention the coordinates in the plane of the sample and Z is the coordinate normal to this plane. The cantilever oscillates with a fine probe deflects as the probe tip scans the surface. The computer, optical mirror, electronics, and laser diode are used to collect the data. and draw the image. Generally, for this study the operation system was Veeco Digital Instruments Dimension 5 Atomic Force Microscope, and the cantilever frequency 300 kHz, radius <10nm. The cantilever was obtained from Budge Sensor Company, Bulgaria.

2.4.1.3. Preparation the samples for atomic force microscope Test

All the silicon wafers were cut into 1x1 cm^2 chips and they were treated with a strong oxidizing agent known as piranha. Piranha solution represents the mixture between sulfuric acid (H_2SO_4) and 30% hydrogen peroxide solution (4:1). It was used to remove most of the organic matter and it also hydroxylates the Si- surface making it highly hydrophilic. After one hour of treatment the chips were washed with deionized water and were dried with nitrogen gas. Then 2 to 3 uL drops were deposited on the Si chip and dried at the room temperature before imaging.

2.4.2. Transmission electron microscope TEM

The transmission electron microscope is common tool in materials science. A high energy beam of electrons is focused and passes through a very thin sample. Scattering of the electrons by the atoms of the sample can be used to demonstrate the structural properties and features of the sample [97]. TEM can provide information about the shape and the size of surface features. In addition, TEM has high resolution compared with AFM. Generally, TEM system contains eight parts: thermionic gun, electron source, electron beam, sample stage, phosphorus, fluorescent screen, condenser, vacuum chamber and electromagnetic lenses as shown in figure (2-8).

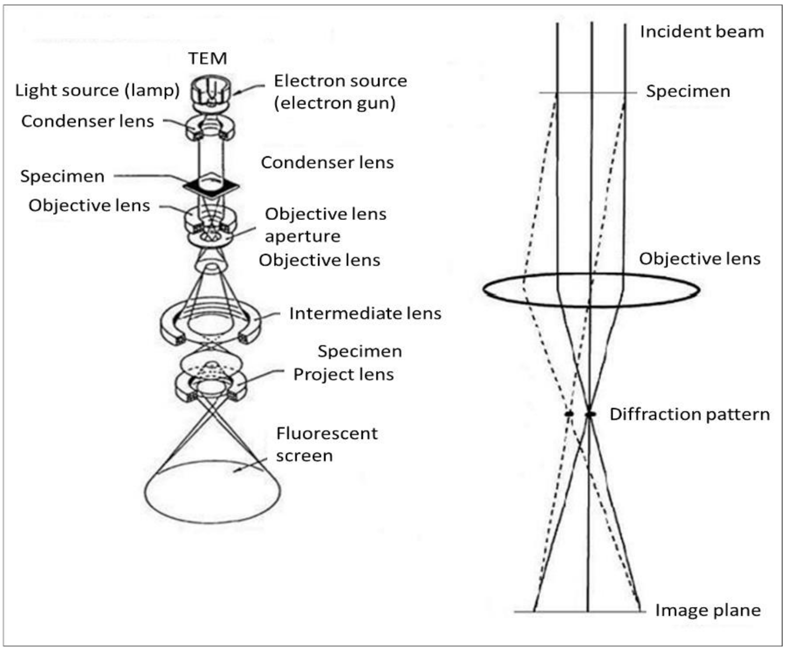

Figure 2-8 General design of a TEM describing the path of electron beam in a TEM [98]

Fig (2-8) shows the layout of a TEM and explaining the path of the e-beam. The limited resolution of light microscopes led to development of the microscope system and use of an electron beam. To explain why the scientists select the electron beam to be used in TEM it is necessary refer to simple optics and physics equations. In optics the numerical aperture (NA) is[99]:

$$d = \frac{\lambda}{2n\ sin\alpha} \cong \frac{\lambda}{2NA} \qquad (2-2)$$

Where: *d* the maximum resolution, λ the wavelength, NA the numerical aperture, *n the* refractive index and α is the collecting angle.

The electron beam can diffract as electromagnetic radiation and according to the de Broglie equation there is a relation between the wavelength of the moving particles and the momentum and the relation between the wavelength of electrons with their kinetic energy as shown below[100]:

$$Einstein's\ equation = E = mc^2 \qquad (2-3)$$

$$Planck's\ equation = E = h\nu \qquad (2-4)$$

Where E is the equivalent energy, m is the mass, c is the speed of light ν is the frequency and h is Planck's constant. (6.626x10^{-34} J.s).

Planck-Einstein law:

$$h\nu = mc^2 \qquad (2-5)$$

and

$$\nu = \frac{c}{\lambda} \rightarrow from\ eq(5) \rightarrow mc^2 = h\frac{c}{\lambda} \qquad (2-6)$$

$$mc = \frac{h}{\lambda} \rightarrow h = \lambda mc \qquad (2-7)$$

For electrons (υ) replaces the speed of light and then the equation (2-7) becomes:

$$h = \lambda m\upsilon \qquad (2-8)$$

The momentum of the particle

$$p = m\upsilon \qquad (2-9)$$

As a result of that

$$p = \frac{h}{\lambda} \qquad (2-10)$$

Equation (2-10) is the *de Broglie* relation.

In TEM technique the velocity of electron can be close to the speed of the light[101] ~ (3x10^8 ms^{-1})

$$\lambda_e \cong \frac{h}{\sqrt{2m_oE\left(1+\frac{E}{2m_oc^2}\right)}} \qquad (2-11)$$

Where: h is Planck's constant, m_o is the mass of electron and E is the energy of accelerated electrons.

According to the equations above the electron wavelength ($\lambda_e = 8$ pm) at 20 keV and it is much smaller that the wavelength of light

Usually, the electrons are generated from thermionic emission by a tungsten filament or by electron field emission, see figure (2-9). The transmitted beam holds all the information about the electrons for example phase, electron density and the periodicity[97].

.

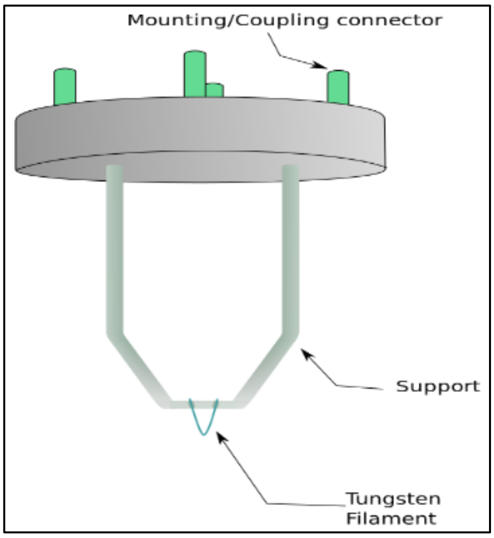

Figure 2-9 Tungsten filament as an emission source[98]

2.4.2.1. The main parts of TEM instrument

For transmission electron microscope there are main parts: *Illumination System, the lens objective and the imaging system.*

The illumination system depends on the electrons which were provided from the electron gun and transfer them to the sample surface (grid), *the lens objective* which is represented the heart of TEM. Lastly, *the imaging system* includes projector lens and intermediate lens[98]

2.4.2.2. The interaction between the specimen and electrons

The active electrons in the microscope strike the sample surface and many reactions can happen on the surface as shown in figure (2-10) .In TEM the detector is underneath the sample while in SEM it is on the top. The detected electrons may be categorized: unscattered electrons, elastically scattered and inelastically scattered[102].

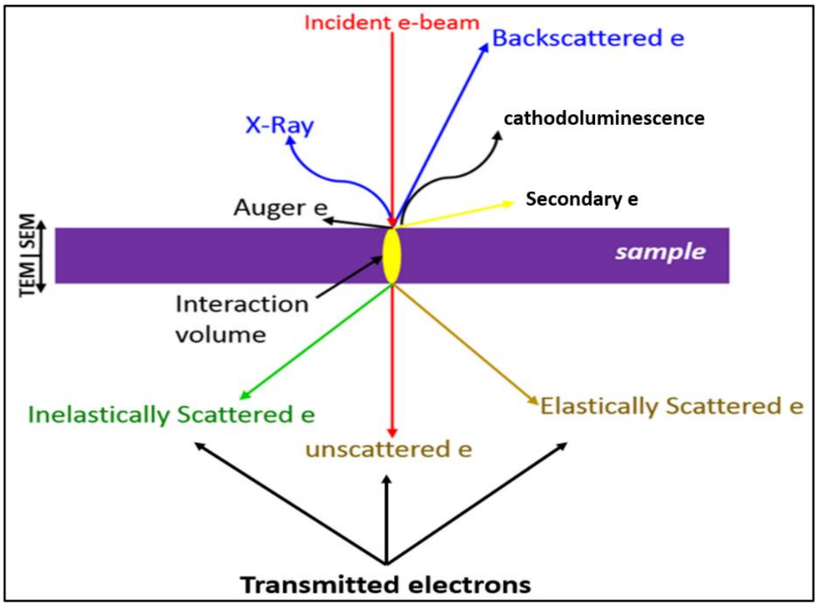

Figure 2-10 Interaction between the electron beam and specimen

Unscattered electrons: from incident electron beam and transmitted to the sample without any interaction inside the pattern. Unscattered electrons decreased as the sample thickness increases. A thicker sample transmits fewer unscattered electrons and appears dark, whereas a thin sample appears lighter. ***Elastically scattered*** incident electrons are scattered by the sample's atoms without any energy loss. These electrons are transmitted through the remaining portions of the sample. In this part the electrons follow *Bragg's law* ($\lambda = 2dsin\theta$) Where: θ is a scattering angle, λ incident wavelength is, d is a path difference (the distance between two layers), n is any integer. All the incident electrons have the same wavelength and energy thus the electron will be scattered by the same angle if they have the same atomic spacing, these electrons will be collected via magnetic lenses to form a model of spots that correspond to a specific atomic plane[98]. This model or pattern can give the information about the atomic arrangement and the orientation. ***Inelastically scattered*** electrons are those scattered with loss of energy. The rest of the beam are transmitted through the sample. The energy loss can be used to give information about the electronic spectrum of the sample. Nevertheless, the ionizing beam can damage the sample, especially polymers, ceramic and most organic materials[97, 98] because of , the high voltage up to 400 kV.

2.4.2.3. Preparation of samples for TEM

400-mesh carbon-coated copper grids (Gilder grids) and Holey carbon 300-mesh HC300Cu were used to prepare samples. 2uL from the materials, CNTs or CNTs/Ppy, were deposited on the grid and the sample was dried before the test. Most of the data were examined on a Philips CM100 TEM (FEI), 40 – 100keV tungsten filament. To collect the digital images a CCD camera (Deben) was used. Fig (2-11) shows the TEM grid.

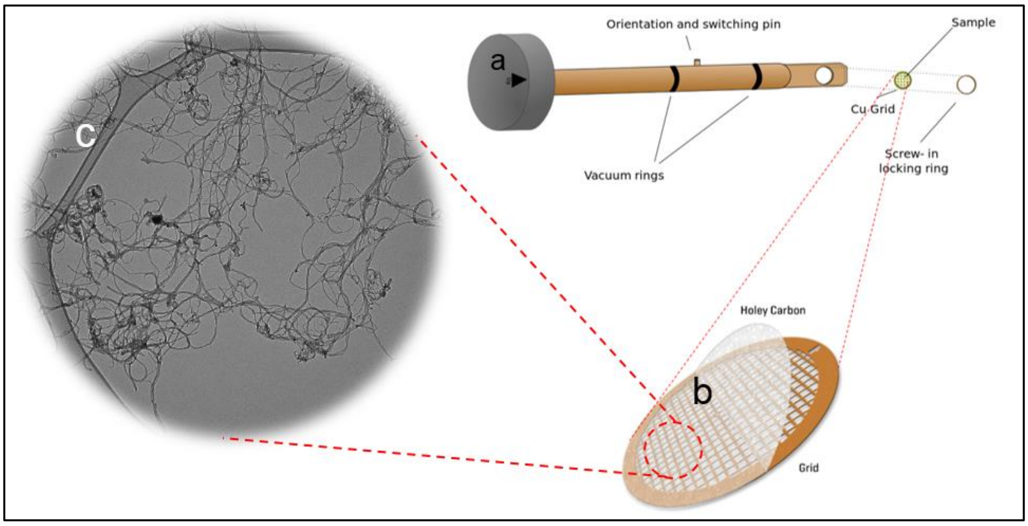

Figure 2-11 a) the sample holder which inserts into TEM goniometer. b) Holey Carbon Grid for TEM. c) multi-walled carbon nanotubes MWCNTs.

2.4.3. Fourier transform infrared Spectroscopy

Fourier transform infrared FTIR experiments were carried out on an IRAffinity-1S spectrometer provided with DLaTGS detector (Deuterated Lanthanum α Alanine doped TriGlycine Sulphate detector exhibits the most effective pyroelectric effect known, the major application of DLaTGS is in FTIR). This type of detector can work uncooled or with temperature stabilisation. Wavenumber range (350 to 7800) cm^{-1} with resolution 16 cm^{-1}.

2.4.4. Raman spectrophotometer

Raman spectroscopy depends on the interaction between the incident light and the chemical bonds of samples[103]. Both Raman and FTIR are powerful techniques to identify inorganic/organic materials but the there is a difference between Raman and FTIR; in FTIR system the energy of infrared over a wide range of the frequencies interacts directly with the sample and the absorption happens when the frequency of the incident radiation corresponds that of a molecular vibration. Thus, the molecules are promoted to an excited vibrational state. It is supposed that the irradiation beam loses energy when pass through the sample and the instrument measures I/I_o where I and I are transmitted and incident beam. In Raman techniques one incident frequency typically in the visible range, is used, which is scattered inelastically with excitation of a molecular vibration. In quantum mechanics, the scattering can be defined as an excitation to an imaginary/virtual state lower in energy than the actual electronic transition with a change in the oscillation (vibration) energy. In addition, the scattering process happens in very short time[104] $<10^{-14}$ s, figure (2-12) shows the Raman scattering.

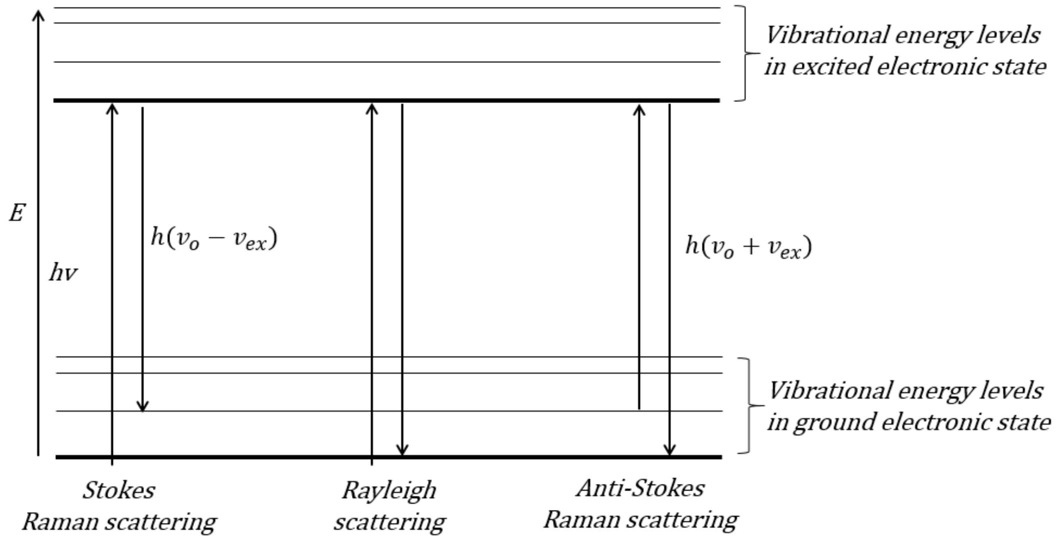

Figure 2-12 the basic of Raman scattering

Equation (2-12) defines the Raman shift[105] :

$$\breve{v} = \frac{1}{\lambda_{incident}} - \frac{1}{\lambda_{scattered}} \qquad (2-12)$$

Where λ is the wavelength in cm.

For all Raman spectra a Witec (alpha CRM200 – Confocal Raman Imaging microscope) was used and the back scattered light was collected by a cooled CCD (KL1500 LCD). The laser wavelength was 488 nm, 60 mW. Figure (2-13) demonstrates the main parts of a Raman microscope.

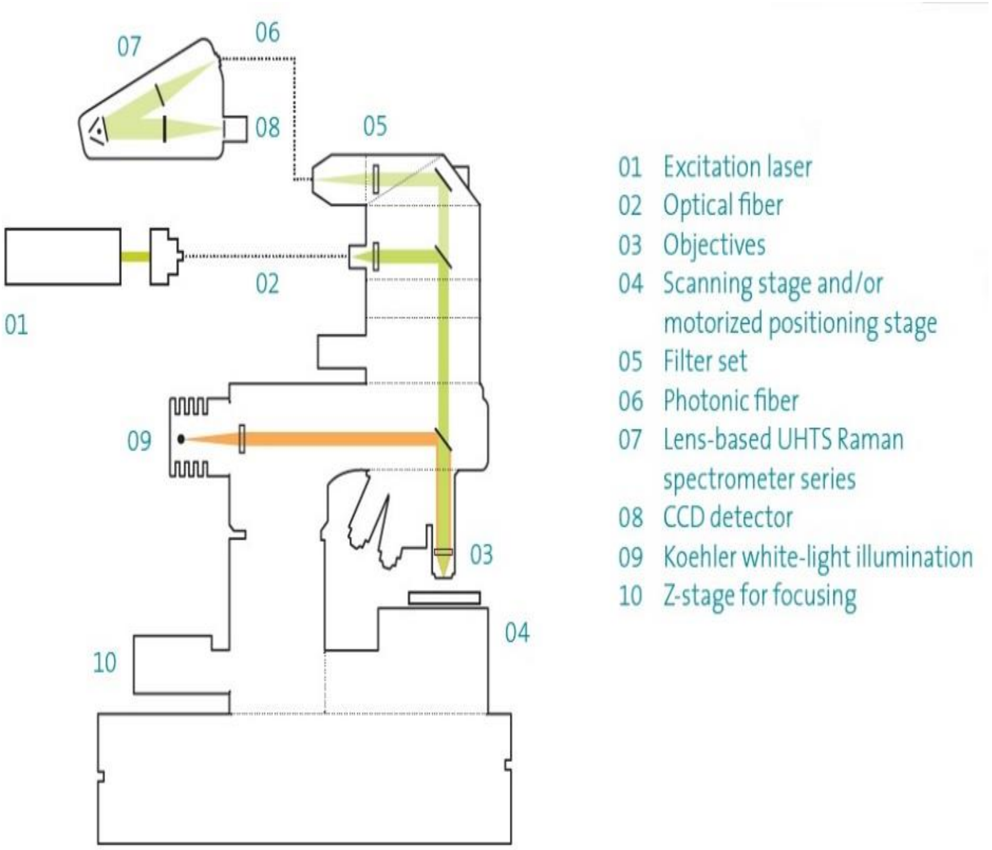

Figure 2-13 The main parts of Raman microscope[103]

2.5. Electrical measurements

2.5.1. I-V characteristics

This study depended also on the effect of temperatures on the electronic properties of bare and hybrid CNTs. A probe station (Cascade Microtech) and 1500A semiconductor parameter analyzer/Agilent was used, as shown in figure (2-14). The applied voltage was from +2 V to -2 V with steps 0.05V.

Nitrogen gas was used to remove humidity in the sealed area. I-V characteristics for both bare CNTs and the nanocomposite films were done in various temperature (213-353) K which were controlled by a thermal chuck system (Model ETC-200 L, ESPEC), Japan. Conductances were calculated from the slope of the I-V plot at zero bias. In some cases, temperature-dependent I-V curves could be measured and the conductance – temperature data was analysed according to the Arrhenius equation which is shown below[106] and as figure (2-15):

$$Slope = \frac{\Delta I}{\Delta V} \qquad (2-13)$$

$$R = \frac{1}{Slope} \quad then \;\; G\ (Siemens) = Slope \qquad (2-14)$$

Where: R is the electrical resistance (Ω) and G the conductance (S)

$$ln\frac{G}{G_0} = -\frac{E_a}{RT} \qquad (2-15)$$

Where R is the gas constant and E_a is the activation energy and is sometimes written as an effective temperature $T_o = E_a / \mathrm{R}$.

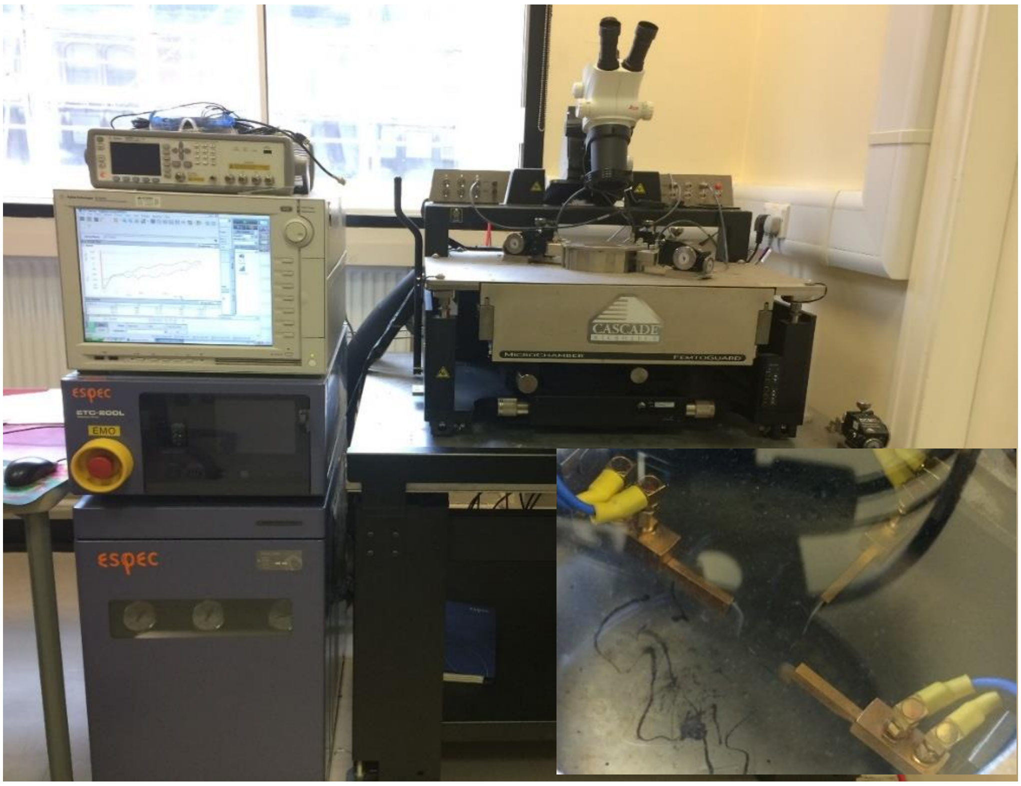

Figure 2-14 A probing station (Cascade Microtech)

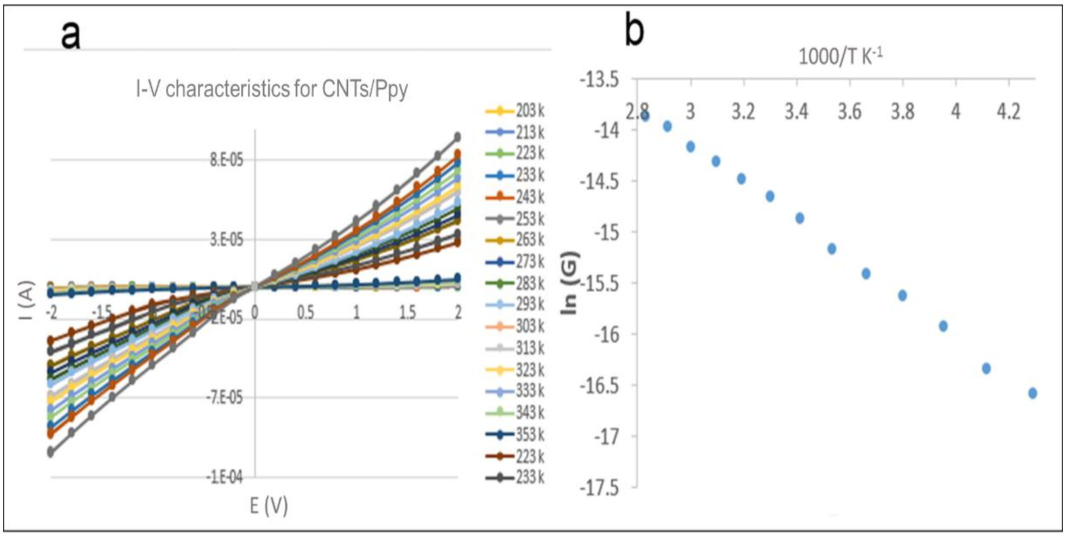

Figure 2-15 a) Current-voltage curves for SWCNTs/Ppy at various temperatures, b) Arrhenius plot.

2.5.2. Impedance spectroscopy IS.

The best description of the impedance is the ability of the electrical circuit to resist the current flow. It is more complex than the electric resistance which is defined by Ohm's Law[107]:

$$R = \frac{E}{I} \qquad (2-16)$$

R is independent of frequency but impedance depends on the frequency, therefore IS can be more general than the electrical resistance and it gives more information about the materials[108] [109]. IS data was analyzed by fitting to an equivalent electrical circuit as shown in table (2-2).

Table 2-2 The comment of electrical elements[107.]

Component	Current Vs. Voltage	Impedance
Resistor	E = IR	Z = R
Capacitor	I = C dE/dt	Z = 1/jwC

From table (2-2) the impedance of a resistance independent of frequency (only real part) and zero phase shift, while the impedance of a capacitor dependent on the frequency and has an imaginary part, $\pm 90^o$ out of phase, as figure (2-15). Generally, the impedance represents the concept of resistance that applies also to capacitive circuit elements.

$$Q = CE \qquad (2-17)$$

Where C is the proportionality constant and is known as a capacitance.

From table (2-2)

$$i = C\frac{dE}{dt} \qquad (2-18)$$

If:

$$E = E_o e^{j\omega t} \qquad then \qquad \frac{dE}{dt} = jwE_o e^{j\omega t} \ = jwE \qquad (2-19)$$

Where

$j = \sqrt{-1}\ , w = 2\pi f\ , f = frequency\ and\ e^{jwt} = \cos(wt) + j\sin(wt)$

In the IS study an ac potential was applied and an ac current was measured which has two parts: a *sine* and a *cosine* component.

$$i = jwCE; \quad or\ \ Z = \frac{E}{i} = \frac{1}{jwC} = -\frac{j}{wC} \qquad (2-20)$$

From the table (2-2) $Z` = R$ for the resistor and the impedance of the capacitance is purely imaginary $Z`` = 1/jwC$. The total impedance for the equivalent circuit that was used in this study, is obtained from a parallel combination of C and Rc (fig (2-16b)).

$$Z = Z' - jZ'' \qquad (2-21)$$

From

$$\frac{1}{Z} = \frac{1}{R_c} + jwC = \frac{1 + jwCR_c}{R_c} \ \ \rightarrow and\ multiply\ by\ \left(1 = \frac{1 - jwCR_c}{1 - jwCR_c}\right)\ then$$

$$Z = \frac{R_c(1 - jwCR_c)}{1 + w^2C^2R_c^2} \qquad (2-22)$$

Therefore, the total impedance of the equivalent circuit in fig (2-16b) expressed as real and imaginary parts is:

$$Z = R_b + \frac{2R_c}{1 + w^2C^2R_c^2} - j\ \frac{2jwCR_c^2}{1 + w^2C^2R_c^2} \qquad (2-23)$$

By eq (2-21) $Z`(real) = \ R_b + \frac{2R_c}{1+w^2C^2R_c^2}$ and $Z''(img) = \frac{2jwCR_c^2}{1+w^2C^2R_c^2}$ $\quad (2-24)$

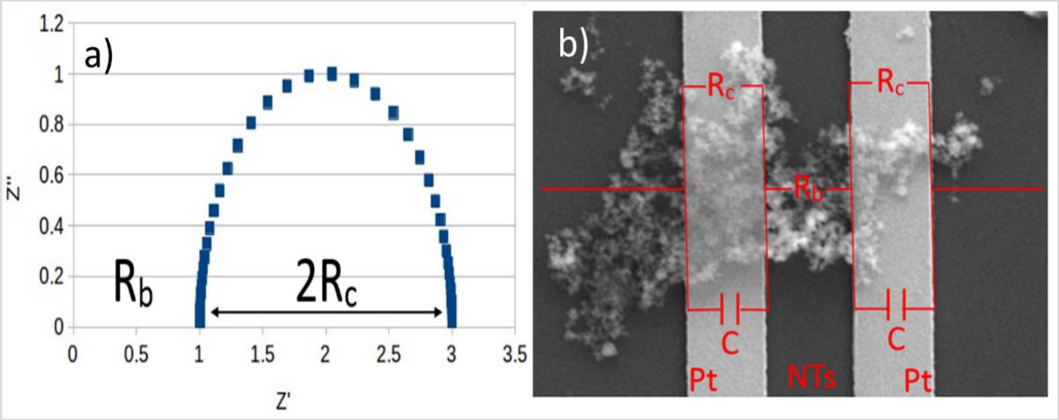

Figure 2-16 a) The Nyquist plot the results for the electrical elements of circuit. b) SEM of MWCNTs/Polypyrrole on the microband electrodes

The range of frequency was (50-20000) Hz and (100uA to 10mA). PDTrace version 4.8 was used as software to analyse the data.

2.5.3. Analysis of current-time transients for two-terminal nanotubes devices.

As shown in figure (2-15b &16) a small drop from CNTs or the nanocomposite on the electrode can occur two terminal devices. In this experiment, different potentials were applied from 1 V to 5 V. Generally, application of a potential results in two different contributions to the current in the circuit: the current flowing in the resistances and the charging of the interfaces. The former corresponds to electrons crossing from the metal into the nanotubes, flowing through the film and afterwards out into the other metal terminal. This type of current depends on the potential and the film’s resistance between two electrodes R_b and contact resistance R_c which is situated at Pt/NTs interface and NTs/Pt interface. The second type of current (capacitive) corresponds to charges, which accumulate at or near Pt/CNTs or CNTs/Pt interface on either side of the device and does not involve electrons flowing through the whole device. This is because the current flows only whilst electrons/ions adjust their positions in response to the applied potential E, which is divided between that across the capacitor E_C and that dropped across the bulk resistance E_R.

$$Q = E_C C \qquad (2-25)$$

Q is the amount of electrical charge and C is the capacitance.

$$E = E_c + E_R \qquad (2-26)$$

$$E = \frac{Q}{C} + iR_b \qquad (2-27)$$

By differentiation of equation (2-26) with respect to time (*t*) and using the fact that *E* is constant for *t* > 0.

$$\frac{dE}{dt} = 0 = \frac{i_c}{C} + R_b \frac{di}{dt} \qquad (2-28)$$

Where $i \neq i_c$ and *i* represents the total current while i_c is the electrical current flowing through the capacitor. The current flowing through the parallel resistor R_c is given by the potential on the capacitor and Ohm's law. This gives:

$$i = i_c + \frac{E_c}{R_c} = \quad i_c + \frac{E - iR_b}{R_c} \qquad (2-29)$$

Substitution of eq (2-28) into eq (2-27) and rearranging gives:

$$R_b C \frac{di}{dt} + i\left(1 + \frac{R_b}{R_c}\right) = \frac{E}{R_c} \qquad (2-30)$$

The solution of (2-29) is

$$i = \frac{E}{R_b} \frac{R_c}{R_b + R_c} e^{-t/\tau} + \frac{E}{R_b + R_c} \qquad (2-31)$$

$$\tau^{-1} = \frac{1}{C}\left[\frac{1}{R_b} + \frac{1}{R_c}\right] \qquad (2-32)$$

In the steady state, the current obeys Ohm’s law as demonstrated in eq (2-30) where $t/\tau \rightarrow \infty$.

$$i_{ss} = \frac{E}{R_b + R_c} \qquad (2-33)$$

The microband electrodes that were used in this study have four parallel bands and four independent terminals. By changing the contact to the terminals for example (1&2), (1&3) and (1&4) it is possible to increase R_b , while retaining the same value for R_c approximately; this facilitates separation of the contact and bulk resistances.

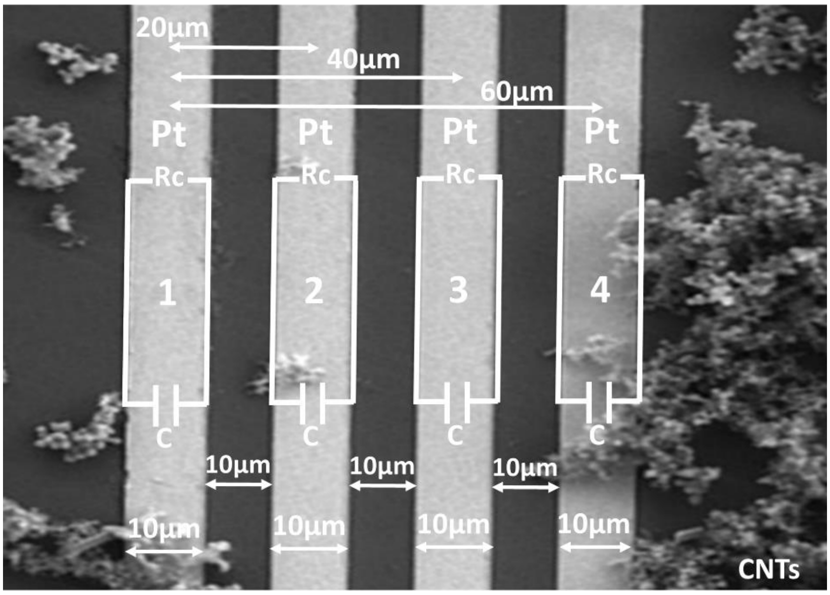

Figure 2-17 The equivalent circuit element are also superimposed image on the question (2-21)

2.5.4. X-Ray photoelectron spectroscopy (XPS)

XPS or electron spectroscopy for chemical analysis ESCA, this technique is used to analyse materials surfaces and determine the chemical/electronic state and the composition of the elements[110]. To obtain XPS spectrum the sample is irradiated by an X-ray beam. Both the number and the kinetic energy of the photoelectrons from the sample are analysed[92]. However, ultra-high vacuum conditions (pressure $<10^{-10}$ Torr) are necessary to avoid the collision of electrons that escape from the surface before reaching the detector[110]. Equation (2-34) describes the kinetic energy of the photoelectrons.

$$\text{Kinetic energy} = \text{h}\nu - \emptyset \qquad (2-34)$$

Where ν is the incident frequency, h is Planck's constant and $\emptyset$ is the work function. XPS spectra describes as a chart of the binding energy of electrons with the number of electrons' core level. Each spectrum has a number of XPS peaks at distinguishing binding energy E_B that match with each element found on the sample surface. These peaks identify the elements within the sample and the number of electrons that are detected is related to the amount of each in the element in the irradiated area[92, 110]. All XPS spectra were carried out on a ThermoScientific K-Alpha XPS spectrometer (East Grinstead, United Kingdom), provided with an Al Kα X-ray source (1486 e.V) 90^o is the take-off angle. All the results were collected and analysed by CasaXPS. Figure (2-18) shows the main parts of the XPS system. Generally, all XPS curves were corrected to 284 eV of hydrocarbon C 1_S peak as a reference. For narrow scan spectra, the pass energy was 50 and 0.1 eV and 150 with 1 eV for a wide scan (survey spectra). The samples were deposited on Si chips after cleaning these chips by piranha solution and was left to dry at room temperature for (10-20) min.

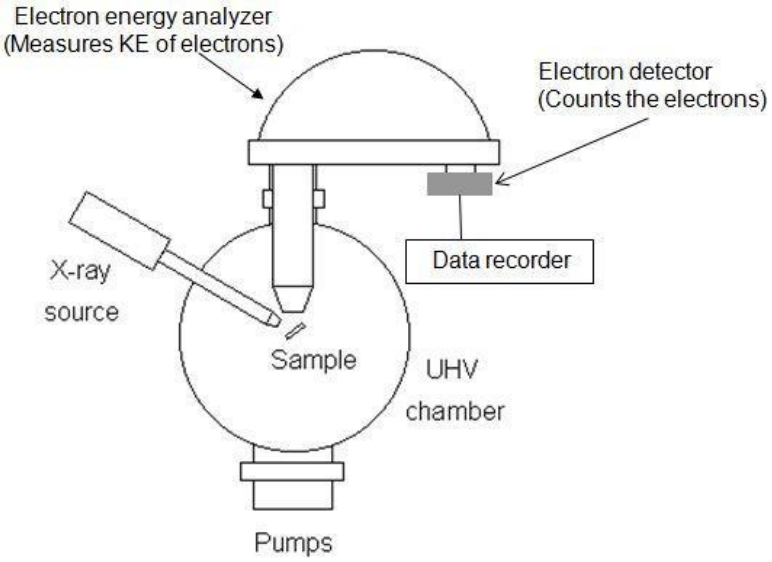

Figure 2-18 The schematic diagram of the X-Ray photoelectron spectroscopy system [92]

2.6. Carbon nanotubes as gas sensors:

This part will present how carbon nanotubes can be used to detect volatile organic compounds (VOC) and gases such as ozone. Two different method were used to measure the sensitivity of the nanotubes to these gases.

2.6.1. Vapour sensor

Methanol, ethanol, acetone and chloroform were studied as volatile organic compounds and the sensitivity of the films was determined by the change in the electrical resistance for the nanotubes before and after exposure to vapour. The electrical resistance was measured by a $6_{1/2}$ digit DMM (34401A, Agilent). DMMs are also known as a Volt-Ohm-Multimeters (VOM) and have many measurement functions in one unit. Typically, DMM can measure current, voltage and resistance. DMMs are more common than analog meter because of the accuracy, the cost and auto ranging [111]. An Agilent 34401A, $6^{1}/_{2}$ Digital Multimeter (Agilent Technologies, USA) was used to measure the resistance value. U1163A Clip-on probe 3A black red 300V (Agilent Technologies, USA) was used to hold the sample as shown in fig (2-19). Lab view was used to monitor the change in the electrical resistance with time over a National Instruments IEEE/USB interface.

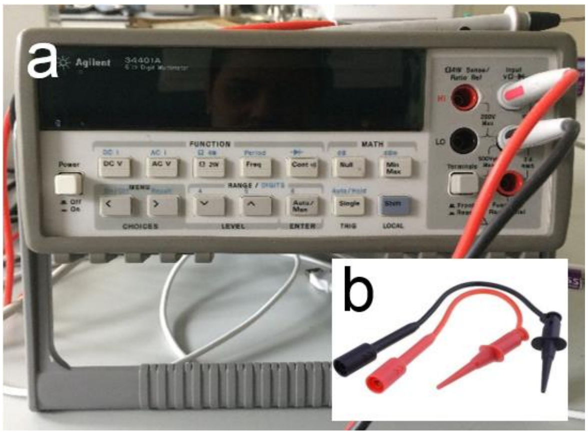

Figure 2-19 a) Agilent 34401A, 61/2 Digit Multimeter instrument was used to measure the electrical resistance of the nanotubes) the probes.

In this sensing system zero air *(zero air is prepared by mixing pure oxygen and nitrogen in a 1:4 ratio and has a much lower level of impurities than ambient air (hydrocarbons < 0.1 vpm;* CO_2 *< 1 vpm;* H_2O *< 2 vpm and NOx < 0.1 vpm))* was used to calibrate the sample. The gas bottle was supplied from (BOC for industrial gases, UK) and the gas flow was controlled by mass flow controllers (MFC) which were purchased from (Flotech Solutions Ltd., UK) and controlled using Brooks Smart Interface 0260 and software which was obtained from (Brooks Instrument, USA). The sensing response is defined as $S = ((R-R_0)/R_0)*100\%$ where R_0 is the resistance in an air atmosphere and R is the resistance at steady-state after exposure to an air/analyte mixture[112]. In general, two MFCs were used, one for the zero air and the second to control the flow of volatile organic compounds (VOCs), as shown in fig (2-20).

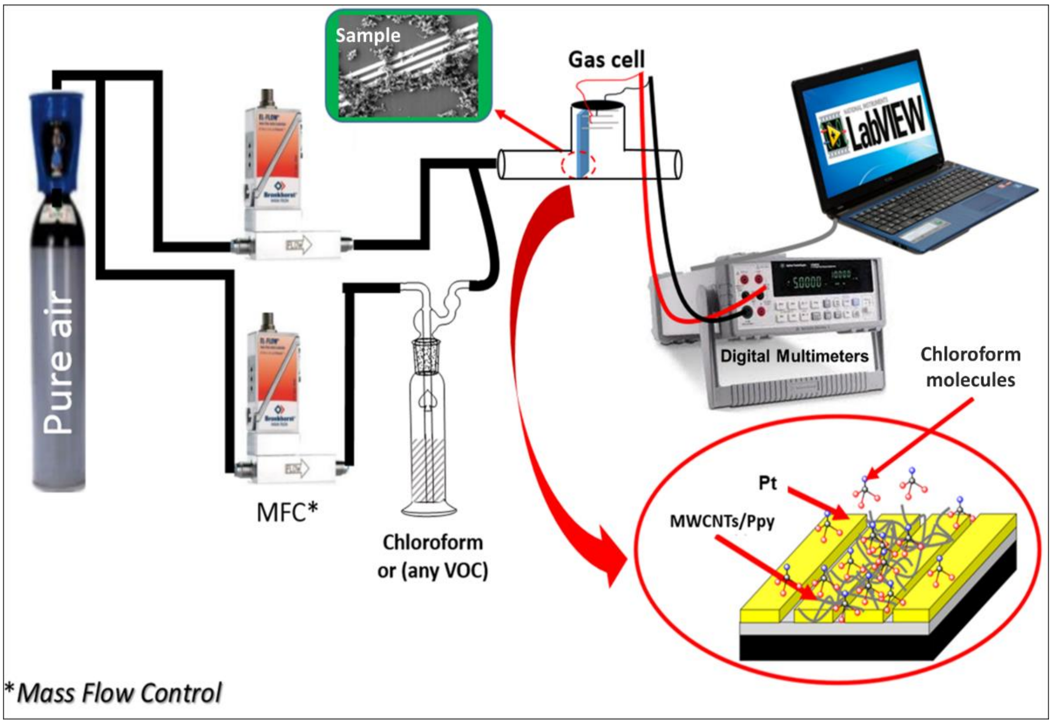

Figure 2-20 Schematic diagram of the sensing measurement system for VOCs sensing.

2.6.2. Ozone gas sensor

An ozone gas UV-generator using 185 nm UV irradiation of air was purchased (UVP, Analytik Jena's Life Science Business Unit, (www.UVP.com). To generate the gas, zero air[2] was used 125 mL.min^{-1} as a gas carrier. Ultraviolet light can dissociate the oxygen molecule to atomic oxygen. Oxygen atoms then combine with O_2 to form ozone (O_3)[113]. Three different concentrations of ozone were used in this test at three different temperatures (20, 40 and 60°C). To control the temperature during the sensing process, a water bath was used which was purchased from (Wolf Laboratories Limited, UK) with temperature range (15-150 °C). As shown in fig (2-21). Ozone concentration was controlled by shielding/unshielding lengths of the UV lamp. This method of controlling the ozone concentration

---

[2] A pure synthetic air made by mixing oxygen and nitrogen. Details in section (2.6.1).

uses a long UV lamp running parallel to the tube containing the flow of air inside the generator. An aluminium shield slides in/out of the generator and covers a fraction of the lamp length: maximum ozone concentration is obtained by uncovering the full length of the lamp and proportionally less ozone is generated by shielding a fraction of the lamp. To measure the absolute concentration of ozone, we used colorimetric analysis of a solution of aqueous KI through which the air/ozone was bubbled. The output of the ozone generator was bubbled through (0.1M, 200mL) of aqueous KI in a Dreschel bottle for 20 minutes. Then the UV-vis spectrum of the solution was measured and the absorbance of the strong peak for triiodide I_3^- at 350 nm was recorded. This peak arises from the oxidation of iodide by ozone and was used to quantify the amount of ozone generated in 20 minutes via Beer's law. (more details on the measurements of ozone concentration are given in Appendix table S1).

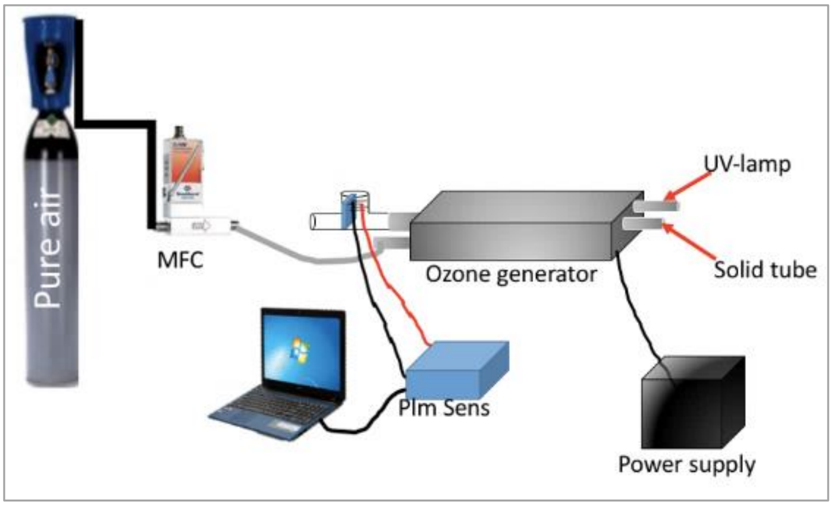

Figure 2-21 The sensing system to detect Ozone gas

Table 2-3 Show the conditions to sense ozone gas by CNTs and CNTs/BNNTs samples.

Ozone / ppm	Exposed lengths of the UV lamp / cm	Temperature / C^o
128	10	20
217.6	17	40
320	25	60

During ozone exposure, the electric properties of the nanotubes change and to observe this behaviour for the bare CNTs and hybrid nanotubes a PalmSens potentiostat (4.8) was used to measure the changes in the current with time before and after exposure. The film sensitivity was measured by the difference between the electrical current before and after gas as shown in eq (2-35):

$$S\% = \frac{(I - I_o)}{I_o} * 100\% \qquad (2-35)$$

Where: S is a film sensitivity, I_o is the current in an air atmosphere and I is the current at steady-state after exposure to ozone.

2.7. Saturated vapour pressure (SVP) calculations

For the sensing study, it was necessary to calculate the saturated vapour pressure for the volatile organic compounds (VOC) to understand the sensitivity level of the nanotubes for the VOC at the different temperature. SVP is known as a pressure extended by a vapour in an equilibrium system with its condensed modes/phases at a specific temperature in closed system[114, 115]. Saturated vapour pressure depends on Antoine's equation parameters as shown in equation (2-36) discovered in 1888 by French engineer Louis Charles Antoine[115].

$$\log_{10} P_{sat} = A - \frac{B}{C + T} \qquad (2-36)$$

Where P_{sat} is the saturated vapour pressure, T is a temperature in Kelvin, A, B and C are the constants (compound specific), their value for each VOC was obtained from the NIST web site (https://webbook.nist.gov). The gas concentration at the sensor was controlled by varying the mixing ratio of zero air at flow rate $V_{f\,(air)}$ to the flow rate of air/analyte, $V_{f(s)}$. The analyte is reported as a partial pressure P_{vap}.

Using P_{sat} from equation (2-36), P_{vap} is given by:

$$P_{vap} = P_{sat}\,\frac{V_{f(s)}}{V_{f(s)} + V_{f(air)}} \qquad (2-37)$$

Where $V_{f(s)}$ is the amount of the gas/vapour flow which is controlled by DMFC and $V_{f(s)}$ for the dry air mL/min.

In our study, four different analyte amounts were used as shown in table (2-4).

Table 2-4 The P_{vap} of the VOCs were investigated in this part of the study. P refers to saturated vapour pressure.*

VOC	$V_{f(s)}$ (mL/min)	$V_{f(air)}(mL/\mathrm{min})$	$P = P_{vap}$
Methanol	125	125	0.5P*
	250	125	0.67P*
	375	125	0.75P*
	500	125	0.8P*
Ethanol	125	125	0.5P*
	250	125	0.67P*
	375	125	0.75P*
	500	125	0.8P*
Acetone	125	125	0.5P*
	250	125	0.67P*
	375	125	0.75P*
	500	125	0.8P*
Chloroform	125	125	0.5P*
	250	125	0.67P*
	375	125	0.75P*
	500	125	0.8P*

2.8. Measuring the response time and recovery time for the sensors

The response times of the gas sensors in this thesis are reported as estimates of the time taken for the measured signal to reach close to steady-state after exposure to the analyte. The equivalent recovery times are estimates of the time taken for the signal to return to the baseline after the gas flow is switched back to zero air. A typical signal-time trace is shown in figure (2-22) with estimates of response and recovery times marked.

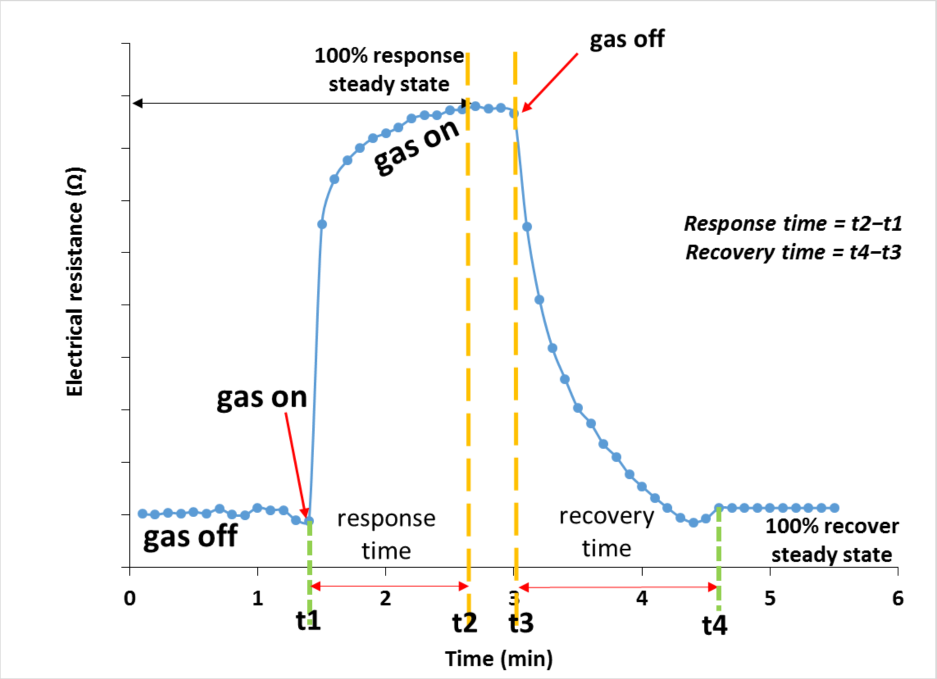

Figure 2-22 Schematic explanation of how the response and recovery time were measured in this thesis for VOCs, ozone and CO gas. In case of ozone sensors, the electrical resistance is replaced by the electric current as shown in chapter four.

Chapter three: Carbon nanotubes/conductive polymer composites

This chapter investigates the structure and electrical properties of carbon nanotubes (single wall and multi walls) and the nanocomposite films CNTs/polypyrrole. Results for the sensing of VOCs by bare and composite CNT films are presented. The effect of laser activation of the CNTs on the sensor characteristics is also reported.

3.1. Structural properties

3.1.1. Atomic force microscope AFM

The morphology of the carbon nanotubes was studied using AFM by depositing a drop of CNTs (~2µL of 100 µg mL^{-1}) and CNTs/Ppy on the surface of Si chips. According to this technique the distribution and the shapes of the carbon nanotubes SW and MW may change with the period of sonication. Three different times were used to prepare the carbon nanotubes: 30 min, 1 hr and 3 hrs and the effect of the sonication time is obvious in figure (3-1). After short sonication times (30 min), the nanotubes appear tangled with a high density and can be described as bundles or yarn. In addition, it was difficult to measure the real diameter of the carbon nanotubes, however after 3 hours sonication the nanotubes are more clearly separated and it was easier to measure a histogram of the diameter of the CNTs.

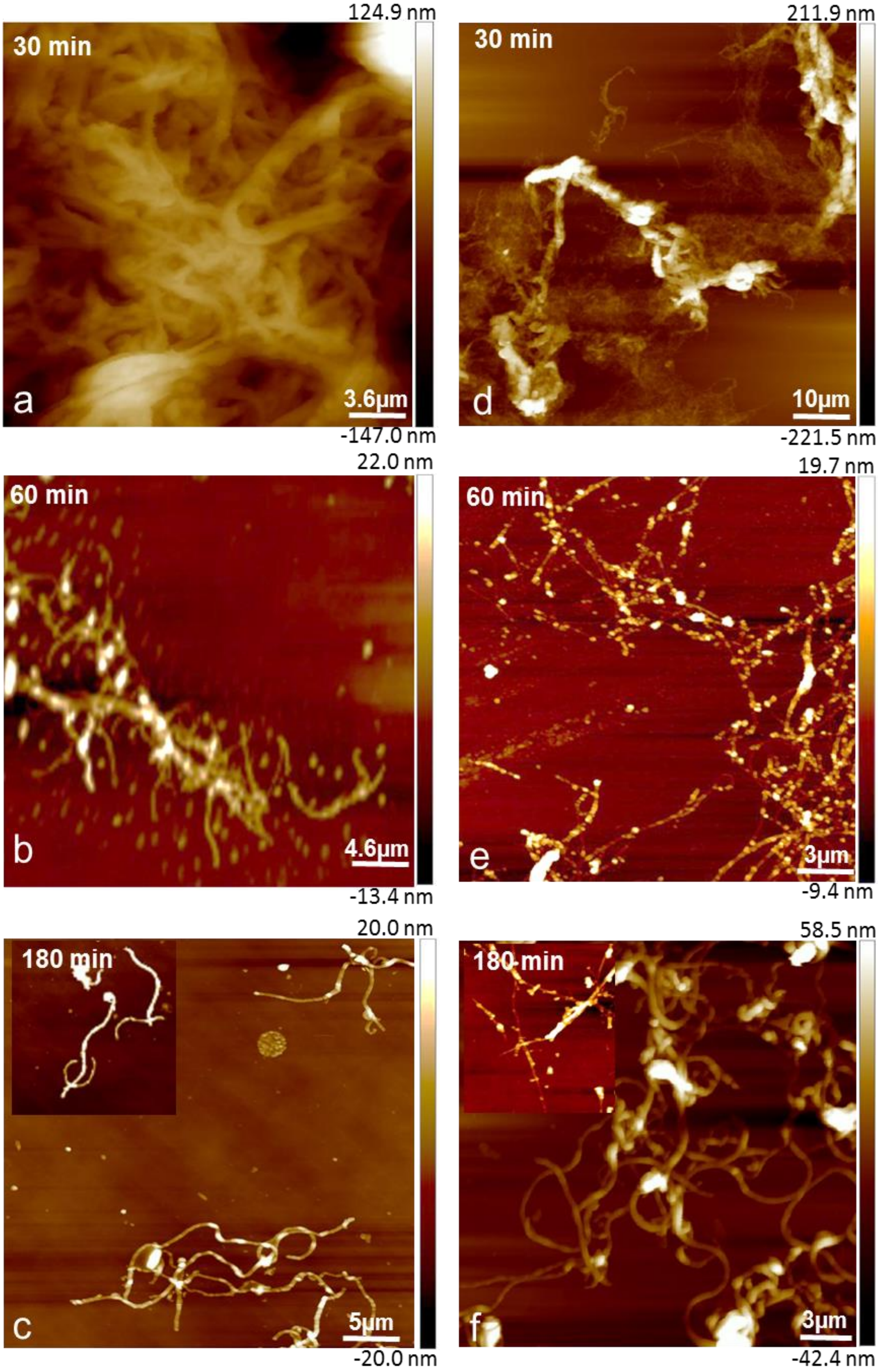

Figure 3-1 The effect of sonication time on the morphology of carbon nanotubes (SW and MW). a) MW at 30 min, b) MW at 60 min and c) MW at 180 min in sonication process. d) SW at 30 min, e) SW at 60 min and f) SW at 180 min.

At 60 min SWCNTs and MWCNTs appear as long tubes with small dots on the surface of nanotubes; these dots can be assigned to the metal nanoparticles used in their preparation [116]. Small knots are also seen, which can be assigned to agglomerates of CNTs, but from figure (3-1 b &e) the nanotubes have fewer agglomerates compared with the 30 min sample and individual nanotubes are apparent. After 180 min it is clear that the number of agglomerates decreased and the nanotubes for both SW and MW have smooth surfaces with few metal nanoparticles evident. The diameter for single wall carbon nanotubes was around (3-4.9) nm and (8-9.9) nm for multi walled carbon nanotubes. For the nanocomposite films, CNTs/CP, the diameters are significantly increased as demonstrated in figure (3-2), with some roughness on the surface of the carbon nanotubes, which points to the conductive polymer (polypyrrole). This indicates CNTs were successfully coated by Ppy. The PPy appears to form a shell around the CNTs as can be seen in the upper image of figure (3-2) where the CNT protrudes from the Ppy coating in the nanotube in the bottom, middle of that image. It is suggested that polypyrrole adheres to the CNTs by non covalent reactions which likely include dispersion forces and $\pi - \pi$ interactions with the sp^2 carbons of the tubes. More AFM images are provided in the appendix, figure (S4). The lower image in figure (3-2) shows a MWCNT/Ppy sample; the rougher nature of the CNTs compared to figure (3-1c) is due to the Ppy coating.

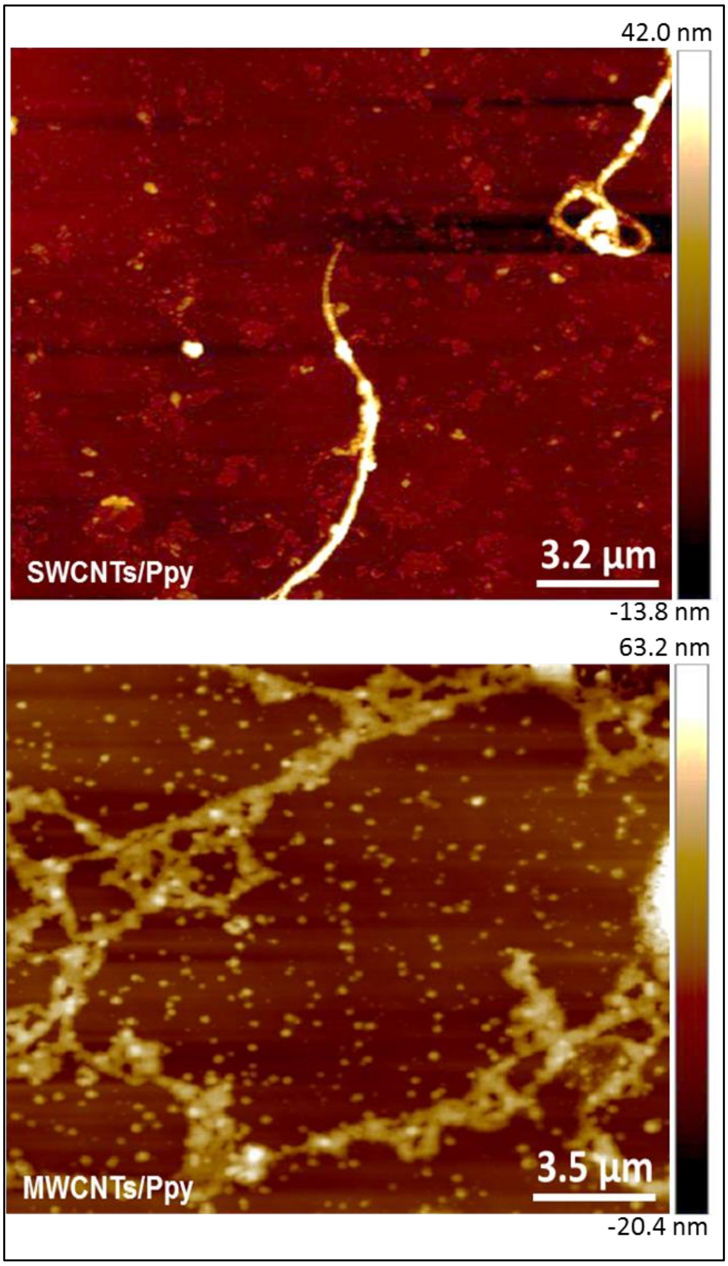

Figure 3-2 AFM images for the nanocomposite carbon nanotubes/polypyrrole.

3.1.2. Transmission electron microscope TEM

More features of carbon nanotubes (single wall and multi walls) have been studied by transmission electron microscopy TEM technique. Generally, in this thesis the multi walled carbon nanotubes have a Russian doll structure as shown in figure (3-3 & 3-4).

Figure 3-3 Russian doll model for multi-walled carbon nanotubes.

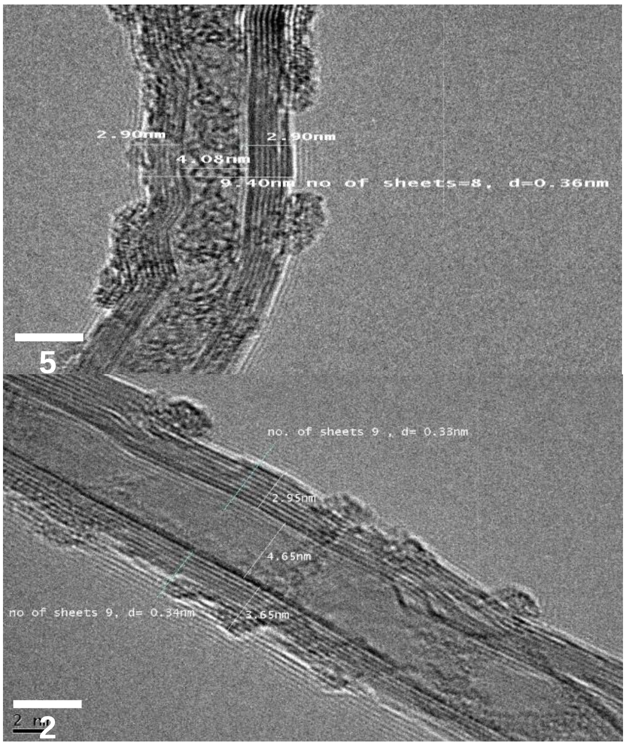

Figure 3-4 HTEM images of MWCNTs as a Russian doll structure prepared by CVD method. a) no. of walls is 8 with diameter 9.4 nm, b) no. of wells is 9 and the width equal 11.25nm.

More details for pristine multi walls carbon nanotubes can be examined by this technique. Nanotubes can be open or have capped ends and at the same time some of these nanotubes have a bamboo shape and possibly include numbers of buds growing on the surface of multi walls carbon nanotubes and hold the same physical properties as the main tube [18, 117] as seen in figure (3-5&6).

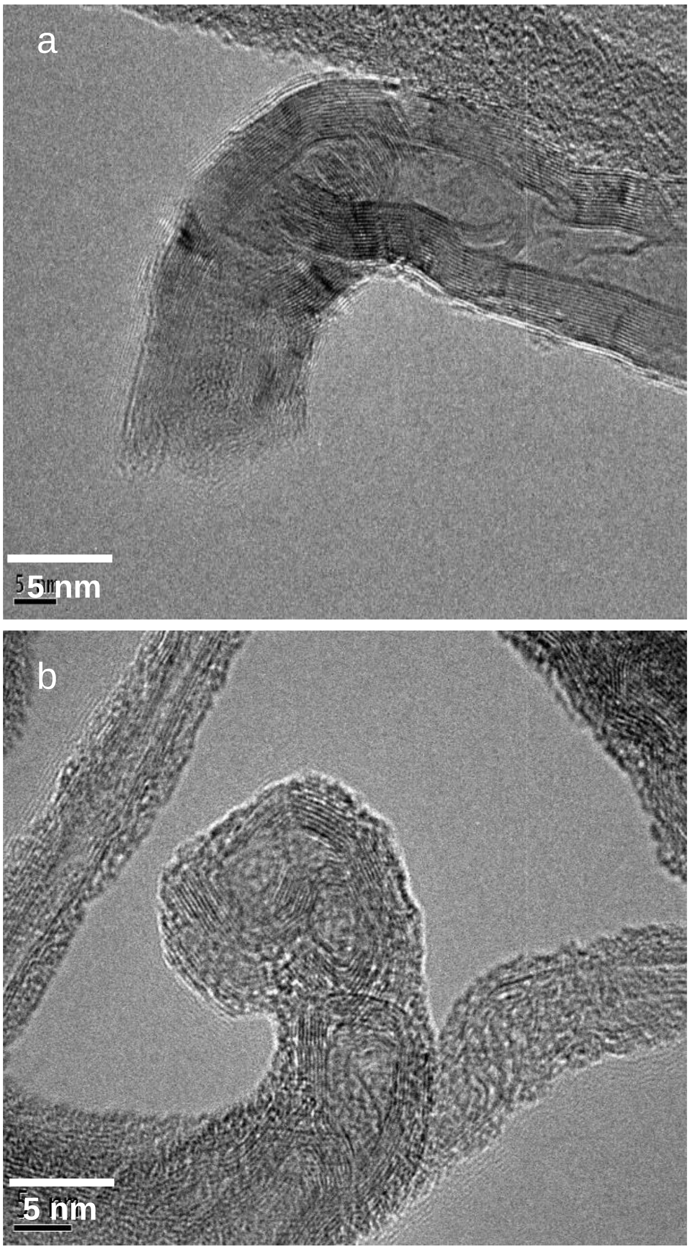

Figure 3-5 TEM images of MECNTs a) opened end, b) capped end.

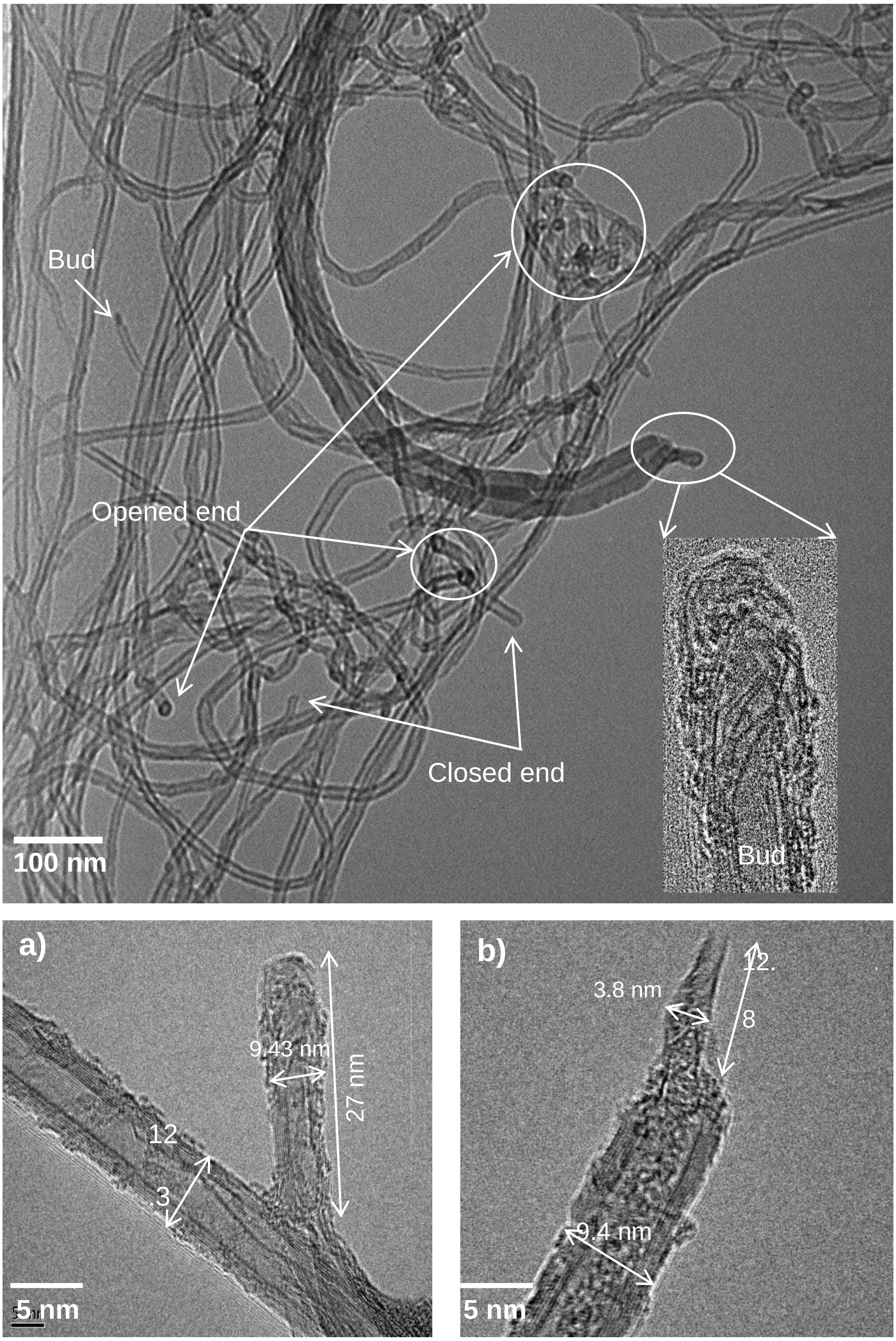

Figure 3-6 HTEM images of MWCNTs demonstrate nanotubes buds in the different position on the nanotubes. a) from the sidewall the tube, b) from the top of the nanotubes.

However, purity represents the main problem to produce carbon nanotubes by chemical vapour deposition. In the CVD approach, three metals (nickel, cobalt and iron) are used in combination or alone. In our carbon nanotubes, iron was used as a catalyst to prepare SW and MW. EDX spectra confirmed the presence of iron particles inside or around the nanotubes[32]. In this study, the purity of MWCNTs is 70% and 90% for single wall carbon nanotubes and TEM images showed small metal particles beside or inside the nanotubes, as shown in figures (3-7 & 3-8). The purity of our nanotubes is 70% (by weight) for MWCNTs and 90% for SWCNTs (according to the supplier, Thomas Swan Ltd.), the impurities are mainly non-CNT graphitic carbons, but with some Fe nanoparticles.

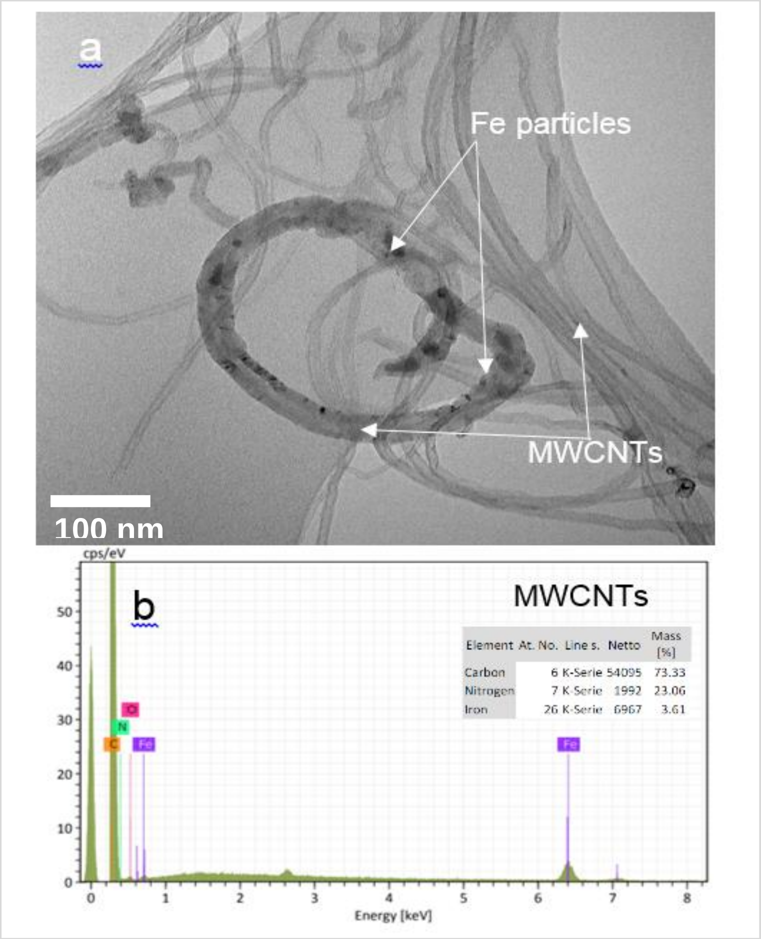

Element	At. No.	Line s.	Netto	Mass [%]
Carbon	6	K-Serie	54095	73.33
Nitrogen	7	K-Serie	1992	23.06
Iron	26	K-Serie	6967	3.61

Figure 3-7 TEM image of bare MWCNTs, b) EDX analysis and iron peaks appearing with carbon matrix.

For bare single wall carbon nanotubes, more tangled perhaps because they are more flexible, we can see the metal particles around the nanotubes. In addition, it was difficult to measure the length of the nanotubes due to the tangling. Generally, TEM for bare carbon nanotubes gave clear images with long and smooth nanotubes with minimal agglomerates or tangles but TEM for SWCNTs are more tangled than MWCNTs.

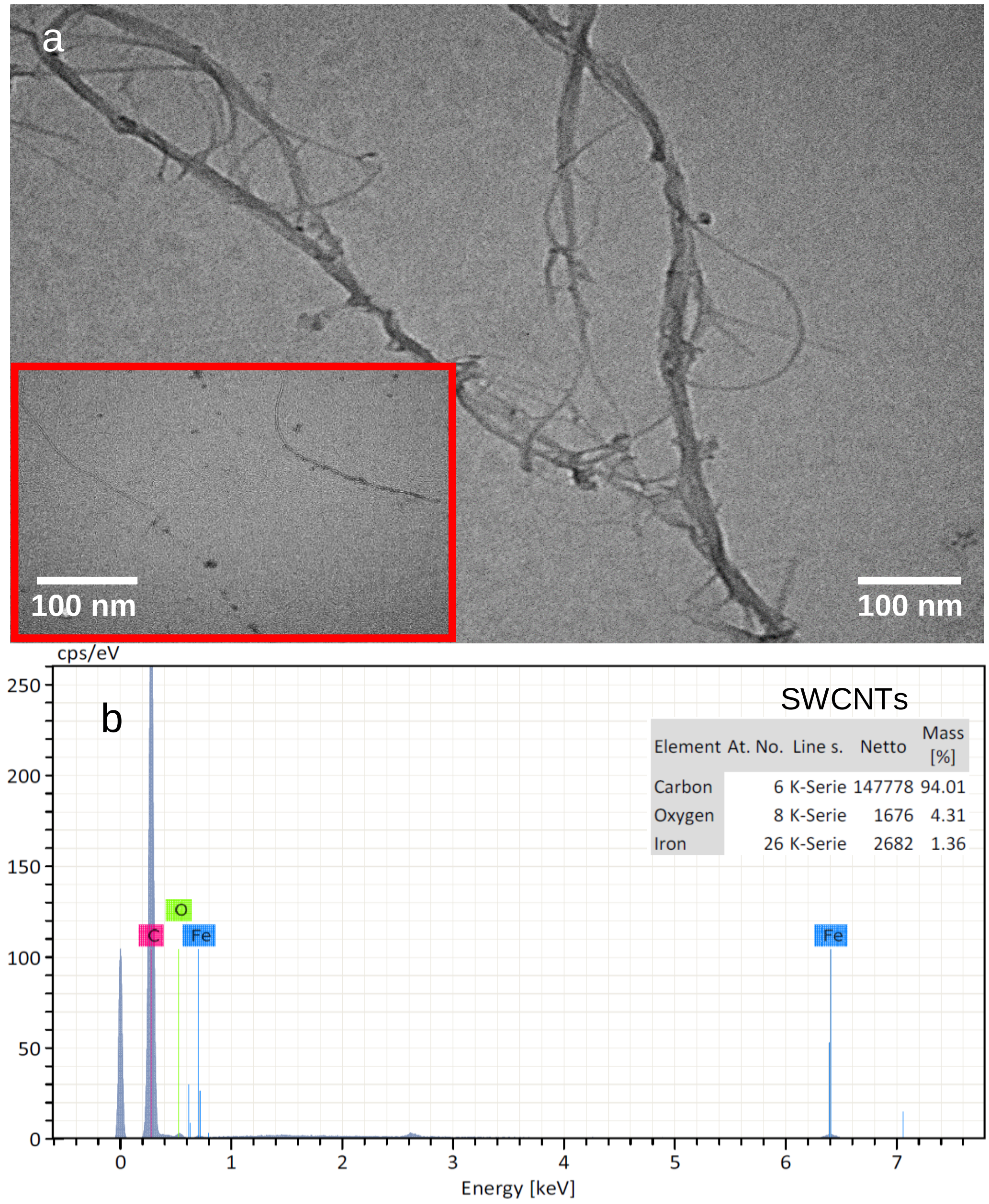

Element	At. No.	Line s.	Netto	Mass [%]
Carbon	6	K-Serie	147778	94.01
Oxygen	8	K-Serie	1676	4.31
Iron	26	K-Serie	2682	1.36

Figure 3-8 a) TEM image of bare SWCNTs, b) EDX analysis and iron peaks appeared with carbon matrix.

TEM of pristine CNTs gave clear images with long and smooth nanotubes with minimal tangles or agglomerates shown in figure (3-9a) for MWCNTs. However, the TEM analysis for SWCNTs demonstrated that the nanotubes are more tangled than MWCNTs as shown in figure (3-9c). The treatment with polypyrrole for the tubes (SW and MW) led to a change in their shape, for example, the length of the nanotubes for MW reduced with some roughness on the surface as seen in figure (3-9b) and for SWCNTs the nanotubes become more tangled than before the reaction with Ppy. Notably, films of polypyrrole appeared closed to the carbon nanotubes as shown in figure (3-9d). However, the significant increase in the width of CNTs after coating with Ppy, for example, the width of MWCNTs before treatment was (7~18) nm which became (21~50) nm, and for SWCNTs was (2~10) nm which increased to (8~35) nm after being coated with Ppy, as shown in figure (3-10). This means that after the polymerization Ppy was immediately created on the surface of CNTs.

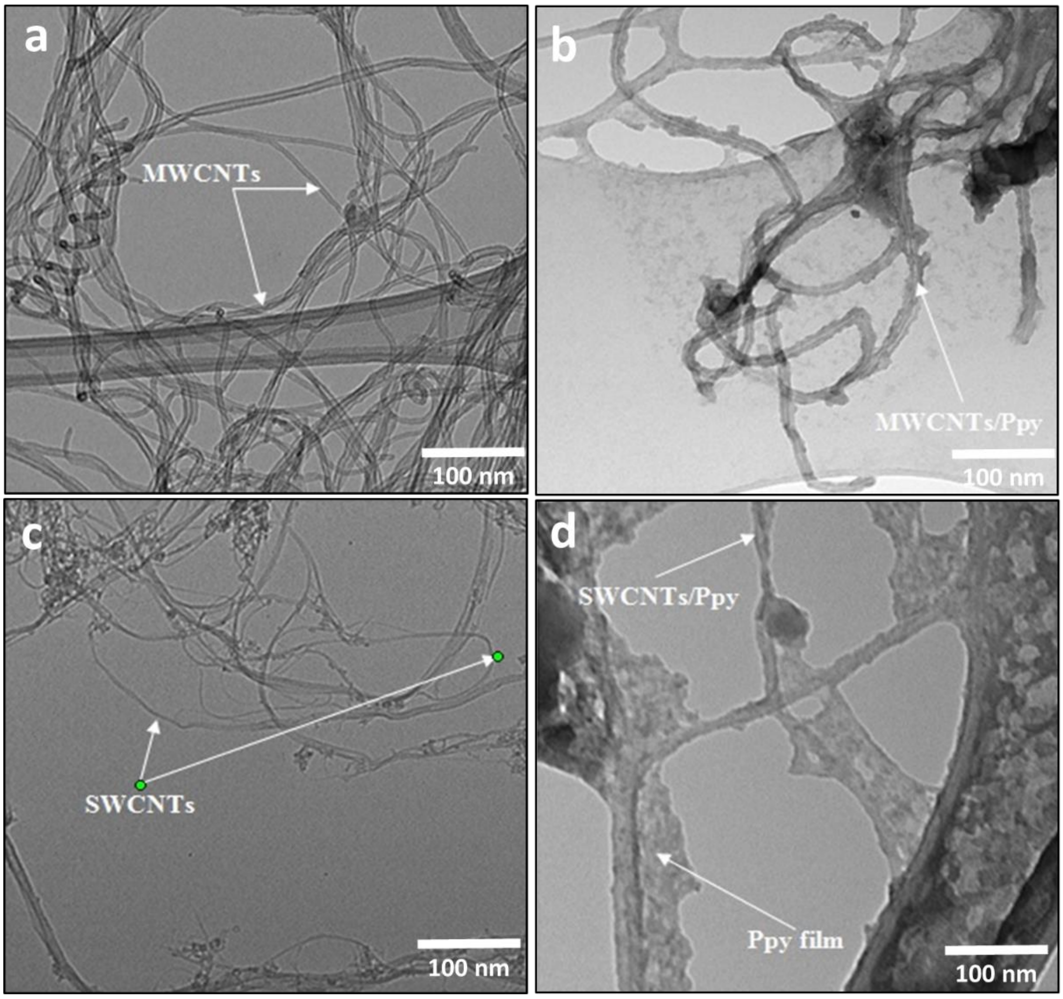

Figure 3-9 TEM images of (a) multiwall carbon nanotubes before coated by Ppy, (b) hybrid MWCNTs (c) bare SWCNTs, (d) SWCNTs after templated by Ppy.

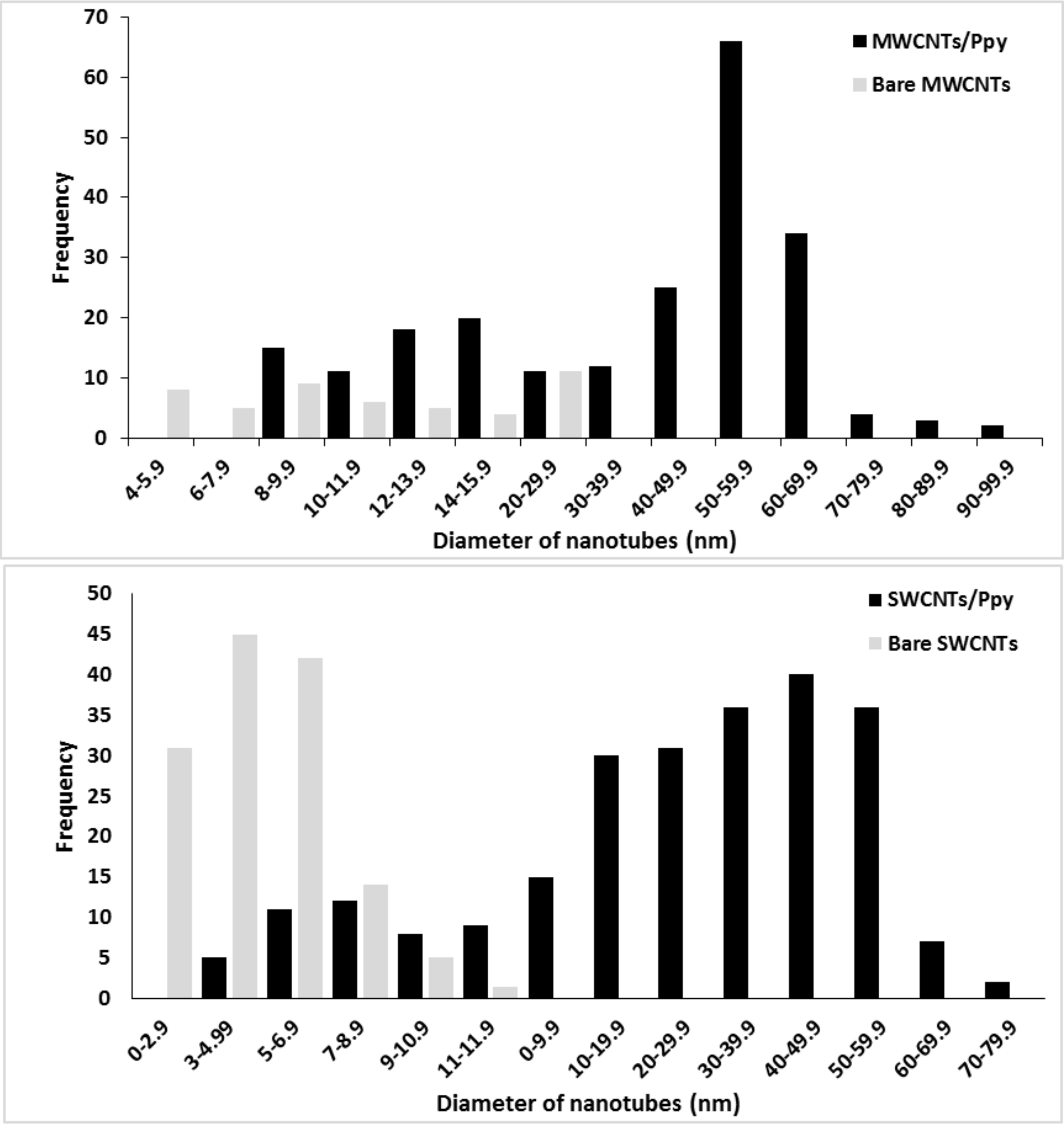

Figure 3-10 The histogram of carbon nanotubes a) bare and hybrid MWCNTs. b) pristine and hybrid SWCNTS. This histogram was depended on TEM images in figure (3-10) and figure (S2) in Appendix.

For all the CNTs/ppy samples in this thesis, the ratio between CNTs:Ppy was (20:1), this ratio was selected after examining three different ratios (50:1), (20:1) and (10:1).TEM images of CNT/Ppy composites for these Ppy/CNT ratios are shown in figure (3-11). At a ratio 50:1, the CNTs are incompletely coated by Ppy – there are substantial sections of uncoated CNT in figure (3-11a). At a ratio (10:1), very large dense deposits of polypyrrole and the nanotubes are hidden by this mass of polymer, as shown in figure (3-11c). The ratio of 20:1 showed CNTs coated with a thick shell of Ppy, which though not smooth, was contiguous.

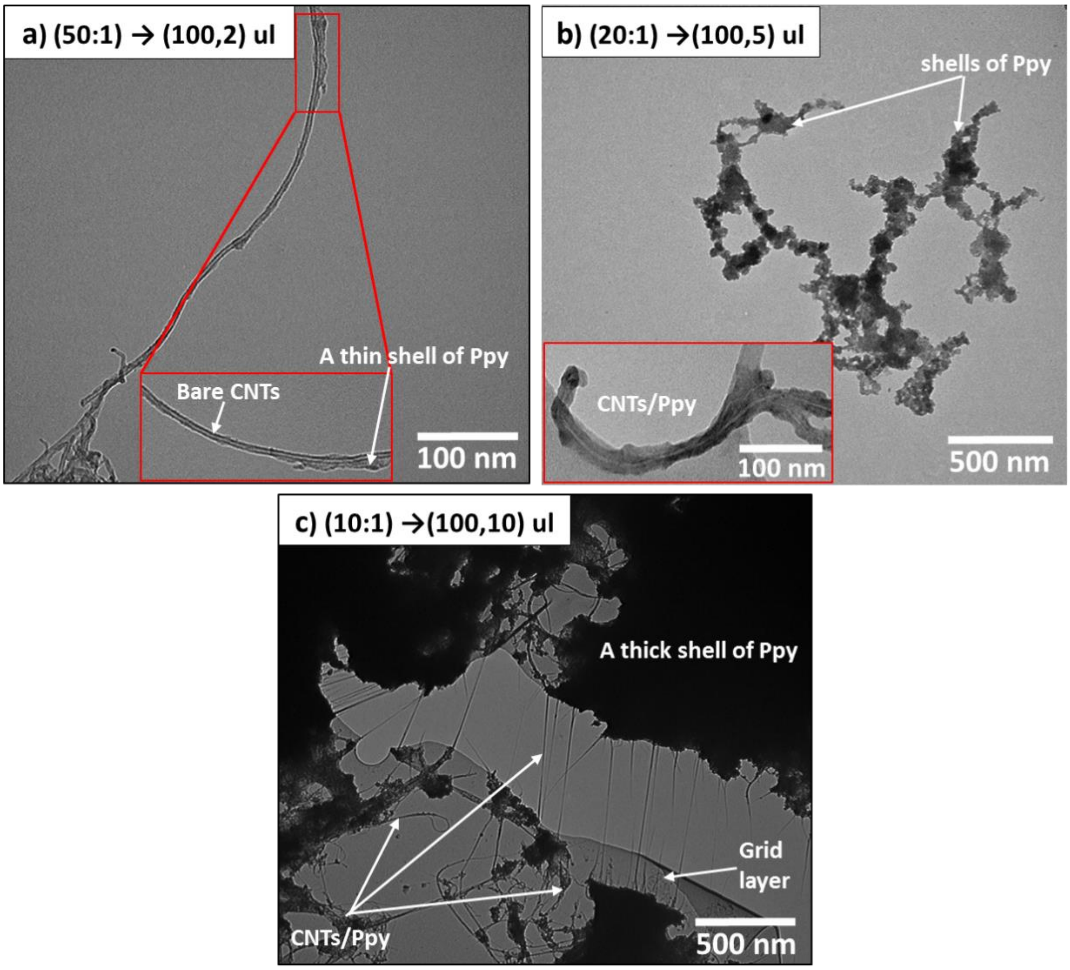

Figure 3-11 TEM images of CNTs/Ppy to show the effect the ratio between CNTs and polypyrrole on coating process.

3.1.3. I-V Characteristics and dependence on temperature for bare carbon nanotubes and hybrid nanotubes.

Two terminal I-V characteristics are an important approach to study the temperature dependence of the conductance of bare carbon nanotubes and nanocomposite tubes. A wide range of temperatures was used from (213 to 353) K and for controlling, monitoring and collecting the data a Casade microtech probe station and a 1500A semiconductor parameter analyser (Agilent) was used. A small drop (3 μL) of CNTs or CNTs/CP was deposited on parallel microelectrodes, dried, then used as demonstrated in figure (3-12).

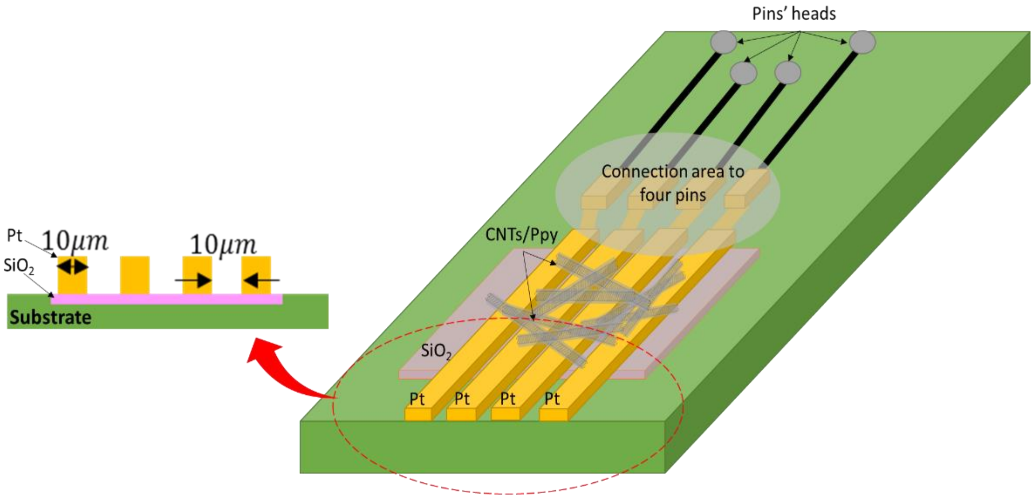

Figure 3-12 Schematic showing the distribution of the nanotubes on the active area of the electrode.

A small applied voltage was stepped between -2 V to +2 V and a linear response was measured over the wide range of temperatures from 213 to 353 K. For both SWCNTs and MWCNTs the current-voltage plots were completely linear, as shown in figure (3-13). However, the conductivity of the bare carbon nanotubes is very high and for SWCNTs the current was 10 mA at 2 V and at 213 K and decreased to ~ 9 mA at 353 K while it was 8.6 mA at 213 K and 7.6 mA at 353 K for multi wall carbon nanotubes. As noted in chapter two (2.1), it is clear that not all the carbon nanotubes are metallic, some nanotubes are semiconducting and it is difficult to separate them. However, in a film comprising a mixture of both in which there are multiple, parallel current pathways, the electrical current will be dominated by the most conducting, i.e., the metallic nanotubes. The conductivity of metallic nanotubes decreases when the temperature increases above 213K for both SW and MW nanotubes. The resistance of the nanotubes increased when the temperature rose above 213 K and the conductivity or the conductance decreased; this is the expected behaviour for metallic materials[118] as demonstrate in figure (3-13).

According to the Drude model, the conductance of the metallic nanotubes is described by equation (3-1)[119] :

$$\sigma = \frac{nq^2\tau}{m} \qquad (3-1)$$

Where: σ is the conductivity in Siemens (S), τ the scattering time (relaxation time), m the electron (or more generally charge carrier) mass, q the magnitude of the electron charge 1.6×10^{-19} C and n is the carrier density. Increasing the temperature leads to excitation of lattice vibrations and reduces the relaxation time, because the charge carriers scatter off lattice vibrations. The relaxation time is proportional to the conductivity of the nanotubes as demonstrated in equation (3-1). The heating of bare CNTs affects the mean free path of the electrons as demonstrated in equation (3-2)[120]:

$$\lambda = \tau\, v_t \qquad (3-2)$$

Where λ mean free path of the charge, τ relaxation time and v_t velocity of the electron, and as a result of the heating process the number of electron-phonon collisions increases, resulting in a smaller mean free path[120]. As the temperature increase, the number of phonons (quantized lattice vibrations) increases. The relaxation time τ is determined by the scattering of charge carriers off phonons, therefore as the temperature increases, τ decreases and the conductivity σ of a metal also decreases.

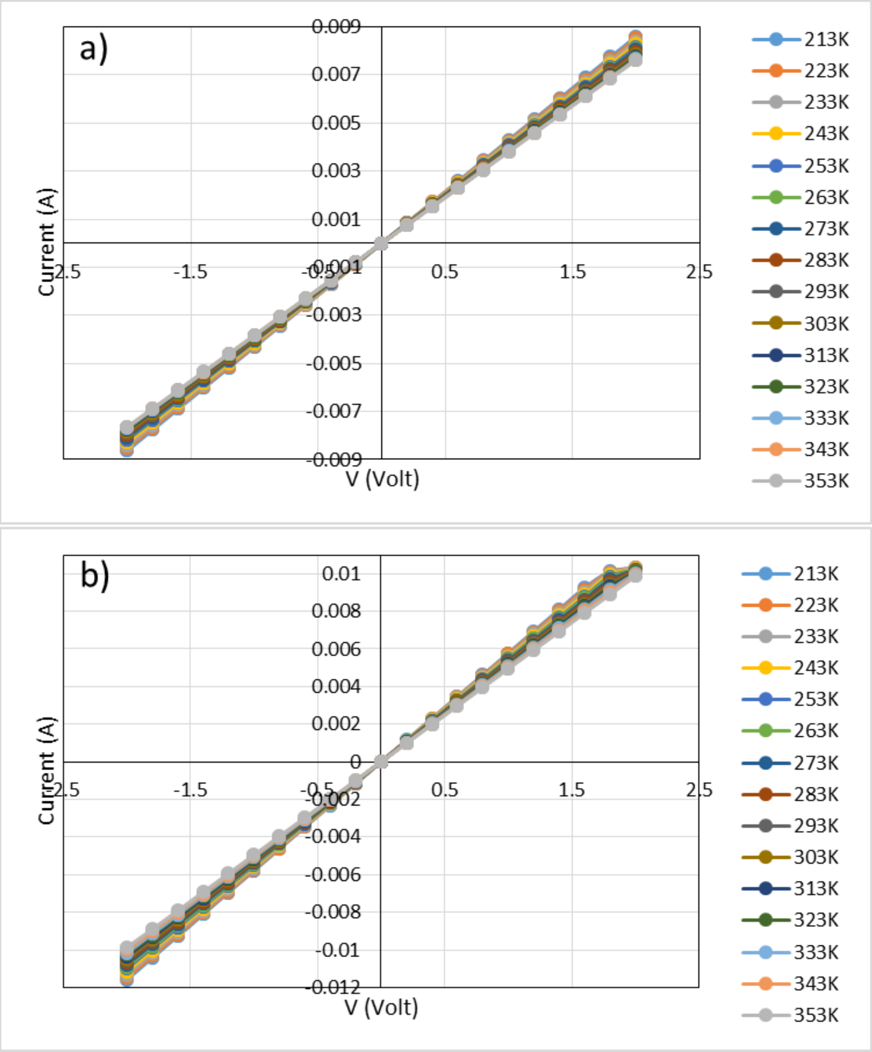

Figure 3-13 I-V curves measured by Casade microtech probe station a 1500A semiconductor parameter analyser (Agilent). a) bare MWCNTs b) bare SWCNTs.

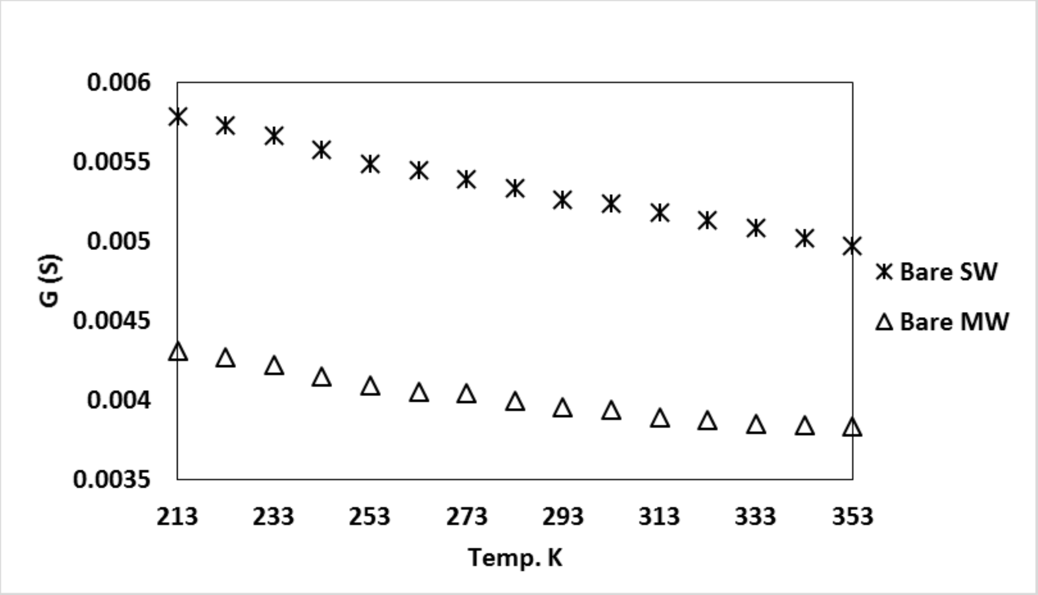

Figure 3-14 Reduction of the conductance of bare carbon nanotubes at different temperatures

The conductance of SWCNTs and MWCNTs was reduced or suppressed after coating by polypyrrole and templated CNTs by polypyrrole can effect on the pathways of the electrons between the nanotubes[121] [122]. Also it has been shown that some types of the conductive polymer may change the carbon nanotubes from p-type to n-type depending on the height of the Schottky barrier[123]. Most conductive polymers such as pyrrole have a significant increase in their conductivity with the temperature and conductivity dominated by charge transport in the conductive polymers[106]. The conductivities of polypyrrole between room temperature and 420K have been reported by Maddison and Tansley[124] to lie between 0.35 to 55.15 S cm^{-1}. Qingwen and coworkers measured the conductivity of bare CNTs to be (10^5-10^6) S m^{-1} at 293 K [125]. It is clear that the conductivity of polypyrrole is much less than that of CNTs. In figure (3-15) I-V measurements of CNTs/polypyrrole composites show a nonlinear behaviour when a small voltage was applied between -2 V and 2 V. The data indicates clearly that the polymer impedes charge transport so the (presumably) greater contact between tubes imparted by the polymer is more than offset by the lower conductivity of the tube-polymer-tube contacts; this is illustrated schematically in figure (3-16). The electrical current of the nanocomposite films increased with the temperature up to 343K and the electrical current was increased from 0.012 µA at 223K to 0.12 uA for MWCNTs/polypyrrole at 343K and from 88 µA at 223K to 128 µA at 343K for SWCNTs/polypyrrole [126].

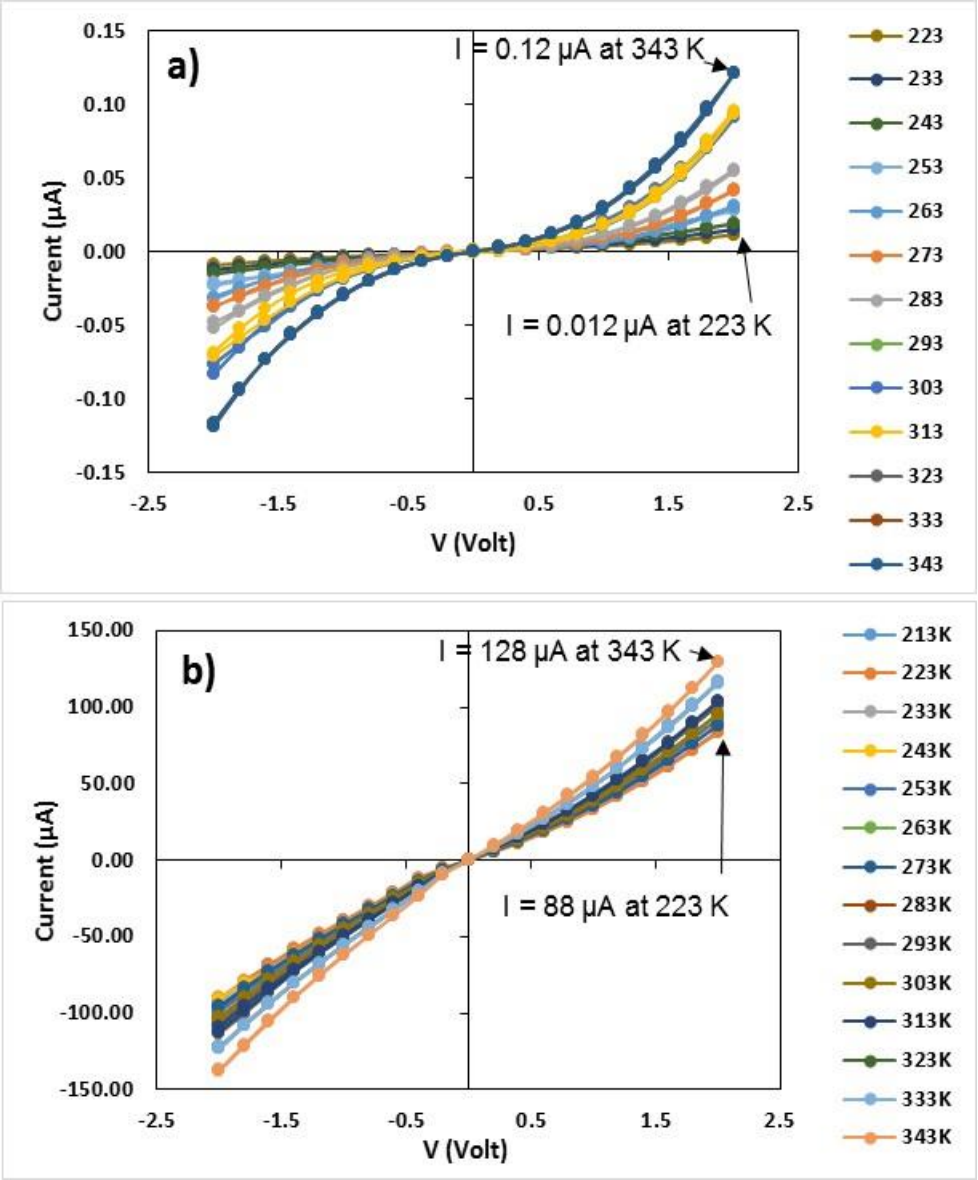

Figure 3-15 I-V measurements for a) MWCNTs/Ppy and b) SWCNTs/Ppy at different temperatures.

It is worth to note that for applied voltages in the range -0.5 V to 0.5 V, linear I-V plots appeared around the origin while the nonlinear curves were observed when the applied potential was larger than 0.5 Volt. This nonlinear behaviour could arise from rate limiting charge transfer across a Schottky barrier between the junction Pt-CNTs/Ppy. Yu and et al in 2010 found that the arrangement and conformation of the conductive polymer chains are a crucial feature in the conductivity of CNTs/CP, as shown in figure (3-16), also they reported that the expanded chains of the conductive polymer (Pyrrole), this expansion reduces the barrier between the inter and intra chain hopping which may enhance the electrical conductance of the CNTs/CP[127].

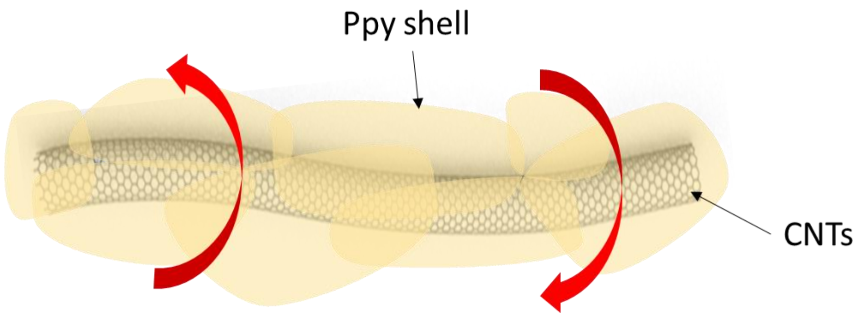

Figure 3-16 Schema demonstrates the effect of polypyrrole configuration on the electrical properties of carbon nanotubes, the arrows refer to the configuration of CP.

The data of figure 3-15 also show that the conductance of the CNT/Ppy composites increases as the temperature is raised, unlike the CNT films which some a decrease (metallic behaviour). In the conjugated polymers the temperature dependence of the conductivity is described by the variable-range-hopping model and the equation (3-3):

$$G = G_o exp^{-(\frac{T_O}{T})^{\beta}} \qquad (3-3)$$

Where T_0 is an effective temperature equal which can be related to an activation barrier E_a/k_B, G_o is a constant and β depends on the theoretical model and the dimensionality of the sample where:

$$\beta = \frac{1}{(n+1)} \qquad (3-4)$$

n=1, 2,…….is the dimensionality

A thick film of polypyrrole demonstrates temperature dependence characterized by 3D VRH where n = 3 and β = 0.25, but for the thin film of polypyrrole β=*0.5,* which is also predicted by the Efros-Shklovski model[128]. In 1D materials, where the electrons or other charge carriers cannot avoid a large barrier, the arguments leading to equation (3-4) break down. The value of β may be controlled by a variety of factors. It has been observed that in one dimension β= 1 is typical and leads to Arrhenius- like behaviour of the conductance [128]. Arrhenius' law originates in the study of chemical kinetics, but applies to conductance measurements when there is a rate-limiting single (or narrowly distributed) activation energy E_a. A plot of $\ln G$ vs 1/T has slope = $-E_a/R$ and G increases as T increases and slope<0 with $E_a > 0$, Where G is the conductance, R is the gas constant 8.314 $J.mol^{-1}$, T temperature (Kelvin), E_a is the activation energy ($J.mol^{-1}$) or eV. Figure (3-17) shows the conductance of CNTs/Ppy at different temperatures, the conductance of the nanocomposite films increases with the heating, which is similar to the semiconductor behaviour, and the hopping rates increase upon raising the temperature. Figure (3-18) displays the linearity of Arrhenius plots for SWCNTs/Ppy and MWCNTs/Ppy and as explained before hopping dominates in this part. According to the Arrhenius plots the activation energy for SWCNTs/Ppy and MWCNTs/Ppy were calculated as 0.14 eV for MW/Ppy and 0.03 eV for SW/Ppy.

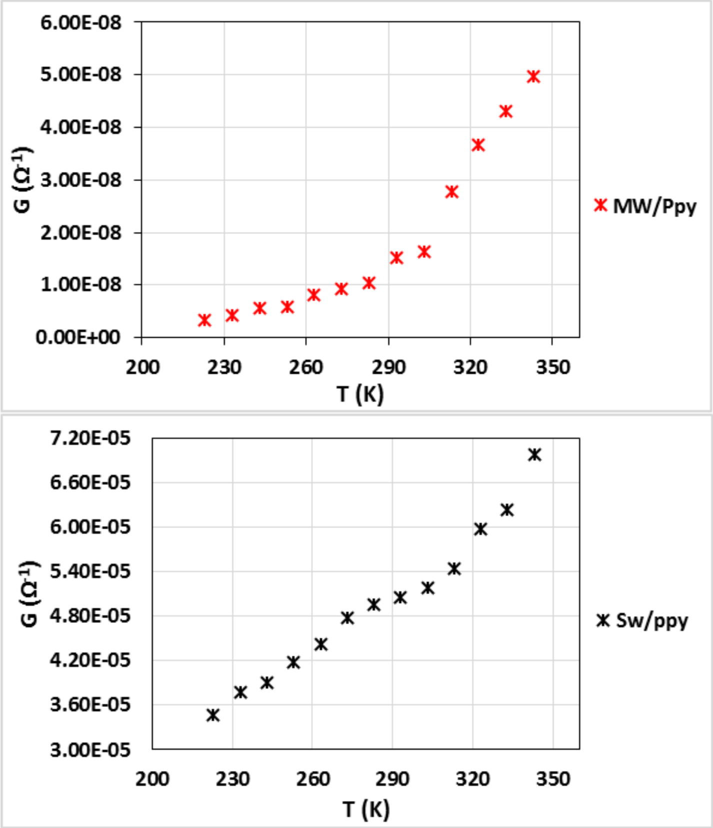

Figure 3-17 The conductance of CNTs/Ppy at a wide range of temperatures.

From figure (3-17) the conductance of the hybrid single carbon nanotubes is higher that MWCNTs/Ppy and this is further evidence that the electrical properties of SWCNTs samples are superior to those of MWCNTs[1, 129].

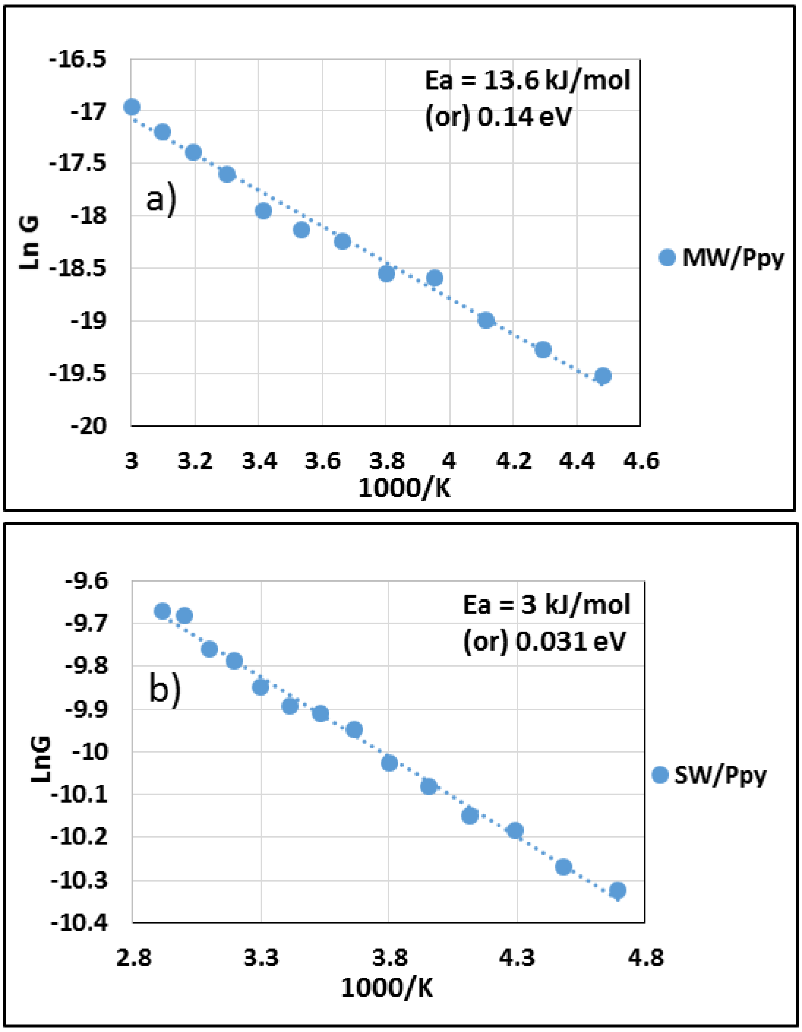

Figure 3-18 Arrhenius curve of the conductivity of the hybrid carbon nanotubes, a) MWCNTs/Ppy and b) SWCNTs/Ppy.

3.1.4. Electronic analysis of two terminal nanotube devices:

Further information on the electrical properties of bare carbon nanotubes and hybrid nanotubes was obtained from impedance spectroscopy and current-time transients. These techniques can provide information on the contact resistance and the behaviour at high applied voltages.

The conductivity of pristine carbon nanotubes is much higher than CNTs/Conductive polymer and, from the linearity of I-V curves for bare carbon nanotubes, the nanotubes obeyed Ohm’s law in figure (3-13). In an impedance spectroscopy experiment a resistor that obeys Ohm's law has a frequency-independent real part and no imaginary part (table (2-2) chapter two). IS is a very important technique to understand and evaluate the electrical properties of materials that have one or more interfaces with contact electrodes [109 107, 108]. In this study IS was measured by applying a small (order of 10 mV) alternating potential to the electrical circuit as shown in figure (3-19) and measuring the alternating current over a frequency range of 5 Hz - 10 kHz. The Nyquist plot for bare carbon nanotubes showed, as expected, that the imaginary component was small compared to the real component and the latter was frequency-independent (figure (3-19)). The real resistance for SWCNTs was ~ 213 Ω and ~ 300 Ω for MWCNTs which is further evidence that SWCNTs have a higher conductivity than MWCNTs.

IS is a small signal technique (small applied bias). The high bias region was investigated by studying the current-time transient in response to an abrupt potential step across the device. We found that both SWCNTs and MWCNTs recorded a high current when a small potential was applied and no capacitive effects due to the Pt-CNTs interface were observed, i.e., the transients had flat tops at the voltages 1,2,3 and 4 V. Some small evidence of capacitive effects are seen only at the highest applied bias of 5 V in figure 3-20. SWCNTs show a high current compared with MWCNTs (5-22) mA and between (3-16) mA for bare MWCNTs as shown in figure (3-20a). The distance between the terminals affected the electrical current in this type of device by changing the length of the current path through the CNT films. As shown in figure (3-20b) the current was reduced for 40 μm and 60µm paths compared with 20µm and the bulk film resistance, R_{i-v} increased as displayed in figure (3-20b). From I-V studies, IS and current-time transients on bare carbon nanotubes for both SWCNTs and MWCNTs it has been found that the film resistance has a similar value in these three techniques ~ 213 Ω for SWCNTs and ~ 300 Ω for MWCNTs. This agreement confirms that the electrical behaviour of the bare nanotubes is well-described by a simple resistance over a range of applied biases and frequencies.

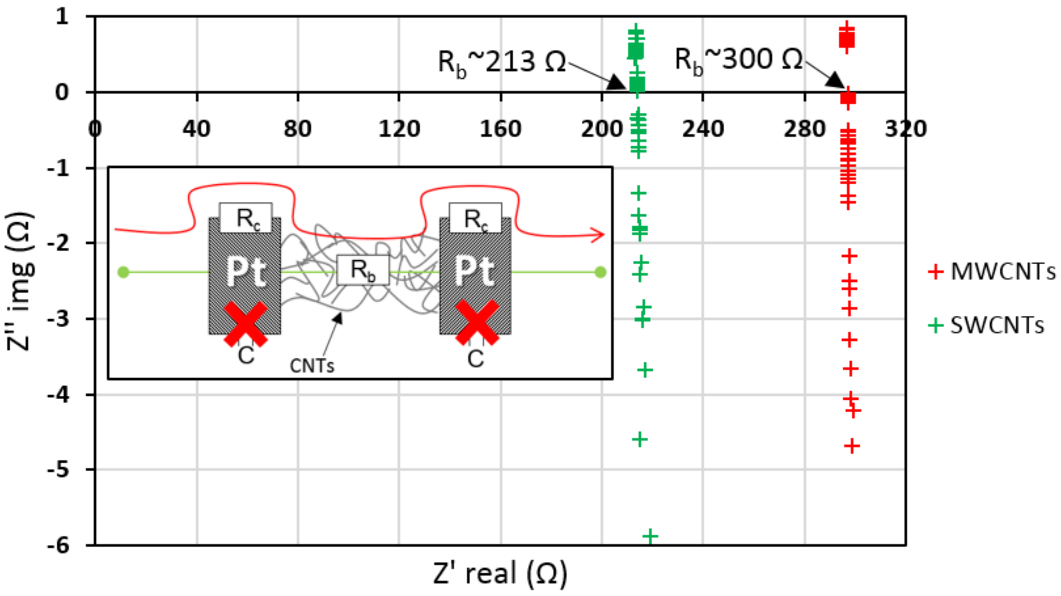

Figure 3-19 a) electric circuit where Rc is the contact resistance and Rb is the film resistance. b) Nyquist plot of bare carbon nanotubes.

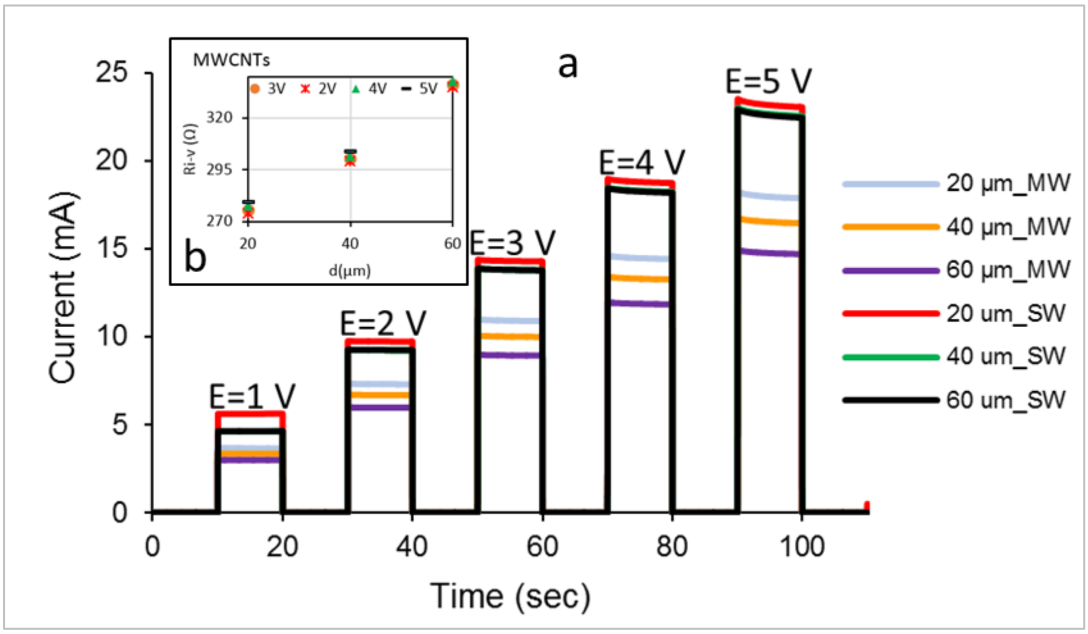

Figure 3-20 a) Current-time transient analysis for SWCNTs and MWCNTs in different voltage applied b) Ri-v of bare MWCNTs at a room tempertature with different distances between the terminals during applied potential

In contrast, the nanocomposite films MWCNTs/Ppy and SWCNTs/Ppy have a different electrical behaviour to the bare nanotubes. IS studies were performed on hybrid nanotubes with the same frequency range (5-10000) Hz. However, both real (Z'_{re}) and imaginary (Z''_{img}) parts were observed in the impedance spectrum. The IS was modelled by an equivalent circuit comprising a pure capacitor representing charge stored at the Pt/composite interfaces, $C=1/(2\pi f\ Z''_{img})$, and a simple resistance for the bulk film. Any barrier between Pt contacts and the CNTs/polypyrrole composite may lead to accumulation of charges at the Pt/CNTs/Ppy interface. Generally, when a potential is applied two types of currents flow inside the device (CNTs/Ppy) as shown in the figure (3-21). The first is the flow of charges through the Pt contacts and through the CNTs/Ppy film. The second corresponds to accumulation of charges at the Pt/CNTs/Ppy interfaces. Both Pt/CNTsPpy and CNTsPpy/Pt interfaces are represented by capacitors in this electrical circuit which is the origin of the imaginary impedance in the system[130]. The film resistance was estimated from the intercept on the real axis at high frequency as Z'_{re} for SWCNTs/Ppy = 0.061 GΩ and 0.2 GΩ for MWCNTs/Ppy. The IS and the transient data provide another way (along with variation of electrode terminal separation) to distinguish contact resistance at the Pt/CNTs/Ppy from the bulk CNTs/ppy film resistance. Large transient currents suggest a substantial contact resistance, R_c, contribution.

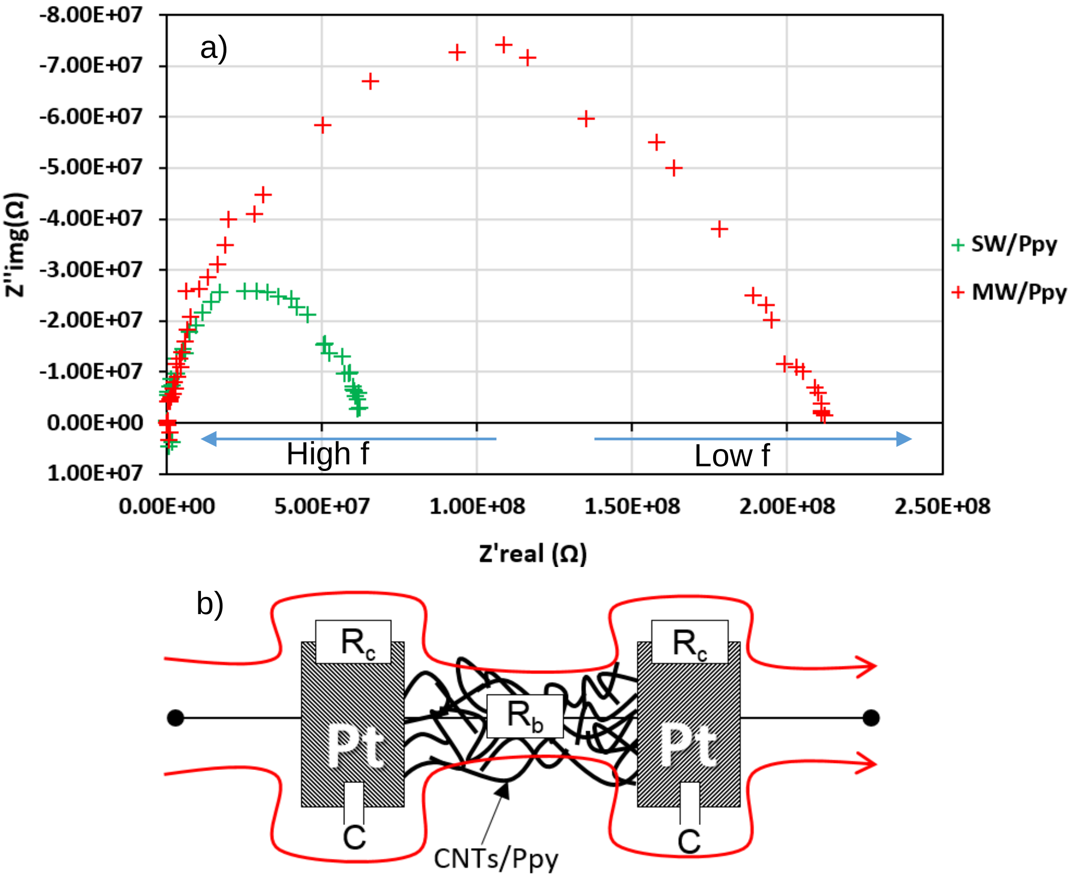

Figure 3-21 a) Nyquist plot of CP/CNT composite. b) scheme of the electric circuit where R_c is the contact resistance, R_b the film resistance, Pt-electrode (terminal). C represents the capacitance at the Pt/composite interfaces.

Current - time transients for the nanocomposite films show a large transient component of the current compared with pristine carbon nanotubes (compare the data in figure (3-24) with that in figure (3-20) for bare CNTs). Using the current immediately after the applied potential step, i_{total}, the steady-state current at long times, i_{ss} and equation (2-31) it is possible to extract values of both R_c, the contact resistance and R_b, the bulk resistance of the composite as shown in figure (3-21). These values are in principle related to the resistance derived from the slope of the steady-state I-V characteristic R_{i-v} $R_{i-v} = R_b + 2R_c$ as displayed in figure (3-22 & 23) and table (3-1). The factor of 2 accounts for the two nominally identical contact resistances at each Pt electrode.

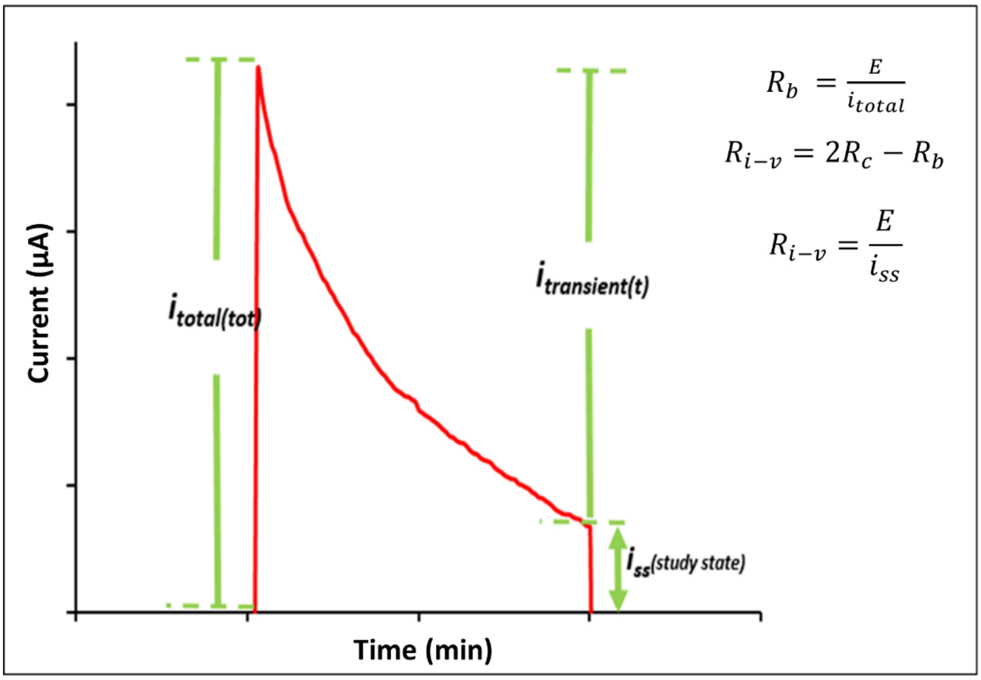

Figure 3-22 Scheme pattern of measuring the electrical resistance by current-time technique.

Figure (3-24) shows the current-time data for SWCNTs/Ppy and MWCNTs/Ppy. There are two regions with different behaviour, labelled A and B. In area A, where the magnitude of the applied voltage is < 2 V, the i-t response has a flat top, $i_{total} = i_{ss}$ and the contact resistance is small. In area B there is a transient current to analyse and the contact resistance is significant. It was also possible to vary the interelectrode spacing and by assigning the change in the resistance to the bulk, R_b, an independent estimate of contact resistance can be made. Figure 3-21 shows the approximately

linear trend for overall resistance against electrode separation; a non-zero intercept indicates a significant contact resistance.

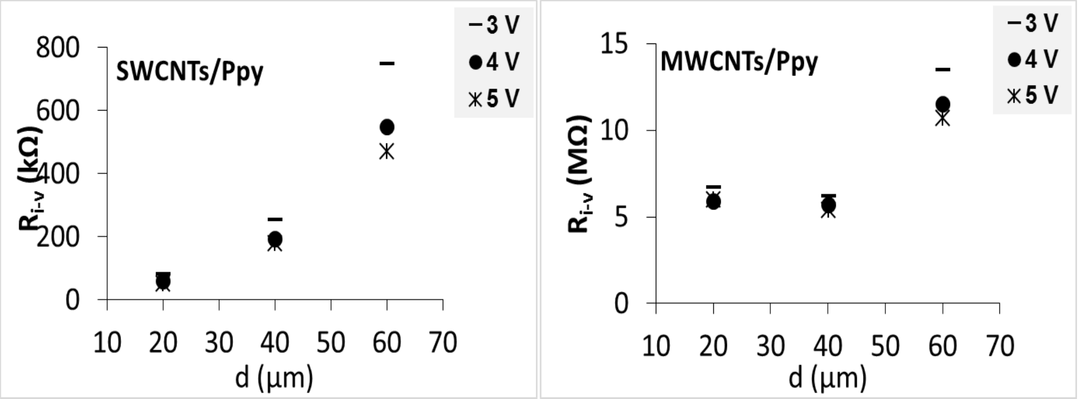

Figure 3-23 Ri-v of hybrid carbon nanotubes at three potentials 3, 4 and 5 V for three terminals (1&2), (1&3) and (1&4) which equals Rb+2Rc

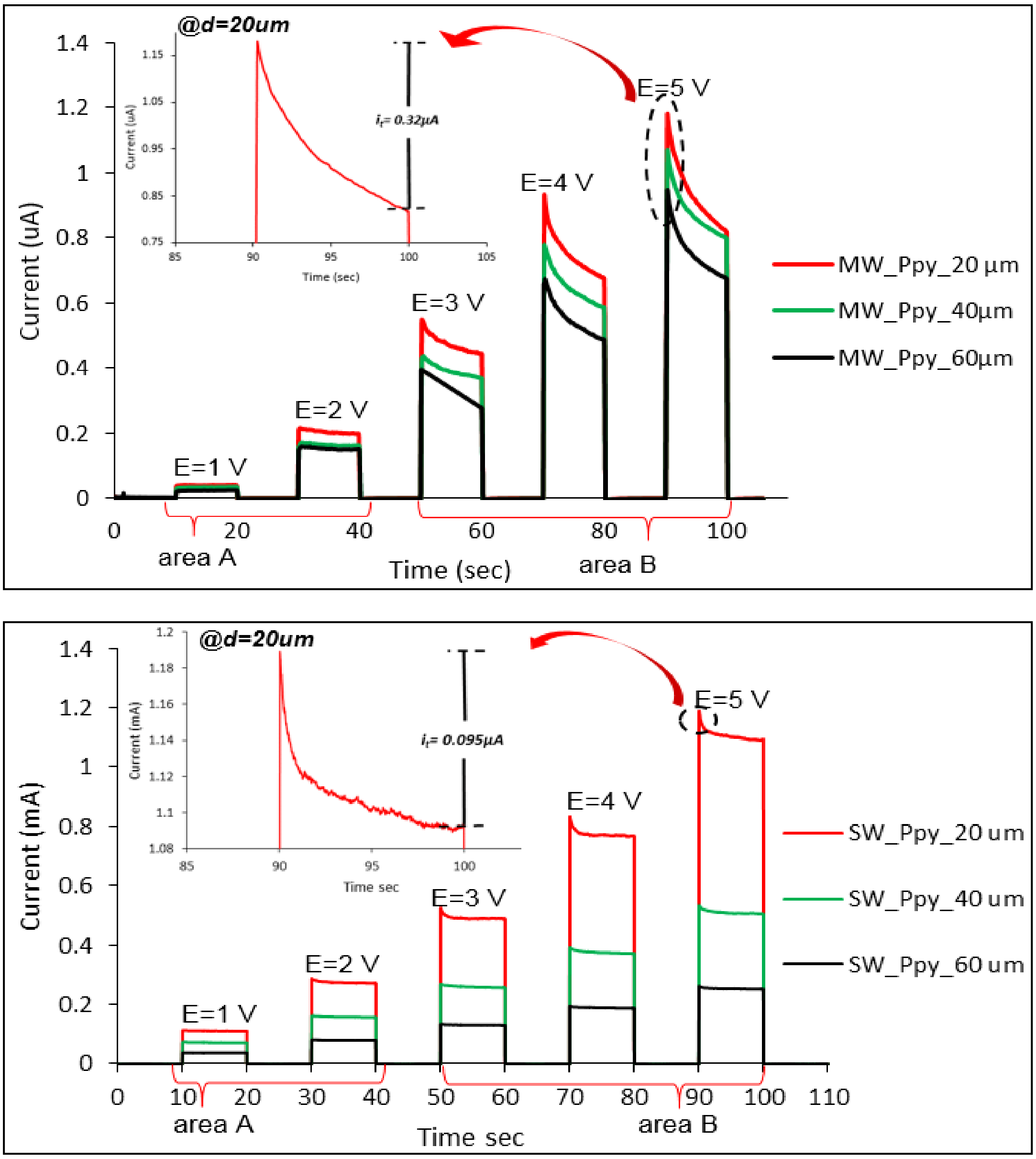

Figure 3-24 Current- time transient of MWCNTs/ and SWCNTs/Ppy after applying different potential at room temperature

Table 3-1 Rc (at one contact) and Rb for MWCNTs/Ppy and SWCNTs/Ppy films at different voltages and for three interelectrode distances.

d (μm)	Voltage (V)	MWCNTs/Ppy		SWCNTs/Ppy	
		Rb / Ω	Rc / Ω	Rb /Ω	Rc / Ω
20	1	7.04 x10^{4}	9.03 x10^{6}	8.9 x10^{3}	1.67 x10^{5}
40		7.57 x10^{5}	2.66 x10^{7}	13.6 x10^{3}	2.11 x10^{5}
60		5.1 x10^{6}	5.1 x10^{7}	27.7 x10^{3}	1.46 x10^{6}
20	2	1.9 x10^{4}	7.09 x10^{6}	6.9 x10^{3}	5.6 x10^{4}
40		3.85 x10^{5}	9.4 x10^{6}	1.24 x10^{4}	1.94 x10^{5}
60		5.3 x10^{5}	1.89 x10^{7}	2.48 x10^{4}	7.3 x10^{5}
20	3	2.33 x10^{5}	5.48 x10^{6}	5.7 x10^{3}	3.85 x10^{4}
40		5.22 x10^{5}	5.75 x10^{6}	1.12 x10^{4}	1.22 x10^{5}
60		6.41 x10^{5}	1.24 x10^{7}	2.25 x10^{4}	3.64 x10^{5}
20	4	3.01 x10^{5}	4.3 x10^{6}	4.8 x10^{3}	2.85 x10^{4}
40		6.7 x10^{5}	5.19 x10^{6}	1.02 x10^{4}	9.25 x10^{4}
60		8.03 x10^{5}	1.02 x10^{7}	2.06 x10^{4}	2.64 x10^{5}
20	5	2.61 x10^{5}	4.24 x10^{6}	4.21 x10^{3}	2.34 x10^{4}
40		8.11 x10^{5}	4.92 x10^{6}	9.37 x10^{3}	8.59 x10^{4}
60		9.15 x10^{5}	9.14 x10^{7}	1.91 x10^{4}	2.26 x10^{5}

Table (3-1) collects the bulk resistance (R_b) and contact resistances (R_c) for MWCNTs/Ppy and SWCNTs/Ppy devices over a range of applied potentials and interelectrode gaps. Consistent with the IS data, the bulk resistances are generally smaller than the contact resistance.

3.2. Optical properties

3.2.1. Raman spectroscopy

Raman spectroscopy is a powerful tool to analyse the composition of the conductive polymer / carbon nanotube samples. The vibrational Raman spectrum of bare carbon nanotubes (single walled and multi walled) was measured as a control to compare that with the spectrum of the nanocomposite CNTs/polypyrrole. A layer of the bare and hybrid carbon nanotubes was applied by drop-coating on a silicon chip which was cleaned by piranha solution. All the spectra were measured by a CRM 200-confocal

Raman microscope (Witec) equipped with a diode laser of wavelength 488 nm. Raman spectroscopy gives unique information about carbon nanotubes and it was easy recognize the spectrum of CNTs by this technique[131]. The spectrum of carbon nanotubes including one phonon emission comprises: G-band, radial breathing mode RBM and D-band[131] .Generally, the D-band is assigned to the breathing mode of sp^3 atoms (defects), while the G-band corresponds to the E_2g mode of hexagonal graphite and relates to the vibration of sp^2 hybridized carbon atoms in a layer of graphite. For pristine carbon nanotubes and as shown in figure (3-25) two bands are observed: the G and D bands. The D-band has a wavenumber of 1328 cm^{-1} and is stronger in the MWCNTs, but can be recognized easily for the nanocomposite films SW/Ppy and MW/Ppy. The typical peak of pristine SWCNTs and MWCNTs is at 1612 $cm^{-1.}$ After a polypyrrole coating forms on the carbon nanotubes' surface, three additional Raman peaks appeared at 1328, 1063 and 1611 cm^{-1} and because silicon was used as substrate, a sharp peaks is found at 521 cm^{-1}. However, the Raman spectrum of polypyrrole was measured also and it was found that Ppy has a peak at 1058 cm^{-1} which corresponds to the C=N in plane deformation of the conductive polymer and the same peak appeared in the spectrum of CNTs/Ppy and that confirms polypyrrole successfully coated the carbon nanotubes[132].

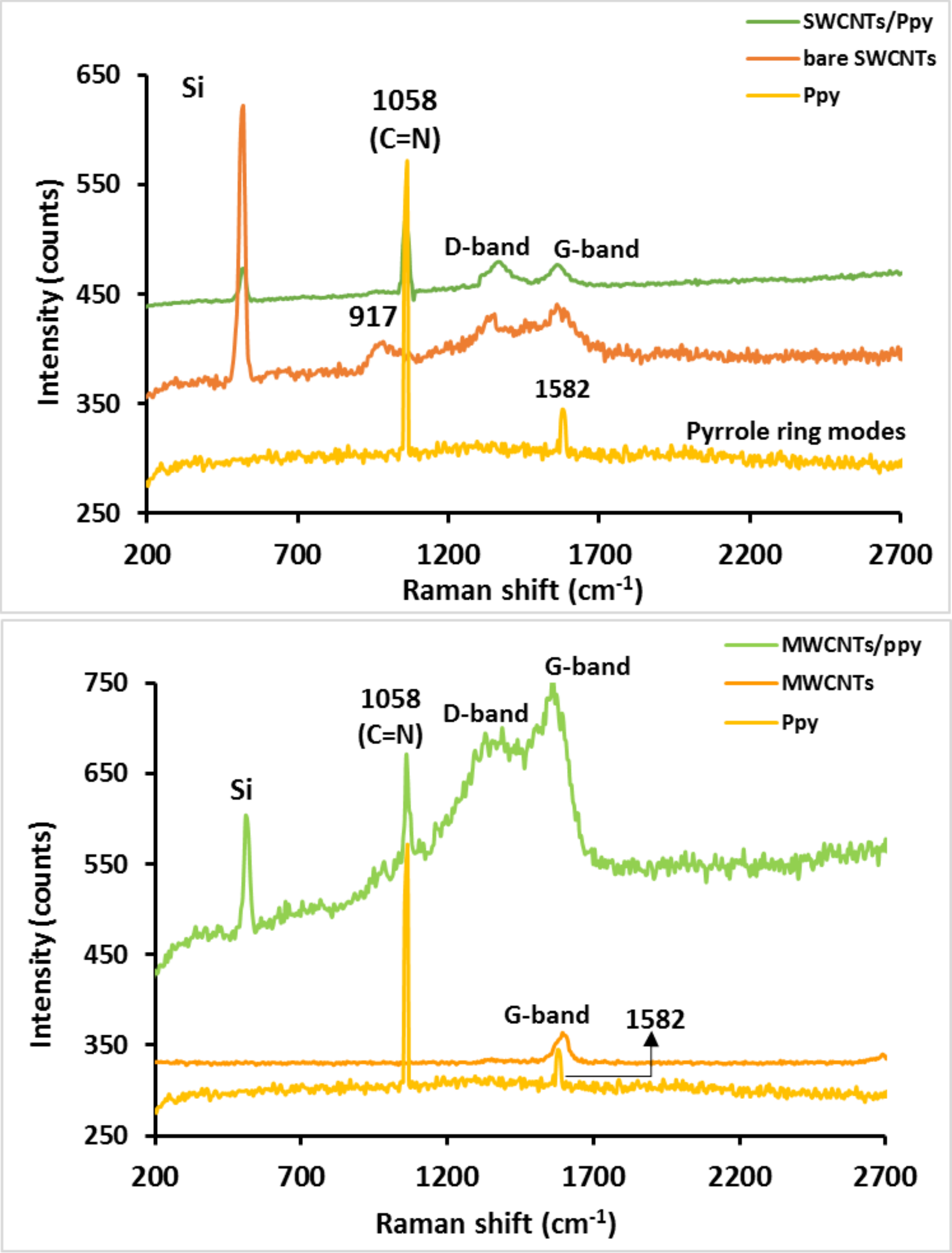

Figure 3-25 Raman spectrum of carbon nanotubes before and after polypyrrole coating. The excitation wavelength was 488nm and the spectrograph used a grating with 600 line/mm. The spectra are offset on the vertical axis for clarity.

3.2.2. Fourier transform infrared spectroscopy (FTIR)

Fourier transform infrared spectroscopy was used to study the optical properties of pristine and hybrid carbon nanotubes. In figure (3-26A&B) most of the spectra include a wide absorption band in the range between 3800-2800 cm^{-1} which is related to O-H, N-H and C-H groups[133] . In figure

(3-26 A) the spectrum of SWCNTs has a sharp peak at 1590 cm^{-1} due to C = C stretching vibrations in the single walled nanotubes walls and another peak at 1485 cm^{-1} of SWCNTs relates to C-C stretches. In addition, the 917 cm^{-1} absorption band is assigned to ring breathing[134]. From FTIR spectra, as shown in figure (3-26 A & B, e), there are specific peaks of polypyrrole in the SWCNTs/Ppy spectrum which are shifted slightly compared to polypyrrole in the absence of nanotubes as shown in figure (3-26A c,e). Examples are the bands at 1046 cm^{-1}, 543 cm^{-1} and 669 cm^{-1}; the 720 cm^{-1} band shifts substantially to 669 cm^{-1} due to the effect of interaction of the polymer with the SWCNTs. A similar shift from 720 cm^{-1} to 667 cm^{-1} is observed in the MWCNTs/Ppy spectrum[133, 135]. For pure polypyrrole, it was easy to recognise the peaks from FTIR such as 1529 cm^{-1}, 1468 cm^{-1}, 1415 cm^{-1}, 1046 cm^{-1}, 1012 cm^{-1}, 876 cm^{-1} and 544 cm^{-1}. 867 cm^{-1} is assigned to C-H wagging[136, 137]. In summary, on comparing FTIR spectra of MWCNTs/Ppy to SWCNTs and Ppy, and SWCNTs/Ppy to SWCNTs and Ppy in figures (3-26A & B), the composites show features from both Ppy and CNTs, but with some small shifts in certain band positions. These spectral shifts show that the composites involve intimate interaction between Ppy and CNTs, probably via weak, non-covalent interactions rather than covalent bonds which would produce new bands.

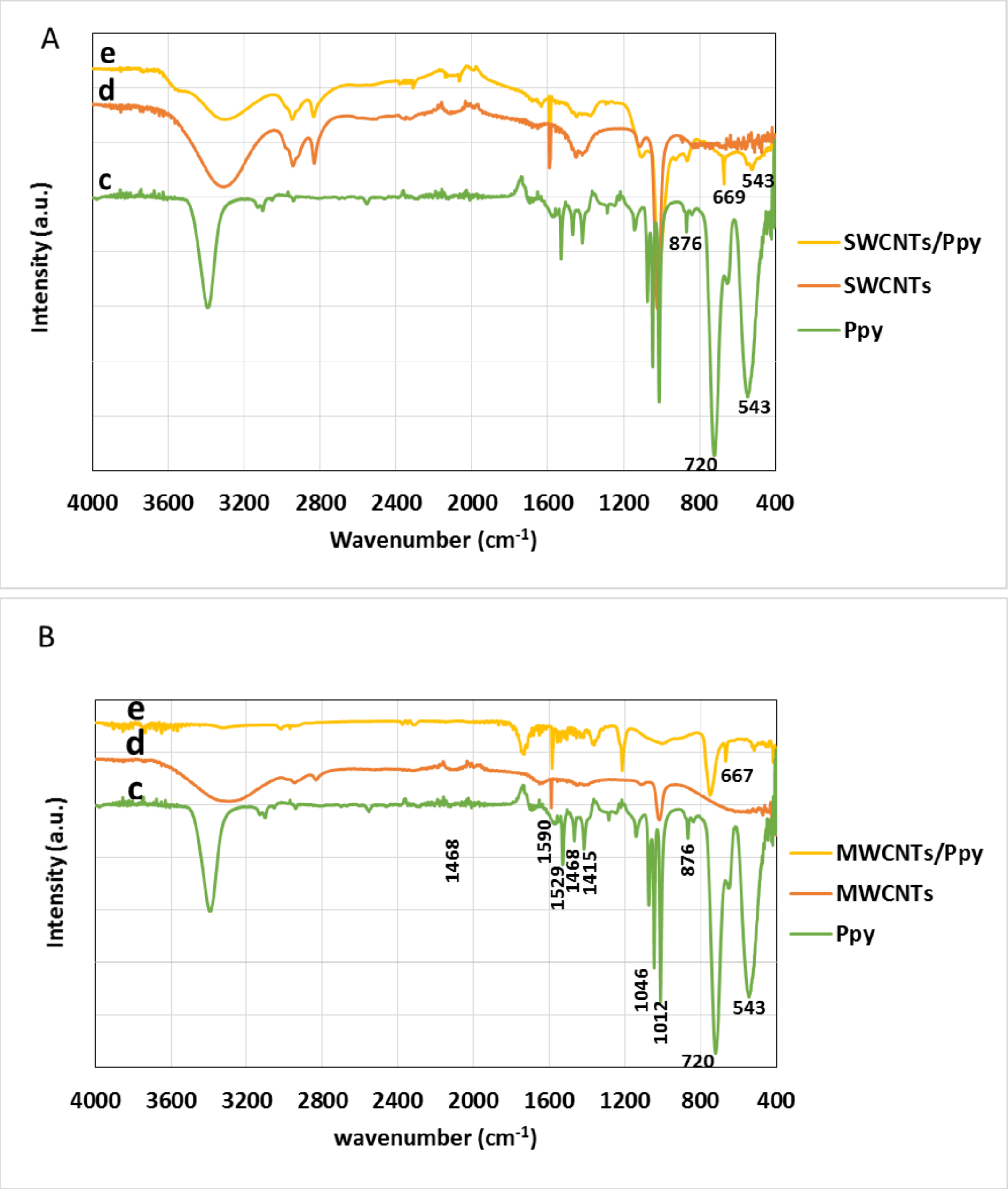

Figure 3-26 A) shows the FTIR spectra of bare and hybrid SWCNTs, e,d and c show SWCNTs/Ppy, bare SWCNTs and polypyrrole, respectively. Figure B) shows the FTIR spectra of bare and hybrid MWCNTs, e,d and c show MWCNTs/Ppy, bare MWCNTs and polypyrrole, respectively.

3.3. The application of CNT/polypyrrole composites as a gas sensor

Since the last decade many studies interested in sensing application depended on nanomaterials to design sensors, using nanowires and nanotubes to detect a wide range of gases and vapors[58, 138 139]. Carbon nanotubes are well suited for sensing because of their unique physical properties for instance; hollow centre, small size, excellent electrical properties, large surface area and high aspect ratio [6, 17, 140 5.] Generally, any sensor should be reliable, low cost, sensitive and with a fast response and a short recovery time[61.] In 1962 Seiyama[5] designed the first gas sensor based on ZnO film at 400 °C as a working temperature, then researchers made big efforts to use nanomaterials as sensors because of their efficiency, sensitivity, selectivity, small size and low power consumption compared with bulk materials[1]. Therefore, carbon nanotubes are promising materials in this type of application[58, 61].Despite the unique properties of carbon nanotubes and fast response with a short recovery time at the room temperature, the sensitivity is limited[141, 142], [143]. In recent years it has been found that many researchers have shifted research in sensing technology toward more sensitive materials that have a small diameter using nanomaterials instead of bulk films[80, 144.] To evaluate CNTs as a gas senor, the nanotubes were deposited on microband electrodes as shown in chapter two section (2.8) and as shown in figure (3-27). This type of sensor is called a two terminal gas sensor[145, 146]. This gas sensor depends on monitoring change in the electrical resistance of the carbon nanotubes/polypyrrole between two terminals[80, 147]as shown in figure (3-28).

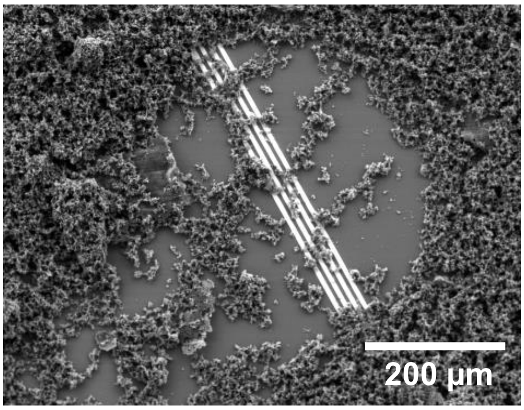

Figure 3-27 SEM image of the distribution of CNTs/Ppy on the electrode. The Pt microband electrodes are visible as uniformly-spaced white lines running through the centre of the image.

In general, the detection of volatile organic compounds (VOCs) is important in safety applications because these compounds are associated with cancer, damage to the liver, kidney and central nervous system, in addition their effect on the respiratory system of the elderly and young. VOC pollution occurs indoors, in homes, and workplaces more commonly than outdoors[148]. Four types of VOCs were studied in this thesis: ethanol, methanol, acetone and chloroform and it was necessary to design/prepare sensors for this purpose.

Both single walled and multiwall nanotubes were evaluated for their analytical response. From the first sensing experiment, it was noted that the sensor has a rapid response for all the VOCs –our analyte target- with a short recovery time. As mentioned before the principle of operation depended on recording the change in the electrical resistance by a DMM and the sensitivity of the VOCs was measured by $S = (R-R_0)/R_0) *100\%$ where R_0 is the resistance in an air atmosphere and R is the resistance at steady-state after exposure to an air/analyte mixture. The normalization of the response in the form of a dimensionless ratio *S* allows for a better comparison between devices because factors relating to device size and amount of material cancel. For bare SWCNTs and MWCNTs sensors, acetone showed the highest sensitivity among VOCs and chloroform showed the lowest, as shown in figure (3-28).

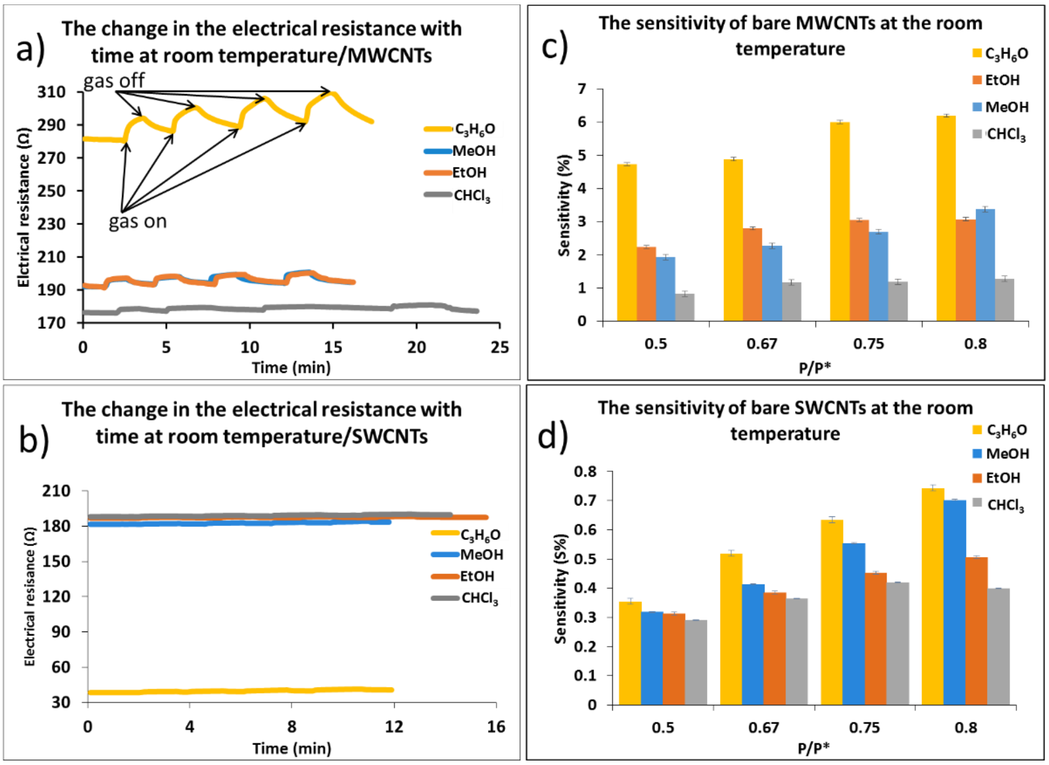

Figure 3-28 (a&b) The change of the electrical resistance of bare MWCNTs and SWCNTs at the room temperature (293K), (c&d) the sensitivity of pristine carbon nanotubes at 293K.

In addition, during observation of the electrical resistance for both SWCNTs and MWCNTs, it was found that the electrical resistance of the film increased when the sensor was exposed to the gas and gradually decreased after gas-off. It is noted that the resistance did not return precisely to the baseline level. Because of the weak change in the resistance value, as demonstrated in figure (3-28 a&b), the resistance-time plot looks almost a straight line, but in fact there is a small change in the resistance and, as shown in figure (3-29) after expanding the Y-axis scale for bare SWCNTs as ethanol sensor, the resistance increased about 3% after vapor exposure.

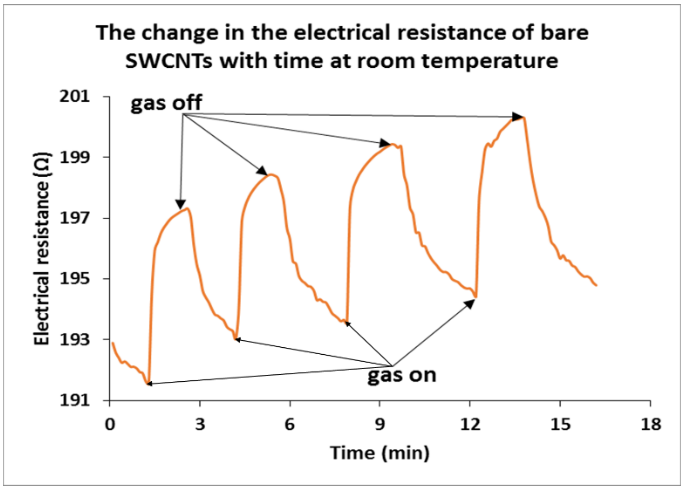

Figure 3-29 Shows the effect of ethanol vapor on the electrical resistance of bare SWCNTs at 293K.

Figure (3-30) shows the effects of the vapor pressure of the VOCs on the size of the response of bare carbon nanotubes at room temperature. The values of the vapor pressure were determined as shown in chapter two section (2-7) and more information in the appendix table S11.

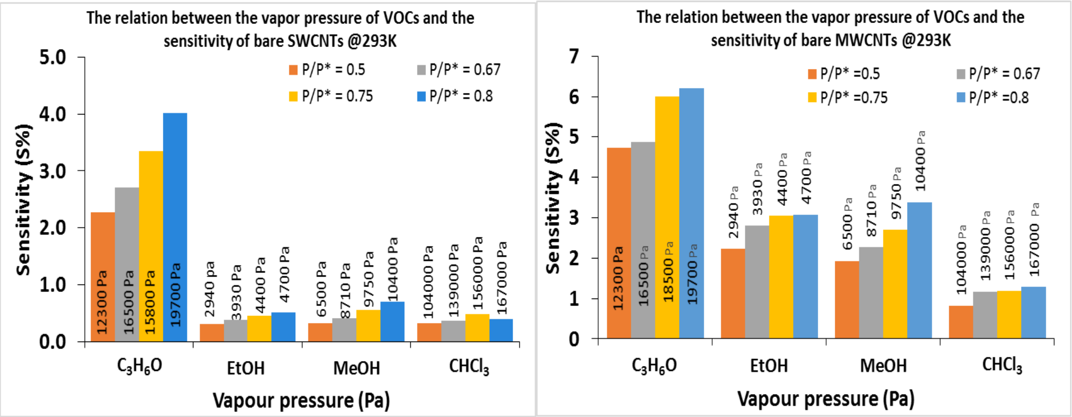

Figure 3-30 Shows the effect of vapor pressure on the sensitivity of bare carbon nanotubes at the 293K.

It is easy to realize that acetone has the greatest vapor pressure at room temperature compared with ethanol and methanol. Interestingly, however, chloroform has a greater vapor pressure than methanol and ethanol but shows a small response size. The response appears to correlate instead with measures of polarity. The dipole moments are 1.03D (chloroform), 2.388D (acetone), 1.70D (methanol) and 1.69D (ethanol)[149]. The largest response was observed for the molecule with the greatest dipole moment and the smallest response for chloroform, which has the lowest dipole moment. The two alcohols have similar responses and similar dipole moments.

These gas sensors have a rapid response with a short recovery time, as shown in figure (3-31).

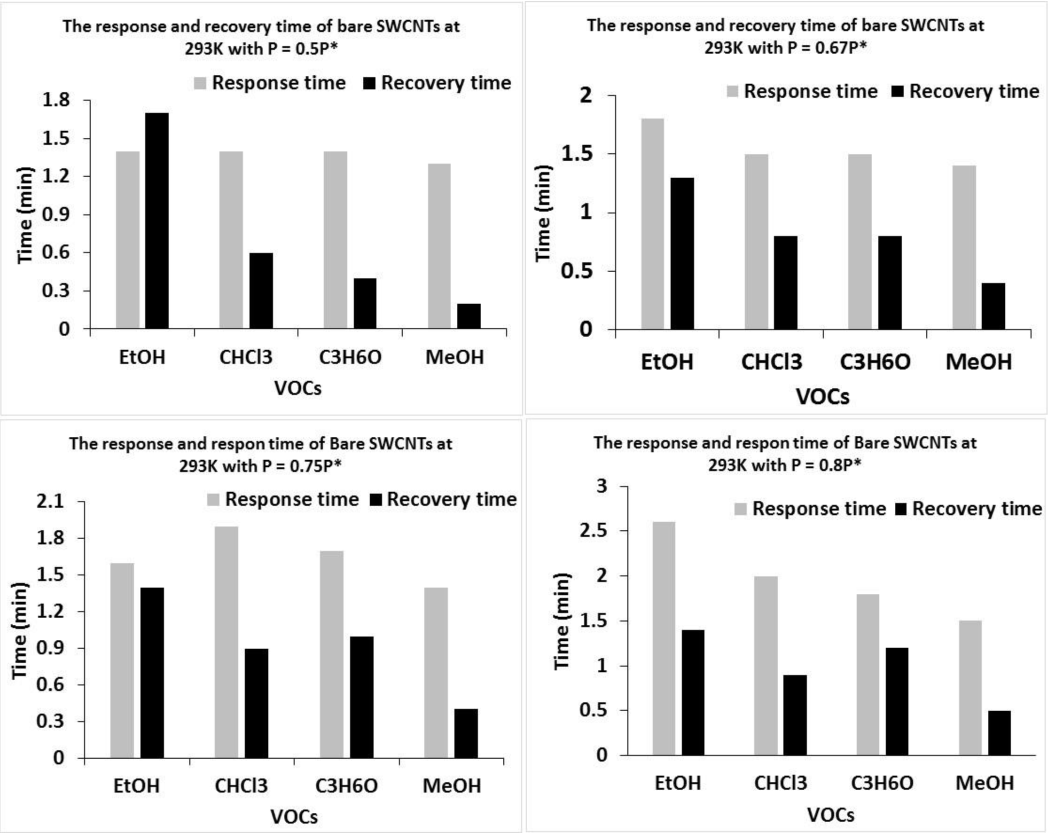

Figure 3-31 The response and recovery times of pristine SWCNTs for different concentrations of VOCs in dry air at 293K (room temperature).

In general, the response and recovery time increased with increases in concentration –VOCs: dry air- , however the SWCNTs film was very sensitive for methanol and had a rapid response (78-90) s with very short recovery time (15-30) s. This suggests the surface of SWCNTs very active and can return to the baseline in a short time. It was found that ethanol shows a longer recovery time (78-90) s and (156-90) s as a response time. However, for MWCNTs films, as demonstrated in figure (3-32), acetone recorded a good response time (66-96) s and acceptable recovery time (102-156) s, while the shortest recovery time for the films was for ethanol (96-144) s compared with other VOCs. On the other hand, MWCNTs film took a long time to respond to the chloroform vapour ~ (72 – 180) s and had a long recovery time (102-288) s although the sensitivity of bare MWCNTs to the chloroform vapour is very weak. Similar observations have been reported before[58].

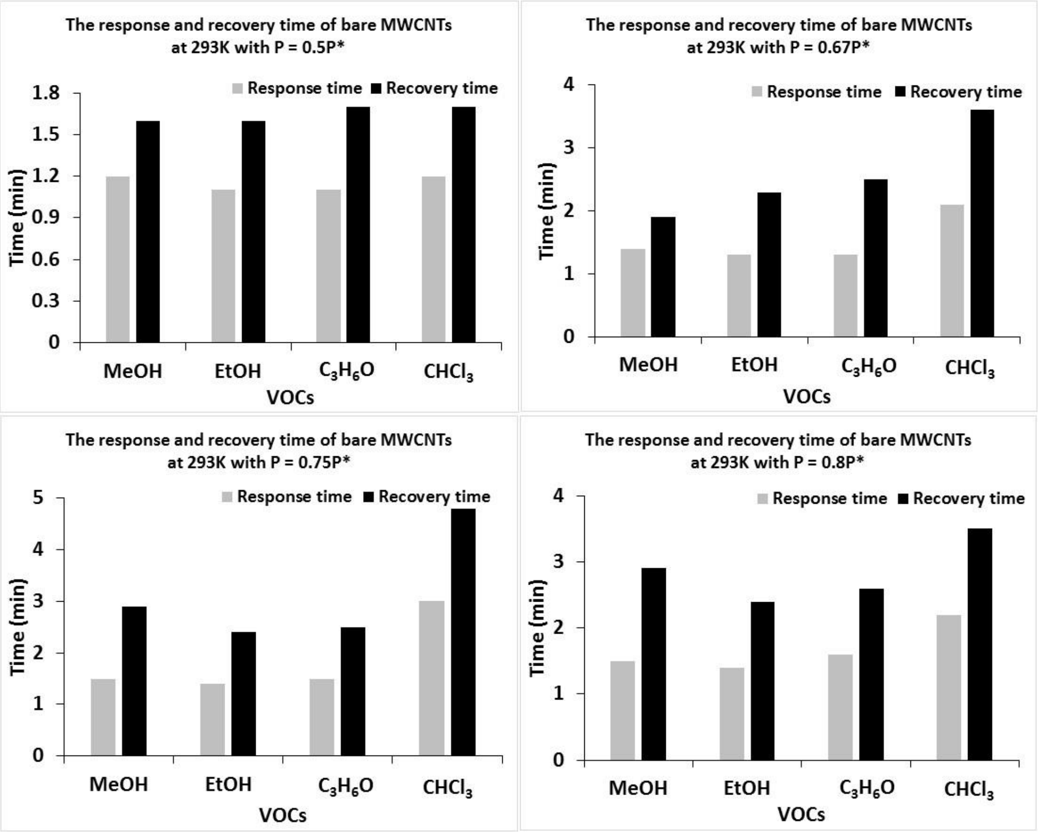

Figure 3-32 The response and recovery time of bare MWCNTs for different mixture concentration of (VOCs:dry air) at 293K (room temperature)

From the results above, it was found that bare carbon nanotubes (SWCNTs and MWCNTs) have a weak response to the volatile organic compounds and it was necessary to enhance the sensitivity by adding other nanoparticles like Cu, Ag and Au or coating the nanotubes by conductive polymer[142, 150]. Many reasons led to the choice of polypyrrole, for example good electrical properties, reasonable stability, easy preparation, low-cost[5, 151]. Moreover, compared with other materials carbon nanotubes are promising material for the polymer composite owing to their electrical and mechanical properties. The CNTs/CPs composite is a good combination in many applications, e.g. supercapacitors[152] and due to their electrical properties CNTs/CPs can be used as electromagnetic interface shielding materials and electrostatic discharge [153-155].

In this study, carbon nanotubes were coated by polypyrrole as a conductive polymer and all the details about how to prepare the samples were given in chapter two. From the first sensing test, it was noted that the sensitivity of carbon nanotubes increased greatly compared to bare CNTs as shown in figure (3-33) and these results are better than obtained in previous studies[140, 142]. In more detail, An et al, used SWCNTs/polypyrrole as a gas sensor to detect 300 Pa of ethanol vapour at room temperature, the nanocomposites were prepared by ''*in situ* chemical polymerization'' and then ''spin-coated'' onto a pattern[142]. They found that the sensitivity of SWCNTs/Ppy for EtOH was S < 2%. On the other hand, Brahim's group[140] tried to enhance the sensitivity of bare SWCNTs by coating CNTs with different metals as, Fe, Pt, Pd, Mn and Ti and they found that the sensitivity of SWCNTs/metal was increased from zero to < 2% for ethanol vapour (1-10) ppm. However, our thin film of SWCNTs/Ppy improved the response from 0.15% to 7% upon coating treatment for ethanol vapour at 334 Pa at room temperature. As can be seen in figure (3-33) acetone recorded the highest response of all the VOCs studied with SWCNT/Ppy sensors. The much larger response of SWCNTs/Ppy than MWCNTs/Ppy to acetone suggests another factor, other than dipole moment, is responsible. It is difficult to identify the precise cause, but a superior permeability resulting from a different morphology of the Ppy in SWCNTs/Ppy is suggested.

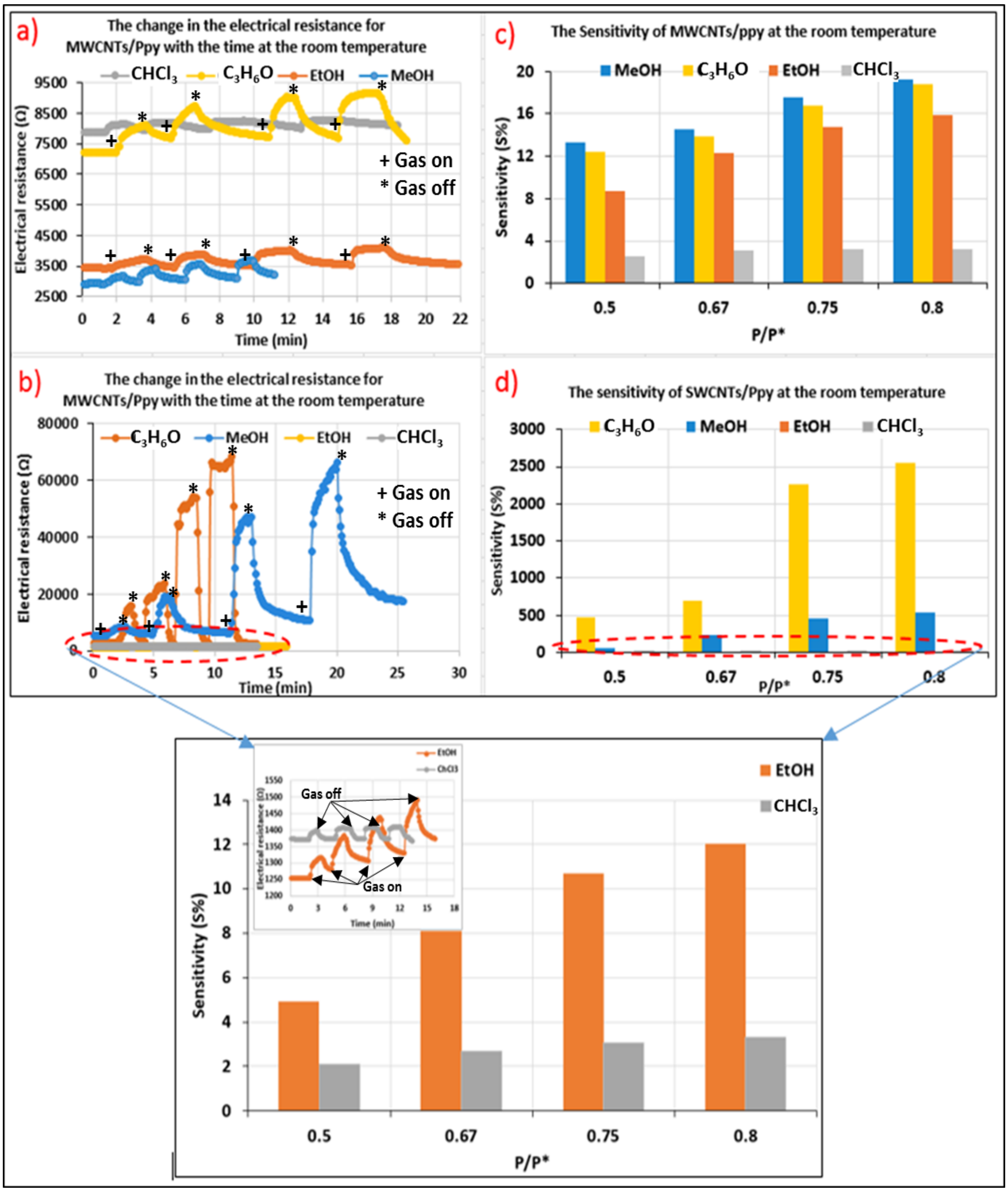

Figure 3-33 (a&b) The change of the electrical resistance of MWCNTs/Ppy and SWCNTs/Ppy films at the room temperature 293K, (c&d) the sensitivity of the hybrid nanotubes at 293K

It is easy to recognise that the sensitivity increased more than 100% for all the VOCs in CNT/Ppy composites compared to CNTs alone (figure (3-30)). Figure (3-34) shows the response and recovery time of SWCNTs/Ppy at different concentrations (VOC:dry air) at room temperature. Both response and recovery times were longer than for bare CNTs. This is suggested to be a result of the penetration of the VOC molecules inside the polymer by diffusion, which is a slower process than adsorption at the bare CNT surfaces or the diffusion in between CNTs.

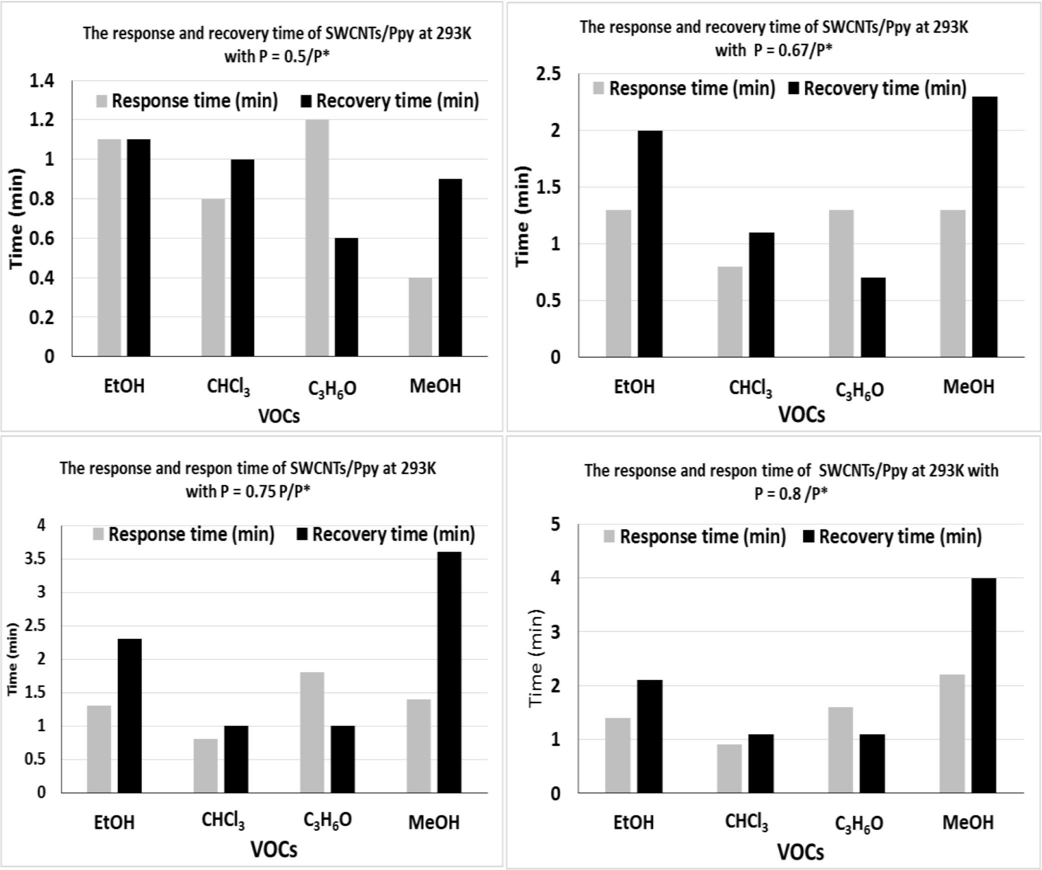
The response and recovery time of SWCNTs/Ppy at 293K with P = 0.5/P*

The response and recovery time of SWCNTs/Ppy at 293K with P = 0.67/P*

The response and respon time of SWCNTs/Ppy at 293K with P = 0.75 P/P*

The response and respon time of SWCNTs/Ppy at 293K with P = 0.8 /P*

Figure 3-34 The response and recovery time of SWCNTs/Ppy for different mixture concentration of (VOCs: dry air) at 293K (room temperature)

Although, the composite films respond more slowly than bare nanotubes, they still have acceptable response and recovery times for all the VOCs. It was noted that increasing the mixture concentration affects the recovery time, which becomes longer, but no more than 4 mins as demonstrated in figure (3-35). At P/P* = 0.5 the longest recovery time was only 2 min. For MWCNTs/Ppy, both the response and recovery time are good, but the response and recovery time increased with increasing concentration of vapour. For example at P/P* = 0.5 the fastest response time was about 24 s with recovery time 56 sec for EtOH while the film took 132 s to respond and 240 s to recover at P/P* =0.8, see figure (3-35). It is likely that the slow-down in response/recovery is related to diffusion of the VOC molecules within the Ppy component of the sensor. In general, the recovery times were longer than the response times at high concentrations, which suggests a significant kinetic component rather than a pure diffusion-limited mechanism. It is suggested that these kinetic effects are related to structural changes in the polymer caused by swelling effects at high VOC concentrations and that the rate of adsorption/desorption and/or diffusion in the dry and swollen polymers is different. We note that the recovery time is roughly proportional to the concentration of VOCs.

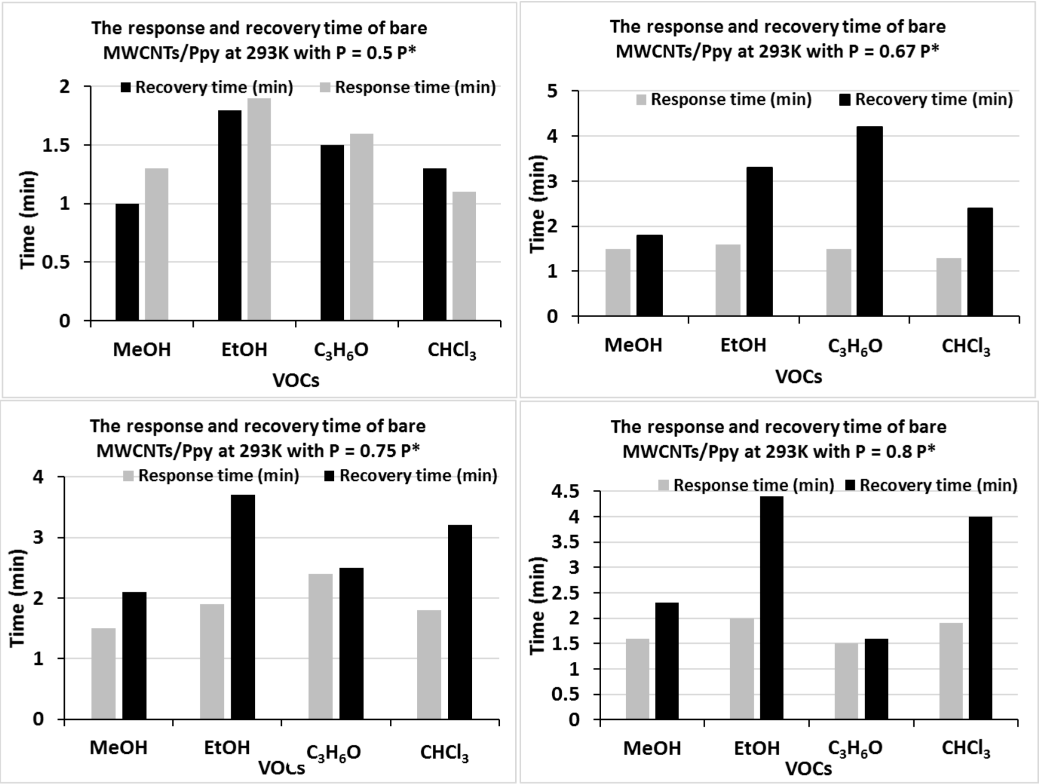

Figure 3-35 The response and recovery time of MWCNTs/Ppy for different mixture concentration of (VOCs: dry air) at 293K (room temperature). The response and recovery time were measured when the electrical resistance reached the steady state level as shown in figure chapter two, section (2.8).

3.3.1. Effect of the temperature on the performance of the carbon nanotubes as a gas sensor

To study the effect of the temperature on the sensitivity of bare and hybrid carbon nanotubes, five different temperatures were used between 20 to 60 °C for all VOCs as shown in table (2).

Table 3-2 shows the temperatures which were employed in this study for pristine and hybrid nanotubes

Sample	SW, SW/Ppy, MW, MW/Ppy			
VOCs	MeOH	EtOH	C_3H_6O	$CHCl_3$
Temp.	(20-60)°C	(20-60)°C	(20-60)°C	(20-60)°C

This part depends on observing the change in the electrical resistance with time during the vapor exposure at the different temperatures.

For bare CNTs, it was found that the maximum working temperature was 50°C for each SWCNTs, while for MWCNTs measureable responses were obtained at temperatures up to to 60°C for MW/Ppy and SW/Ppy. However, the response size decreased with the temperature for each bare and hybrid device for all the VOCs. The highest sensitivity was at 20 °C and decreased dramatically at 60 °C, as shown in figure (3-36). In addition, from the same figure one can recognize that the sensitivity of CNTs increased also with the vapor pressure for the VOCs. Generally, a small amount of polypyrrole can enhance the sensitivity of the nanotubes at the high temperatures compared with the bare nanotubes[156]. On the other hand, acetone has the highest response size, proportionally greater than a simple comparison of vapour pressures would predict. There is relatively little difference in the sensitivity of ethanol, methanol and chloroform relative to their vapour pressures as shown in figure (3-36 a-d). However, for the hybrid SWCNTs, acetone and methanol have the largest response size, but the weakest sensitivity was for chloroform vapor throughout the temperature range. Interestingly, at 50^{o}C and 60^{o}C the sensitivity of ethanol, methanol and chloroform can be almost the same as shown in figure (3-36 e-j). The response of the MWCNTs and MWCNTs/Ppy also changed with heating, for example, the sensitivity of MWCNTs for acetone vapor decreased about 26% at 30^{o}C, 34.7% at 40^{o}C and 43% at 50^{o}C, as shown in figure (3-37). The highest response was for acetone vapour and chloroform recorded the lowest response size. Moreover, from monitoring the vapor pressure, the sensitivity increased with increasing partial pressure and it is difficult to explain the low sensitivity to chloroform although it has a high vapor pressure compared with ethanol and methanol, the calculations of the vapour pressure can find in the appendix, table S2. This effect was analysed in terms of an adsorption equilibrium of the analyte on the polymer/CNT composite and the enthalpy of adsorption/desorption could be extracted from the data by plotting lnS against 1/T as shown in figure (3-38&39).

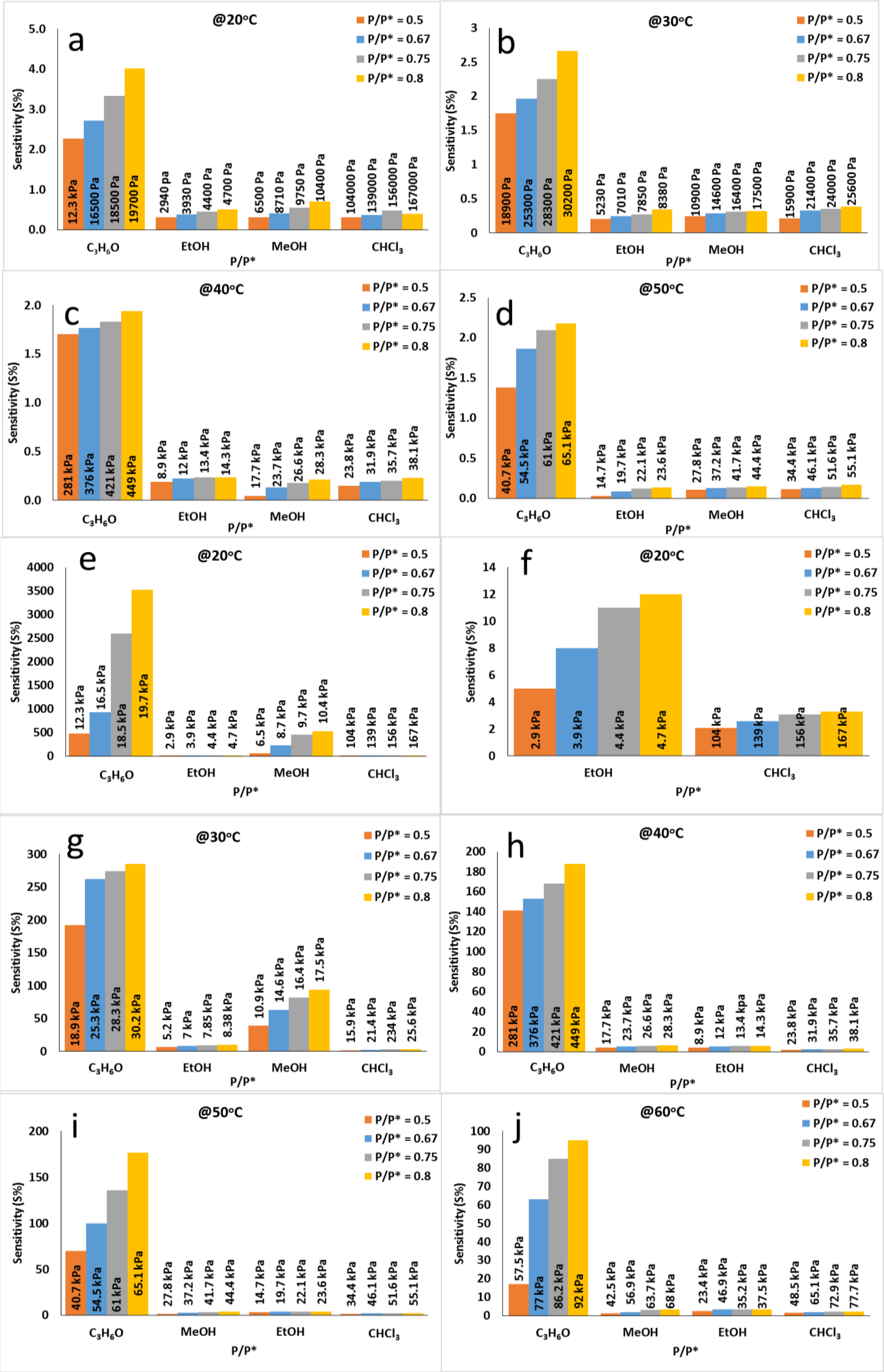

Figure 3-36 Shows the sensitivity of the nanotubes (a to d) the response size of bare SWCNTs at different temperature, (e-j) the sensitivity of SWCNTs/Ppy at the wide range of temperatures between (20 to 60)^{o}C with different mixture concentration of (VOC: dry air).

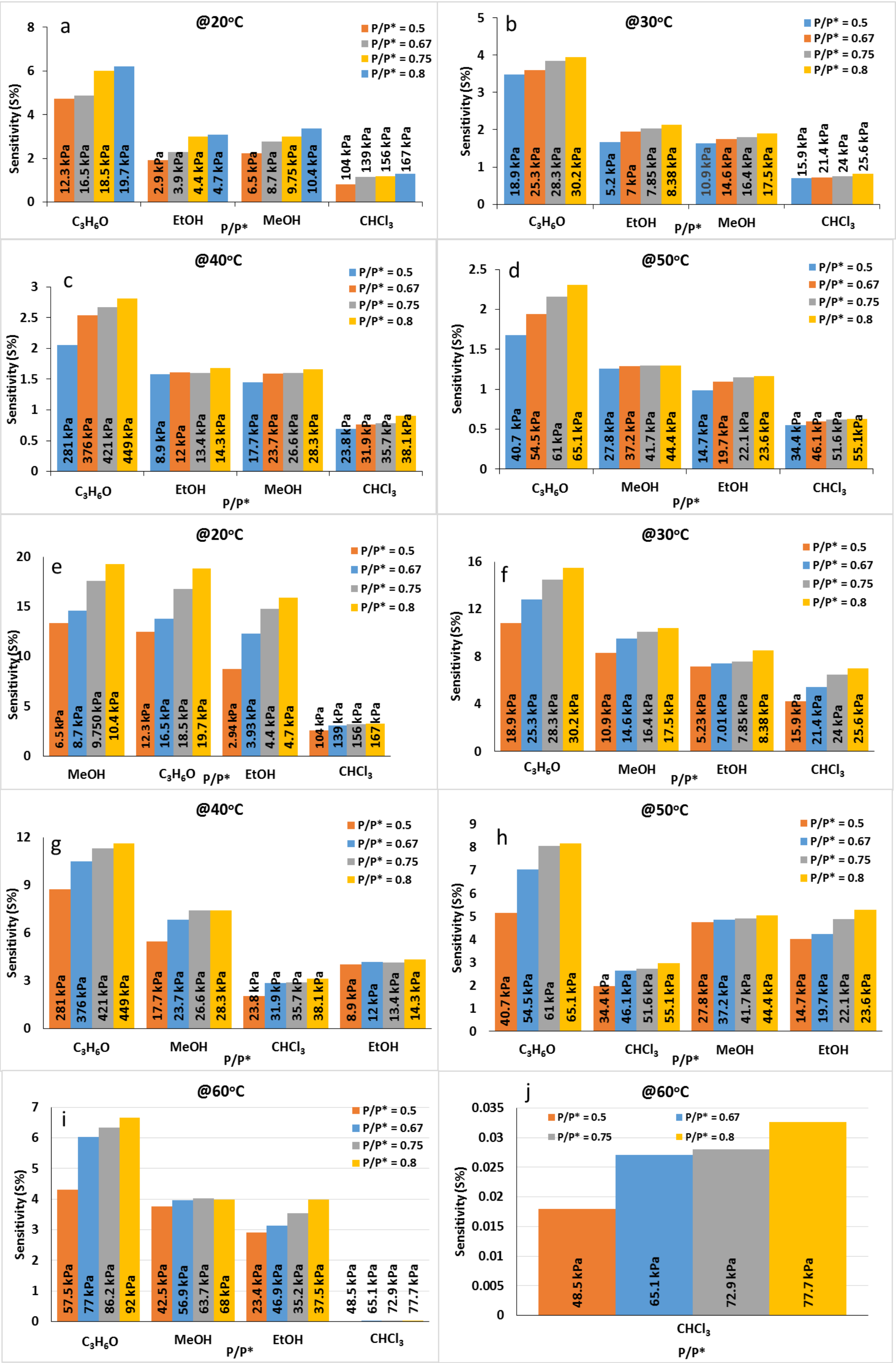

Figure 3-37 Shows the sensitivity of the MWCNTs (a to d) at different temperature, (e-j) the sensitivity of MWCNTs/Ppy at a wide range of temperatures between (20 to 60) ^{o}C with different mixture concentration of (VOC: dry air).

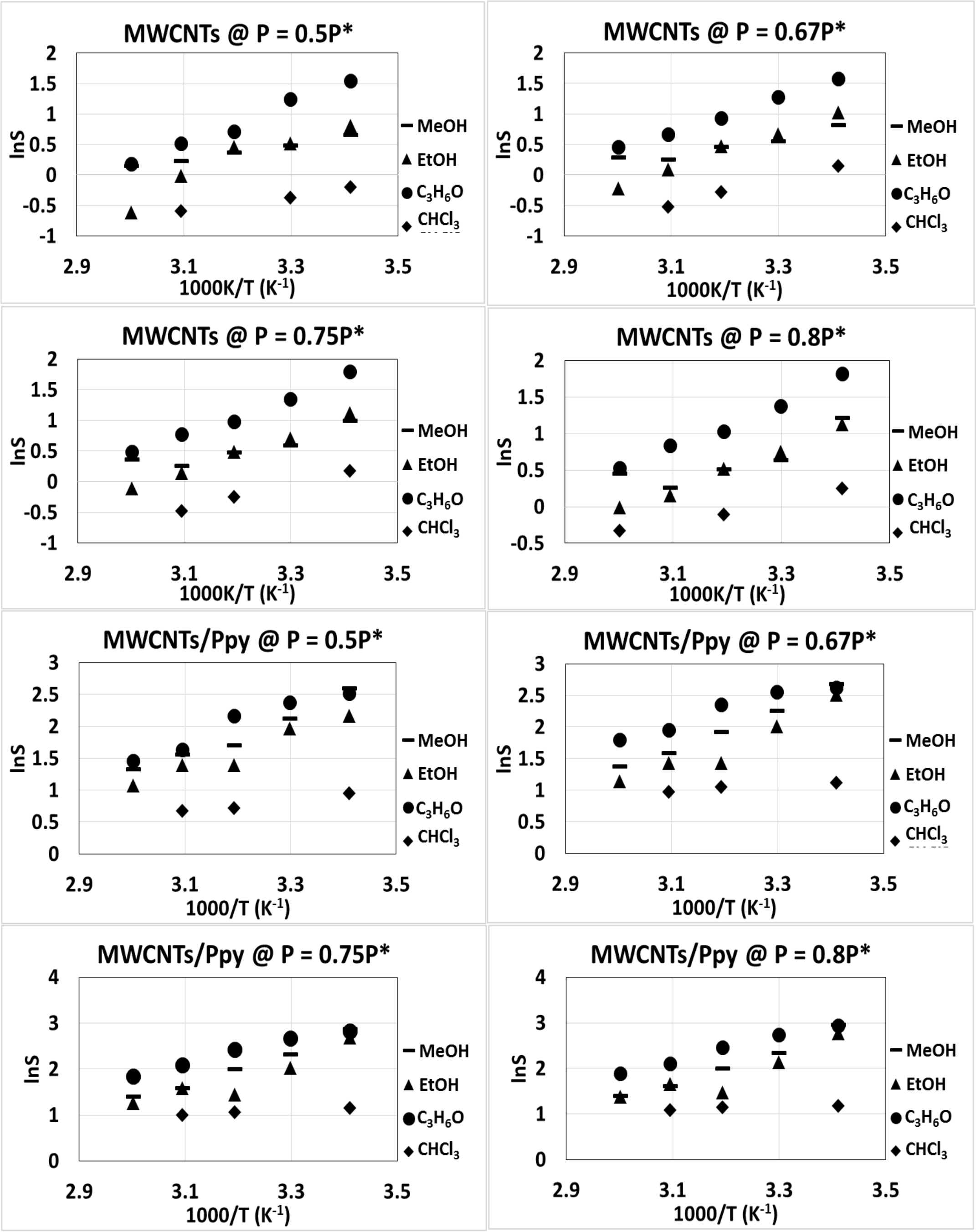

Figure 3-38 Shows the relation between lnS and temperature for the different concentrations of the analyte (VOCs: dry air) for bare and hybrid MWNTs.

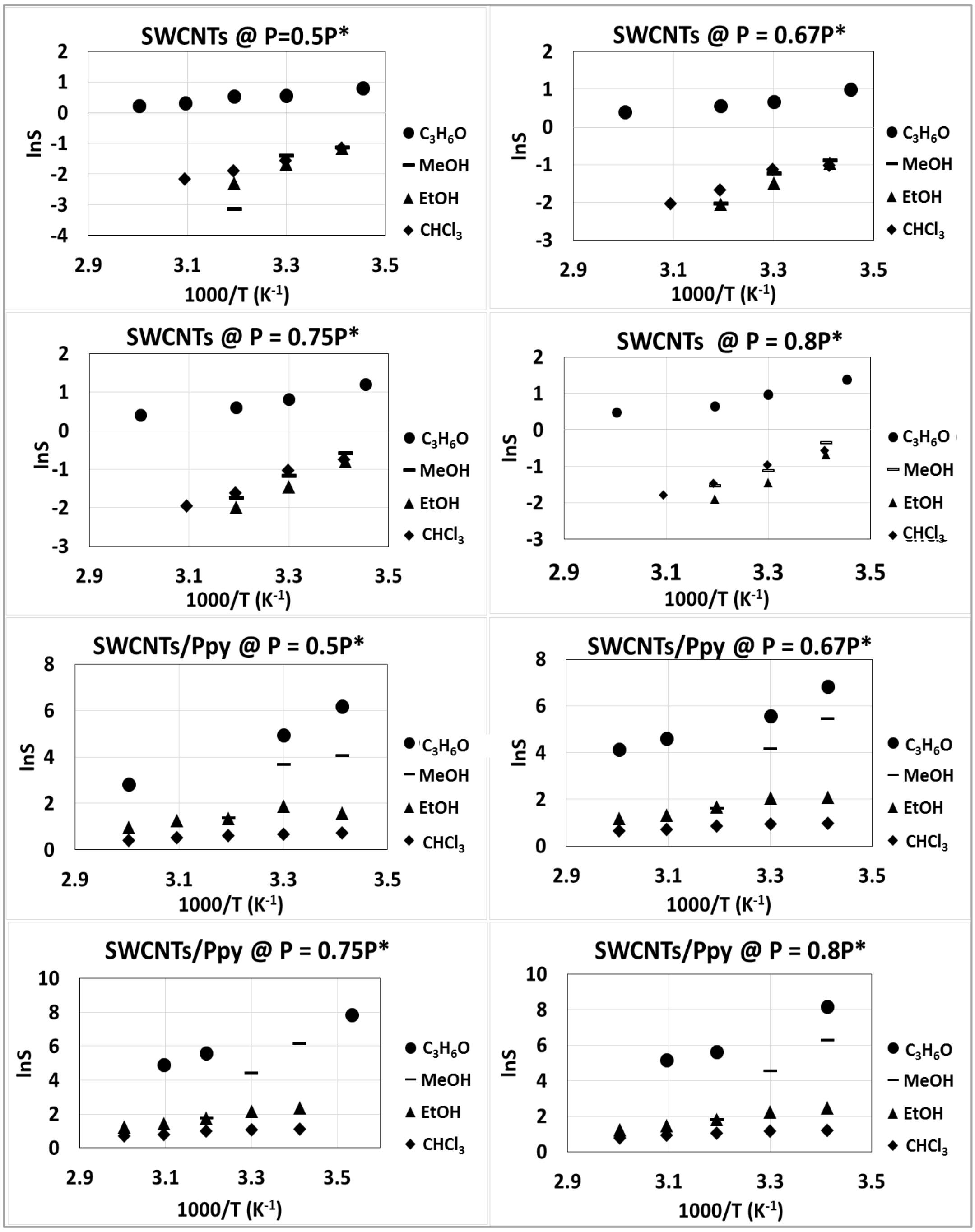

Figure 3-39 Shows the relation between lnS and temperature for the different concentrations of the analyte (VOCs: dry air) for bare and hybrid SWNTs.

The Van't Hoff equation was used to understand the effect of temperature on the performance of the nano-vapor sensor as shown in figure (3-40) for the pristine and hybrid nanotubes. The Van't Hoff equation refers to the change of the equilibrium constant of a chemical reaction with temperature change. The variation of equilibrium constant change with temperature depends on the change in standard enthalpy for the reaction. The Van't Hoff equation gives information about the nature of the interaction of gas with the sensor surface as shown by the lnS Vs 1000/T plots in figures (3-38 & 39). ∆H can be determined as shown below:

$$\Delta \mathrm{H}^{\Theta} = \frac{\Delta(lnS)}{\Delta\left(\frac{1000}{T}\right)} x - R \qquad (3-5)$$

From figure (3-41&42) :

$$Slope = \frac{\Delta(lnS)}{\Delta(\frac{1000}{T})} \qquad (3-6)$$

Where R is the gas constant 8.314 J $K^{-1}mol^{-1}$.

$\mathit{\Delta}_{ads}H^{\Theta}$ was negative for bare and hybrid nanotubes as demonstrated at figure (3-40); the negative value is necessary for consistency of the analysis based on a model of adsorption equilibrium because the entropy of adsorption is always negative. The $\mathit{\Delta}_{vap}H^{\Theta}$ of these VOCs by (NIST webbook) are all larger in absolute value than the magnitudes of the apparent adsorption enthalpies $|\mathit{\Delta}_{ads}H^{\Theta}|$ from the van’t Hoff analysis. For example $\mathit{\Delta}_{vap}H^{\Theta}$ of MeOH at 303 K is 38.7 kJ/mol[157] while $|\mathit{\Delta}_{ads}H^{\Theta}|$ was 31.4 kJ/ mol at (P = 0.8P*), the same for C_3H_6O $\left|\mathit{\Delta}_{ads}H^{\Theta}\right|$ was 22.04 kJ mol^{-1} at (P = 0.8P*) while $\mathit{\Delta}_{vap}H^{\Theta}$ equals 41.2 kJ/mol[158] at 303 K. This indicates the VOCs molecules were adsorbed by the sensor material and not simply condensed as a liquid film on the device.

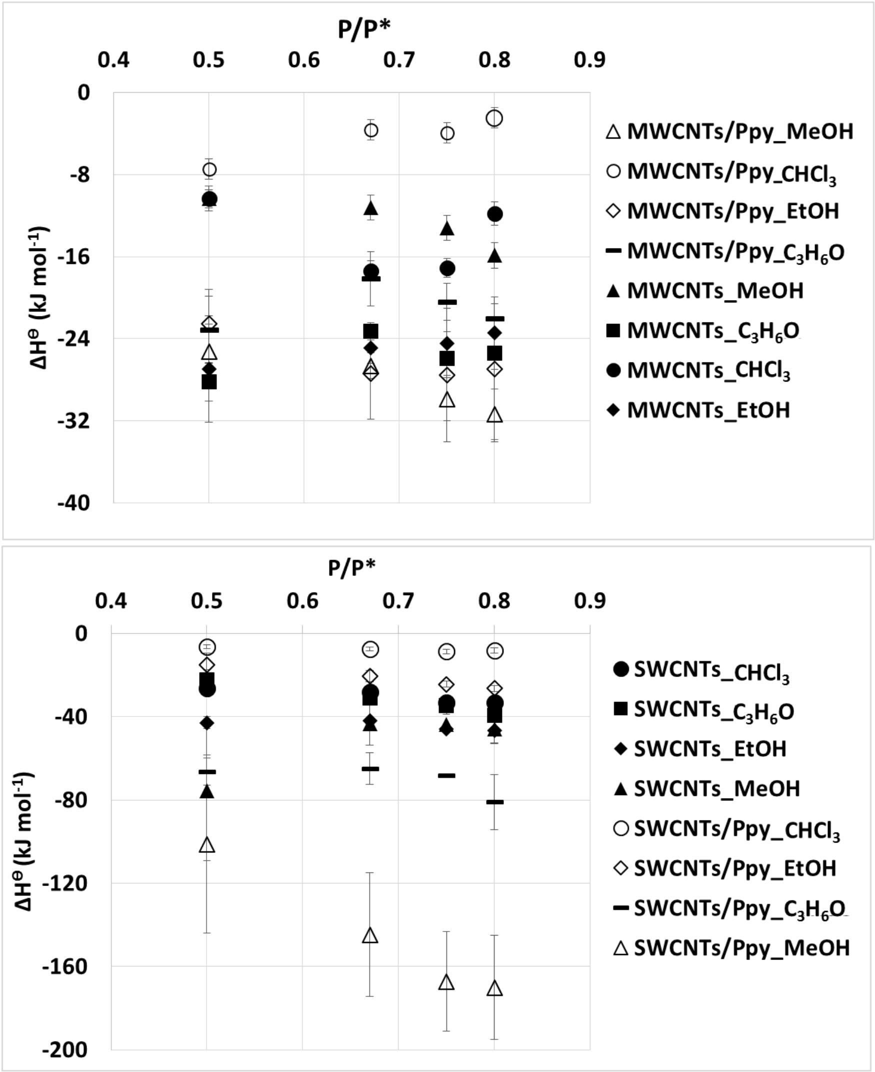

Figure 3-40 Shows the change in enthalpy of a system which is referred to the exothermic reaction for each pristine CNTs and CNTs/Ppy for the VOCs:dry air.

Figure (3-41) shows a schematic diagram of the amount of gas molecules absorbed at the surface of the nanotubes at the different temperatures.

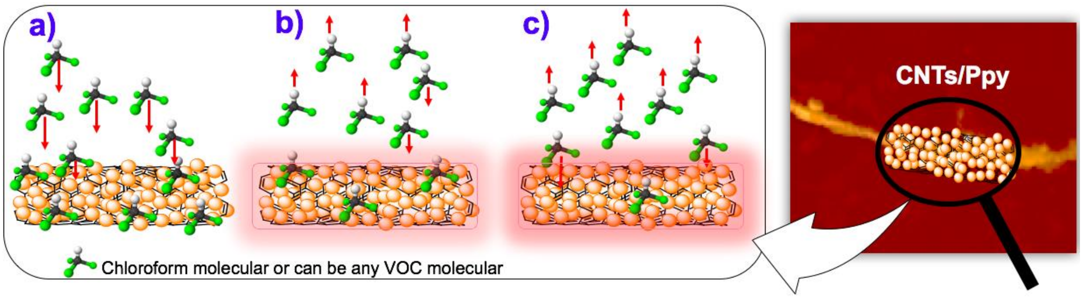

Figure 3-41 Effect of the temperature on the adsorption process for the organic compounds molecules. a) at 20^{o}C, b) 40^{o}C and c) 60^{o}C.

To study the effect of temperature on the sensitivity of our sensor a simple isotherm model was designed for the adsorption of the VOCs.

$$S = \alpha \mathit{\Gamma} \qquad (3-7)$$

Where S represents the signal which is assumed proportional to the adsorbed amount of the analyte, $\mathit{\Gamma}$ is the surface excess of the analyte (VOCs: dry air) in mol.m^{-2}. The Langmuir model was used describe the adsorption isotherm in as simple a manner as possible. If the analyte has a weak adsorption on the surface of nanotubes, the isotherm reduces to a linear relation between P_{VOC}(partial pressure) in the gas phase and $\mathit{\Gamma}$. If instead the surface coverage reaches a plateau at ($\mathit{\Gamma}_m$)- monolayer coverage- the response size would not depend on the analyte pressure and would have no particular interest for a sensor: In the linear region:

$$\frac{\mathit{\Gamma}}{\mathit{\Gamma}_m} \cong K\, P_{VOC} \qquad (3-8)$$

Where $\mathit{\Gamma}_m$ is the complete monolayer coverage, P_{VOC} is the partial pressure of VOC and K is the equilibrium constant. Note that P_{VOC} depends on the temperature of the Dreschel bottle not the temperature of at the sensor. Our model therefore has a sensor temperature dependence originating from K alone and therefore on the Van't Hoff equation applies.

$$\frac{\partial \operatorname{Ln} S}{\partial 1/T} = -\frac{\Delta H^{\theta}}{R} \qquad (3-9)$$

Where ΔH^{θ} is the enthalpy of the adsorption reaction. Figure (3-38 & 39) shows the plots of lnS Vs $1/T$ for CNTs and CNTs/Ppy for methanol, ethanol, acetone and chloroform. $\mathit{\Delta}_{ads}H^{\Theta}$ is shown in figure (3-40).

3.3.2. Evaluation of the nano-vapor sensor for a small amount of the volatile organic compounds.

This section describes the sensitivity of the nanotubes to small amounts of VOCs $P/P^*<0.2$. On observing the change in the electrical resistance of the nanotubes upon exposure to the analytes it has been found that CNTs are insensitive to VOCs $S<0.45$ %, but the sensitivity increases when the CNTs are coated with polypyrrole: $2\% < S < 17\%$. Figure (3-42) shows the response of the nanotubes for $P/P^*<0.2$. When S is plotted against P/P^* (S5 and S6 in the appendix), a linear calibration is observed for most of VOCs as judged by the correlation coefficients. R^2 was between 0.99 to 0.91 for bare CNTs and for hybrid CNTs R^2 values were between 0.79 to 0.95 for C_3H_6O, EtOH and MeOH. However the correlation coefficient was much lower for $CHCl_3$ at both MWCNT/Ppy and SWCNT/Ppy devices for which values of R^2 = 0.22 and 0.68 were determined. The low values of R^2 and nonlinear calibration curves (S5, S6, appendix) suggest that the interaction between the analyte and the nanocomposite film is more complex than with the bare CNTs. Previous workers have suggested that adsorption of VOC molecules at the conductive polymer is followed by diffusion to the active sites [77]. Clearly there is a difference in the shape of the calibration curve for $CHCl_3$ which is nonlinear for SWCNT/Ppy as shown in figure (3-42g) and almost independent of P/P* in figure (3-42h) for MWCNT/Ppy. It is worthwhile to note that the size of the response of SWCNT/Ppy devices to $CHCl_3$ is similar to other VOCs, therefore there is clearly some interaction between Ppy and $CHCl_3$. We suggest that the data can be rationalized if Ppy becomes saturated with $CHCl_3$ at relatively low values of P/P*. Other analytes, such as MeOH, EtOH and C_3H_6O may still be in the linear region of the adsorption isotherm and therefore the devices show a more linear calibration.

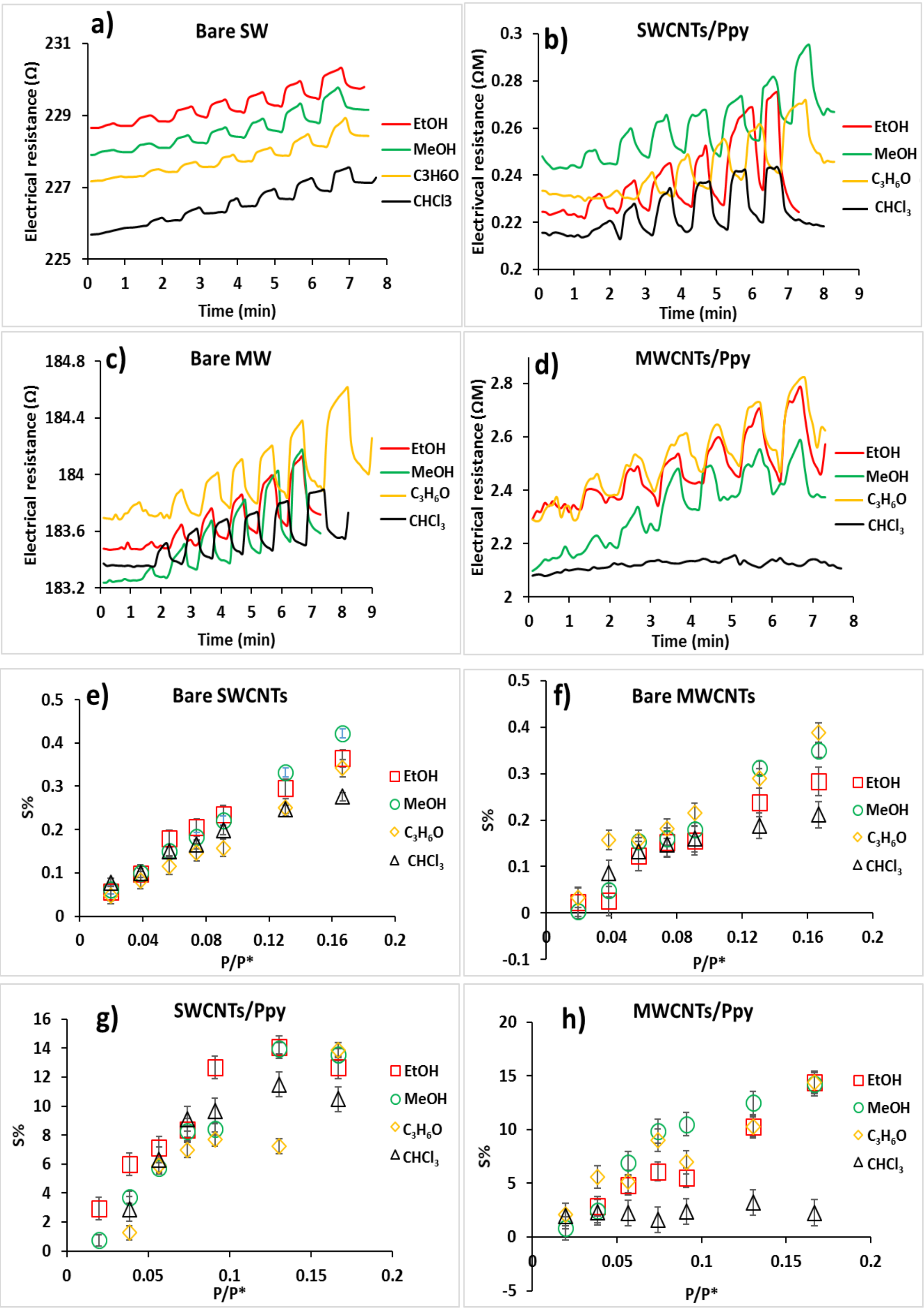

Figure 3-42 (a-d) show the change in the electrical resistance with vapour pressure of (SW, SW/Ppy, MW & MW/Ppy) respectively, (e-h) show the sensitivity of pristine and hybrid nanotubes for the low concentration of (VOCs:zero air) at room temperature. More statistics analysis in the appendix figures S5 and S6.

3.3.3. Effect of the concentration of the conductive polymer on the sensitivity of the carbon nanotube sensors.

Generally, two concentrations were used in this study for the conductive polymer (0.5 M and 1 M) and by TEM images, it was easy to recognize that at the high concentration, the CP coated the CNTs completely while the low concentration of polypyrrole covered the nanotubes in interrupted form, as demonstrated in figure (3-43).

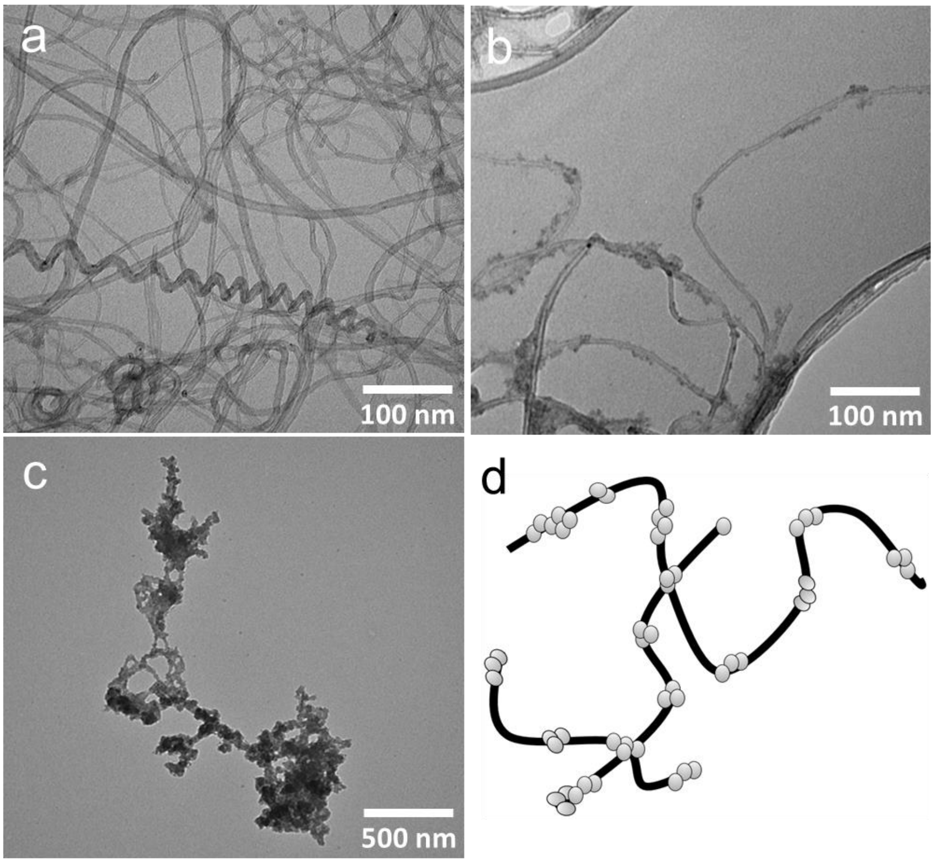

Figure 3-43 shows TEM images of how the conductive polymer coated the nanotubes in two different concentration, (a) bare MWCNTs, (b) MWCNTs/Ppy with 0.5M of CP, (c) MWCNTs/Ppy with 1M of polypyrrole,(d) schematic distribution of the CP on the surface of CNTs prepared from 0.5 M concentration.

Although, the sensitivity of the CNTs/Ppy is smaller with a low concentration of the conductive polymer, the response to VOCs is still larger than in the case of bare nanotubes. That suggests a small amount of pyrrole can make a significant change in the sensitivity of carbon nanotubes and enhance the performance of the nanosensor[159]. As can be seen in figure (3-44) it was observed that the sensitivity to chloroform was most strongly affected by pyrrole concentration of all the VOCs studied. The nature of the coating affects the response size of the nanotubes for VOCs – our target- as shown in figure (3-44). This shows that the CNT: Ppy ratio can also can affect the selectivity of the sensor. Low concentrations of pyrrole produce interrupted coating; these samples have the lowest conductivity, but an improved sensitivity. High pyrrole concentrations do not regain the conductivities of pristine CNTs, but have good sensitivities. Figure (3-43d) illustrates schematically how small amounts of Ppy can have significant effects. The conduction path between the two terminals of the device involves hopping between multiple CNTs where these cross. If the conductive polymer coats the CNTs at these crossing points, the tunneling barrier may be strongly affected. An increase in these tunneling barriers will reduce the conductivity of the device because Ppy coatings at the crossings will separate the CNTs slightly and increase overall resistance. However, the Ppy will also increase the sensitivity S because adsorption of VOCs by the Ppy at the crossings may have a large effect on the tunneling barrier, e.g. by swelling of the polymer and a separation of the CNTs at the crossings.

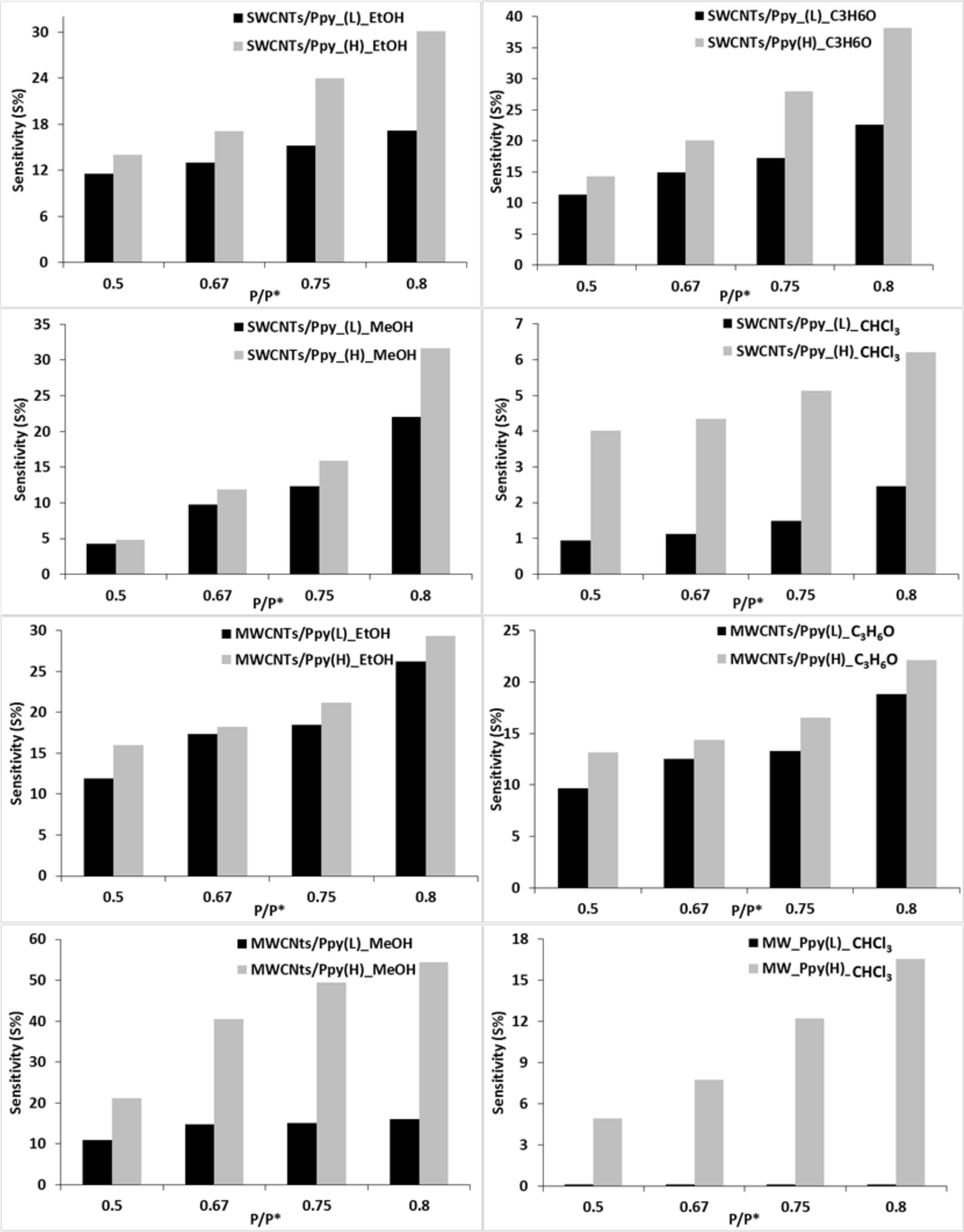

3-44 Shows the change in the sensitivity of the hybrid nanotubes for the VOCs with two different concentrations of the conductive polymer (L=0.5M) and (H=1M) at the room temperature.

Figure (3-45) shows the change in the I-V measurements of bare and hybrid CNTs at 293K for 1 M and 0.5 M of the conductive polymer.

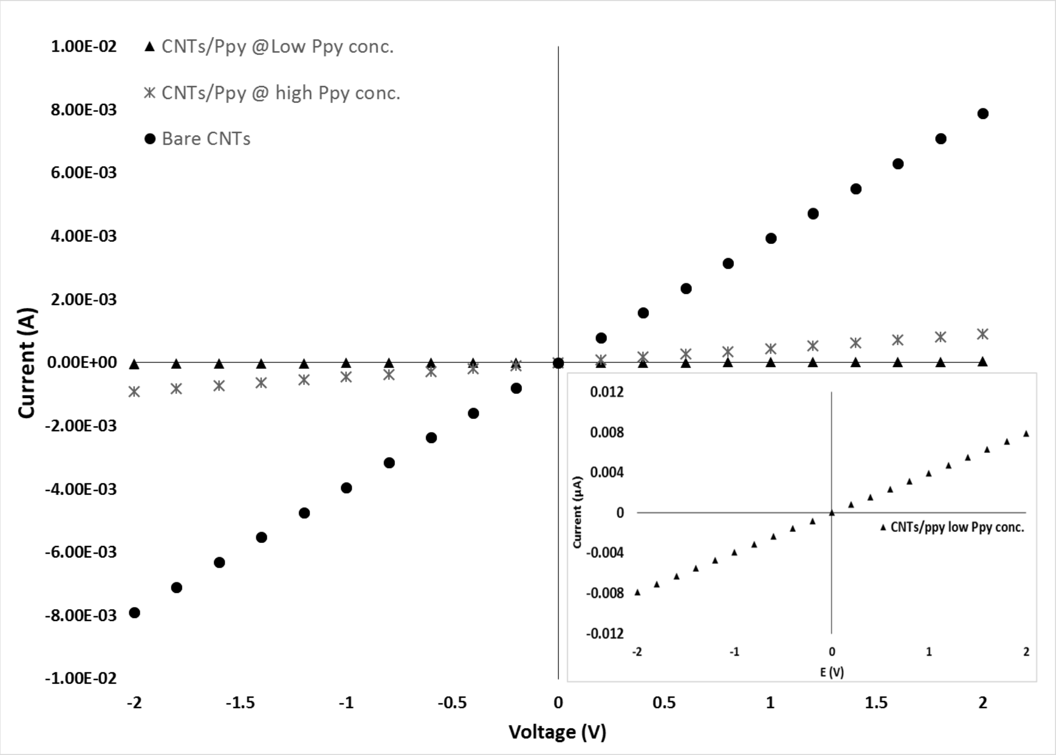

Figure 3-45 I-V charactrazation of bare and hybrid CNTs with concentrations of polypyrrole 1 M and 0.5 M.

3.3.4. Evaluate the performance of bare carbon nanotubes as a nano-sensor after laser treatment.

Many studies have tried to improve the sensitivity of carbon nanotubes as a gas sensor to detect VOCs. For example by decorating the nanotubes with nanoparticles such as Au and Ag or making composites with conductive polymer[70, 159, 160]. This section investigates an alternative: the effect of laser irradiation on the response of bare CNTs. Briefly, a diode laser was used as a pulsed laser source with wavelength 532 nm, the laser power was 250 watt with a spot diameter 1.5 mm, and the CNTs were exposed for 1 min, the intensity of laser was 1.4 x 10^8 W/m^2.

The intensity of the laser was measured as shown in equation (3-10)[161].

$$Intensity = \frac{P(watt)}{A(m^2)} \qquad (3-10)$$

Where (P) is the laser power in watt and (A) the spot area.

From monitoring, the change in the electrical resistance of the carbon nanotube film it was found that the sensitivity of bare carbon nanotubes for chloroform increased significantly compared with ethanol, methanol and acetone as shown in figure (3-46). So the laser radiation enhances the sensitivity of chloroform of MWCNTs to become more selective for the chloroform vapour over other VOCs. It was found that the bare MWCNTs sensor treated with laser radiation shows a higher sensitivity to chloroform than without any laser treatment, while the sensitivity to acetone, ethanol and methanol decreased after laser treatment for instance the response size of C_3H_6O dropped to 80% and to 66% and 55% for EtOH and MeOH. Simultaneously the sensitivity to $CHCl_3$ jumped to 230%. Bare CNTs are more selective for chloroform vapor than the other VOCs. Laser irradiation of CNTs therefore provides another useful means to alter the selectivity of CNTs sensors.

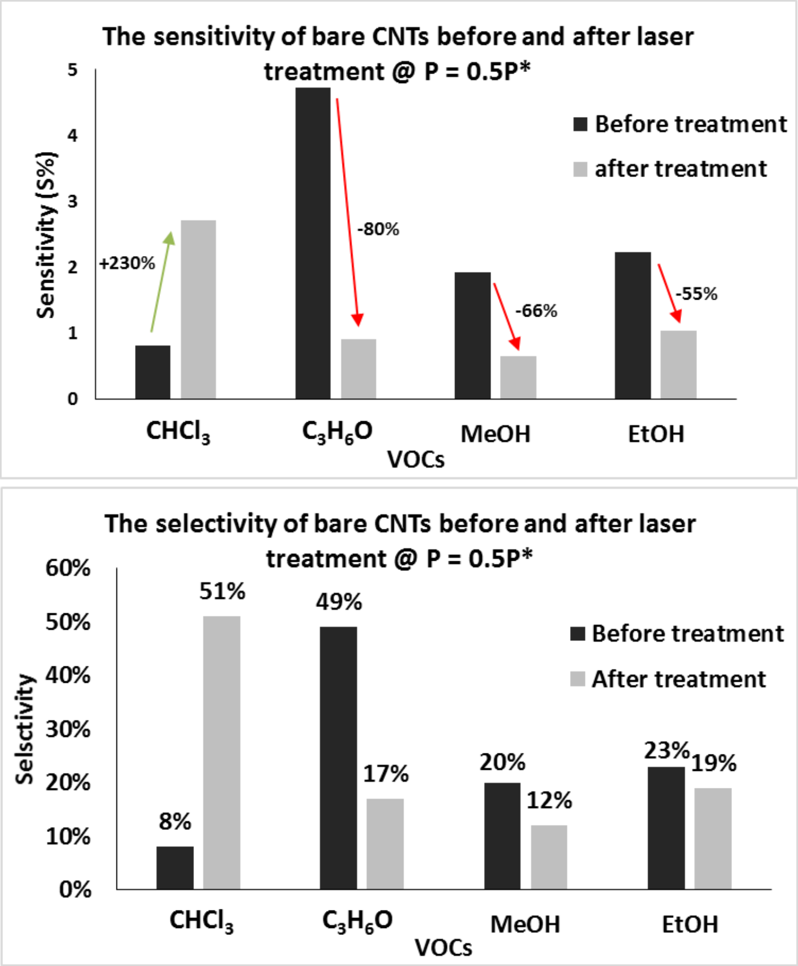

Figure 3-46 Shows the change in the sensitivity and the selectivity of the bare MWCNTs before and after laser treatment with P=0.5P for the (VOCs:dry air).*

Interestingly, the nanotubes in this thesis were prepared by chemical vapor deposition with a purity of 70% by mass for MWCNTs with some Fe particles as shown in EDX spectrum in chapter 3 figure (3-7b). It has been reported that laser treatment of the nanotubes can modify –only the spot area of the MW film- and decrease the impurity content of the nanotubes[162]. In addition, laser ablation with wavelength 532 nm (SHG[3])[163] is a more efficient method to produce high purity CNTs than the CVD approach but it is expensive [164]. According to the Raman spectrum of CNTS

---

[3] S.H.G : divided the wavelength of Nd:YAG laser (1064 nm) to 532 nm by using a KDP crystal to obtain the doubled frequency with high intensity.

before and after there is a significant change in the structure of MWCNTs as shown in figure (3-47); similar results were identified before in previous studies [162, 165-167] and the ratio of the D-band to the G-band for bare carbon nanotubes decreased. The relative decrease of D:G bands suggests fewer sp^3 defects remain after irradiation.

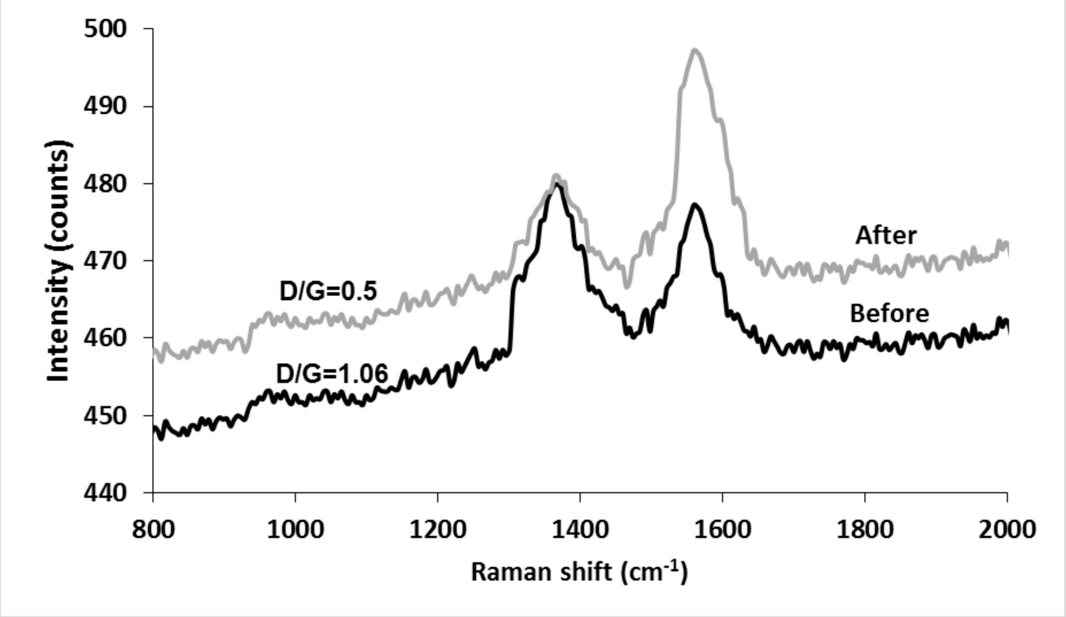

Figure 3-47 Shows the Raman spectrum of bare MWCNTs before and after laser treatment.The excitation wavelength is 488 nm. The spectrograph used a grating with 600 line/mm.

3.3.5. Repeated measurements

A good gas sensor should be stable, reliable, with a good life time and to evaluate the stability of CNTs as a gas sensor it was necessary to use the same mixture concentration (P/P*) for each VOC for around 30 min to check the behaviour of the nanotubes over time as shown in figure (3-48&49). It was found that the change in the electrical resistance of the CNTs films was stable for all the VOCs.

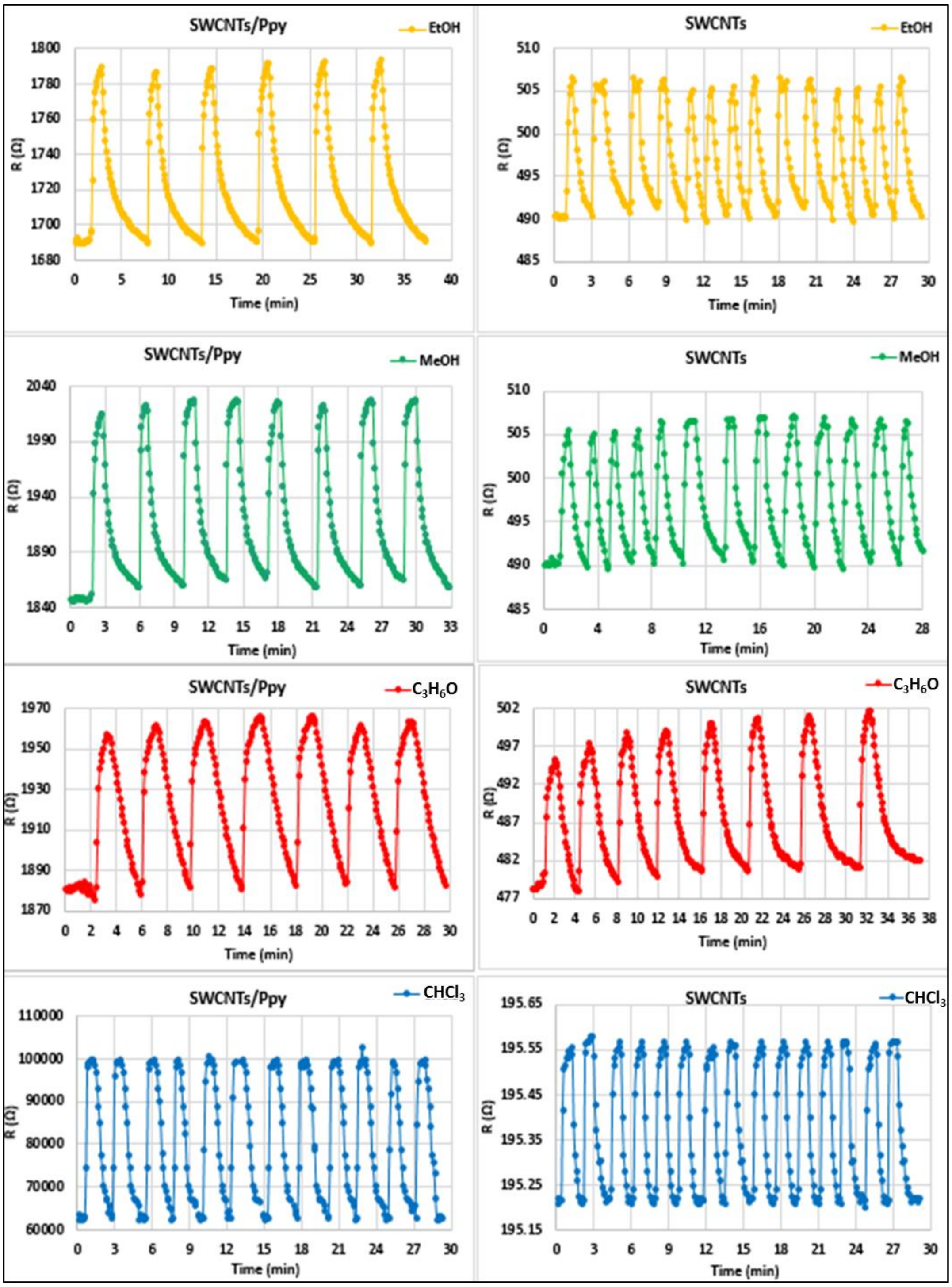

Figure 3-48 Shows the stable change in electrical resistance of SWCNTs and SWCNTs/Ppy in (P=0.5/P) for VOCs at the room temperature.*

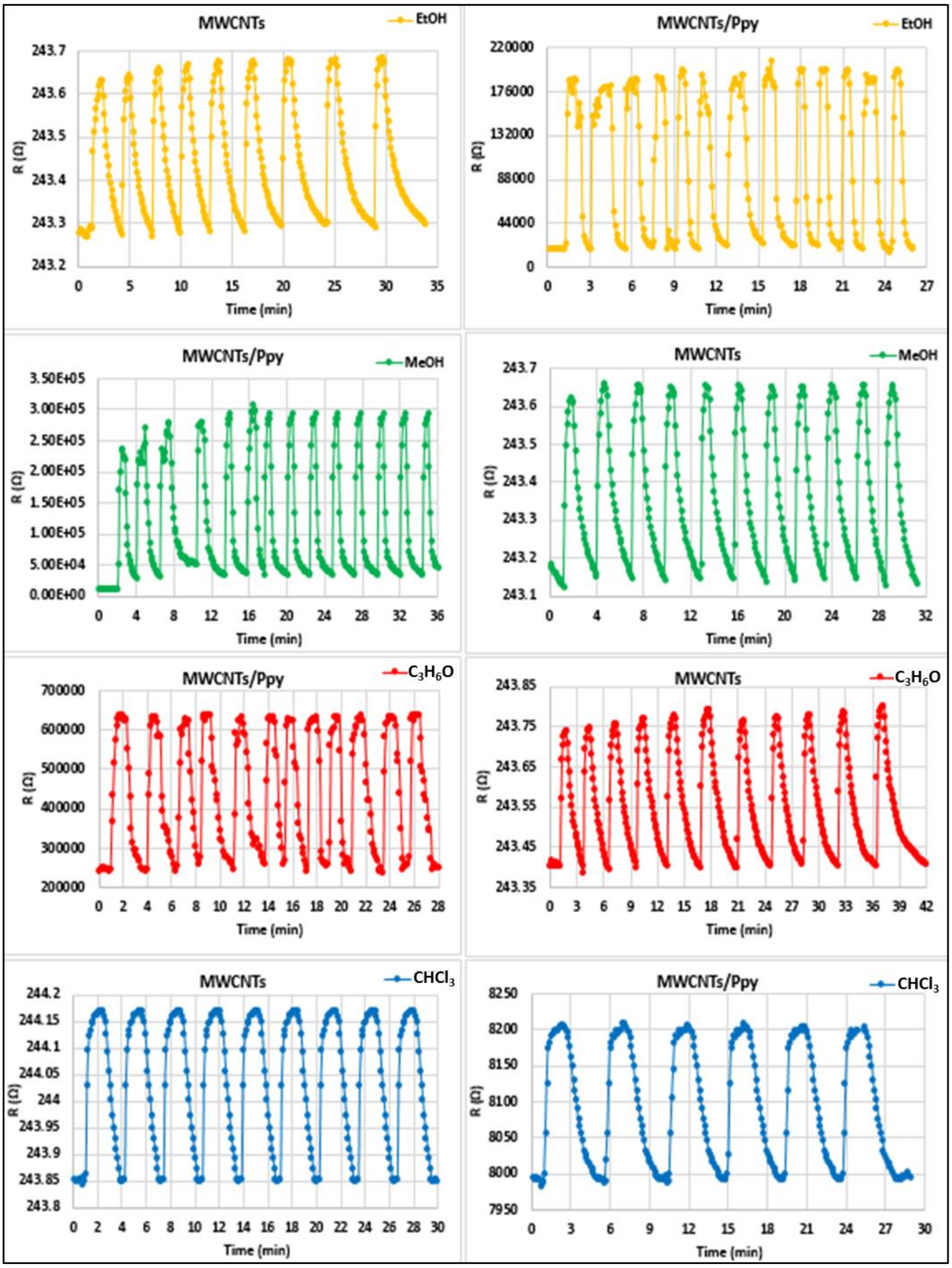

Figure 3-49 Shows the stable change in electrical resistance of MWCNTs and MWCNTs/Ppy in (P=0.5/P) for VOCs at the room temperature.*

In addition, the sensor was examined for ten days to sense acetone vapour at (P = 0.67 P*) and from observing the change in the electrical resistance it was found that the film's resistance decreased with the time and the response size decreased also as shown in figure (3-50). Upon checking the film under microscope it was noted that there were cracks in the film of CNTs/Ppy. These cracks may expose bare CNTs reduce the sensitivity of the sensor.

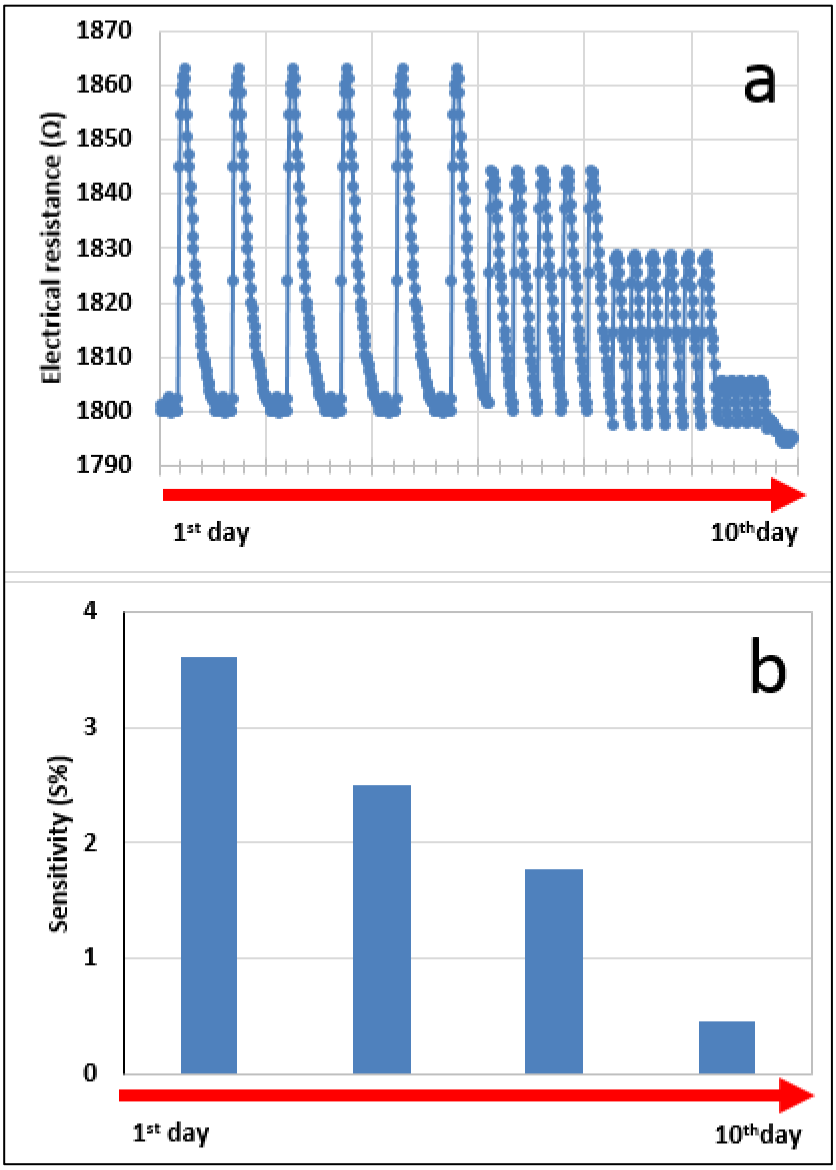

Figure 3-50 Shows the change in the electrical resistance of CNTs for acetone vapor (P = 0.67/P) at room temperature in ten days*

3.3.6. The mechanism of the response of carbon nanotubes as a nanosensor.

The operating principle work of the nanogas sensor depends on the change in the electrical resistance of the films before and after gas exposure[138]. The change in the electrical resistance or the conductivity can arise from different mechanisms. First, charge transfer between the vapor molecular (analyte) and the conductive polymer in the nanocomposite films or between vapor molecular and the nanotubes in the case of bare NTs films might alter the carrier density. This seems unlikely for the VOCs studied in this work, which are relatively unreactive, stable molecules, not easily oxidised under ambient conditions. Such a mechanism, based on charge transfer reactions of organic species would also be unlikely to be reversible. Second, it is possible that adsorption of the VOCs by the polymer produces conformational changes and/or swelling of the polymer that affects the hopping process responsible for the polymer's conductivity. This type of mechanism is much more likely on the basis of the data discussed above which showed reversible responses under ambient conditions and a decrease in response at higher temperatures, consistent with a mechanism based on adsorption.

As shown previously in this chapter the main mechanism of electrons transport inside the CNTs and CNTs/Ppt depends on the variable range hopping (VRH) and tunnelling transport (TT)[5]. However, it has been reported that the main part in the sensing mechanism is the interaction between the coating layer and the analyte and according to the observation of the electrical properties of the films during the sensing process it was noted that the electrical resistance for bare and hybrid nanotubes increased with gas exposure. From I-V characterization, the Schottky barrier at the contact electrodes also increased and the work function decreased for CNTs/Ppy[168]. Generally, in the sensing experiments, the adsorption of the gas' molecules on the surface of the nanotubes can relate to the surface coverage [4],[169]. Mostly, any small amount of polypyrrole on the CNTs will increase the sensitivity of the nanosensor for VOCs. However, the response of the composites may even change sign as a function of target analyte concentration; this suggests that a simple mechanism based on swelling and its effect on the percolation behavior of CNTs in the polypyrrole matrix is insufficient to explain the data. In addition, in some sensing tests of chloroform and acetone vapor it was found that the electrical resistance decreased during gas exposure and from observing the sample by atomic force microscopy it was noted that the diameter of polypyrrole increased or swelled which led to a change the electrical conductivity and decreased the sensitivity of the film as shown in figure (3-51). In 2010 Yakovlev and et al found the best description of this case is related to re-aggregation of the carbon nanotubes and the CP concentration below the percolation threshold, a new arrangement between CNTs and the conductive polymer effects the sensing response with decreasing resistance value due to the weak interaction between the nanotubes and pyrrole[127].

---

[4] Surface coverage is known as an occupation of vapor/ gas molecules on the surface of materials as nanotubes.

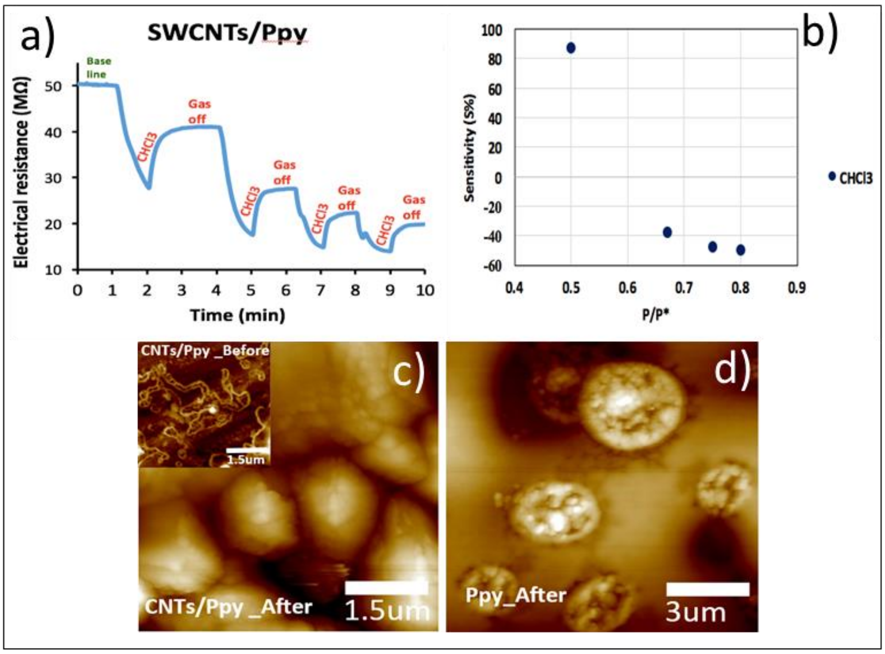

Figure 3-51 Shows a) the negative change in the electrical resistance of SWCNTs/Ppy for CHCl$_3$: dry air exposure,b)reduce the response size of the film during the sensing process,c)AFM images of hybird nanotubes before and after gas exposure, d)the effect of swelling on the polypyrrole size after gas exposure.

3.4. Conclusions

Polypyrrole/CNTs composites were synthesised succssesfully using the *in situ* chemical oxidative polymerization method. Morphology and electrical properties were studied for MWCNTs/Ppy, SWCNTs/Ppy, pure Ppy and pristine CNTs. The results show that the multi wall and single wall carbon nanotubes were nanocomposites effectively synthesised using the oxidative polymerization method. As demonstrated by AFM and TEM, the diameter of CNTs increased after treatment with Ppy, which suggests that the polypyrrole covered most of the surface of the nanotubes. In addition, as demonstrated in FTIR and Raman experiments, Ppy covered most of the surface of CNTs. I-V characterization showed that the electrical conductance of CNTs decreased after the coating process. However, the sensitivity of bare CNTs for VOCs was increased after Ppy coating by more than ten-fold. Upon evaluation of the peformance of bare and hybrid CNTs gas sensors at different temperatures, it was been found that the device sensitivity decreased with temperature. The temperature dependence is consistent with the Van't Hoff equation and reversible adsorption of the analyte on the device. For all sensing measurments, bare and hybrid CNTs have a fast response time $\cong$ (1-2) min and fast recovery time $\cong$ (1-4) min MeOH, C_3H_6O and EtOH have a good response size, in contrast, $CHCl_3$ had the lowest sensitivity at pristine and hybrid CNTs, while the sensitivity of $CHCl_3$ increased after laser treatment of CNTs. It has been noted that the sensitivity for MeOH, C_3H_6O and EtOH was decreased after laser treatment and this method made CNTs partially selective to chloroform over other VOCs. CNTs and the nanocomposite thin films show a stable response for a constant gas concentration for 30 min. However,on conducting the sensing experiment for ten days, the film sensitivity decreased. The reason for this was probably associated with the appearance of cracks in the polypyrrole film; these would expose bare CNTs and alter the way in which the analyte is adsorbed.

Chapter four: CNTs/BNNTs as ozone gas sensors

This chapter will demonstrate how carbon nanotubes can be used to sense ozone gas and the effect of boron nitride nanotubes BNNTs on the sensitivity of carbon nanotubes in this matter. Exposure to ozone at ground level leads to damage to the lung and nervous system. Therefore, the development of ozone sensors for use in urban pollution monitoring is important. In addition, ozone is hazardous to not only humans but also plants and animals. Near ground level ozone gas forms from the action of sunlight on NO_2 (nitrogen dioxide) from soil emissions and from burning fuels in cities. The choice of BNNTs to make composites with CNTs is motivated by the observations in the previous chapter that decreasing the conductivity of CNT films often leads to an increase in sensitivity of the gas sensing devices. Ozone is an extremely reactive molecule, therefore the material used to prepare the composite should be chemically robust: BNNTs are both robust (similar to CNTs) and insulating.

4.1. Carbon nanotube and boron nitride films.

Generally, the good physical properties of carbon nanotubes encourage researchers to use this material in a wide range of sensing applications. CNTs show utility to detect different types of volatile organic compounds and gases[170-175]. It is worthwhile to note that CNTs/Ppy films did not work well as a sensor for ozone gas. Although a fast response was initially recorded, the electrical resistance during gas exposure was unstable and it was difficult to evaluate the film sensitivity, see figure (4-1). This is due to the extreme oxidizing power of ozone which reacts with organic polymers in an irreversible manner. A more inert second component of the composite was required and BNNTs were observed to produce more stable devices in combination with CNTs.

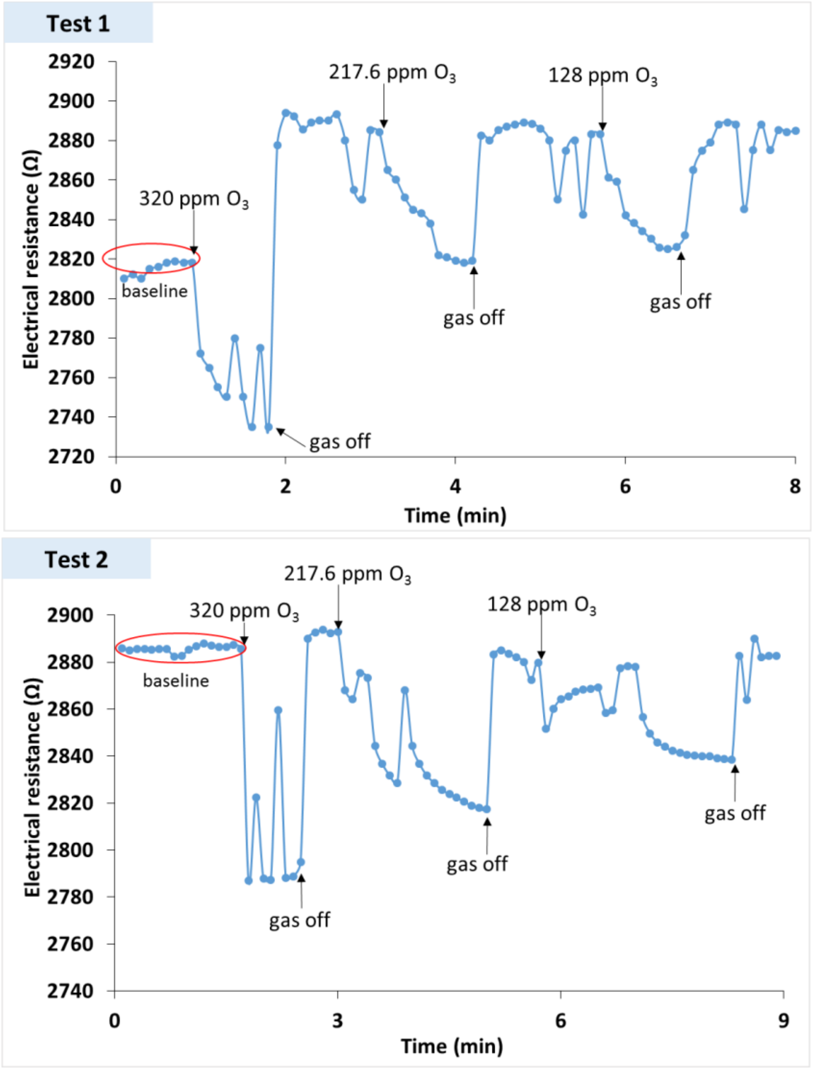

Figure 4-1 The unstable change in the electrical resistance of CNTs/Ppy as ozone gas sensor at room temperature with different concentrations of the gas.

It has been noted from previous studies that to design a CNT ozone sensor one needs a high working temperature (optimum working temperature) (330-650) K in order to recover rapidly under vacuum. The recovery time can be (1-2) h at room temperature and depends on the gas concentration[176]. In this part of the study, three types of nanotubes were used: multiwall carbon nanotubes MWCNTs, single wall nanotubes

SWCNTs and also boron nitride nanotubes BNNTs. Chapter two includes all the details of these nanotubes and preparation of the films. The coupling between carbon nanotubes and boron nitride nanotubes can enhance the sensitivity of carbon nanotubes as ozone sensor, improve response, and retain a good recovery time at different temperatures. For bare carbon nanotubes, although the response time was fast ~ 1 to 2 min with good sensitivity, the recovery time was very long ≅ 27.8 min for bare MWCNTs at 320 ppm as shown later in this chapter. Combining carbon nanotubes with BNNTs can improve the recovery time and enhance the sensitivity. BNNTs are one-dimensional (1D) nanostructures and have recently attracted significant interest from the scientific community. BNNTs are close analogues to carbon nanotubes. BN-nanotubes are electrical insulating with a large band gap ~ (5.9 to 7.1) eV[177]. Chemically and thermally BNNTs vary stable with excellent thermal conductivity[178, 179].

4.2. Synthesis of CNTs/BNNTs films.

Chapter two, section 2.4 demonstrated how to prepare the thin films. 2-3 μL was taken from the mixing solution (CNT/BNNTs) (100 μL:100 μL) of 100 μg mL^{-1} for CNTs and BNNTs and drop cast as a thin film on the microband electrodes to examine the I-V characterizations and the impedance spectroscopy IS of the film or on silicon chip for FTIR and Raman. Many techniques were used to study the physical properties of CNTs after mixing by BNNTs: TEM, Raman spectra, FTIR, I-V characterization and IS.

4.2.1. Transmission electron microscopy TEM.

More structural properties of CNTs and BNNTs have been studied by transmission electron microscope. Figure (4-2) show TEM images of bare and hybrid nanotubes. BNNTs appear as wrapped up CNTs and can be in parallel with CNTs and from the histogram the diameter of CNTs increased after mixing with BNNTs as shown in figure (4-3).

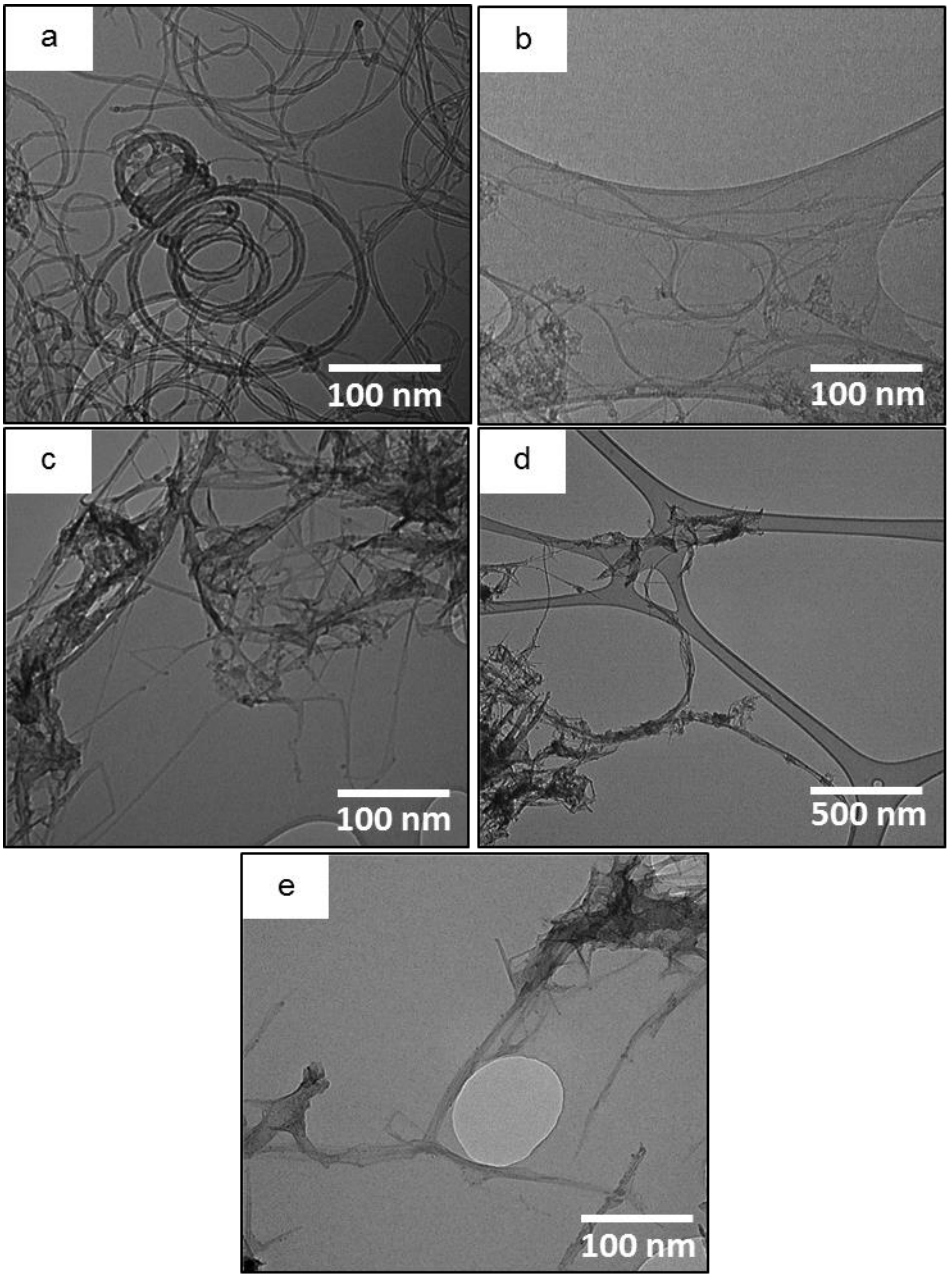

Figure 4-2 Shows TEM images of a) bare MWCNTs (b) bare SWCNTs, (c) bare BNNTs, (d) SWCNTs/BNNTs, (d) MWCNTs after templated by BNNTs.

SWCNTs and MWCNTs after mixing look more tangled; this is related to the natural structure of BNNTs[52, 180]. The tangles occur due to the π-π interaction and Van der Waals forces between BNNTs and CNTs[52, 180].Figure (4-2) demonstrates the average diameter of SWCNTs and MWCNTs after mixing with BNNTs.

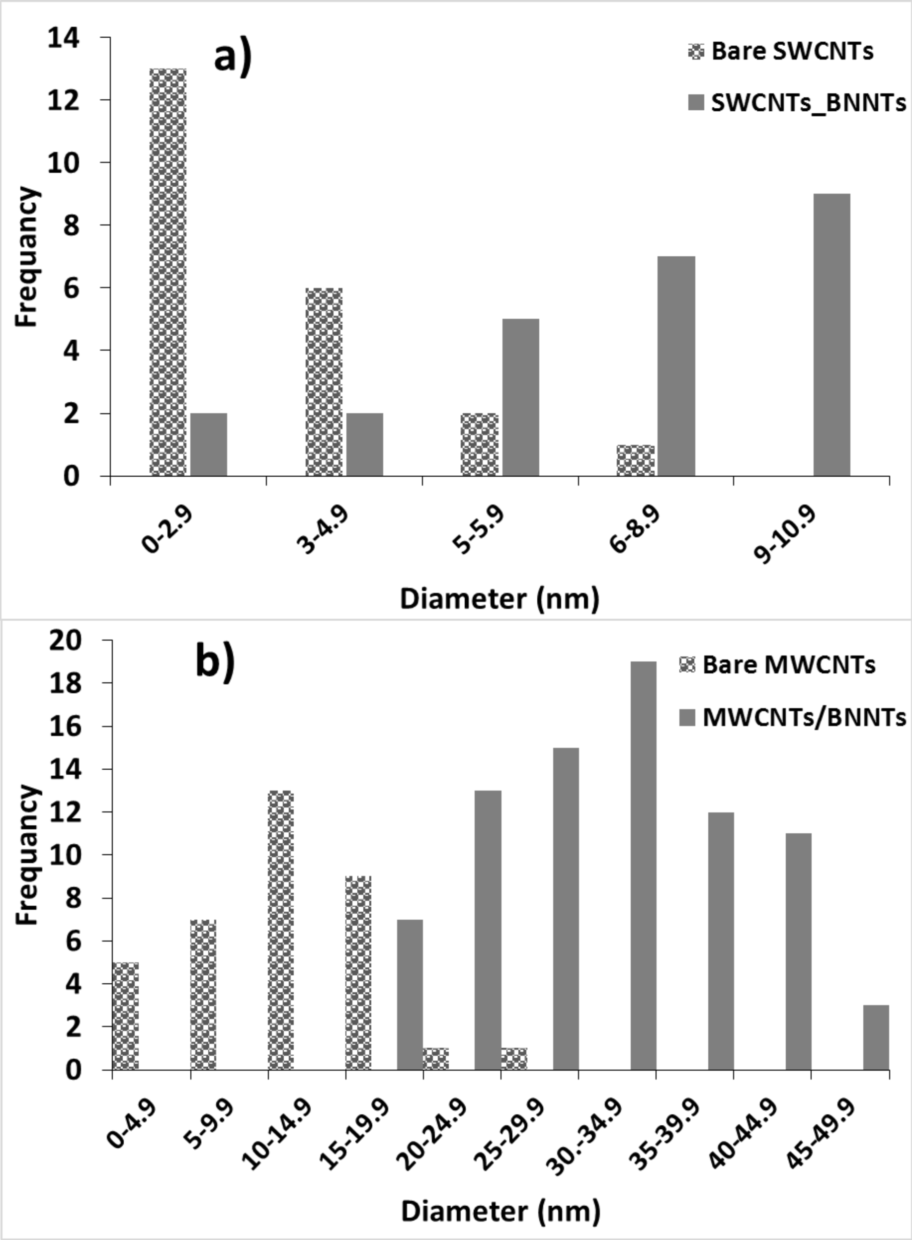

Figure 4-3 The histogram data of the distribution of the nanotubes by TEM technique a) bare and hybrid SWCNTs, b) MWCMTs before and after mixing with BNNTs.

4.2.2. Electronic analysis of two terminal nanotubes devices:

I-V characterizations were carried out with a small applied voltage (1V to -1 V) and the results were collected and monitored by a Casade Microtech probe station as described in chapter two. Figure (4-4) shows the linear, Ohmic plot of carbon nanotubes before and after mixing with BNNTs at room temperature. In general, carbon nanotubes show a linear plot and there is no evidence of any barrier between at the Pt/NTs contacts. Adding BNNTs to the nanotubes reduced the current from 8 mA to 1.4 mA for MWCNTs and 5 mA to 1 mA for SWCNTs at the applied voltage (-1 to 1) V. This indicates the BNNTs partially interrupt the current flow between CNTs. The working hyposthesis was that modulation of this effect by the analyte would generate improved analytical sensitivity compare to pure CNT devices.

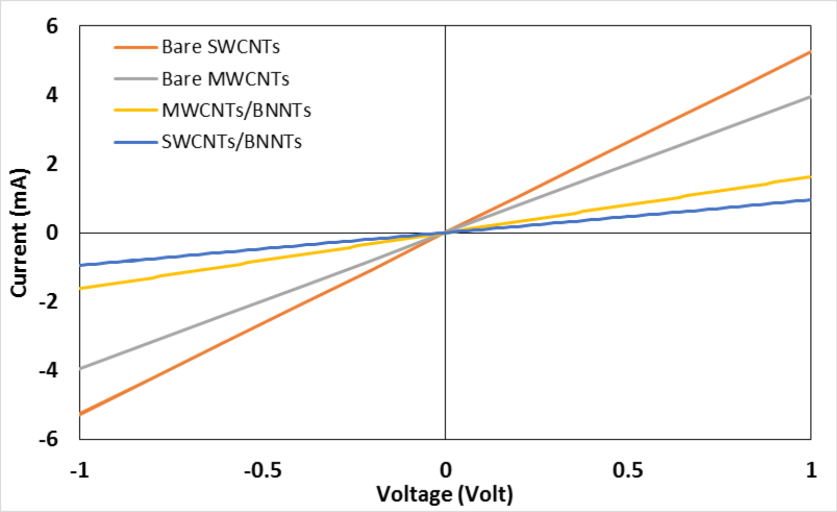

Figure 4-4 The change in the I-V characterizations of carbon nanotubes before and after coated by BNNTs at room temperature.

4.2.3. Impedance spectroscopy IS

The impedance spectroscopy is a useful technique to understand the electrical behaviour of the samples after mixing with BNNTs. Figure (4-5) shows the Nyquist plot of CNTs/BNNTs thin films and bare CNTs. For each bare and hybrid nanotube it was noted that there is no imaginary part or Z'' for these films and the spectra show only the real resistance Z' (part Z'=R=V/I). However, as demonstrated before, carbon nanotubes are metallic tubes and from IS measurements in chapter three it has been found that both SWCNTs and MWCNTs have a high electrical current with a small Rb ~275 Ω and 213 Ω for MWCNTs and SWCNTs respectively. Mixing CNTs with BNNTs did not result in a change in the shape of the impedance spectrum, but did shift the spectrum along the real axis. This suggests that the BNNTs only partially interfere with current flow between MWCNTs and the film properties are still mainly due to the highly conductive MWCNT fraction. The effect of mixing with BNNTs was larger for the case of SWCNTs; the resistance increased by an order of magnitude as shown in figure(4-b5).

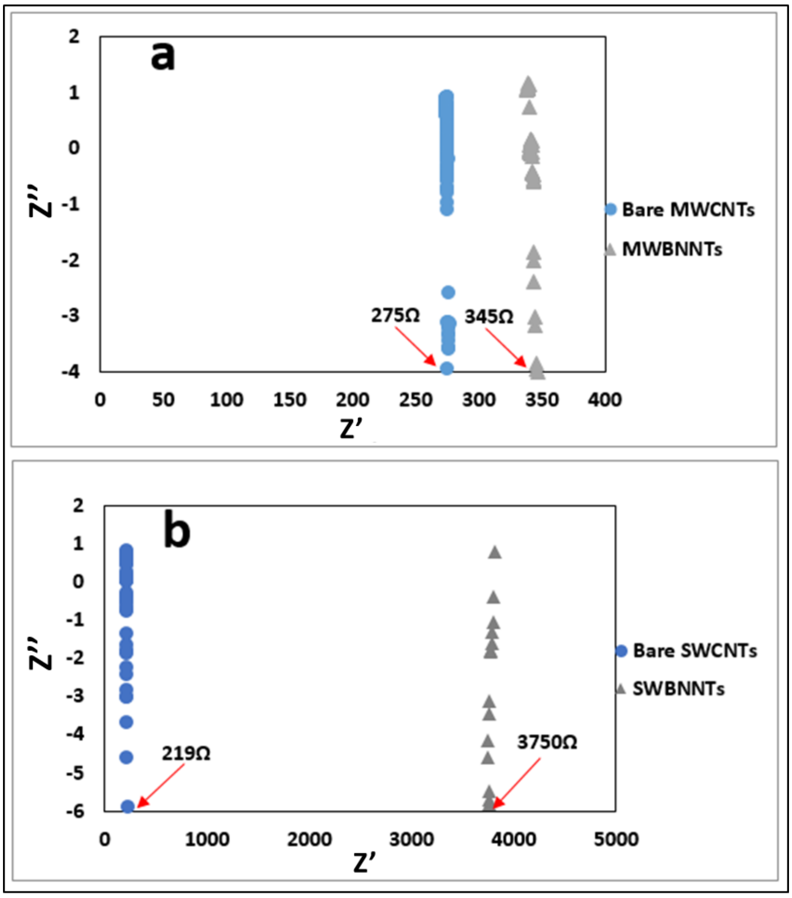

Figure 4-5 Nyquist plot of a) bare MWCNTs and MWBNNTs, b) pristine and hybrid SWCNTs.

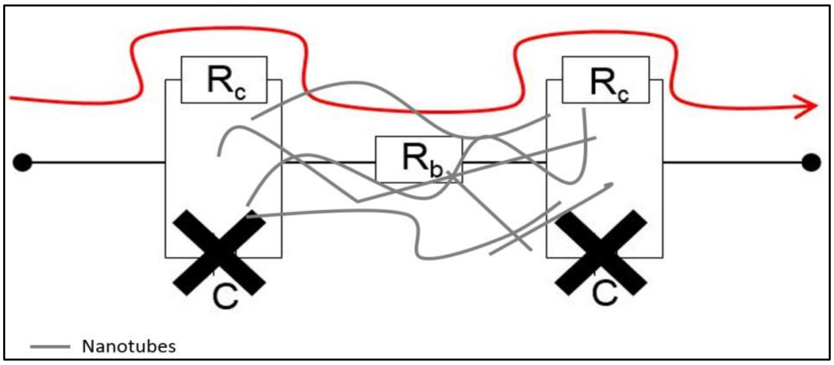

Figure 4-6 The equivalent circuit of (Pt-NTs-Pt) devise, the cross sings refers to there is no carriers passed in this part of the circuit.

All IS measurements were carried out with frequencies between 5-10000 Hz and from Nyquist plots for both SWCNTs and MWCNTs the ohmic bulk resistance was the main behaviour in these electrical devices, see figure (4-6).

4.2.4. Raman spectroscopy

The mixing led to the appearance of new peaks in CNTs/BNNTs spectra as shown in figure (4-7). Generally, bare CNTs spectra have three main peaks G, D bands and RBM [177, 181] with stronger intensity for G-band than D-band. For SWCNTs spectra, the D-band is found at 1351 cm^{-1} and the G-band at 1588 cm^{-1}. For MWCNTs, the D-band has been noted at 1360 cm^{-1} and the G-band at 1590 cm^{-1}. BNNTs added new peaks for example, the peak with wavenumber 981 cm^{-1} appeared in the SWCNTs/BNNTs spectra and 1076 cm^{-1} at MWCNTs/BNNTs spectra. Obviously, pure BNNTs spectra have shown a wide range of peaks, which have been recorded at 981cm^{-1}, 1258 cm^{-1}, 1645 cm^{-1}, 2104 cm^{-1} and 2077 cm^{-1}. It is not possible to resolve all the peaks of BNNTs in BNNTs/CNTs mixture.

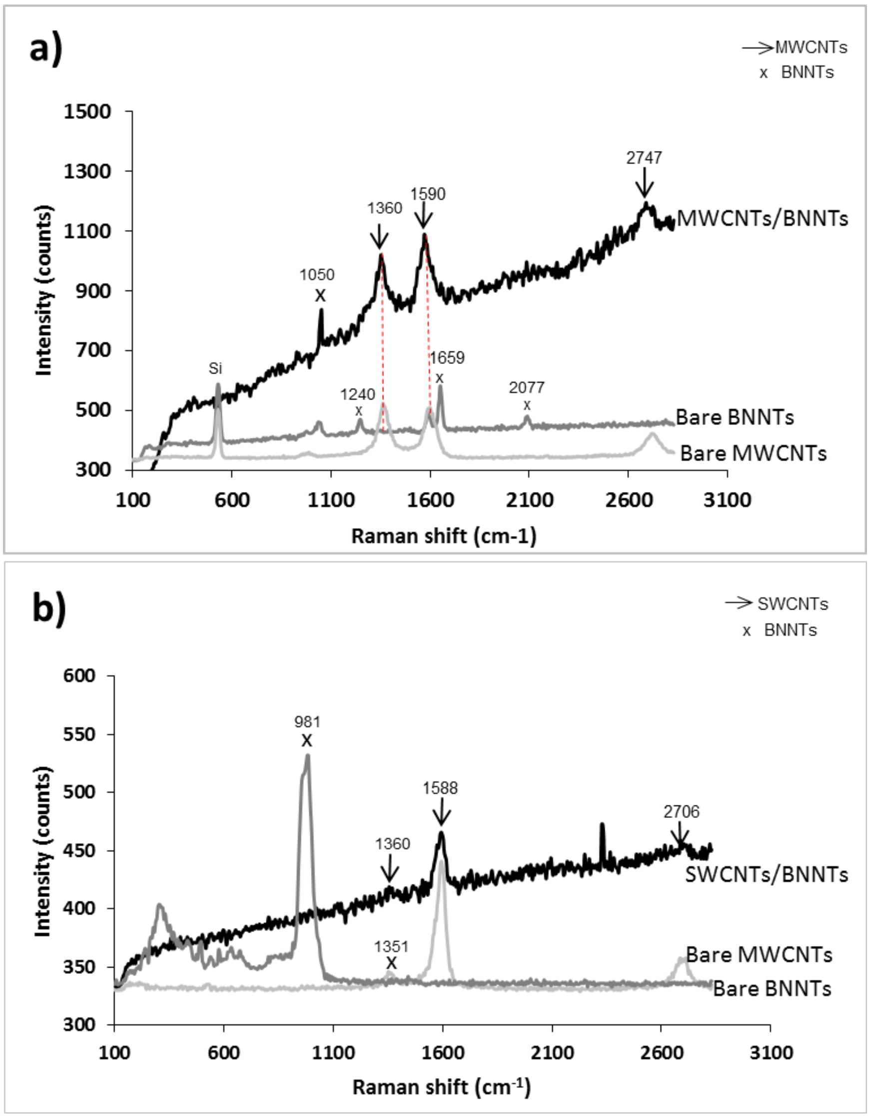

Figure 4-7 Raman spectra of a) Bare MWCNTs before and after coated by BNNTs, b) pristine SWCNTs before and after coated by BN nanotubes.at the room temperature. The excitement wavelength is 488nm with the spectrograph used a grating with 600 line/mm.

. Table 4-1 The wavenumbers of bare and hybrids CNTs peaks in Raman spectra

Wavenumber (cm^{-1})	Description
Plot (A)	
1050	BNNTs
1240	BNNTs
1360	CNTs (D-band)
1590	CNTs (G-band)
1659	BNNTs (analogous to G-band of CNTs)
2077	BNNTs
2747	CNTs
Plot (B)	
981	BNNTs
1351	BNNTs (analogous to D-band of CNTs)
1360	CNTs (D-band)
1588	CNTs (G-band)
2706	CNTs

4.3. Ozone generation

One of the general approaches to generate ozone in the laboratory is the ultraviolet light technique. Both dry air and UV-light with a wavelength 185nm were used to generate the ozone. The UV-lamp was supplied by UVP, LLC/ UK. Basically, dry air is passed over the UV-tube and leads to dissociation of the oxygen gas (O_2), these atoms ($O^{\cdot}$) try to stabilize by reaction with O_2 molecule and create ozone molecules[182]. Figure (4-8) shows a schematic diagram of the generation of ozone gas by a UV-lamp.

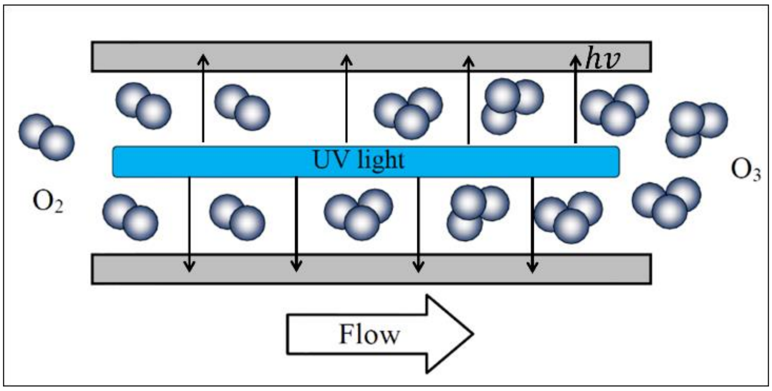

Figure 4-8 Schematic diagram of ozone generation by using UV-lamp with the wavelength 185 nm (absorption energy to break the O-O bond) $O_2+hv \rightarrow O+O$ *(these atoms try to stabilize by reaction with another oxygen molecule)* $O+O_2 \rightarrow O_3$ *and finally ozone molecule will destroy with more UV absorption* ($O_3+hv \rightarrow O+O_2$) *all these steps are happened in close cycle of destruction and formation of the ozone, this method is cheaper and lower cost than other methods*[182]

However, table (2) demonstrates the conditions and the parameters that were used in this part of this thesis for ozone sensing.

Table 4-2 The conditions and the parameters were used for ozone sensing.

Ozone (ppm)	Dry air (mL/min)	Temperature (K)	Thin films / Sensor material
128	125	293,313, 333	(SW, MW, SWBNNTs, MWBNNTs)
217.6	125	293,313, 333	
320	125	293,313, 333	

4.4. Ozone gas sensor based on carbon nanotubes.

The sensing process of ozone gas depends on observing the change in the electrical current using a potentiostat as shown in chapter two section 2.8.2. This part depended on measuring the current instead of resistance because the resistance was very small and more precise measurements could be obtained by observing current at fixed applied potential. An irreversible increase in current was observed upon exposure of CNTs to ozone. The likely mechanism of this effect is injection of positive charge into the CNTs, which increases the hole concentration, however the oxidation reaction can also lead to irreversible chemical changes to the CNTs. SWCNTs are more sensitive than MWCNTs, probably because the oxidation process happens rapidly because smaller diameter tubes are more strained and are oxidized more speedily than larger diameter tubes[183, 184].

Picozzi et al[185] used bare CNTs[5] in ozone gas sensors (90 ppb to 200 ppb); they found that the decrease in electrical resistance was irreversible. Recovery of the film resistance after removal of ozone took no less than 150 min at room temperature. In our devices the maximum recovery time for our samples was ~ 27 min at room temperature. They suggested that charge transfer was the main mechanism responsible the conductance change upon gas adsorption. Generally, for CNTs, the reaction with ozone molecules occurs at the sidewall and end caps of CNTs[186]. On the other hand, Picozzi et al in their theoretical study reported that the reaction of ozone molecules with CNTs can effect the density of states in the vicinity of the Fermi level and this can be represent another mechanism of gas detection. A few previous studies found that the conductance of CNTs decreases during gas exposure and that was ascribed to a reduction in the density of states near the Fermi level[186]. Our first sensing results showed a fast response time with a good sensitivity for ozone but a long recovery time ~ (10-27) min which depended on the gas concentration. Figure (4-9) shows

---

[5] Picozzi et al treated CNTs by heating up to 563 K to remove the amorphous carbon.

the change in the electrical current during gas exposure. The device sensitivity $S = \frac{I - I_o}{I_o} \times 100\%$ where I_o is the current in air atmosphere and I is the electrical current at steady-state after exposure to ozone gas.

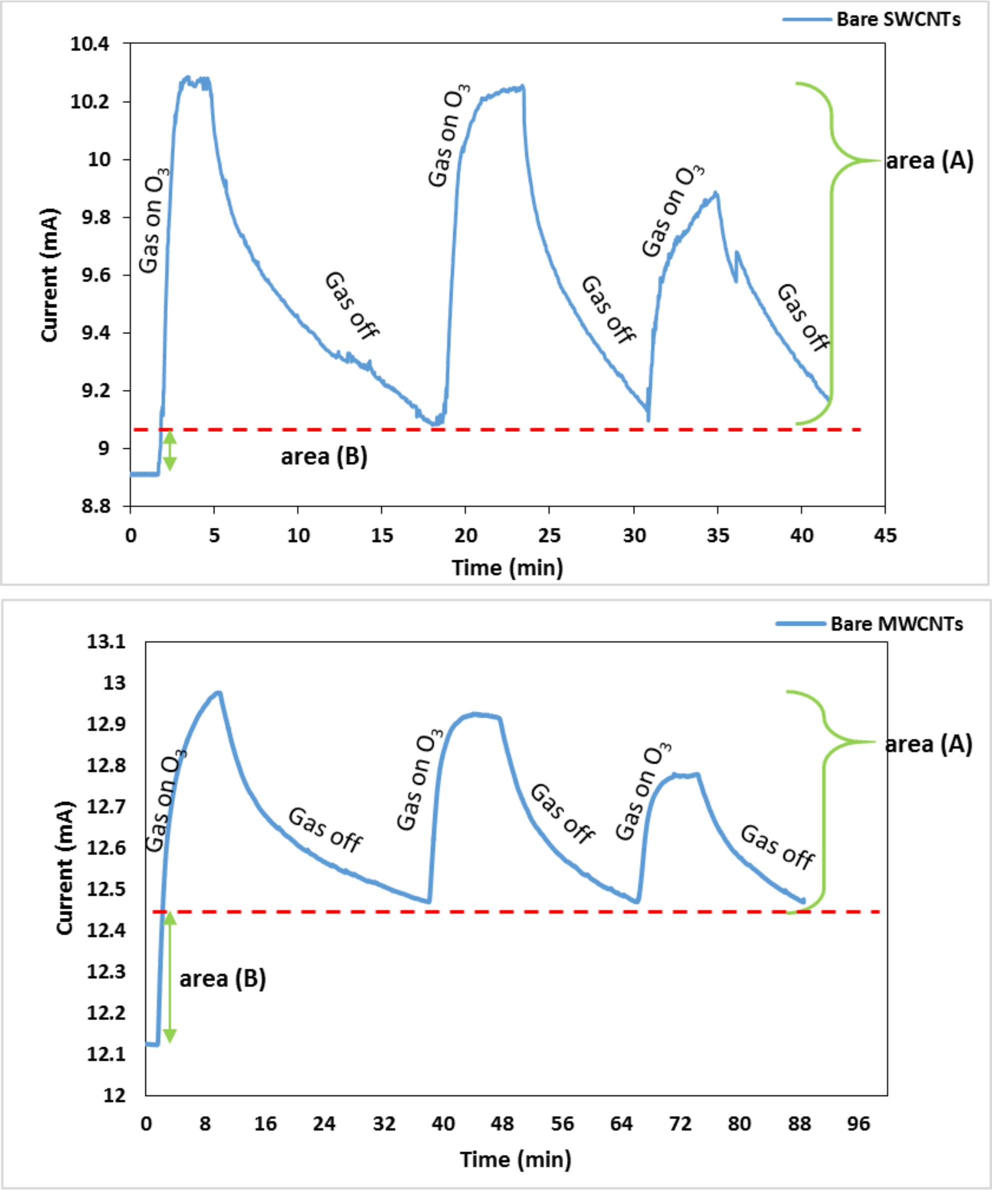

Figure 4-9 The change in the electrical current of bare CNTs as ozone gas sensor at 293K.

Figure (4-9) shows two regions A and B. In area (A), the response is almost reversible (returns to baseline after gas-off) and corresponds to reversible charge injection. Area (B) of figure (4-9) is the region is change in current which is never recovered and corresponds to the irreversible chemical change that was clear in the XPS analysis in section (4.6.) below. By monitoring the current change with time it was noted that the current increased rapidly during ozone exposure [113, 187] with a good response time and good sensitivity, however the recovery time was long ≅ 25 min. This is one of the main disadvantages of using bare nanotubes in this kind of gas detection because an important practical feature of any reusable gas sensor is a fast response with a short recovery time. The response and recovery times are summarised in fig (4-10).

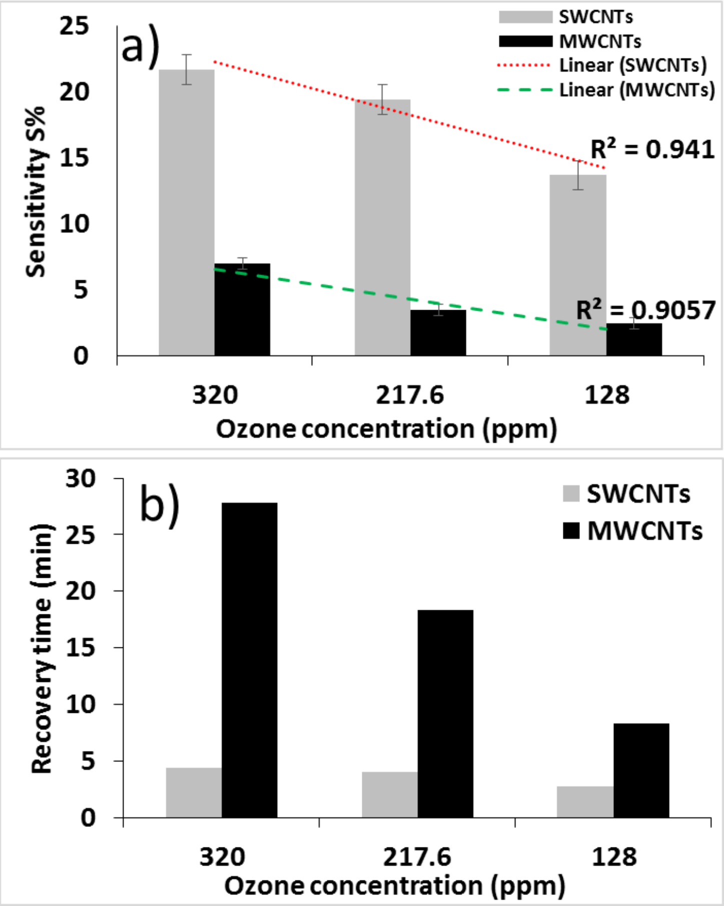

Figure 4-10 a) The sensitivity of SWCNTs and MWCNTs as ozone gas sensor and shown a strong adsorption of ozone on the SWCNTs than MWCNTs with high sensitivity than MW, b) the recovery time of SWCNTs and MWCNTs, SWCNTs recorded a short recovery time (3-5) min than MWCNTs (8-27) min.

The recovery time became longer with an increase the concentration of the gas. Ozone has an effect on the electrical properties of bare carbon nanotubes because it is a strong oxidant. From IS measurements it was found that the film behaves electrically as a simple resistance, dominated by a real impedance, (Z'_{re}). The resistance of SWCNTs decreased ~ 9.3% and ~ 14% for MWCNTs after ozone treatment as shown in figure (4-11).

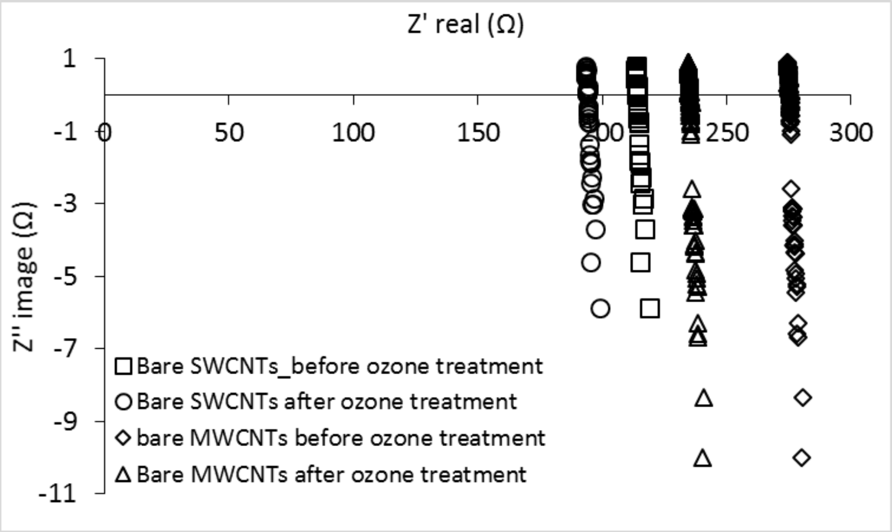

Figure 4-11 Nyquist plot of bare carbon nanotubes before and after ozone treatment at 293K.

Mixing carbon nanotubes with boron nitride nanotubes affected significantly the sensitivity of carbon nanotubes. Upon current monitoring of CNTs/BNNTs films, it was found that the current increased during the sensing process, but did not completely return to the background level after switching off the UV-light to remove ozone from the gas flow as shown in figure (4-12b&d).

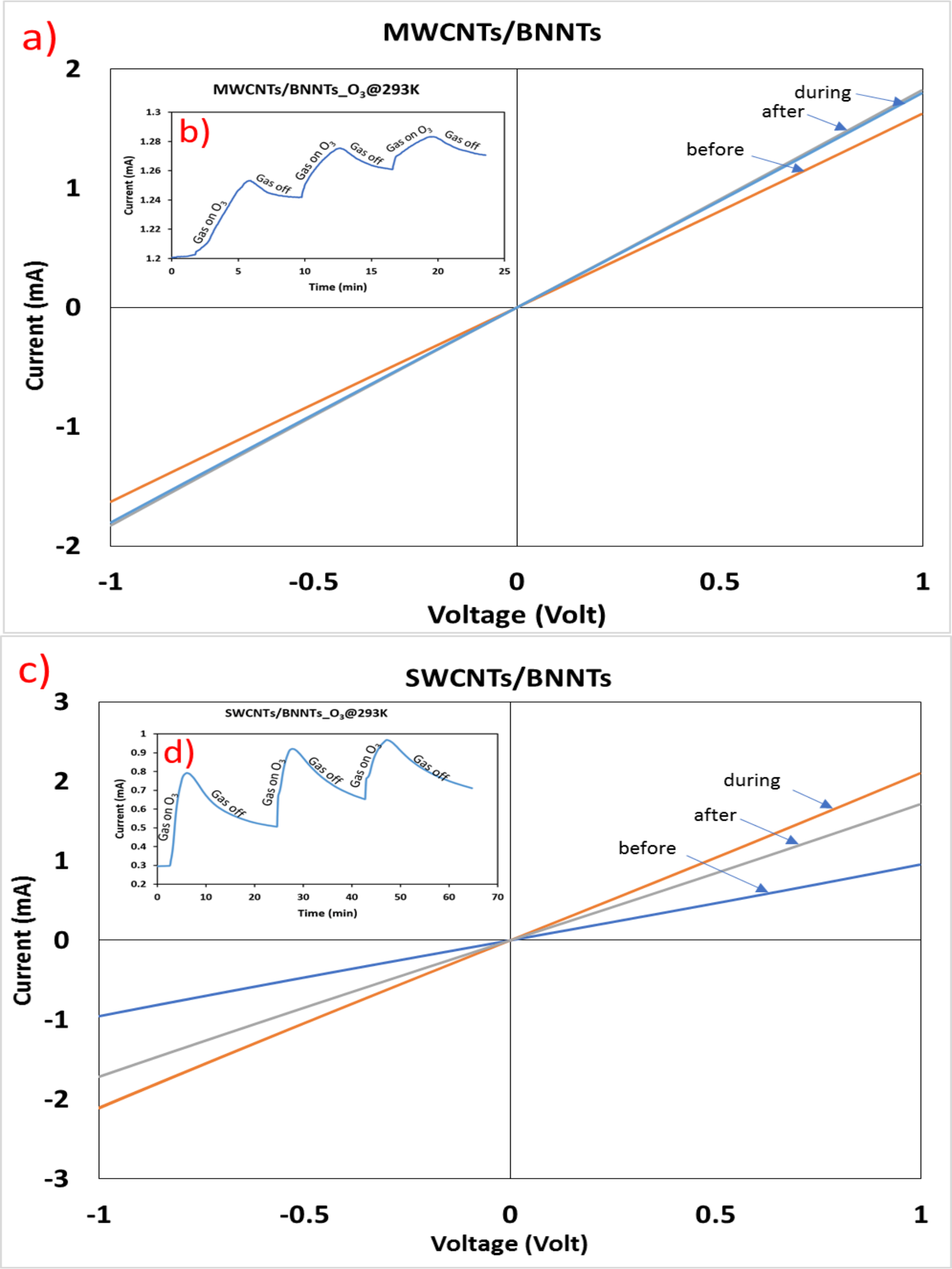

Figure 4-12 (a&c) I-V characterizations of MWCNTs/BNNTs and SWCNTs/BNNTs films before, during and after ozone treatment (oxidation process), (b&d) the change in the electrical current of CNTs/BNNTs with a time during ozone sensing process.

SWCNTs have a greater sensitivity to ozone gas than MWCNTs. BNNTs enhance the sensitivity of SWCNTs. The response increases ~ 261-645% compared to bare SWCNTs, but with a long recovery time ~(10-17) min. In comparison pristine SWCNTs recover in (2.5-4) min. In contrast, MWCNTs mixed with BNNTs showed a drop in the sensitivity of 39-60 % dependent on the gas concentration, as shown in figure (4-12). From above it appears that there is a relationship between the recovery time and the response of the nanotubes. In general, BNNTs enhance the sensitivity of SWCNTs more than they do MWCNTs at room temperature 293K. Ozone is a very strong oxidant and it has been shown that SWCNTs are more sensitive to ozone than MWCNTs; ozone causes the formation of more defects on the sidewalls of SWCNTs than MWCNTs[188-190]. In addition, the external tube in MWCNTs can act as protective layer to shield the inner tubes from interaction with gas molecules. Raman spectra of SWCNTs and MWCNTs show an increase in D/G[6] ratio after ozone exposure[176], as shown in figure (4-13).

The effects of the reaction between BNNTs and ozone gas are different than the effect of ozone on CNTs. Ozone molecules adsorb on the sidewalls and end caps of CNTs and led to depletion of electrons from the π-system, but in BNNTs ozone also causes a decrease in the energy gap[191-193] from 5.5 e.V to 0.96-1.29 eV. This changes the electrical behaviour from insulating to semiconducting. Therefore the analytical sensitivity of SWCNT/BNNTs mixtures to ozone increased over pure SWCNTs. In addition, XPS data (section 4.6) give further evidence of major chemical changes to BNNTs upon exposure to ozone. Such chemical

---

[6] D/G: refers to the ratio between two bands D-band and G-band of CNTs. G-band is related to vibration mode of C-C and D-band is pointed to dislocate in graphene. This ratio has been change after ozone treatment.

changes are likely a cause of the increased recovery time observed in figure (4-13d).

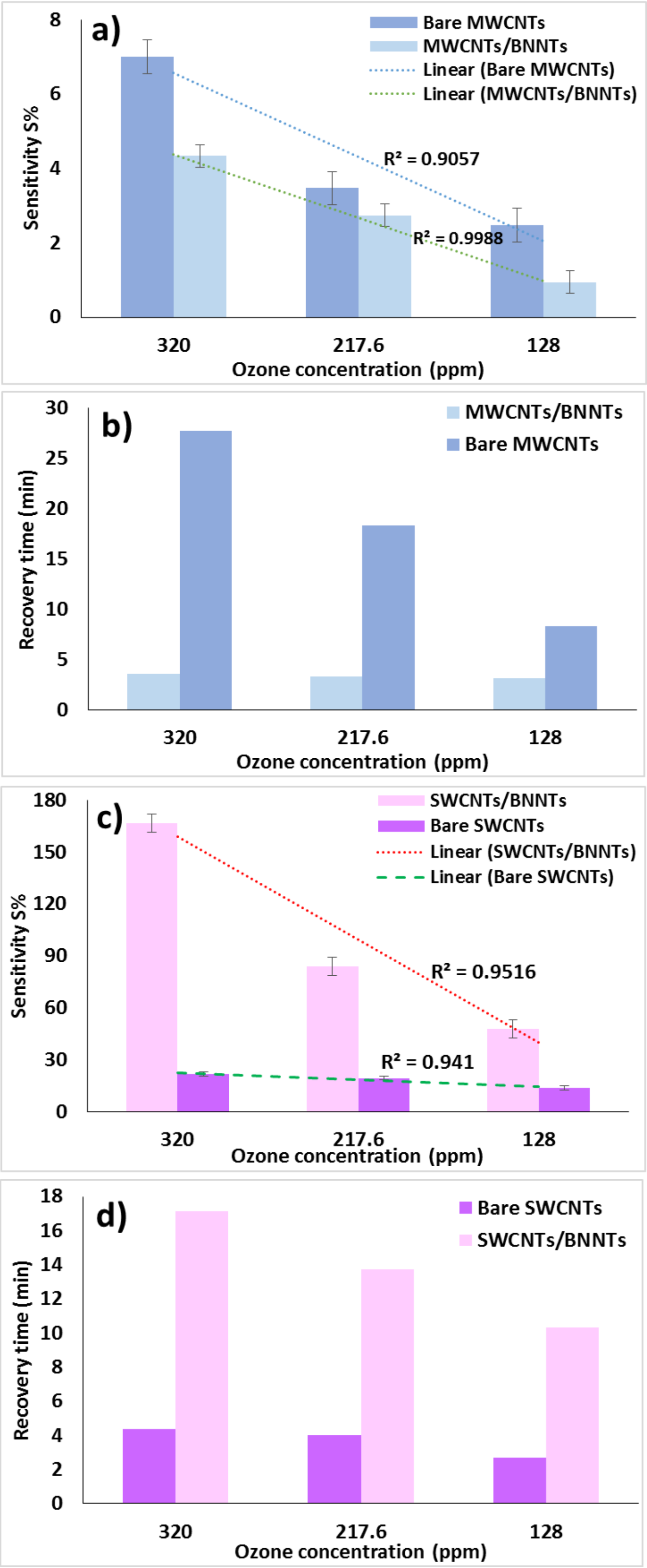

Figure 4-13 (a,c) the change in the sensitivity of bare and Hybrid nanotubes as ozone gas sensor, (b&d) the recovery time of the bare and pristine nanotubes at the 293K.

Table 4-3 Shows the sensitivity, response and recovery time of pristine and hybrid carbon nanotubes for different concentration of ozone at room temperature.

Ozone conc. (ppm)	Sensitivity (S%)				Response time (min)				Recovery time (min)			
	SWCNTs	SWCNTs/BNNTs	MWCNTs	MWCNTs/BNNTs	SWCNTs	SWCNTs/BNNTs	MWCNTs	MWCNTs/BNNTs	SWCNTs	SWCNTs/BNNTs	MWCNTs	MWCNTs/BNNTs
128	13.7	159	2.46	0.94	1.3	3.25	8.6	4.2	2.7	10.3	8.3	3.15
217.6	19.4	80	3.47	2.73	1.6	2.6	5.18	3.05	4.03	13.7	18.3	3.28
320	21.7	43	6.9	4.33	2.2	2.8	3.4	2.8	4.35	17	27.8	3.55

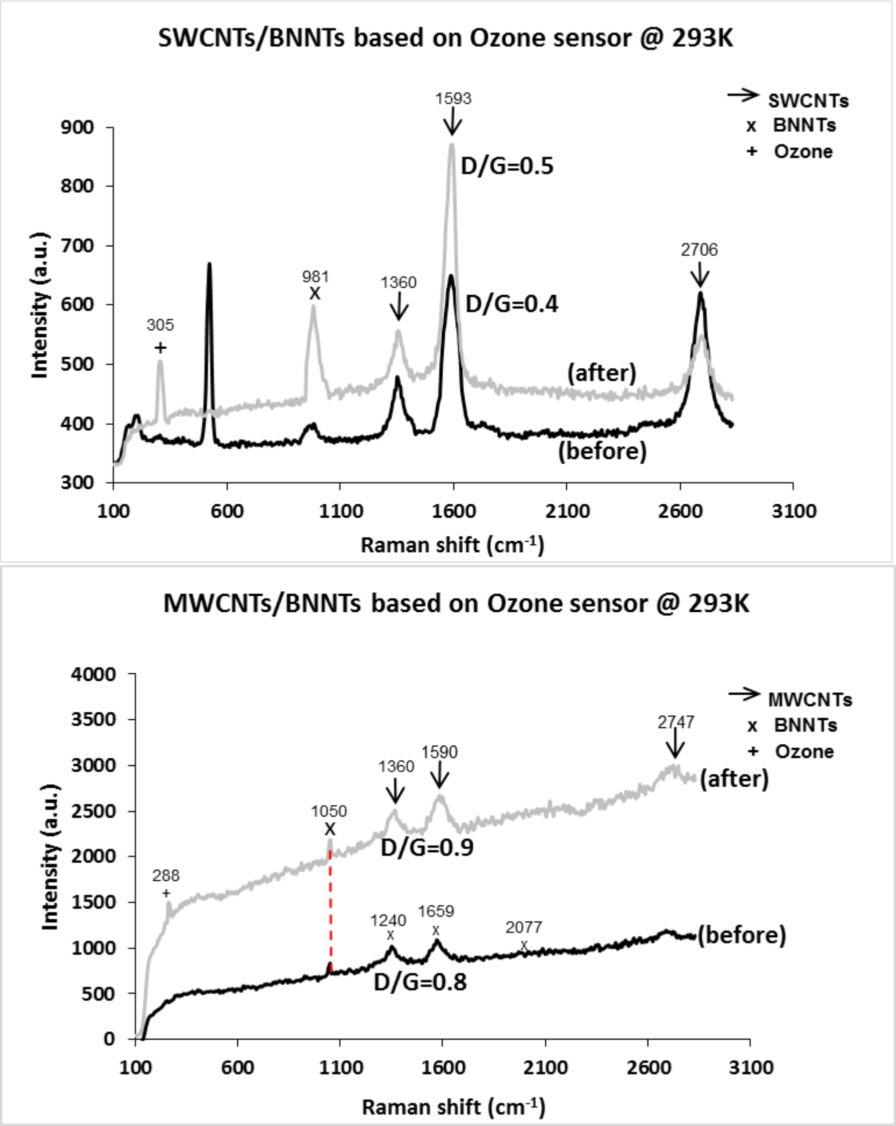

Figure 4-14 Raman spectra of CNTs/BNNTs before and after oxidation process with higher sensitivity for SWCNTs/BNNTs than MWCNTs/BNNTs and it has been noted that D/G ratio increased after exposing to O3 at room temperature which is assigned to the defect in the structure of CNTs after ozone exposure. The excitement wavelength is 488 nm with the spectrograph used a grating with 600 line/mm. these figures were offset in intensity by 100 and 1000 for clarity of presentation ,respectively.

4.4.1. Effect of the temperature on the sensor performance

This section discusses the effect of the working temperature on the sensitivity of (bare and hybrid nanotubes) films. Two temperatures were used 313K and 333K in addition to the room temperature. It has been found that the thermal treatment increases the response size and the recovery time for bare and hybrid nanotubes. Figure (4-15) presents the change in the sensitivity of CNTs at different temperatures and from observation of the change in the electrical current at 313K and 333K it was easy to recognize that oxidation led to an increase in the current for both CNTs and CNTs/BNNTs films. Interestingly, the recovery time was shorter at higher temperatures (figure 4-15). The decrease in recovery time upon increasing the temperature suggests the process is limited by chemical kinetics. Analysis of the temperature-dependence of the sensitivity *S* according to the Van't Hoff equation gives an enthalpy $\Delta H^{\ominus} > 0$. An adsorption mechanism is therefore an unlikely explanation because the loss of translational entropy upon adsorption requires it to be exothermic. It is likely that mechanism is based on a chemical reaction between ozone and CNTs (oxidation) that is faster at higher temperature, figure (4-16) the relation between lnS and the temperature for different gas concentrations and figure (4 -17) shows the positive values of $\Delta H^{\ominus}$ these thin films. In the case of ozone / CNTs / CNT/BNNTs, $\Delta H^{\ominus}$ should be interpreted as an activation energy and the rate-limiting process is most likely a chemical reaction following Arrhenius' law:

$$k = Ae^{-\frac{E_a}{RT}} \qquad (4-1)$$

Where k is a rate constant, A is a pre exponential or frequency factor, E_a is an activation energy, R is the gas constant 8.314 J mol^{-1} K^{-1} and T is a temperature in K.

$$S \,\alpha\, k\, [O_3] \qquad (4-2)$$

Where S is the signal, which is proportional to the amount of the analyte.

$$\frac{\partial \ ln S}{\partial \ 1/T} = -\frac{E_a}{R} \qquad (4-3)$$

Our ΔH^{Θ} is corresponds to the activation energy E_a and does not represent a thermodynamic quantity, such as the enthalpy of adsorption.

Figure (4-17) shows the change in I-V properties of CNTs films. The shortest recovery time was for SWCNTs and SWCNTs/BNNTs (2.6-3) min at 80 ppm of ozone which increased gradually with increased concentration of the gas.

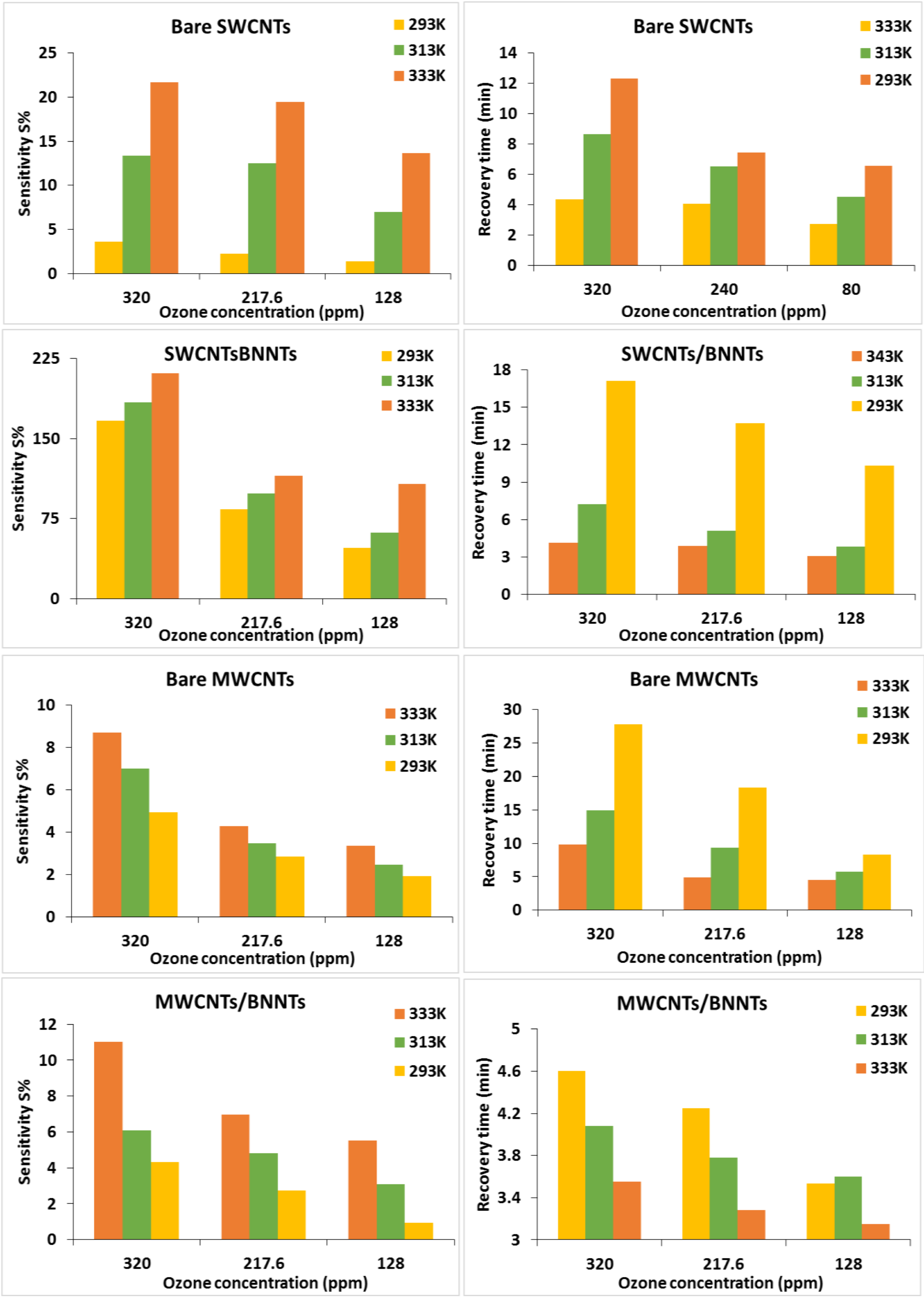

Figure 4-15 Shows the change in the sensitivity of bare and hybrid nanotubes at 293, 313 and 333K and the improvement in the recovery time for the thin films of CNTs at the same conditions after ozone treatment.

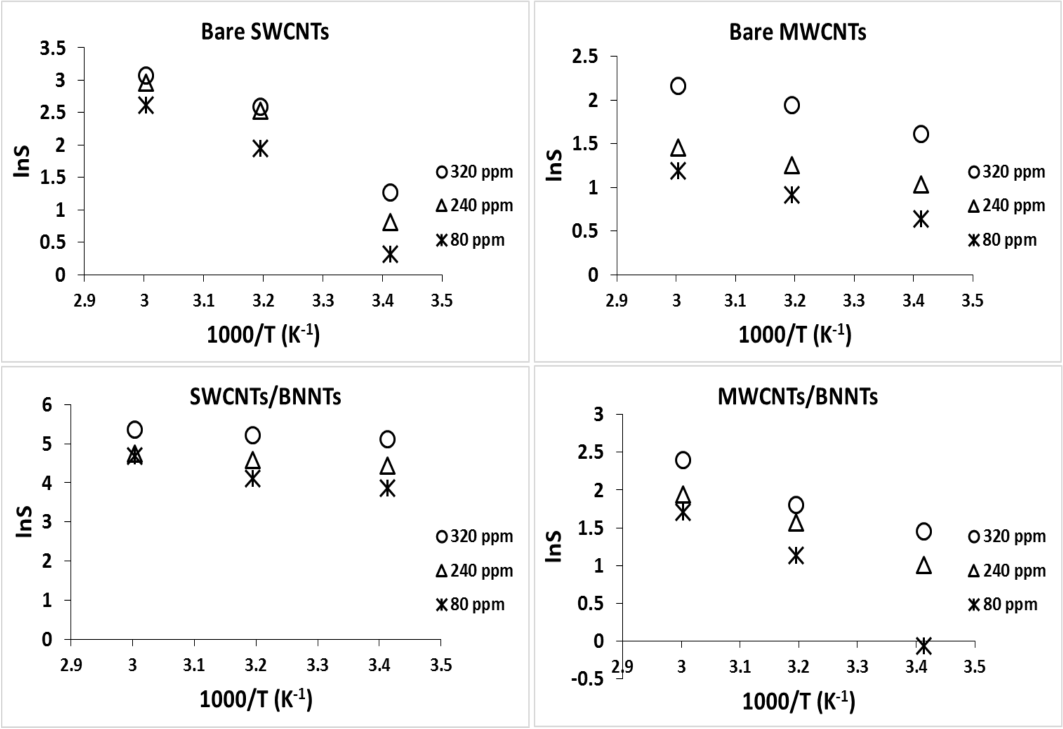

Figure 4-16 Shows the relation between lnS and temperatures for the different concentrations of the ozone for bare and hybrid CNTs.

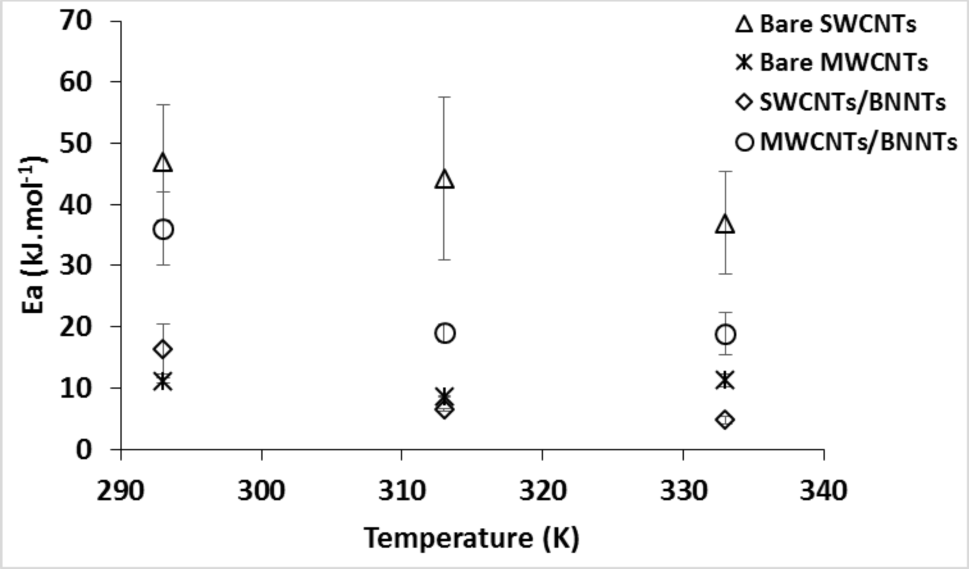

Figure 4-17 Shows the change in activation energy (E_a) of the system. The sensitivity of the films increases with temperature, which indicates a chemical kinetic mechanism (Arrhenius behavior) rather than an adsorption mechanism (van't Hoff equation with exothermic process) best describes the response of these films to ozone.

The Nyquist plots (insets on figure 4-18)) demonstrate the effect of temperatures on the electrical properties of CNTs after gas exposure. The film resistance decreased with increased temperature for both SWCNTs/BNNTs and MWCNTs/BNNTs as shown in figure (4-18). This is unusual for a metal-like conductor, but may be rationalised on the basis of a chemical process as described by equation (4-3).

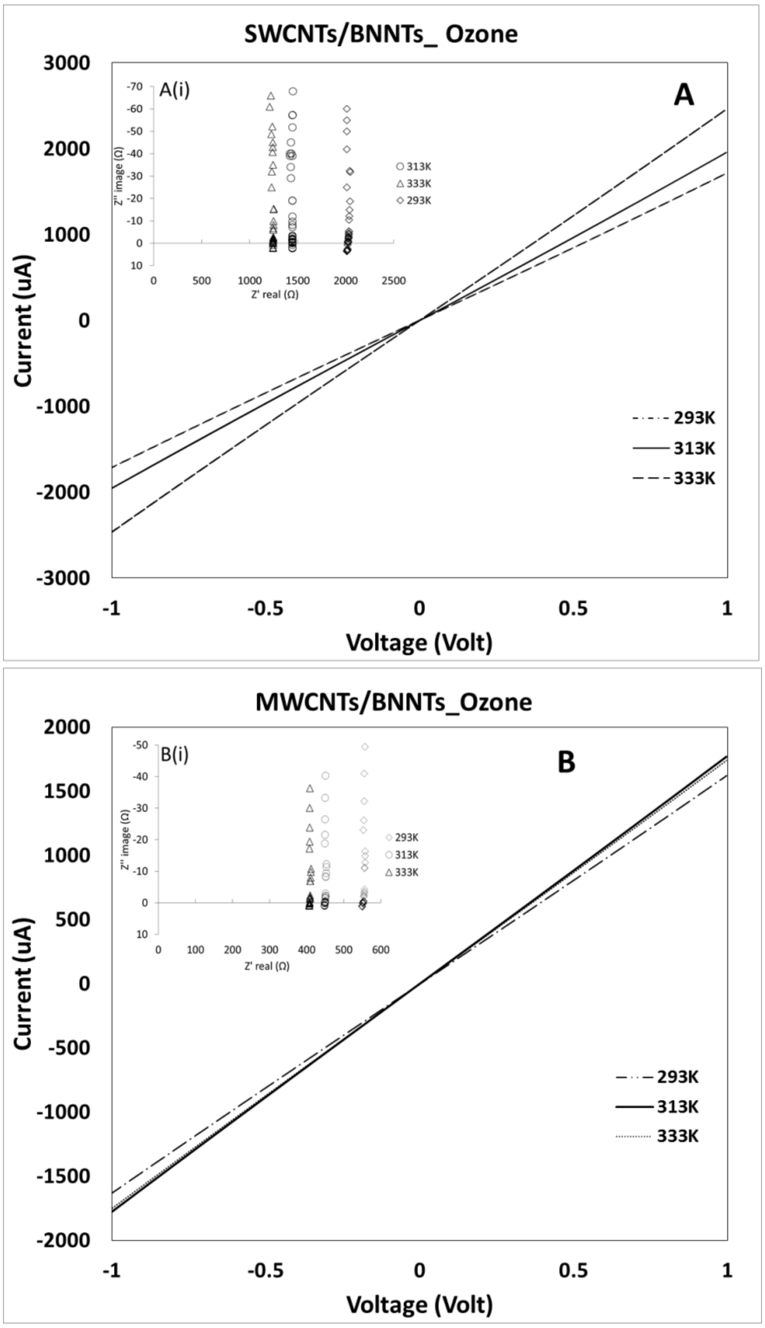

Figure 4-18 (A and B) show the effect of temperature on the I-V characterizations of MWCNTs/BNNTs and SWCNTs/BNNTs after oxidation prosess, (A(i) and B(i)) Nyquist plot of hybrid nanotubes at different temperature and it appears that the IS measurements of CNTs/BNNTs has a real part (Z' real) without imaginary resistance.

Raman spectra give worthwhile information about the effectiveness of ozone treatment at different temperatures. It has been shown that the oxidation process at 313 K and 333 K increased the defect density in the nanotubes.

Table (4-4) and figure (4 -19) show the change in the G/D ratio for SWCNTs/BNNTs and MWCNTs/BNNTs at different temperatures after ozone exposure.

Table 4-4 Shows the change in G/D ratio because of ozone at different temperature.

Thin film	Temperature in ^{o}C	G/D
MWCNTs/BNNTs	20	1.06
	40	1.08
	60	1.67
SWCNTs/BNNTs	20	1.4
	40	1.44
	60	1.96

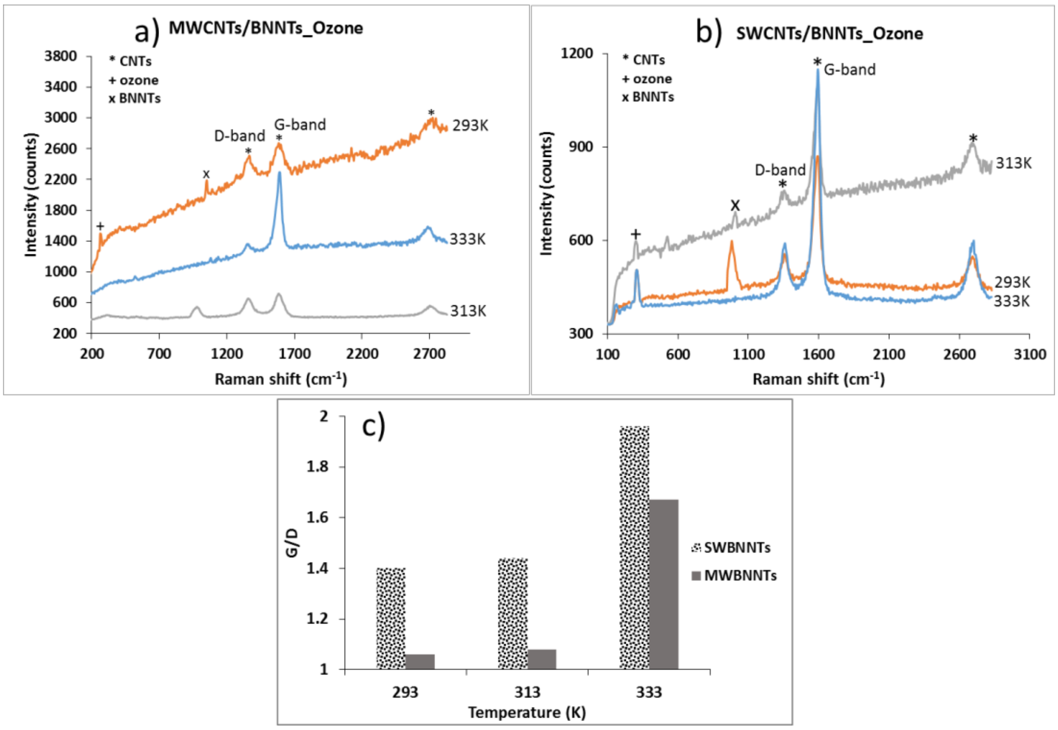

Figure 4-19 (a&b) show the Raman spectrum of MWCNTs/BNNTs and SWCNTs/BNNTs after ozone exposure, c) effect the ozone treatment on G/D ratio at different temperature.

The change in the G/D ratio probably effects the formation of hydroxide and carboxyl groups on the nanotubes's sidewall and breakage of C-C [176, 187, 194, 195].

4.5. The mechanism of the electrical current change of CNTs and CNTs/BNNTs films as an ozone sensor.

Ozone is a strong oxidant and during adsorption process on the surface of nanotubes there is transfer of electrons from carbon nanotubes to ozone. Ozone depletes electrons from carbon nanotubes and increases the hole concentration as majority chargers in the nanotubes network. Increases of the observed currents are seen in figures (4-7&10). However, it has been shown that after removal of ozone, the recovery was limited at room temperature (4 - 27) min. This points to a strong binding between carbon nanotubes and ozone molecules or an irreversible chemical reaction. In several studies a vacuum system was used to rapidly recover from ozone exposure and break the contact between CNTs and O_3 [176, 196, 197].

4.6. X-ray photoelectron spectroscopy (XPS)

XPS was carried out to study the chemical composition of bare and hybrid SWCNTs. All XPS studies were calibrated using C 1s at 284 eV. Figure (4-20a) shows the survey spectra of bare SWCNTs before the oxidation process with ozone and shows three peaks, which are related to C 1s, O 1s and Si (substrate). Figure (4-20b) shows the high-resolution C 1s spectra. There are five peaks: C1, C2, C3, C4 and C5, which are assigned to C-C sp^2 at 284 eV, C-C sp^3 at 284.86 eV, C-O at 285.76 eV, C=O at 286.8 eV and C5 is assigned to O-COO at 289.78 eV[198-200]. Figure (4-20c) shows the O 1s spectrum of pristine SWCNTs before ozone treatment and comprises two peaks, 531.68 eV assigned to =C-O- while the weak peak is assigned to C=O at 533.62 eV. Figure (4-20a*) is the survey spectrum of bare SWCNTs after ozone treatment and presents three peaks C 1s, O 1s and

Si, the Si peak appears simply because of the sample substrate. The C 1s spectrum shows five carbon peaks: C1 is assigned to sp^2 C at 284 eV, C2 is assigned to sp^3 C at 284.95 eV, C3 is assigned to C-O[200] at 285.9 eV, C4 is assigned to C=O[199, 200] at 287.18 eV and C5 is assigned to O-COO[199] at 289.54 eV, as seen in figure (4-20b*). After ozone treatment, it a small change in the area of these peaks was found. As shown in table (4-5) sp^2 C, C-O and C=O as were increased to 1%, 3% and 7%, respectively. A small shift in the binding energy of 0.1 eV for C-O, 0.35 eV and 0.14 eV for C-O, C=O and O-COO respectively was observed. O 1s spectra after ozone treatment show two peaks at 531.67 eV assigned to =C-O and 533.44 eV assigned to C=O with a small shift of 0.2 eV for C=O compared to its BE before the oxidation process. In addition, the intensity of the =C-O peak was increased by about 4% after gas exposure compared to C=O, as shown in figure (4-20c*) and table (4-5). Figure (4-21d) presents the survey spectrum of SWCNTs/BNNTs before oxidation process and shows carbon C 1s, boron B 1s, nitrogen N 1s, Oxygen O 1s and Si (substrate). Figure (4-21e) shows the core peak of carbon with five components: C1, C2, C3, C4 and C5, which are assigned to sp^2 (C-C) at 284 eV, sp^3 (C-C) at 285.7 eV, C-graphite at 284.55, C-O at 286.89 eV and C=O at 288.13 eV, respectively. After ozone treatment, four peaks appeared as shown in figure (4-21e*) and can be described as: sp^2 and sp^3 C-C, C-O and >C-O at 284 eV, 285.29 eV, 286.5 eV and 287.9 eV, respectively[199]. However, ozone treatment produced an obvious effect on the carbon spectra of the SWCNTs/BNNTs film, especially on the sp^2 component. The sp^2 peak increased more than 100% compared to sp^3 as shown in table (4-5). Boron (B 1s) spectra before ozone treatment have two peaks B-N at 190.27 eV and B-B at 186.9 eV[201], after ozone treatment there is a small shift for B-N from (190.2 to 189.9) eV while a big shift from 186.9 eV to 190.9 eV for B-B[202] that is likely due to oxidation of B-B to B-O. From the same survey spectra of SWCNTs/BNNTs, nitrogen spectra N 1s shows two peaks at 397.72 eV assigned to Si_3N_4[203 204] and 398.45 eV assigned to B-N, as shown in figure (h). Figure (h*) shows two peaks for N 1s after ozone treatment with two main peaks at 397.54 eV which is assigned to Si_3N_4 and another peak assigned to B-N at 398.62 eV. B and N in SWCNTs/BNNTs have a significant change after oxidation process which is evidenced by an increase in the peak area B and N with a small shift < 0.2 eV. Oxygen (O 1s) shows two peaks in the survey spectrum of hybrid SWCNTs before and after the oxidation process. Before ozone treatment, two peaks appeared at 531.87 eV and 533.7 eV, which were assigned to C=O and C-O, respectively. However, after ozone treatment it can be seen that there is a shift from 531.87 to 531.65 eV in the first and 533.7 eV to 533.28 eV in the second. There is also an increase of 11% of the intensity of the C-O component, as shown in figure (4-21g & g*). In summary, the XPS data shows that ozone treatment of CNTs results in the formation of oxidised carbon species. Similar, but larger, effects are seen in BNNTs where oxidation of B atoms occurs.

Table 4-5 XPS analysis of bare and hybrid SWCNTs before and after ozone exposure with the description of the peaks, ''ratio'' was determined from the area of each element per the summation of all the peaks under core spectra for each sample, for example the area of C1/(C1+C2+C3+C4+C5) and the same procedure for all the elements under the core spectra

C 1s @ SWCNTs	**before**		**after**				
peaks	Description	BE ev	peaks	Description	BE ev	ratio before	after
C1	sp^2 C-C	284	C1	sp^2 C-C	284	75.87	76.49
C2	sp^3 C-C	284.86	C2	sp^3 C-C	285	13.05	12.18
C3	C-O	285.76	C3	C-O	285.9	5.63	5.87
C4	C=O	286.838	C4	C=O	287.2	2.80	2.90
C5	O-COO	289.68	C5	O-COO	289.5	2.65	2.56
O 1s @ SWCNTs	**before**		**after**				
peaks	Description	BE ev	peaks	Description	BE eV	ratio before	after
O1	=C-O	531.6855	O1	=C-O	531.7	91.35	94.46
O2	C=O	533.625	O2	C=O	533.4	8.65	5.54
C 1s @ SWCNTs/BNNTs	**before**		**after**				
peaks	Description	BE eV	peaks	Description	BE eV	ratio before	after
C1	sp^2 C-C	284	C1	sp^2 C-C	284	15.81	41.24
C2	sp^3 C-C	285.7	C2	sp^3 C-C	285.3	48.63	46.70
C3	C-graphite	284.55	C3	>C-O	287.9	24.12	1.92
C4	C-O	286.889	C4	C-O	286.5	8.49	10.14
C5	C=O	288.13				2.96	
B 1s @ SWCNTs/BNNTs	**before**			**after**			
peaks	Description	BE eV	peaks	Description	BE eV	ratio before	after
B1	B-N	190.27	B1	B-N	189.9	94.76	83.03
B2	B-B	186.9	B2	B-O	190.9	5.24	16.97
O 1s @ SWCNTs/BNNTs	**before**			**after**			
peaks	Description	BE eV	peaks	Description	BE eV	ratio before	after
O1	C=O	531.877	O1	C=O	531.6	21.30	13.08
O2	C-O	533.7134	O2	C-O	533.3	78.70	86.92
N 1s @ SWCNTs/BNNTs	**before**			**after**			
peaks	Description	BE eV	peaks	Description	BE eV	ratio before	after
N1	Si$_3$N$_4$	397.72	N1	Si$_3$N$_4$	397.5	65.92	86.50
N2	B-N	398.45	N2	B-N	398.6	34.08	13.50

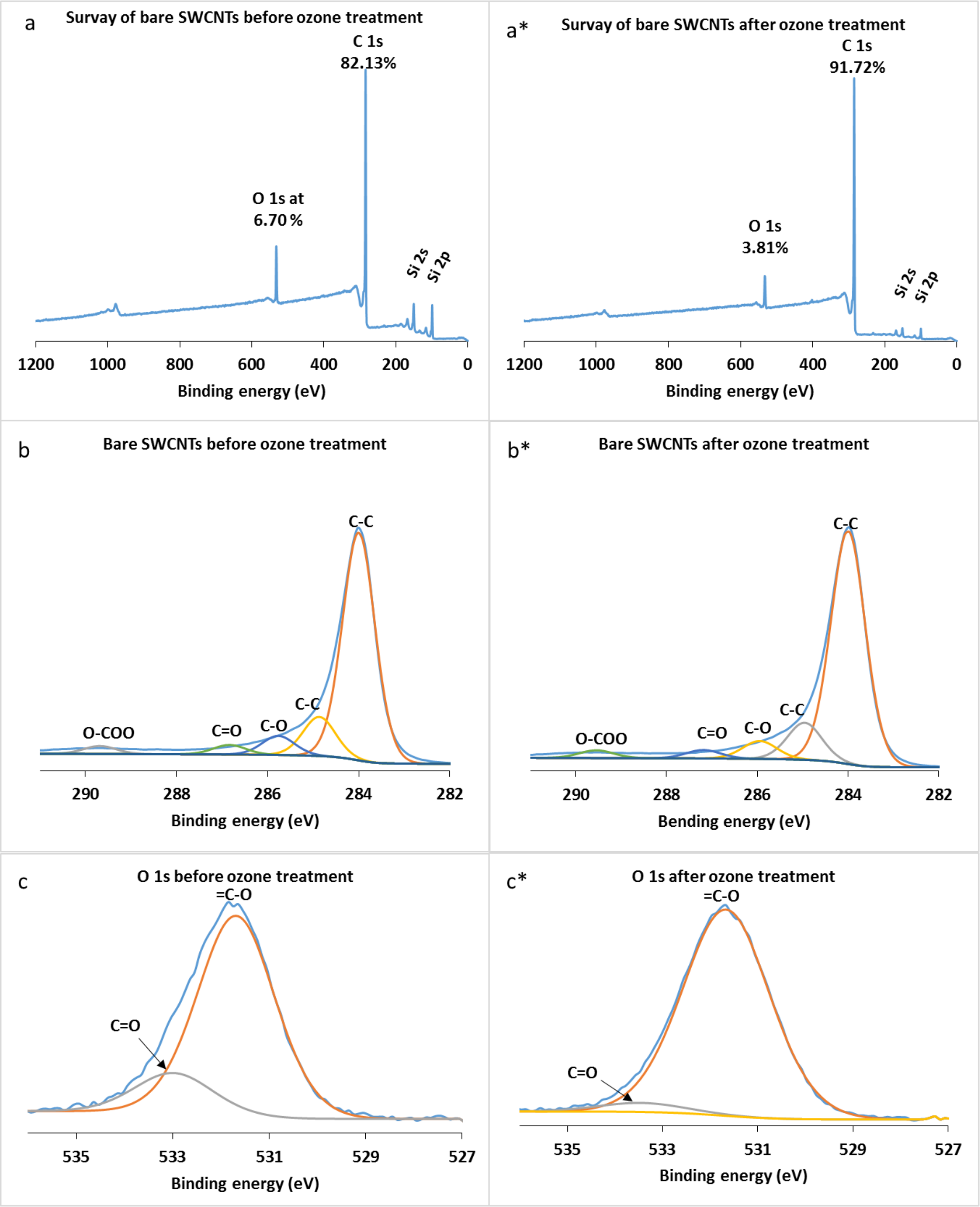

Figure 4-20 XPS spectra of (a&a) the survey spectra of bare SWCNTs before and after gas exposure, (b&b*) high resolution scan of carbon before and after treatment, (c&c*) XPS plots in high resolution scan of oxygen before and after ozone treatment.*

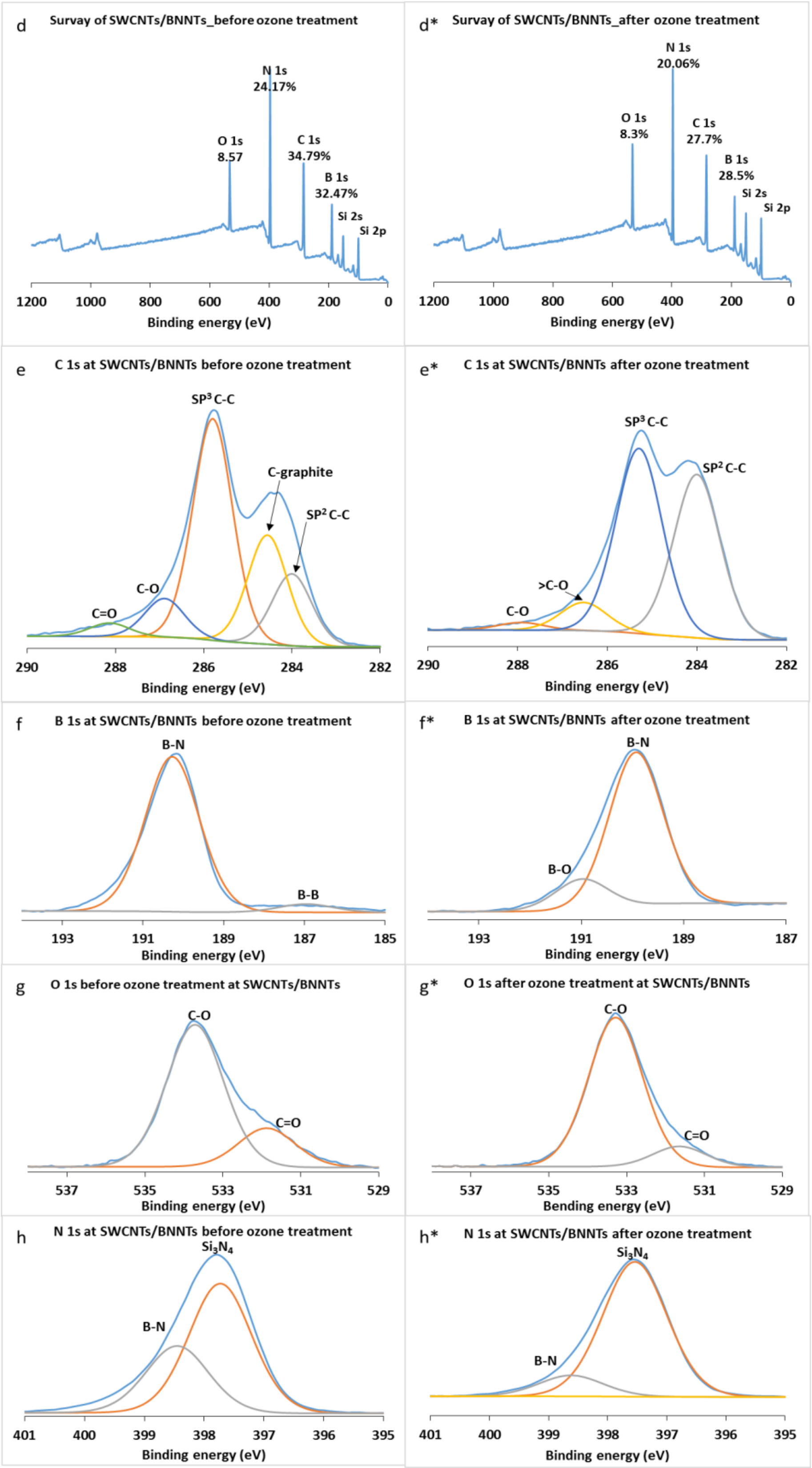

Figure 4-21 XPS spectra of (d&d) the survey of SWCNTs/BNNTs before and after gas exposure, (e&e*) carbon before and after treatment, (f&f*) boron before and after ozone treatment, (g&g*) oxygen before and after oxidation process, (h&h*) nitrogen before and after gas exposure.*

4.7. Conclusions:

Carbon nanotubes show a good sensitivity for ozone molecules at room temperature with a fast response time but a long recovery time ~27 min. Mixing SWCNTs with BNNTs led to an increase the sensitivity of carbon nanotubes but also increased the recovery time. The sensitivity of MWCNTs to ozone was not much affected by mixing with BNNTs. Thermal treatment improved the recovery time with a significant increase in sensitivity of SWCNTs and MWCNTs. The conductivity of carbon nanotubes increased with temperature after BNNTs coating. Our interpretation is that the insulating BN-nanotubes partially separated CNTs and introduced tunnel junctions.

Analysis of the sensing data as a function of temperature according to the Van’t Hoff equation gave an apparent positive enthalpy for the sensing reaction. Along with the effect of temperature on recovery, this strongly suggests that the sensing reaction is a kinetic process and should not be described in terms of simple adsorption of ozone on the nanotubes. Spectroscopic data (especially XPS) confirm the formation of oxygen-containing species in the nanotube films after ozone exposure via the observation of increased amounts of B1s or C1s components at higher binding energy. The effect was most noticeable in BNNTs which appear to be more reactive towards ozone than CNTs. The lack of complete reversibility remains a serious issue for CNT-based ozone sensors and may limit their lifetime and restrict their use in quantitative measurements.

Chapter five: A Carbon monoxide sensor based on carbon nanotubes

The concept of this chapter is to study the sensitivity of carbon nanotubes as a carbon monoxide gas sensor. Carbon monoxide is a toxic gas and indoors is commonly associated with faulty heating systems. Environmentally, vehicle exhaust is the main source of this gas. In general, it forms from incomplete combustion of fuels. Carbon monoxide is a dangerous gas because it has no colour, no odour and can be explosive if its concentration is between 12-74% [80, 90]. Also, CO is one of the main sources of ozone gas near ground level due to a photochemical reaction: $CO+O_2+h\nu \rightarrow O_3+CO_2$ [205].

Since 1991 when carbon nanotubes were discovered by Iijima, they have become an important nanomaterial and candidate for a wide range of applications due to their unique properties for example, high aspect ratio and high surface area[6]. Carbon nanotubes have been used as sensing materials for a wide range of gases NO_2, NH_3, CO_2, CO, O_3 and VOCs [58, 170, 206-208]. Many studies found that CNTs have a weak response to CO gas in pure form. It is usual to decorate the nanotubes by CPs, NPs[90], or to pre-heat the nanotubes[77, 151, 209, 210]. In our study, we used bare and hybrid Ppy/carbon nanotubes as carbon monoxide sensors and studied the effect of temperature on the sensor performance.

5.1. Sensing test.

Figure (5-1) shows the gas sensing system which is included the gas bottle, mass flow controllers (DMFC) and the resistance measurement (DMM) –

more details about the DMM are given in chapter two-. However, a drop of CNTs was deposited on the microband electrode as shown in figure (5-1) and was dried at the room temperature. Dry air was used to purge the surface of CNTs before and after gas exposure and help to dilute the gas concentration. Two strategies were applied in this part; bare CNTs and CNTs/conductive polymer composite gas sensors and both types of device were examined at different temperature as shown in table (5-1).

Table 5-1 Shows the sensing system conditions of CNTs as CO gas sensor.

Films	Temperature in K	CO concentration in ppm
SWCNTs	293, 313, 333	1923, 1960, 1974, 1980
MWCNTs	293, 313, 333	1923, 1960, 1974, 1980
SW/Ppy	293, 313, 333	1923, 1960, 1974, 1980
MW/Ppy	293, 313, 333	1923, 1960, 1974, 1980

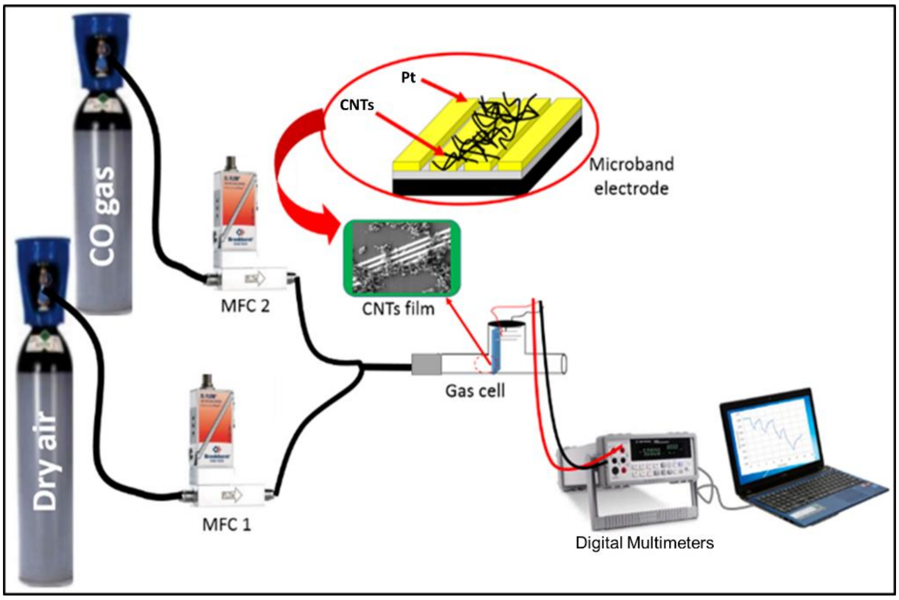

Figure 5-1 Shows the diagram of measuring the sensing system

5.2. Carbon monoxide sensor based on carbon nanotubes

The evaluation of CNTs a gas sensor depended on observation of the change in the electric resistance of CNTs films in a two-terminal device. From the first sensing test, bare SWCNTs and MWCNTs showed a low sensitivity for CO gas and this matched previous studies in this field[80]. Many researchers reported that pristine carbon nanotubes have a weak response for CO gas if there is no catalysis of electron exchange between the gas and the surface of bare nanotubes[80]. According to the first sensing experiments a low sensitivity of bare CNTs for CO gas, was seen as shown in figure (5-2).

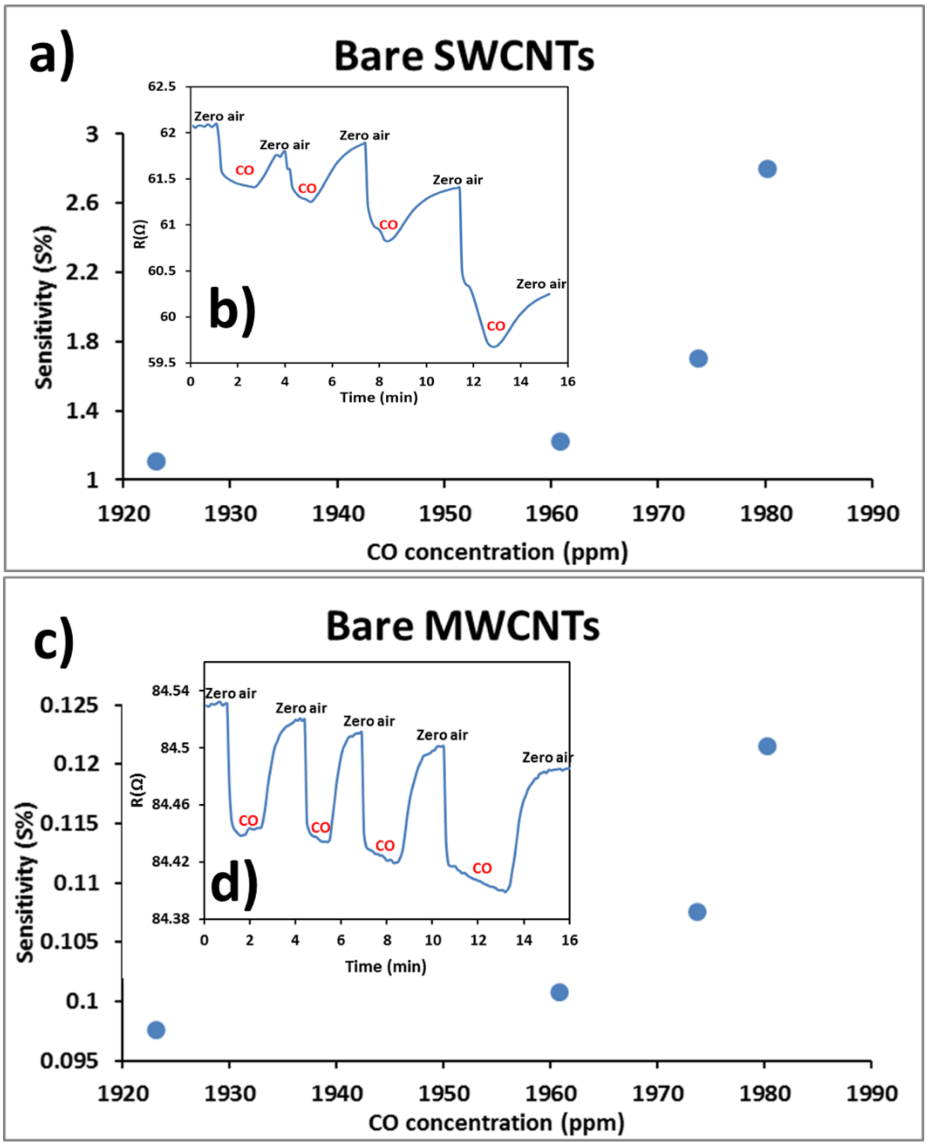

Figure 5-2 (a&c) the response size of bare CNT for of CO gas, (b&d) the change in the resistance of the films with different concentrations of carbon monoxide gas at 293K.

It is clear that the film resistance decreased during gas exposure and partially recovered in zero air. Afrin et.al reported at room temperature the reduction in the electrical resistance and assigned it to the electrons that are donated from gas molecules to the nanotubes [211]. However the mechanism remains unclear because , as noted in the last chapter, injection of holes by ozone is also suggested to reduce CNT film resistance. In general, the film sensitivity S was measured by relative resistance resistance $S = \frac{R_S - R_O}{R_O} \times 100\%$ where Rs is the film resistance during gas presence, Ro the film resistance under air exposure only. A poor change in the film sensitivity has been shown from Nyquist plot special for MWCNTs S_{mw}~0.12% <S_{sw}~2.8% at 1980 ppm, but with a fast response time as shown fig (5-2 b&d) ~ 30 s. Single wall carbon nanotubes are more sensitive to the CO gas than multi-walled carbon nanotubes; this can be ascribed to the structure of SWCNTs. Previous studies have found that SWCNTs have a higher adsorption capacity than MWCNTs because of their smaller diameter than MWCNTs[212].In addition the adsorption can affect the entire SWCNT while, for MWCNT, most occurs on the first layer, therefore MWNTs are expected to be less sensitive than SWNTs because many layers are not exposed to CO, as shown in figure (5-3). In some application researchers prefer to use reactions in the edge of the nanotubes to be more active[213]. From a comparison of the response and recovery time, SWCNTs have a longer response time than MWCNTs, as shown in figure (5-4).

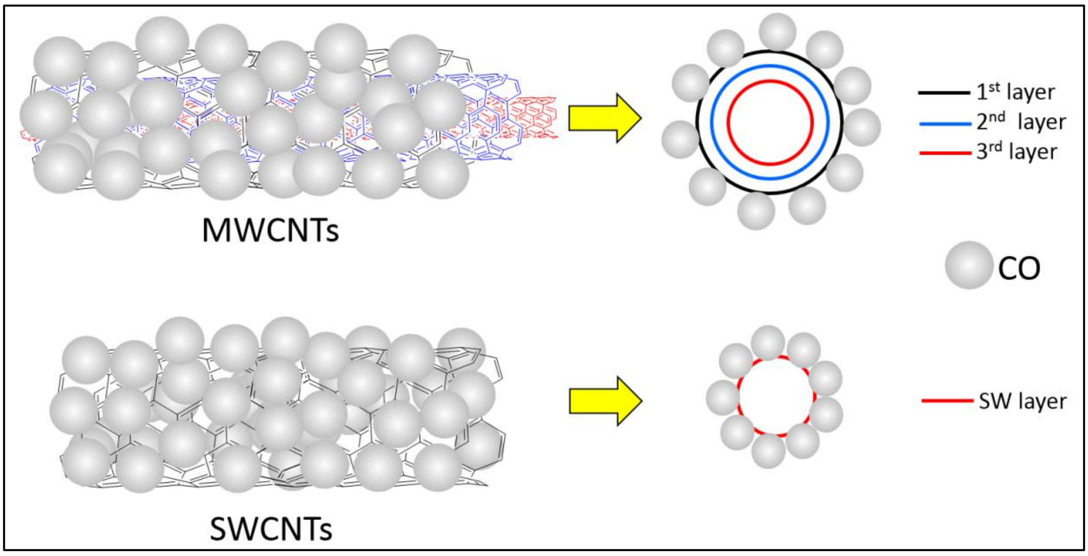

Figure 5-3 A schematic diagram illustrating how the adsorption can occur on the surface of CNTs

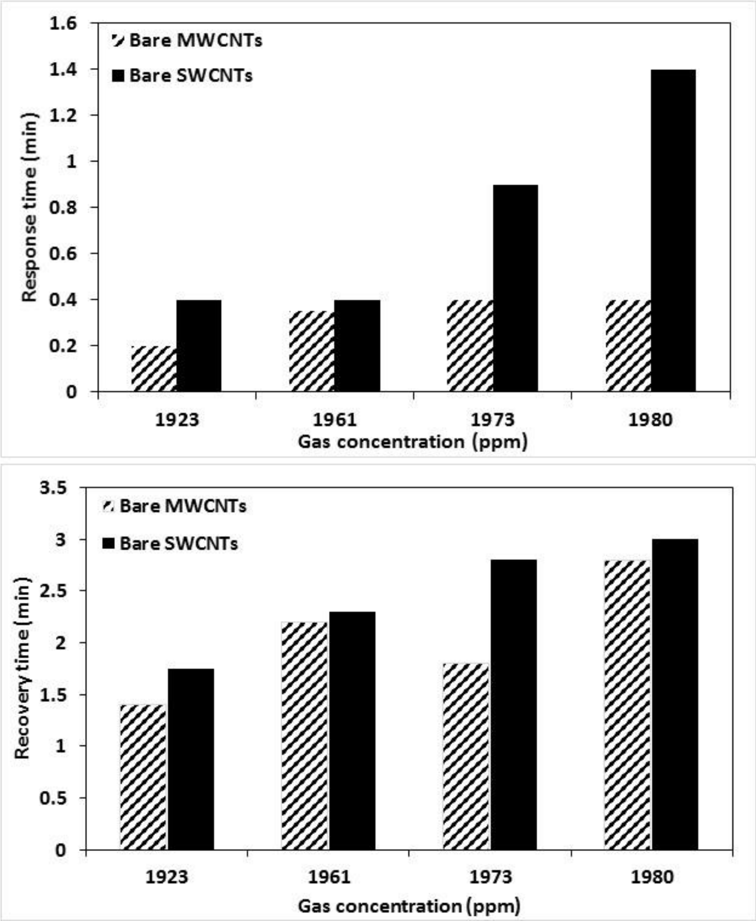

Figure 5-4 The response time of Bare SWCNTs and bare MWCNTs as CO gas sensor at room temperature at different concentration of the gas target.

Impedance spectroscopy (IS) was used to study the effect of CO gas on the electrical properties of CNTs; bare CNTs have only the real part ($R=1/Z_{re}$) where Z_{re} is the bulk film resistance. Carbon monoxide did not have a large effect on the electrical properties of bare nanotubes and as shown in the Nyquist plot of figure (5-5) for SWCNTs and MWCNTs. The resistance of bare MWCNTs decreased ~1.14% during the gas exposure and increased ~0.08% after gas off, while for SWCNTs it was reduced about ~9.5 % during presence the gas and increased to ~6.4% when the gas was off. On the other hand, the resistance level did not return to the baseline level after gas off, which suggests not all CO molecules were released from the nanotubes surface. Return to the baseline level will be very difficult to access as in MWCNTs (less sensitive) and can be more notable for SWCNTs (more sensitive).

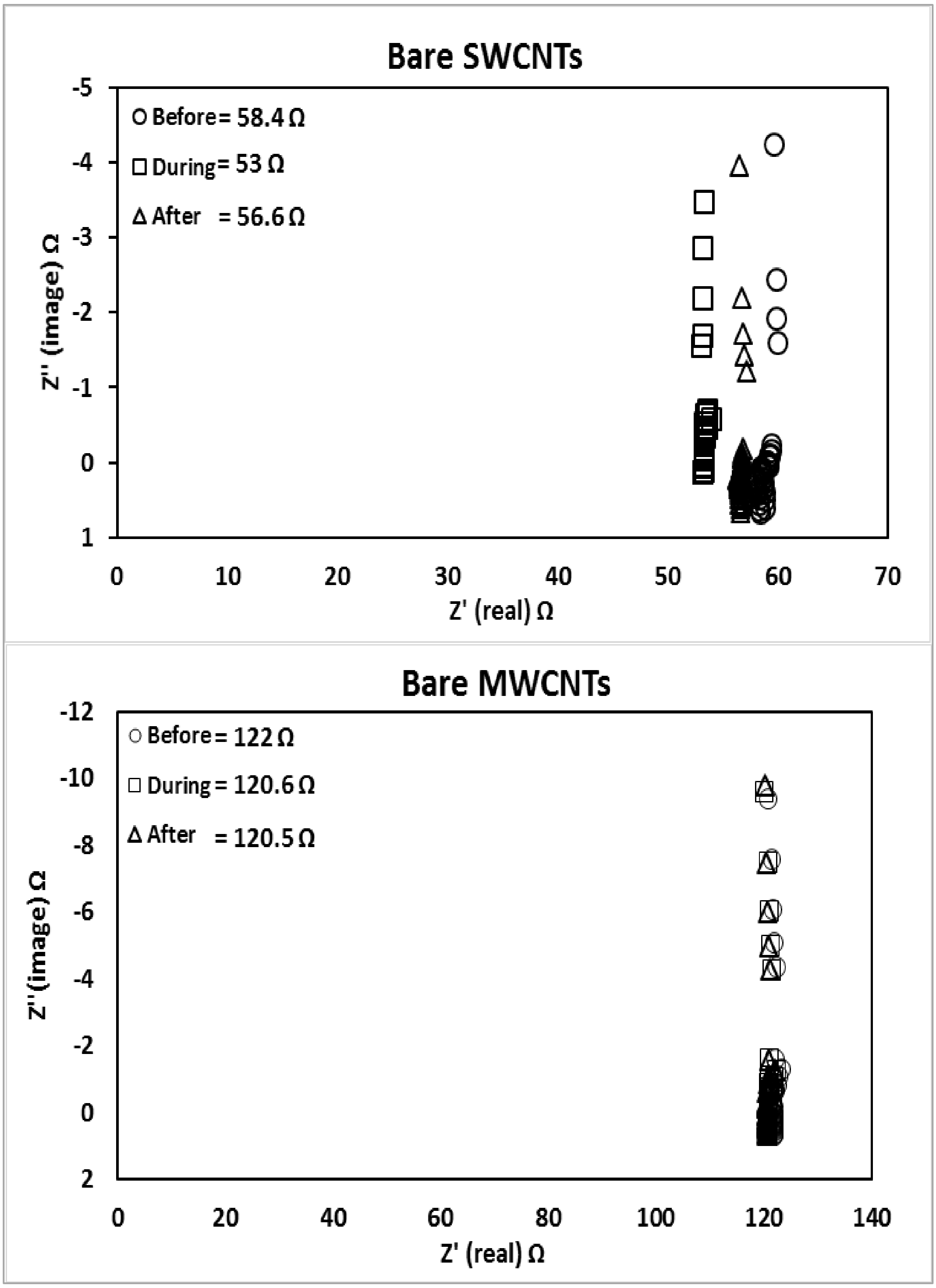

Figure 5-5 Shows the Nyquist plot of bare SWCNTs and bare MWCNTs before, during and after gas exposure at 293K. The ohmic contact is the main behaviour in this electrical circle.

In 2008 Star and Kauffman reported that the carbon monoxide doesn't participate in charge transfer to the pristine carbon nanotubes[80] and Bockrath and Matrange suggested CO can adsorb by hydrogen-bonds with hydroxyl groups on the CNT[214]. Although, carbon monoxide is not involved in charge transfer to the bare nanotubes, the gas displays other sensing mechanisms. Varghese et.al[145] found that defects can be introduced to the nanotubes during the exposure to the gas. Otherwise to enhance and develop the sensitivity of carbon nanotubes as a CO gas sensor, it has been found that decorating these tubes by metal oxide, conductive/unconducive polymers helps to increase the response of the carbon nanotubes[58]. Conductive polymers couple easily with CNTs and are promising films in the application. Preparation of these samples was explained before in chapter two. Figure (5-6 a, b&c) shows the significant change in the sensitivity after coating the nanotubes, for instance SWCNTs/Ppy recorded dramatically increased responses compared to bare SWCNTs. In contrast, a small increase in the response size of MWCNTs after coating was seen. On the other hand, although increase in the sensitivity was noted, the response time for hybrid nanotubes became longer than for pristine CNTs. This suggests the gas molecules take time to interact with plypyrrole/CNTs or perhaps they must diffuse into the polymer. An increase in the recovery time over pristine CNTs can occur because gas molecules need more time to desorb from sites specially new sites which were added after coating by polypyrrole, as shown in figure (5-6 g,h&i). The resistance decreases during gas presence and increases when the gas is switched off, but the film resistance does not always return to the baseline level prior to exposure to CO. This suggests some molecules are not released completely from the surface of the nanocomposite films, as demonstrated in figure (5-7). In addition, the resistance chart of MWCNTs/Ppy looks smoother than SWCNTs/Ppy.

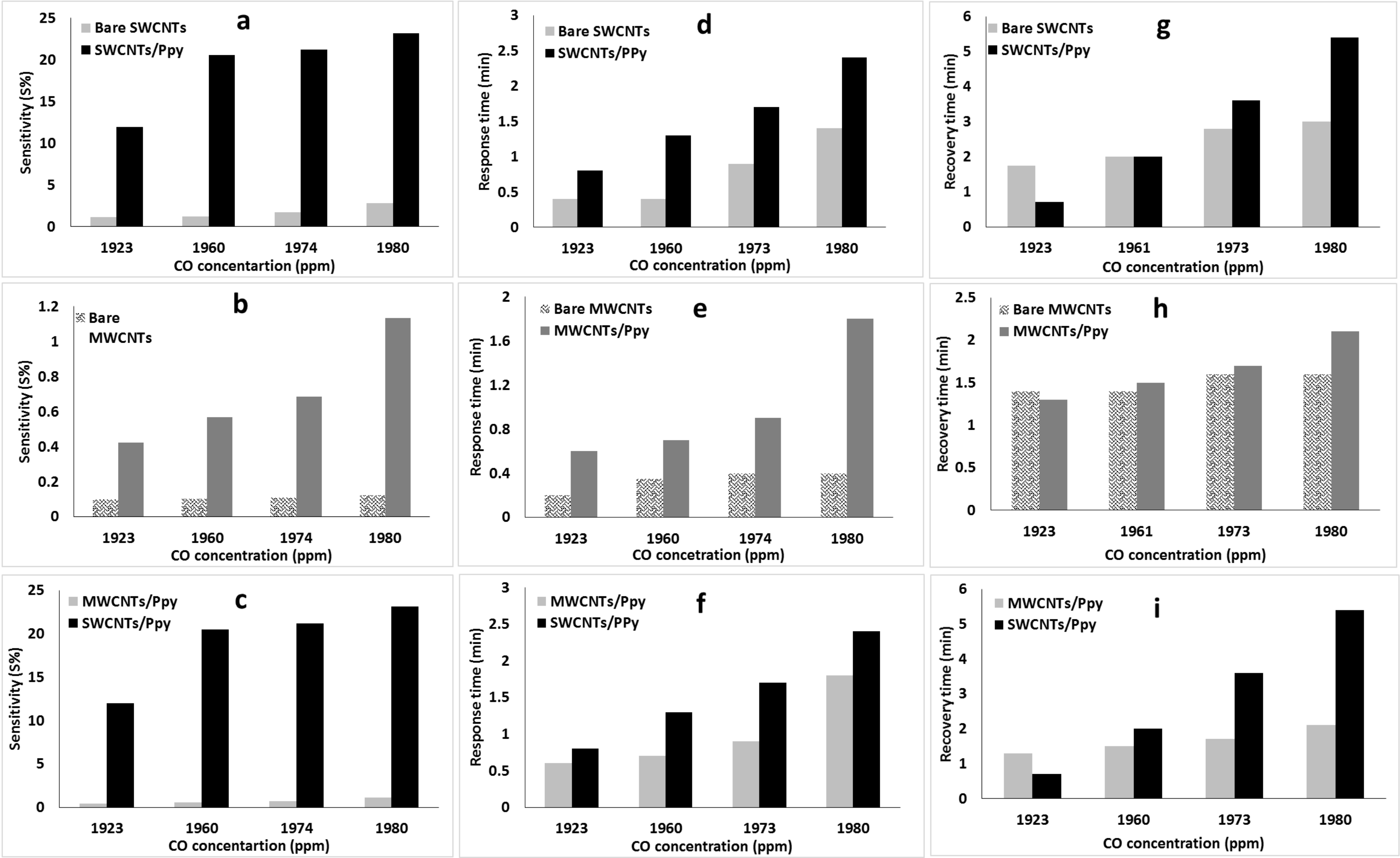

Figure 5-6 (a,b &c) the sensitivity of CNTs and CNTs/Ppy at different concentration of the gas target, (d,e&f) the change in the response time for the films during gas exposure, (g,h&i) the recovery time of the CNTs films after gas off.

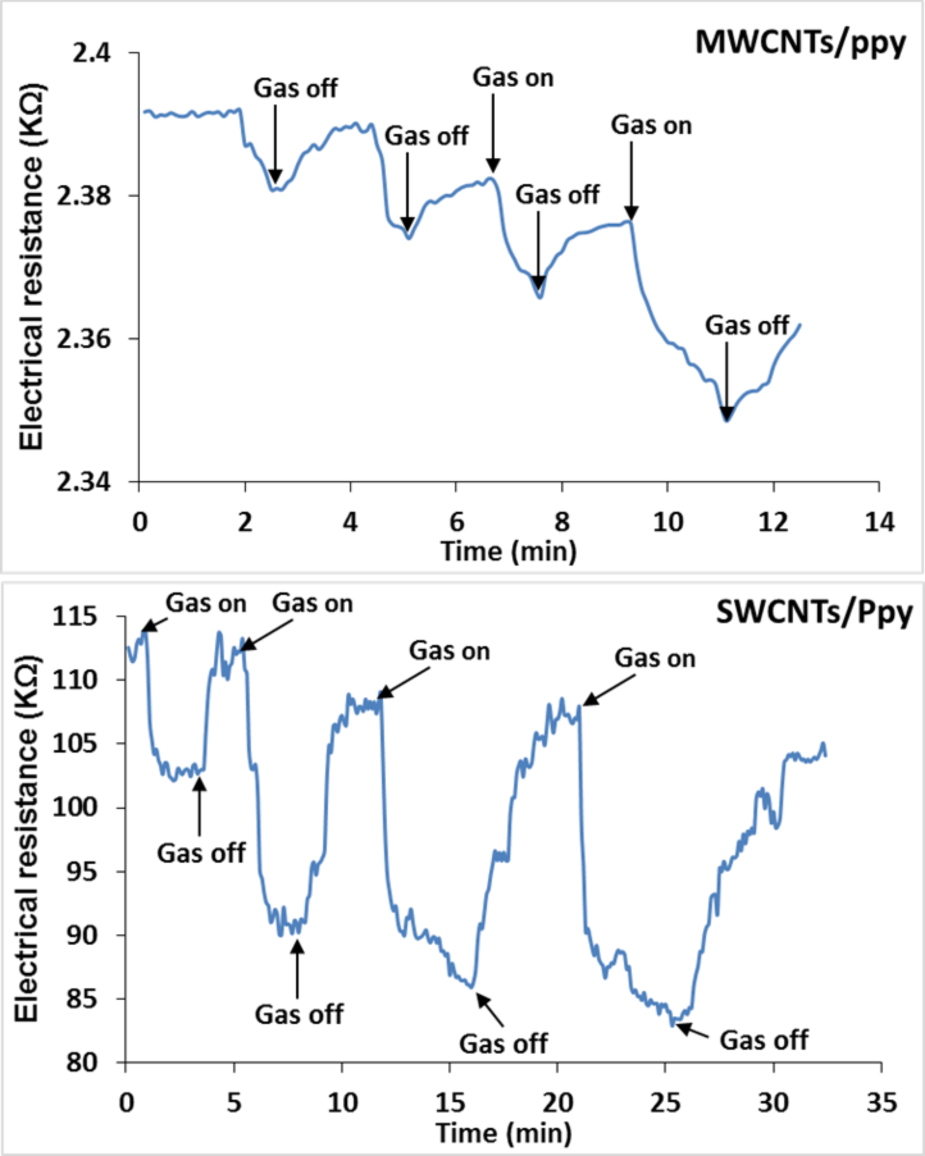

Figure 5-7 Shows the change in the film resistance of MWCNTs/Ppy and SWCNTs/Ppy at 293K with different concentrations of CO gas. The resistance change is partially reversible, but there is some drift in the baseline after gas exposure.

The IS technique demonstrates the change in the resistance of SWCNTs/Ppy and MWCNTs/Ppy before and after gas exposure as shown in figure (5-8). As explained in chapter three polypyrrole coating of the CNTs causes a change in the electrical properties of CNTs and the nanocomposite film (CNTs/Ppy) which now is represented by an equivalent circuit that includes capacitive elements related to the electrode contacts.

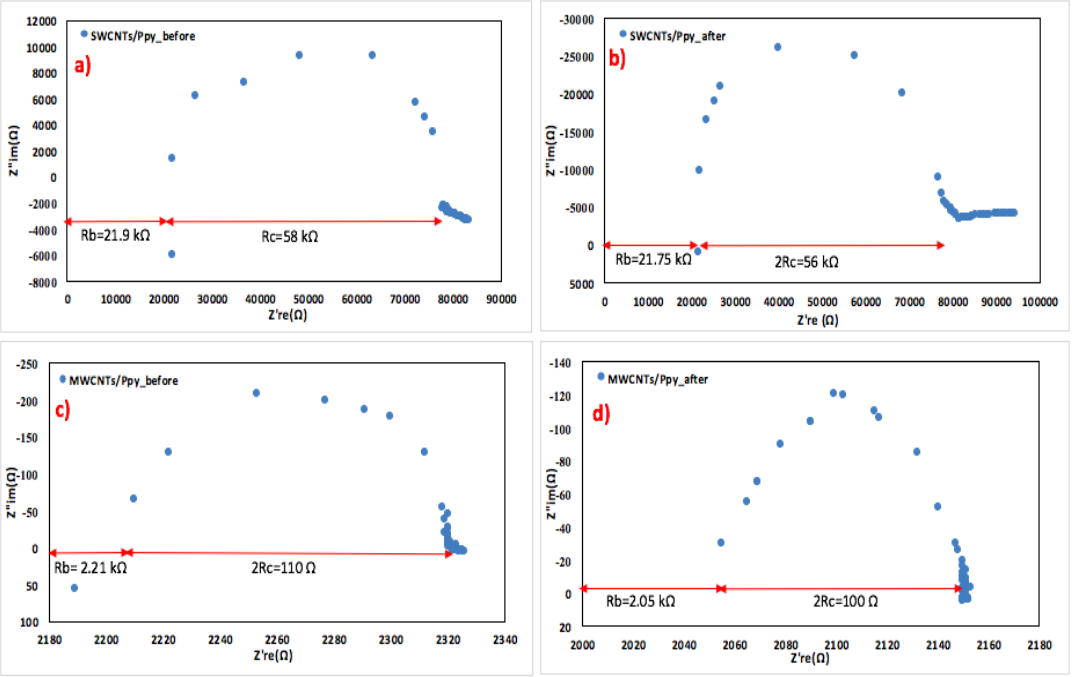

Figure 5-8 Shows the Nyquist plot of (a&c) SWCNTs/Ppy and MWCNTs before gas exposure,(b&d) the change in Z''im and Z're after CO treatment at 293K.

From the Nyquist plots, it is easy to see that the film resistance R_b decreased a little after the gas treatment and table (5-2) displays the change in the R_b and R_c for the hybrid films before and after gas treatment, where R_b is the film resistance (between electrodes) and R_c is a contact resistance.

Table 5-2 The change in the film resistance of SWCNTs/Ppy and MWCNTs/Ppy before and after carbon monoxide treatment.

Thin Films	Rb (kΩ)	2Rc (kΩ)	Rc (kΩ)
SWCNTs/Ppy (Before)	21.9	58.1	29.05
SWCNTs/Ppy (after)	↓21.75	↓56	↓28
MWCNTs/Ppy (Before)	2.21	0.11	0.055
MWCNTs/Ppy (after)	↓2.05	↓0.1	↓0.05

5.2.1. The effect of temperature on the performance of the gas sensor.

In this part of the study 1923 ppm was used as the test CO concentration and 293K, 313K and 333K were used as the working temperatures. The heating affects negatively the sensitivity of bare and hybrid nanotubes and the decrease in sensitivity with temperature can be described by the Van't Hoff equation as an adsorption equilibrium. Table (5-2) shows the effect of temperature on the sensitivity of pristine and the nanocomposite films.

Table 5-3 Shows the effect of temperature on the sensitivity of bare and hybrid nanotubes.

Thin Films	*ppm*	*S% @293K*	*S% @313K*	*S% @333K*
MWCNTs	1932	0.96	0.135	0.097
MWCNTs/Ppy	1932	3.214	2.51	1.2
SWCNTs	1932	1.23	0.93	0.86
SWCNTs/Ppy	1932	13.5	2.69	1.8

Figure (5-9) the relation between lnS and the temperature for different gas concentrations and figure (5-9c) shows the ΔH^{Θ} values of these thin films.

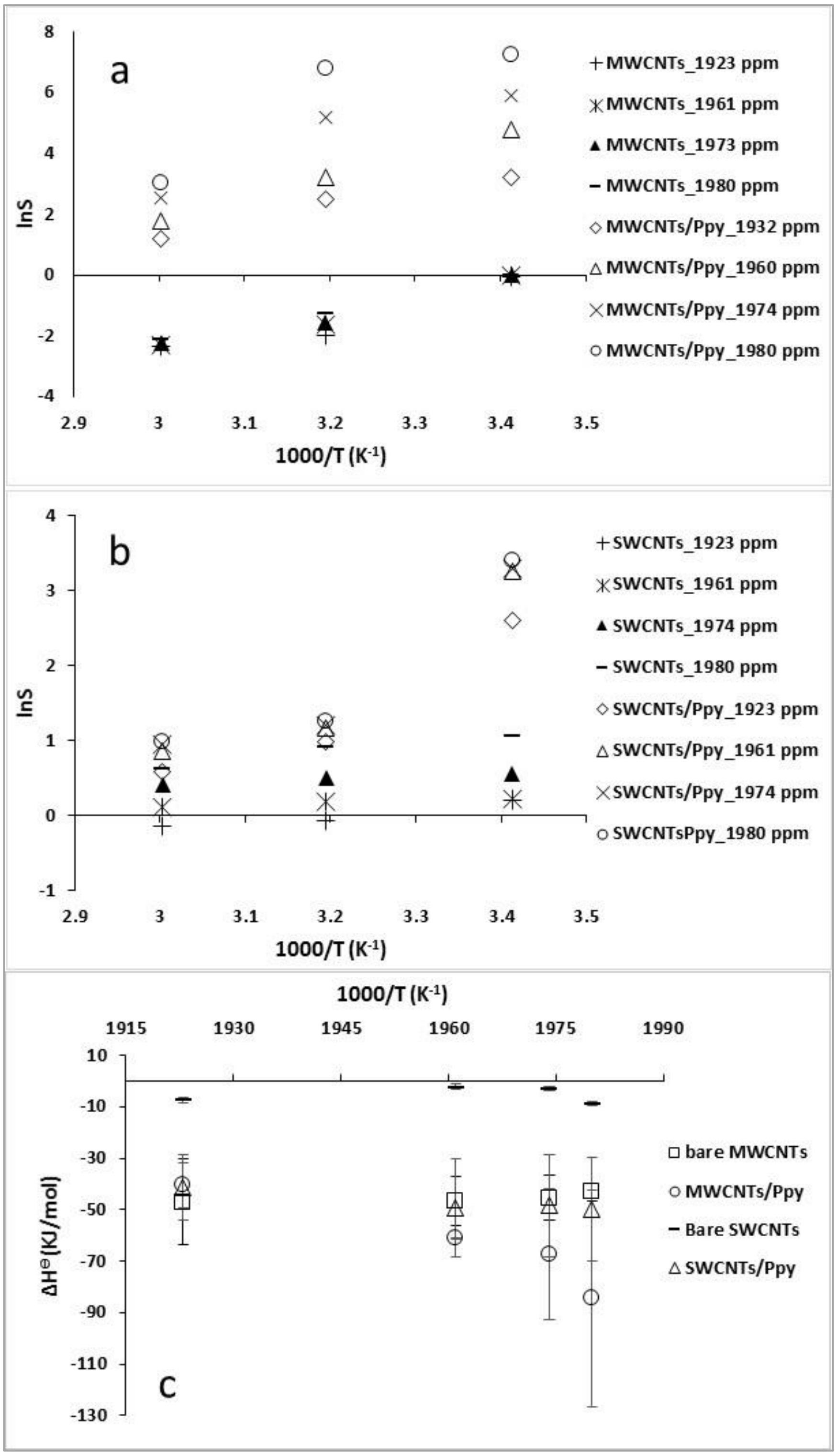

Figure 5-9 (a&b) show the relation between lnS and temperatures for the different concentrations of CO for bare and hybrid CNTs, c) Shows the change in enthalpy of the system, the sensitivity of the films decreased with increase the temperature.

5.2.2. The effect of the gas flow and the gas concentration on the response size of CNTs and hybrid CNTs.

Two experiments were performed to study the effect of gas concentration and the gas flow on the response size of CNTs and CNTs/Ppy. In the first part the gas flow was constant and the second part is related with fixing the concentration of the gas along the sensing process. ***In the first experiment*** the amount of the gas flow was fixed at 100 mL min^{-1} in total as shown in table (5-4) and it led to an increase in the sensitivity with increasing the gas concentration gradually for each bare and hybrid nanotubes. In contract with the first experiment, the ***second experiment*** depended on passing the same concentration of the gas during the sensing process, but at different flow rates. No change in the sensitivity of the devices was observed as shown in table (5-5). Figure (5-10) shows the observation of the change in resistance of CNTs' films in the two experiment for bare and hybrid CNTs and how the gas concentration has affected the response of the nanotubes.

Table 5-4 Shows the significant change in the response size of the films at the different concentration of the mixture (CO:zero air) at 293K.

CO mL/min	Dry air mL/min	Flow total mL/min	Conce. ppm	Sensitivity S%			
				SW	MW	MW/Ppy	SW/Ppy
20	80	100	400	0.2	0.006	11.2	40
30	70	100	600	0.31	0.009	15.3	45
40	60	100	800	0.4	0.02	16.5	51
50	50	100	1000	0.48	0.04	23	49
60	40	100	1200	0.54	0.06	28	57
70	30	100	1400	0.6	0.062	33.2	59
80	20	100	1600	0.67	0.064	40	75
90	10	100	1800	0.75	0.07	47	114
100	0	100	2000	1	0.08	53	117

Table 5-5 Shows the constant change in the response size of the sensor at the same concentration of the mixture (CO: zero air) at 293K.

CO mL/min	Dry air ml/min	Flow total mL/min	Conce. ppm	Sensitivity S%			
				SW	MW	MW/Ppy	SW/Ppy
20	20	40	1000	0.52	0.035	10	111
30	30	60	1000	0.52	0.035	9.7	112
40	40	80	1000	0.52	0.035	10	111
50	50	100	1000	0.52	0.036	9.7	112
60	60	120	1000	0.53	0.036	9.7	112
70	70	140	1000	0.53	0.036	10	111
80	80	160	1000	0.53	0.035	10	112
90	90	180	1000	0.53	0.035	10	112
100	100	200	1000	0.53	0.035	10	112

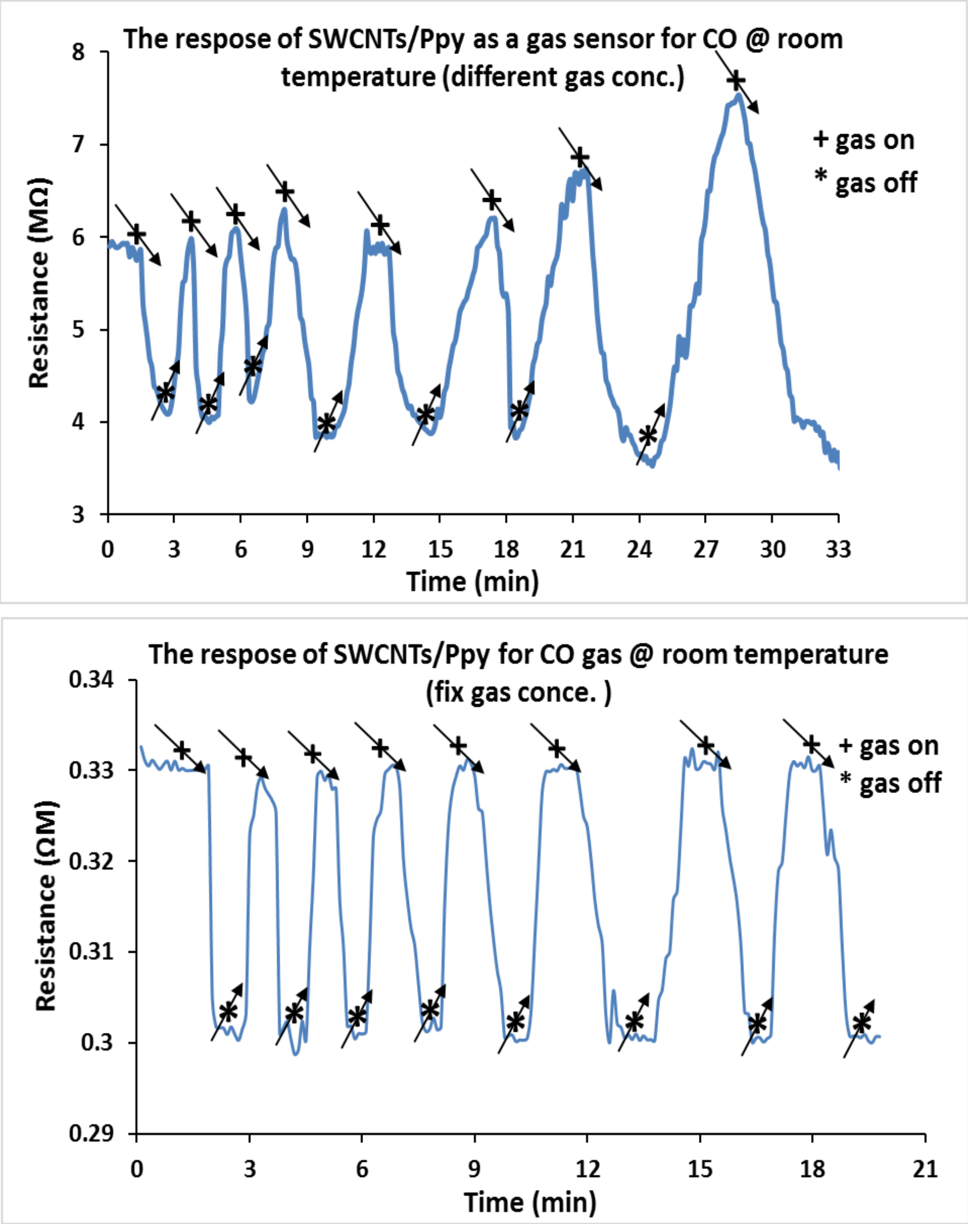

Figure 5-10 a) The change in the resistance of SWCNTs/Ppy at different concentrations of the mixture (CO:zero air) at 293K and as shown in table (5-4), b) No change in the resistance of SWCNTs/Ppy at fix concentration of (CO:zero air) at 293K and as shown in table (5-5).

Furthermore, from the observation of electrical resistance of the nanotubes in the sensing system it was noted that CNTs have a weak response size while the film’s resistance increased to the MΩ-level after treatment by the conductive polymer –polypyrrole- with a high response size because after polymerization process polypyrrole adds new active sites to CNTs[215]. The gas sensing mechanism of the nanocomposite films (CNTs/polypyrrole) relies on the interaction with gas molecules changing the electrical properties of CPs. The *charge transfer* from gas molecules and the *swelling* of the conductive polymer are the main mechanisms proposed when CPs are used in gas sensing[5]. At ambient temperature, however, the charge transfer mechanism seems unlikely for CO/polypyrrole. Typically, CNTs are sensitive to the gaseous environment when electron/hole transfer between the gas and the CNTs may occur. The case of ozone in the previous chapter is an example. However, CNTs show rather weak responses (low sensitivity) to gases which are not strongly oxidising/reducing, such as CO at ambient temperature. Instead, the interface between the conductive polymer and the carbon nanotubes has a major effect on the sensing process. Adsorption of CO by the polymer causes conformational changes and swelling of the polymer. This in turn affects the charge transport through the film as the electrons/holes hop from one nanotube to the next.

5.3. Conclusions

Although they have a fast response and short recovery time, carbon nanotubes have a weak response to carbon monoxide gas S%< 0.1. The sensitivity of the nanotubes increased after coating by polypyrrole via the chemical polymerization in situ) with a fast and a short recovery time. Thermal treatment led to a decrease in the sensitivity of the bare and hybrid nanotubes consistent with a mechanism based on adsorption of the gas which can be described as an exothermic reaction at 313K and 333K. The observation of increased sensitivity of CNTs/Ppy to CO compared to CNTs alone is another example of the phenomenon in which the decrease in conductivity of the film produced by incorporation of conductive polymer is actually beneficial to the performance of the film in gas sensor applications.

Chapter Six: DNA/CNTs gas sensors

CNTs are promising materials in sensing applications due to their physical properties [216] [217]. The surface of CNTs are sensitive to gases and VOCs and the sensitivity increases after decoration by NPs, CPs, RNA and DNA or thermal treatment [133, 217-219]. Although, CNTs have unique and good physical properties, they have a weak response to VOCs [218]. As observed in previous chapters materials that reduce the conductance of films of CNTs tend to increase their sensitivity to VOCs. DNA is known to adhere strongly to CNTs[220]. Therefore, a combination of CNTs with DNA suggests itself as an alternative method to enhance the sensitivity of these nanotubes.

The simple description of DNA is a polymer, which is made of monomer units named nucleotides[67, 220]. The structure of DNA contains phosphate, deoxyribose sugars and one of the nitrogenous bases which can be guanine G, thymine T, adenine A or cytosine C. Double stranded DNA (dsDNA) includes two chains of polynucleotide which nitrogenous bases are linked by hydrogen bond[221]. According to this arrangement, each strand reflects the other as an antiparallel direction or orientation of the sugar phosphate backbones. In 1952, R. Franklin was the first scientist who saw saw clear X-ray diffraction patterns of DNA [222, 223], as shown in figure (6-1).

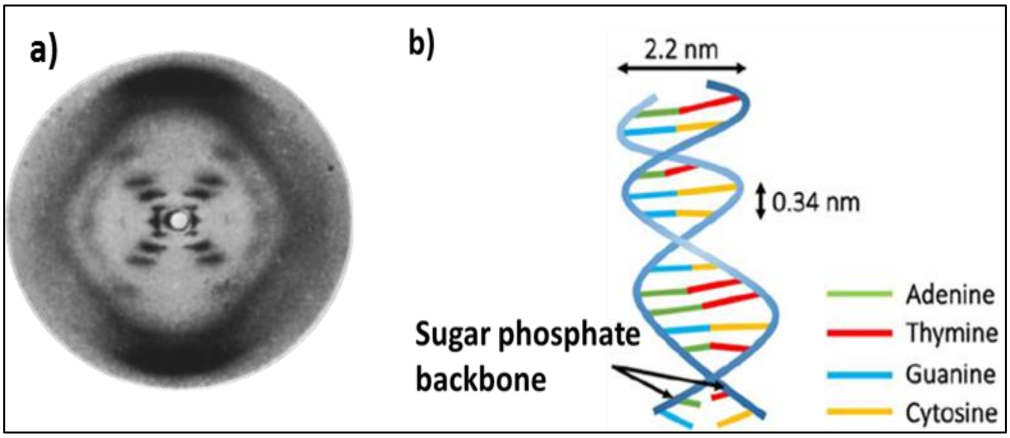

Figure 6-1 a) The first X-Ray diffraction image of DNA by R. Franklin in 1952,by this image it was able to measure the molecules distance inside the helix structure and by this image it was able to measure the molecules distance inside the helix structure1, b) schemed of dsDNA structure[224].

In 2003, Zheng et.al. presented the first combination between CNTs and ssDNA to disperse the nanotubes [220] and in 2004 Nakashima et.al. used dsDNA to coat SWCNTs [225]. Some studies have shown that the sensitivity of CNTs increases when these NTs are better dispersed in order to increase the active area and give more space on the surface to increase the adsorption of gas molecules. For example, polymers such as polyaniline have been used to disperse CNTs to increase the sensitivity of CNTs to CO gas and DNA was used to disperse CNTs and increase their sensitivity to limonene enantiomers and dimethyl sulfone [220, 225-227].

In sensing applications dispersed nanotubes are more active than tangled nanotubes and coating nanotubes by DNA, hydrophilic proteins, SDS-sodium dodecyl sulphate, or peptides [71] have been tried. Some technical applications depend on the polymer/DNA combination to purify CNTs which is affected by the nanotubes chirality. Chirality is important because the physical properties (electrical and optical) of the CNTs depend on the chiral vector $Ch = na1 + ma2$ where n and m are integers and a_1 and a_2 are unit vectors of the graphene surface [2, 71]. The coupling between dsDNA and CNTs was also used to regulate the assembly of particles [228, 229].

6.1. Preparation of the DNA@MWCNTs films

MWCNTs Elicarb^{TM} were purchased from Thomas Swan, UK with diameter (2-10) nm. Lambda DNA (λ-DNA) was supplied from England New Bio labs Ltd. While methanol was purchased from Fisher Scientific Ltd., UK. The solution of CNTs was prepared after sonicating 0.0001g MWCNTs in 10 mL of MeOH in 3h by using micro tip ultrasonic (750 W, 20 kHz, amplitude 20%, 230 Volt, ultrasonic processor) to reduce the agglomerate of the tubes. Figure (6-2) shows the preparation stages of DNA@MWCNTs.

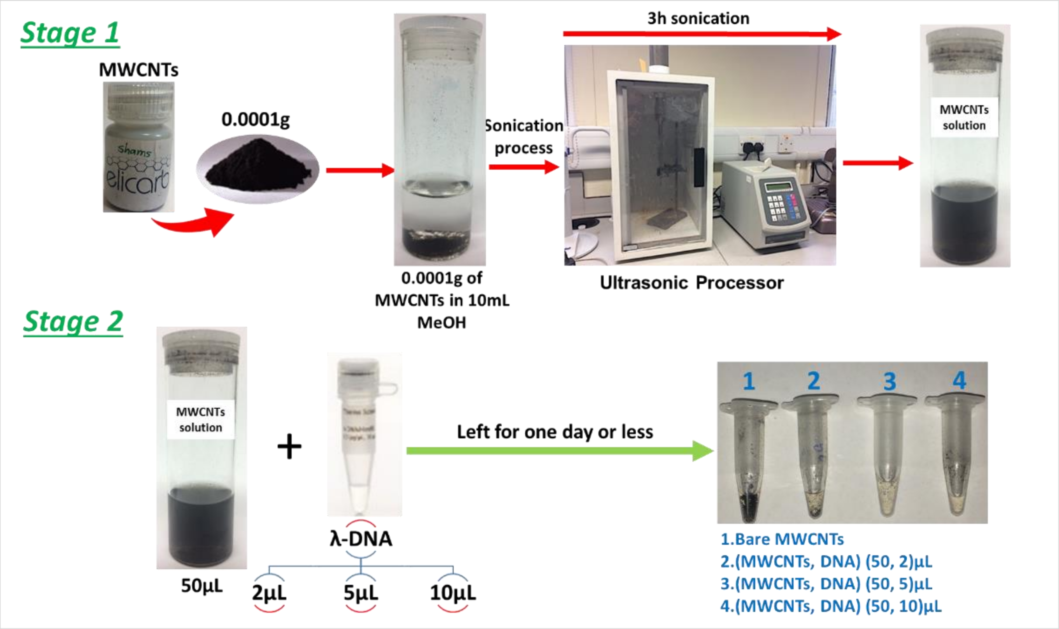

Figure 6-2 Schematic of preparation DNA@MWCNTs. In stage (1) MWCNTs as a solution was prepared and in the stage (2) DNA was added to the bare CNTs in three different ratio.

In this study, three samples were prepared in three different ratio of CNTs:DNA by adding 2µL, 5µL and 10µL respectively to 50µL of MWCNTs solution as shown in table (6-1).

Table 6-1 Shows the amount of bare MWCNTs and DNA in this part of the study.

MWCNTs in µL (100 µg mL^{-1})	DNA in µL (500 µg mL^{-1})	Ratio of the mixture (CNTs: DNA)
50	2	10:0.4
	5	10:1
	10	5:1

Many techniques were used to examine the properties of DNA@CNTs, for example, AFM, I-V characterisations, UV-Visible spectroscopy, FTIR and Raman spectroscopy.

6.1.1. Atomic Force Microscopy AFM

Tapping mode was used to investigate the structural properties of DNA@CNTs. The films were drop cast from solution (3µL) onto Si chips and were dried at room temperature. Silicon wafers (dopant boron and <111> oriented p-type, resistivity 0.09-0.12 Ohm.cm) of diameter 100±0.3 mm were purchased from Pi-KEM Ltd. Figure (6-3Aa) shows bare MWCNTs with long tubes and some tangled nanotubes. Figure (6-3Ab-d) shows the hybrid nanotubes with different DNA:CNT ratio. At a CNTs:DNA ratio (10:0.4) figure (6-3Ab) shows less DNA adhered to the CNTs. Figure (6-3Ac) of (CNTs:DNA) ratio (10:1) shows more separation in the nanotubes with short lengths and it appears DNA coated NTs as particles or can be described as agglomerations on the CNTs . For the 10:1 ratio, the nanotubes appeared more tangled and agglomerated than 10:0.4 and 5:1 as shown in figure (6-3d). Figure (6-3 Ab-d) show the agglomerates of DNA, the number of which increase with increases in the ratio of CNTs:DNA. Figure (6-3A b) also shows a thin, unstructured layer which we tentatively ascribe to the organic solvent that was used to prepare DNA@CNTs. Additional AFM images are provided in the appendix as figures S8 & S9.

Histograms of DNA, CNT and DNA/CNT diameters are shown in the appendix S10. The histograms show a substantial increase in the apparent diameter of the CNTs after interaction with DNA, which supports the schematic interpretation of figure 6-3B. There is a wide spread of diameters (up to 75 nm) and this suggests there is also some bundling of multiple tubes in the presence of DNA.

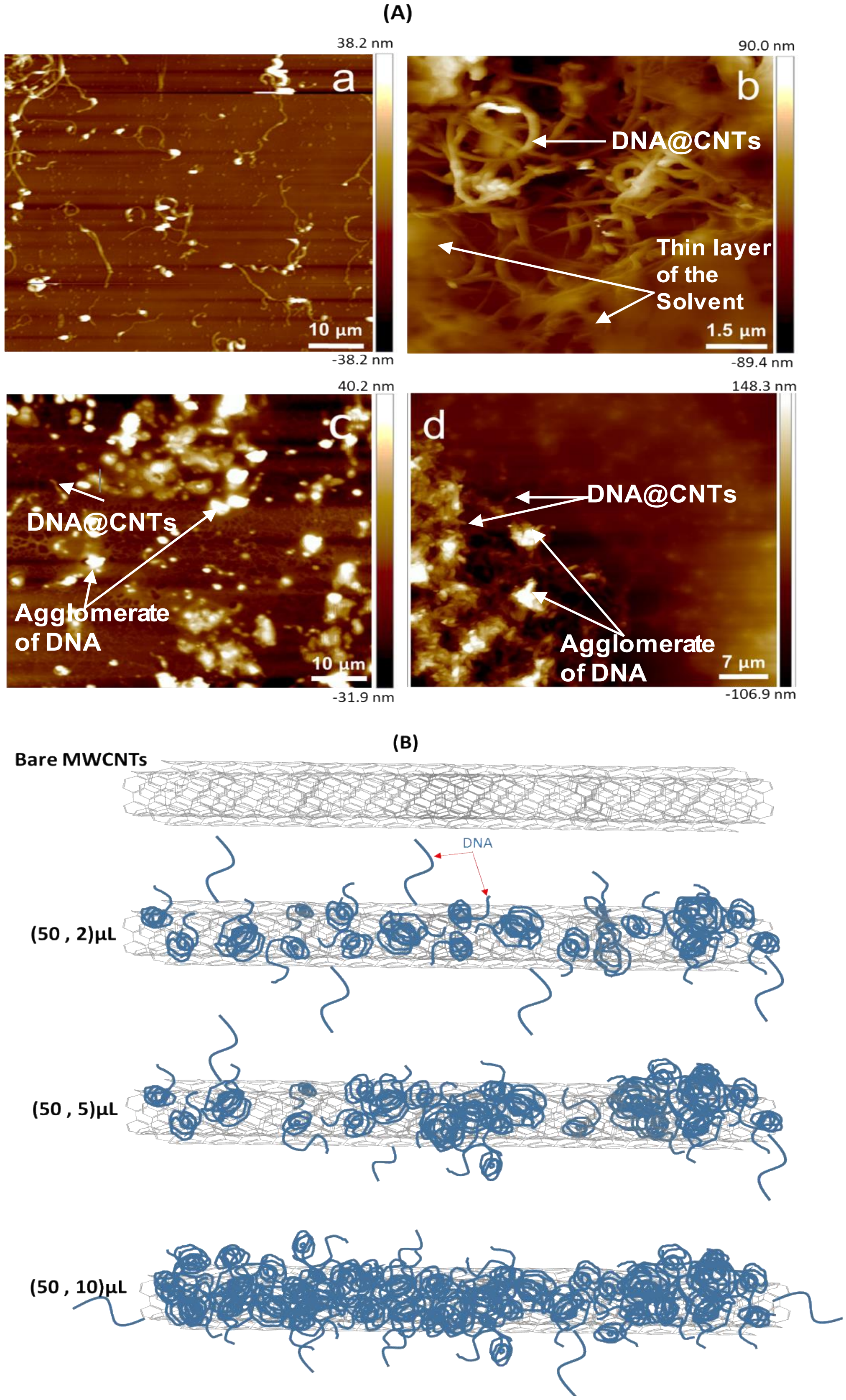

Figure 6-3 (A) AFM images of a) bare MWCNTs, b) CNTs:DNA ratio (50,2)µL, c) CNTs:DNA ratio (50,5)µL and d) CNTs:DNA (50,10)µL. (B) Schematic diagram of DNA sticking as agglomerations on the sidewalls of MWCNTs for different ratios of MWCNTs to DNA

6.1.2. I-V characterizations (current-voltage measurements)

According to the AFM images above, which show that the CNTs are coated with DNA, DNA is expected to impact the electrical properties of films of DNA@CNTs. About 3 µL of CNTs:DNA in water was deposited on interdigitated Pt microelectrodes with a 5 µm gap. The samples were dried at the room temperature. A probe station (Cascade Microtech) and 1500A semiconductor parameter analyser (Agilent) was used, as shown before in fig (1-14). The applied voltage was from +2 Vto -2 V with steps of 0.05 V. Nitrogen gas was used to keep the sealed area dry. I-V characteristics for both bare CNTs and the nanocomposite film were measured at various temperatures (293-333 K) which were controlled by a thermal chuck system (Model ETC-200 L, ESPEC), Japan. Figure (6-4) shows the I-V plots of bare and hybrid nanotubes and from observing the change in the current during applied voltage -2 V to +2 V there are two things we can recognize. First, the current decreased after DNA coating. Second, the device current decreases with increases of the DNA:CNTs ratio. In addition, during heating the conductance of bare CNTs is reduced because the heating leads to increased electron scattering from lattice vibrations.

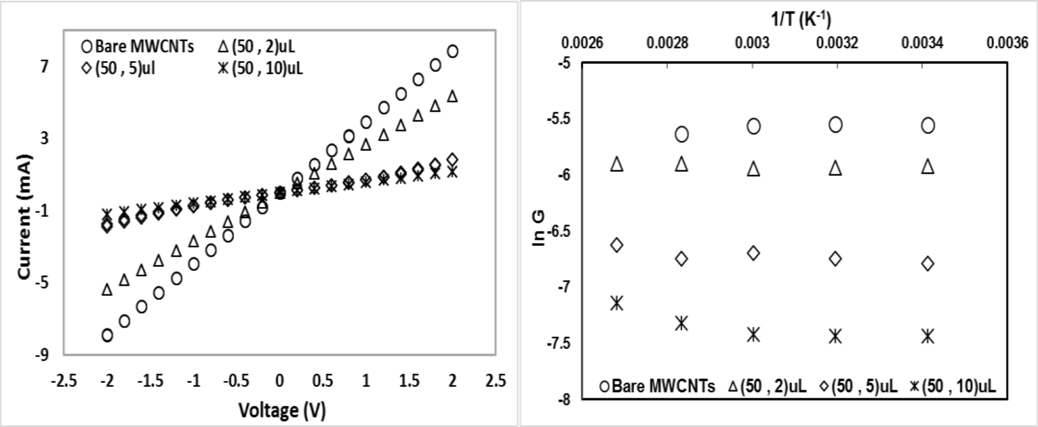

Figure 6-4 a) I-V plots of bare CNTs and CNTs/DNA nanocomposite, b) Arrhenius plot of MWCNTs and DNA@MWCNTs at different mixing ratios.

On the other hand, the current of the DNA/CNTs films at the highest DNA:CNTs ratio increases with temperature. In these films, contact between CNTs can be described as a ‘tunnel junction’ as shown in figure (6-5).

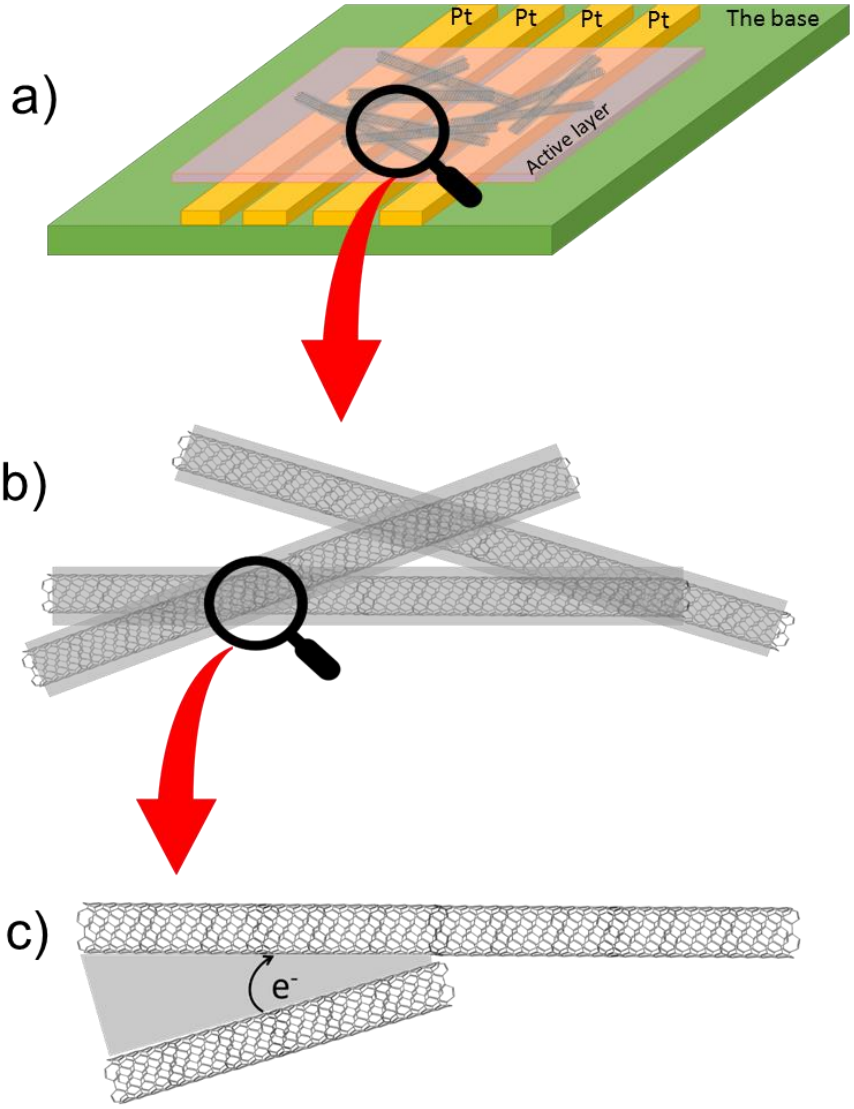

Figure 6-5 Schematic clarification of the transport of electrons in DNA@MWCNTs device. a) DNA-MWCNTs film deposited between two Pt- electrodes, electrons hop between the NTs to cross the interelectrode gap; b) and c) describe a single tunnelling barrier between two DNA@CNTs.

The effect of the insulating DNA coating on the CNTs is to separate CNTs at the point at which they cross and introduce an additional barrier to change transport that alters the temperature dependence of the conductance. Electrons in carbon nanotubes cross between the two Pt terminals by transport along the individual nanotubes and hopping between junctions where CNTs cross.

The resistance of CNTs can be described as a linear function of temperature, as shown below.

$$R_{CNTs} = a + bT \qquad (6-1)$$

Where a and b are proportional to the CNTs length. The resistance at the tunnel junction between DNA coated MWCNTs follows a VRH -variable range hopping- model.

$$R_{gap} = R_o \exp\left(\frac{T_o}{T}\right)^B \qquad (6-2)$$

Where $T_o = E_a/K_B$ and $0 < B < 1$ and E_a is the activation energy. So, the conductance of DNA/CNTs is formulated as shown below.

$$G = \left(R_{CNTs} + R_{gap}\right)^{-1} \qquad (6-3)$$

Equation (6-3) qualitatively describes the switch from metal-like behaviour for bare CNTs to hopping behaviour as the DNA:CNTs ratio increases in figure (6-4b) and the resistance of the junctions, R_{gap} increases.

Table 6-2 Shows the activation energy of DNA-coated MWCNTs at different MWCNTs:DNA ratio, Ea change proportional with MWCNTs:DNA ratio.

DNA@MWCNTs ratio (µL)	Ea (e.V)	error
50:2	0.0032	0.0005
50:5	0.015	0.00053
50:10	0.019	0.00131

6.1.3. The optical properties of DNA@CNTs films

6.1.3.1. UV-Visible spectroscopy.

UV-Visible spectroscopy is a useful technique to understand the reaction between CNTs and DNA. All UV-visible measurements of aqueous MWCNTs and DNA@MWCNTs were carried out on a Nano-drop absorption spectrometer which was obtained from Thermo Fisher Scientific Ltd with wavelength range between (200-400) nm. 2µL of methanol was used as a background and the sample was 2 µL of DNA@MWCNTs (aqueous solution) as shown in figure (6-6) and (200-400) nm.

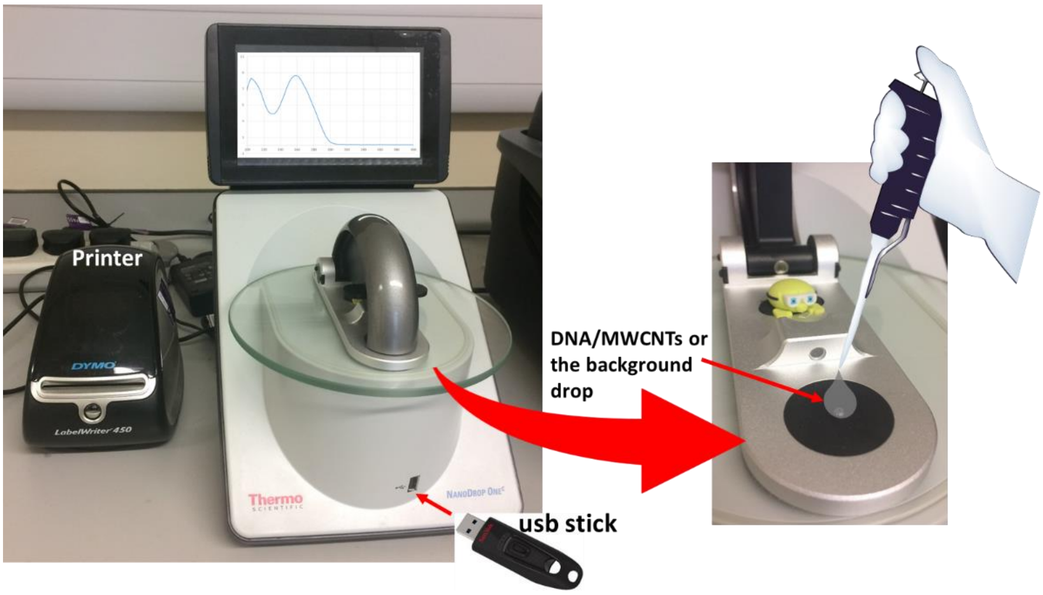

Figure 6-6 Shows UV-visible spectroscopy and how the measurements have been taken.

Generally, the operating principle of UV-vis absorption is dependent on the Beer-Lambert law[230].

$$A_{(absorbance)} = log_{10}(I_o/I_t) \rightarrow -log_{10}T = \varepsilon bc \qquad (6-4)$$

Where I_o is the intensity of the incident light, I_t the transmitted intensity, ε constant or extinction coefficient, c the concentration of the sample and b the cell path length of the light[230]. The UV-Vis spectrum shows three curves for bare MWCNTs, λ-DNA and λ-DNA-coated MWCNTs as presented in figure (6-8). UV-vis of bare CNTs in previous studies is somewhat inconsistent because of amorphous carbon. Some workers reported two absorbance bands assigned to the CNTs[231, 232] and some reported one main peak for naked CNTs and a broad shoulder in the range (237-307) nm [233], which is similar to the spectrum shown in figure 6-7. λ-DNA has a well-known spectrum with a sharp peak at 260 nm [232] assigned to π-π* transitions in DNA bases as shown in figure(6-7c). The DNA spectrum shows no absorption at wavelengths longer than about 300 nm and from figure 6-7 it is clear that DNA dominates the UV Vis spectrum of the composite.

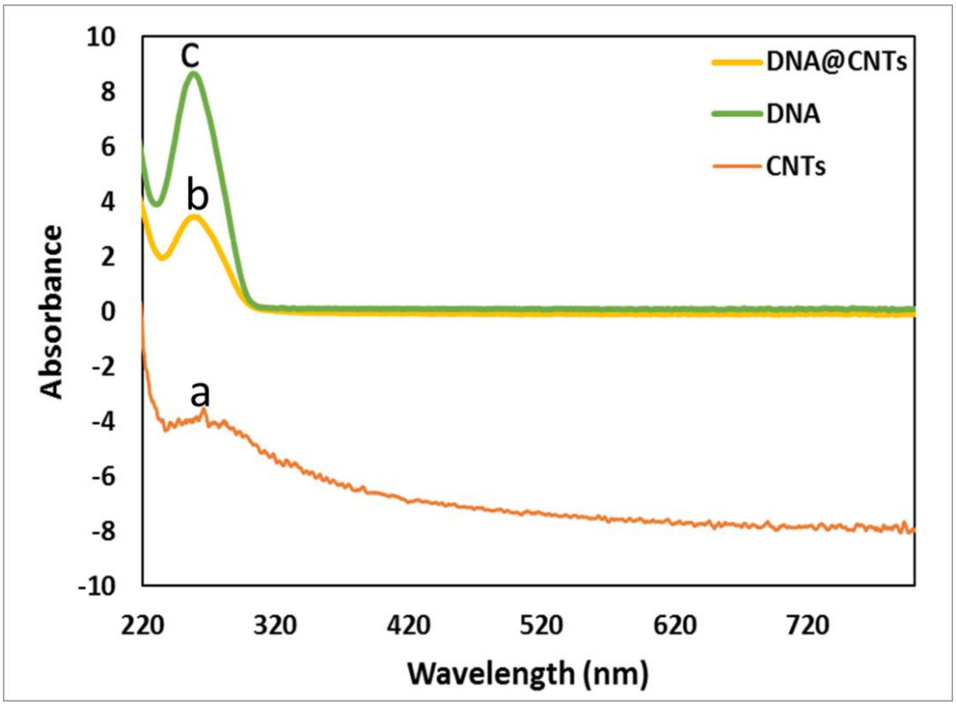

Figure 6-7 UV-vis plots of aqueous bare MWCNTs, DNA and DNA-coated MWCNTs. The CNT spectrum is offset on the y-axis for clarity. The absorbance is scaled by the Nano-drop instrument to that which would be observed for a 1 cm pathlength conventional cell.

6.1.3.2. Raman spectroscopy

For Raman measurements 3μL of each sample (bare MWCNTs, λ-DNA and DNA@MWCNTs) was drop cast on an Si chip and the samples were dried at room temperature. All the Raman spectra were measured on a CRM200 (confocal Raman imaging microscope, Witec) with a laser wavelength of 488 nm and output power of 60 mWatt. The wavenumber range of the spectrum was between (0-3100) cm^{-1}. Figure (6-8) presents plots of pristine MWCNTs, DNA and hybrid nanotubes. Bare CNTs show two main peaks in 1375cm^{-1} and 1590cm^{-1} for D and G bands, respectively. DNA chart shows a signal peak at the wavenumber 805cm^{-1} for phosphate vibration mode. A small defect increase happens for CNTs after DNA stacking and increased the ratio between G/D from 0.9 to 1.004. On the other hand, for DNA@MWCNTs a simple shift (~ 6 cm^{-1}) of the G band in 1584 cm^{-1} and ~4 cm^{-1} for D-band in 1379cm^{-1} is observed. These shifts can be attributed to the interaction through oxygen group of CNTs and DNA molecules[234, 235].

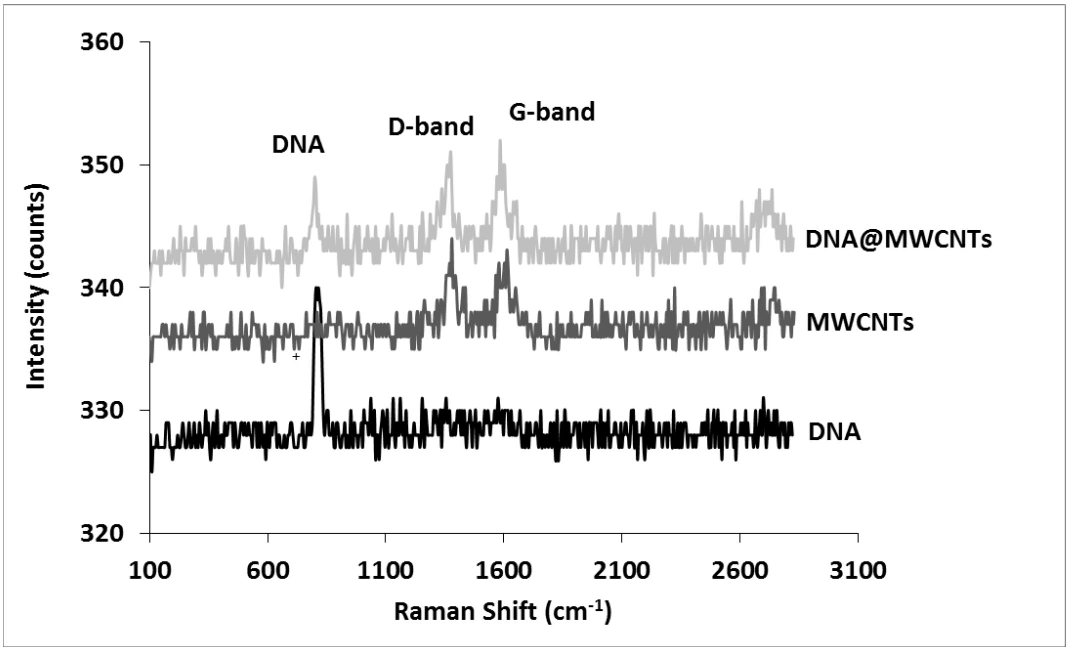

Figure 6-8 Raman spectra of a) bare MWCNTs, b) DNA and c) DNA@MWCNTs. The excitement wavelength is 488nm with the spectrograph used a grating with 600 line/mm.

6.1.3.3. Fourier transform infrared spectroscopy (FTIR)

FTIR was used to investigate DNA adhered to the surface of CNTs. The measurements were performed on an IRAffinity-IS spectrometer with DTGS detector. The attenuated total reflectance (ATR) method was used, so 2 µL from each samples were dropped on the ATR substrate as shown in figure (6-9). 2 µL of methanol was examined first as a background. ATR technique has many advantages; it is compatible with thick samples and many forms of the materials including solids and liquids. This method also needs a minimal amount of sample[236, 237]. All the FTIR measurements were carried out over the range (400-4000) cm^{-1}.

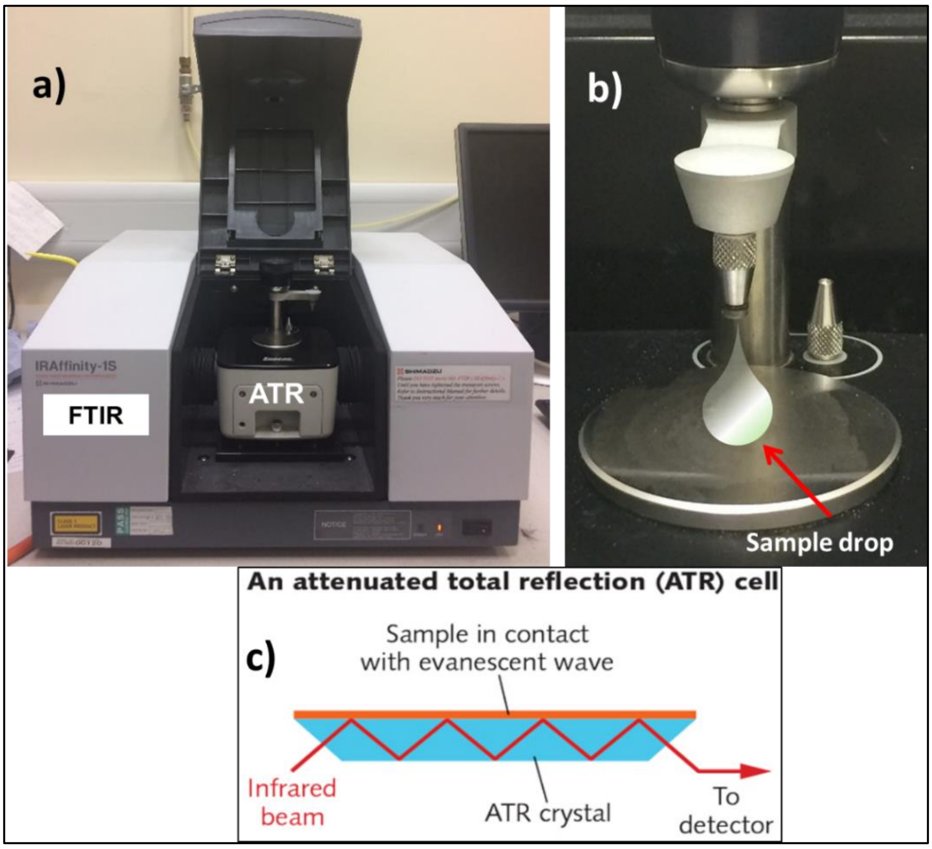

Figure 6-9 a) FTIR instrument, b)ATR technique, here we increased the size of drop for clarification only c) the principle works of ATR and shows how the incident beam (IR) is reflected many times before detecting[237].

Figure (6-10) presents the FTIR spectra of bare and hybrid nanotubes. FTIR spectra of bare MWCNTs show many peaks in 1112cm^{-1},1541cm^{-1} and 1705 cm^{-1} [238] . 1448 cm^{-1} points to D-band of CNTs[239] . Figure (6-10b) shows a number of DNA peaks, in area (A) for DNA plot, the lower wavelength area (400-800) cm^{-1} is referred to the sugar and phosphate group vibrations [240, 241]. Other peaks for pure DNA appear at the wavenumbers 960 cm^{-1} ,1069 cm^{-1} assigned to stretching modes of phosphate groups and nucleobase modes at 1631 cm^{-1} [242] . Area (B) is assigned to –OH and –NH stretches due to bound water and NH groups of

DNA. The peaks from 3000 cm^{-1} to ~3740 cm^{-1} are OH stretching vibrations [240].

In the case of DNA-coated MWCNTs films, many shifts have been noted for MWCNTs and DNA due to interaction between them. The MWCNTs band at 1257 cm^{-1} shifts to 1230 cm^{-1} [243]. The D-band for MWCNTs has been shifted from 1448 cm^{-1} to 1460 cm^{-1} [244]. Another shift occurs for the 1707 cm^{-1} band to the lower wavenumber 1675 cm^{-1}. DNA in the DNA@MWCNTs curve has a shift also at 1253 cm^{-1} to lower wavenumber 1244 cm^{-1} this feature is assigned to sugar vibrations CH_2-O-P-O [234, 238]. These shifts are evidence the samples involve intimate interaction of DNA and CNTs and are not simple mixtures.

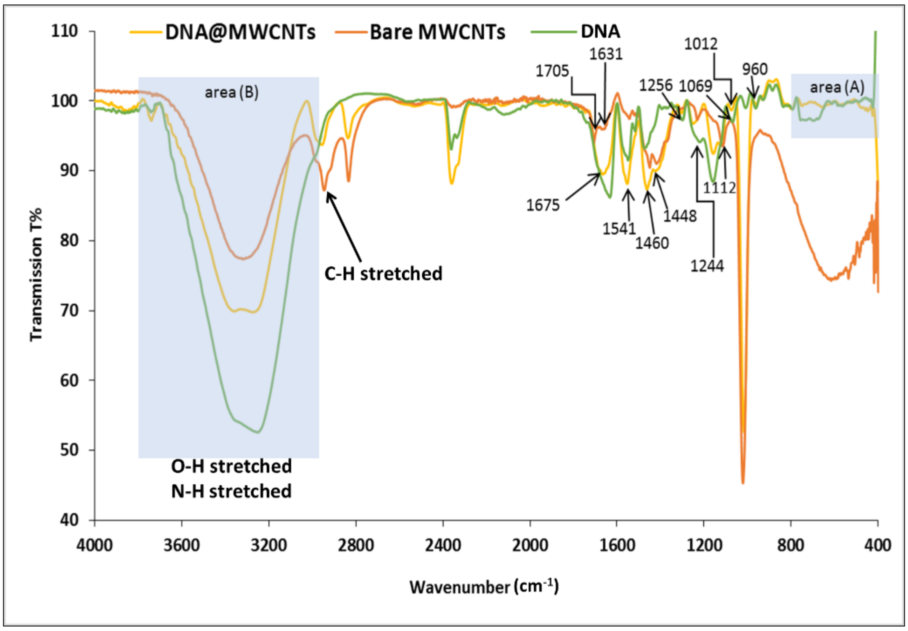

Figure 6-10 FTIR spectra of bare MWCNTs, DNA and DNA-coated MWCNTs films with baseline correction, resolution 8cm^{-1} and scan number 16.

6.2. Sensing.

We investigated DNA:CNTs combinations because bare CNTs have a low sensitivity. DNA is also used to enhance the sensitivity of CNTs [245]. Modification of the surface of carbon nanotubes was necessary to improve their sensitivity [68, 246] . Bare carbon nanotubes are not selective for a wide range of gas molecules around their environment so treatment of them can increase their selectivity for gases by coating these nanotubes by enzymes, RNA or conductive polymers[219, 247, 248]. In 2005 Staii et.al. found that CNTs have a weak response for methanol (in the gas phase) and after coating by DNA the electrical properties of the nanotubes did not change and showed a small response for methanol[67], while in this thesis, it has been found that there is a significant change in the sensitivity of CNTs after adding DNA which is let to change in the electrical properties of the CNTs. The sensing study in this chapter depended on the same sensing system for Ppy@CNTs as shown before in chapter two. However, 3µL (500µg mL^{-1} of DNA and 100 µg mL^{-1} CNTs) of aqueous samples were drop cast on Pt-integrated microband electrode and were dried at the room temperature. Two DMFCs (digital mass flow controllers) were used to control the flow rate for VOCs and zero air. Air was passed through a Dreschel bottle to introduce VOCs and then mixed with zero air before passing to the gas cell/sample as shown in figure (6-11). Equation (6-5) shows the adjustment of the mixing ratio of V_{VOCs} and V_{air} .

$$P_{VOC} = P^{*} \frac{V_{VOC}}{V_{VOC} + V_{air}} \qquad (6-5)$$

Where P^{*} is the saturated pressure of volatile organic at the Dreschel bottle temperature which was measured by a K-type thermocouple. All the data for vapour pressure were obtained from Antoine equation parameters A, B and C as shown below in equation (6-6) and obtained from NIST webbook site (https://webbook.nist.gov).

$$log_{10}P^{*} = A - \frac{B}{T + C} \qquad (6-6)$$

In this study, nonpolar and polar molecules were used to study the sensitivity of DNA/MWCNTs films: methanol, ethanol, acetone and chloroform. The film sensitivity was calculated by observing the change in film resistance.

$$S = \frac{R - R_o}{R_o} * 100\% \qquad (6-7)$$

Where R_o is the film resistance in the zero air (in background) and R is the film resistance during the analyte exposure (VOCs:dry air).

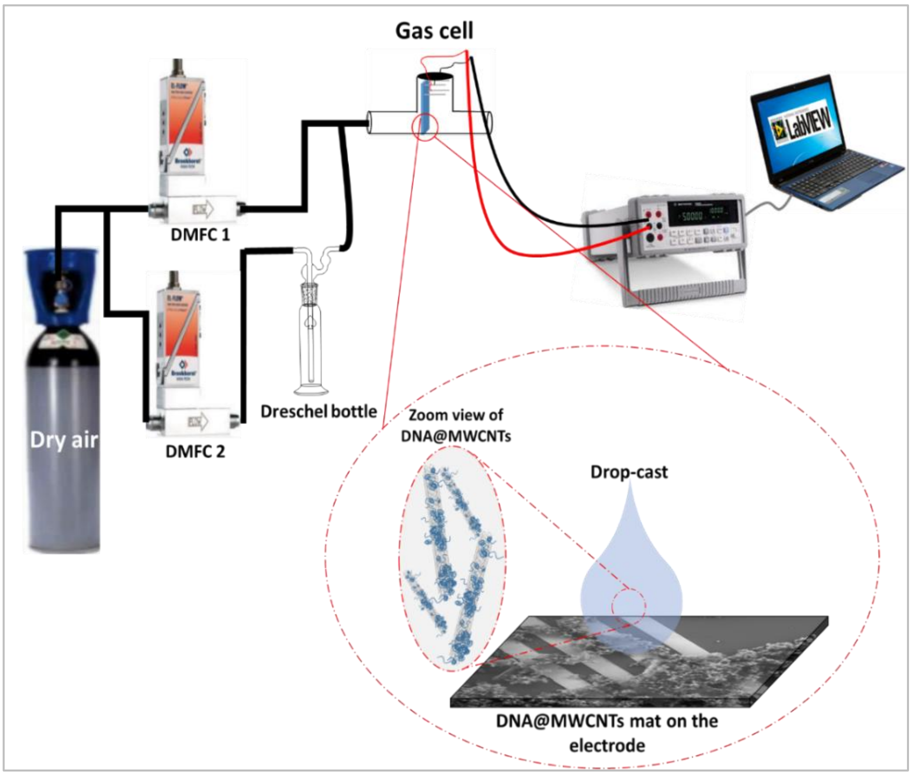

Figure 6-11 Scheme of the dynamic vapour sensing device

.

DNA has a significant effect on the sensitivity of carbon nanotubes for VOCs (MeOH, EtOH, C_3H_6O and $CHCl_3$) and it was noted that the largest response was for MeOH and the lowest response size for $CHCl_{3.}$ Two different amounts of DNA were used: 2 µL and 5 µL of DNA concentration (500 µg mL^{-1}) and were mixed with (50 µL:100 µg mL^{-1}) of MWCNTs, individually. It has been found that the CNTs:DNA ratio (50:2) µL gave the largest response, but both ratios increased the sensitivity of CNTs compared with bare CNTs. Increasing amounts of DNA impeded electron transport between the nanotubes as was very clear from the I-V measurements in figure (6-4). The electrical current of bare MWCNTs was decreased after coating by DNA and the value decreased further with increasing ratio between DNA:CNTs. In the sensing measurements, observations of device resistance were used to find the film sensitivity, as shown in figures (6-12 to 14).

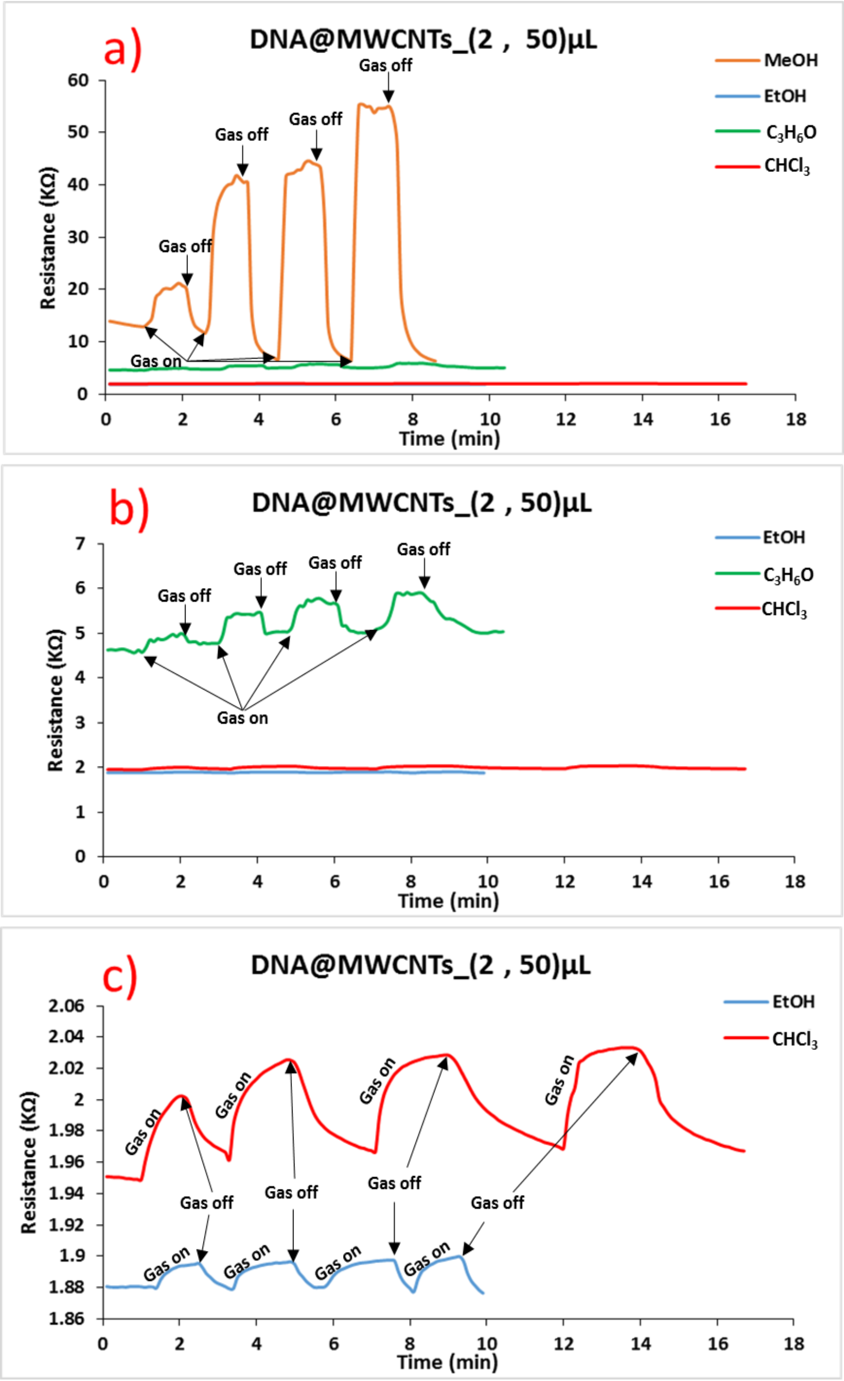

Figure 6-12 The change in the film resistance of DNA-Coated MWCNT (2 , 50)µL, it is clear that there is a dramatic change in the film resistance during methanol exposure in the gas phase and the other VOCs seem as a straight line compared with MeOH plot. Chart (a) has been expanded in two charts (b) and (c) to see easily the change in the resistance of the device for the rest of VOCs.

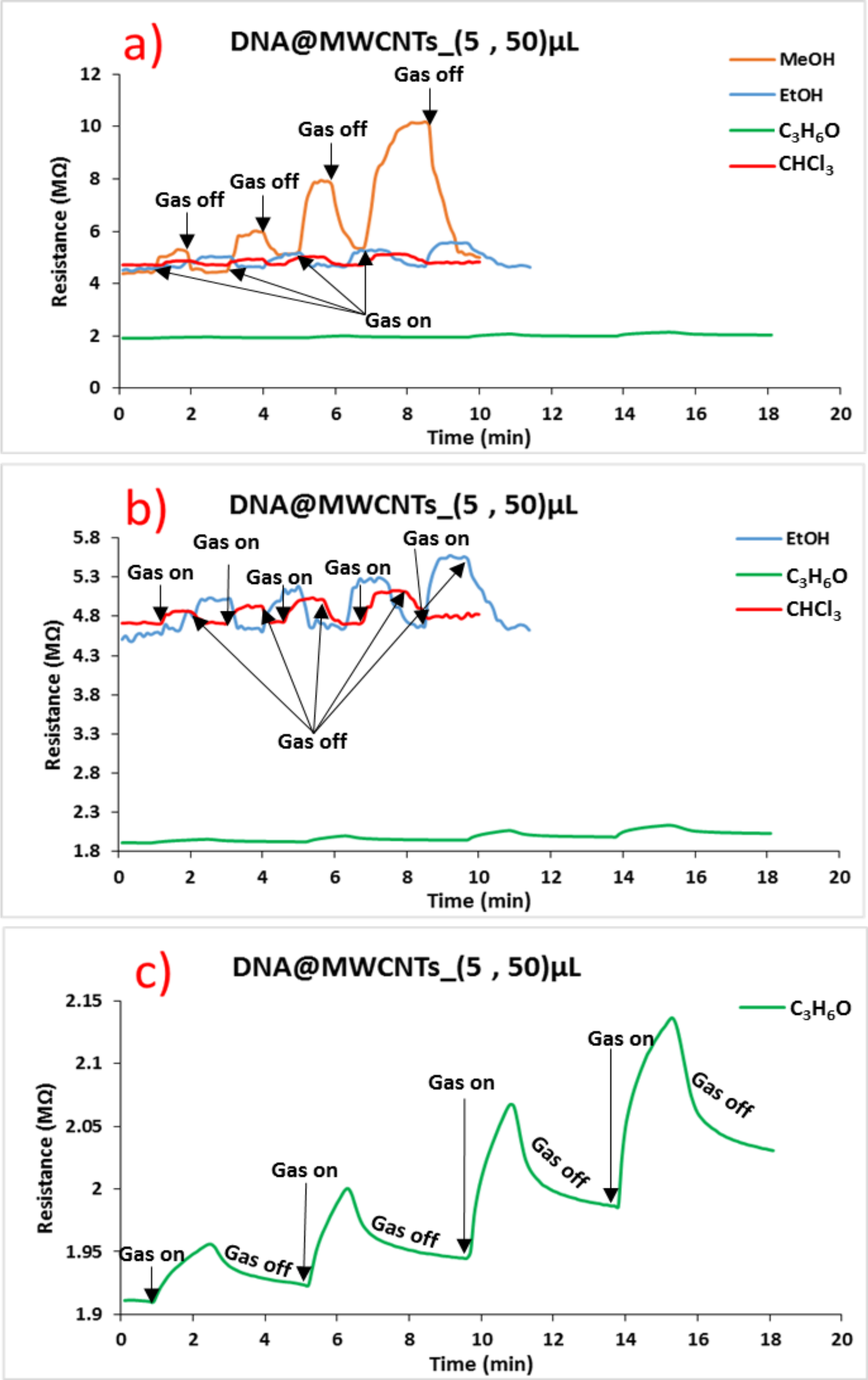

Figure 6-13 The change in the films resistance of DNA-Coated MWCNT (5 , 50)µL, it is clear that there is a large change in the film resistance during methanol exposure in the gas phase and the other VOCs seem as a straight line compared with MeOH plot . Chart a) has been expanded in two charts b) and c) to see the change in the resistance of the device for acetone vapour

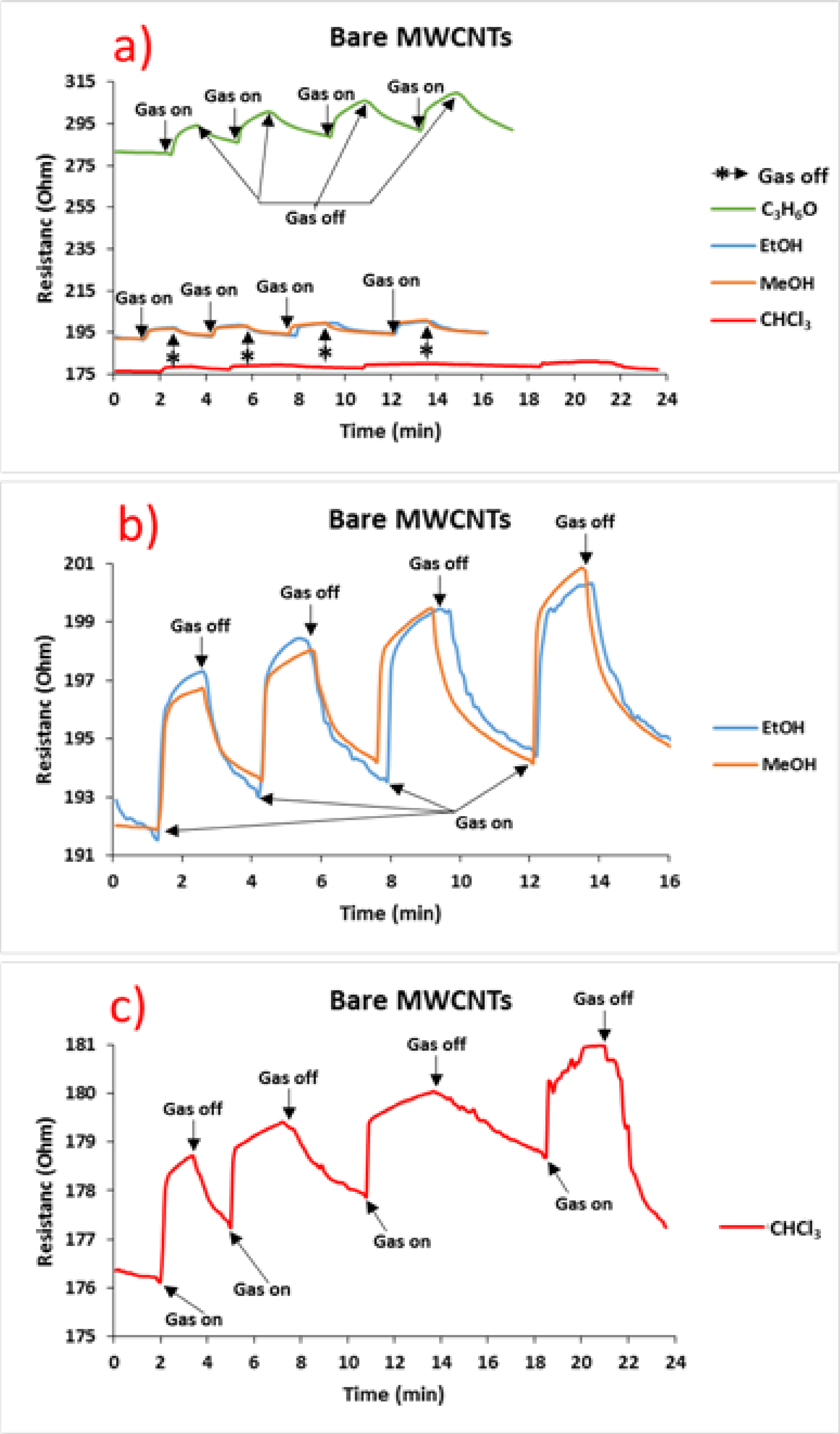

Figure 6-14 The change in the films resistance of bare MWCNTs, for pristine nanotubes the significant change in the resistance was for acetone compared with the other VOCs. (a) Chart is expanded in two charts (b) and (c) for more clarification.

From figures (6 – 12, 13 and 14) it can recognise that the film resistance increased after DNA treatment, for example, in bare MWCNTs the resistance was in Ohm (Ω) and jumped to kilo ohm (kΩ) and mega ohm (MΩ) after the DNA coating process. This is explained by the introduction of tunnel barriers between the nanotubes. The resistance increases more with the ratio of DNA:CNTs in contrast to bare CNTs, figure (6-5). Figure (6-15) shows the response size of the devices in two different vapour concentrations P=0.5P* and P=0.8P*.

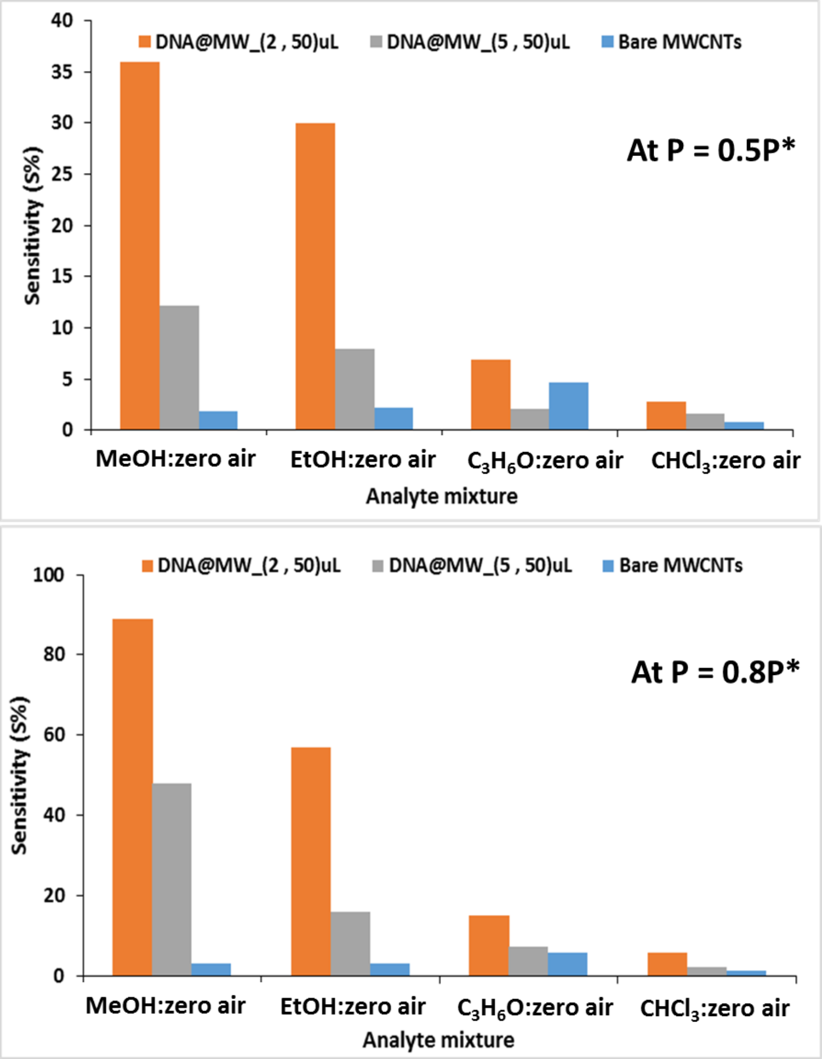

Figure 6-15 The change in the response size of bare and hybrid MWCNTs. DNA@CNTs in (2,50)µL is recorded the highest response size compared with bare MWCNTs and (5,50)µl.

The data for the highest ratio (1:5) of DNA:CNTs has not been given because the resistance was bigger that the DMM full scale value. On the other hand, the device sensitivity also depended on the system temperature, which was explained previously in chapter 3 section (3.3.1) equations (3 - 7 to 9) in terms of an adsorption equilibrium. Figure (6-16) shows the change in the sensitivity of bare and hybrid CNTs at different temperature to a different ratio between CNTs and DNA. Figure (6-17) shows the plots of ∂lnS Vs $1/T$ for CNTs and DNA/MWCNTs at different ratios of CNTs:DNA for methanol, ethanol, acetone and chloroform. The adsorption enthalpies, ΔH^{θ} are given in figure (6-17d).

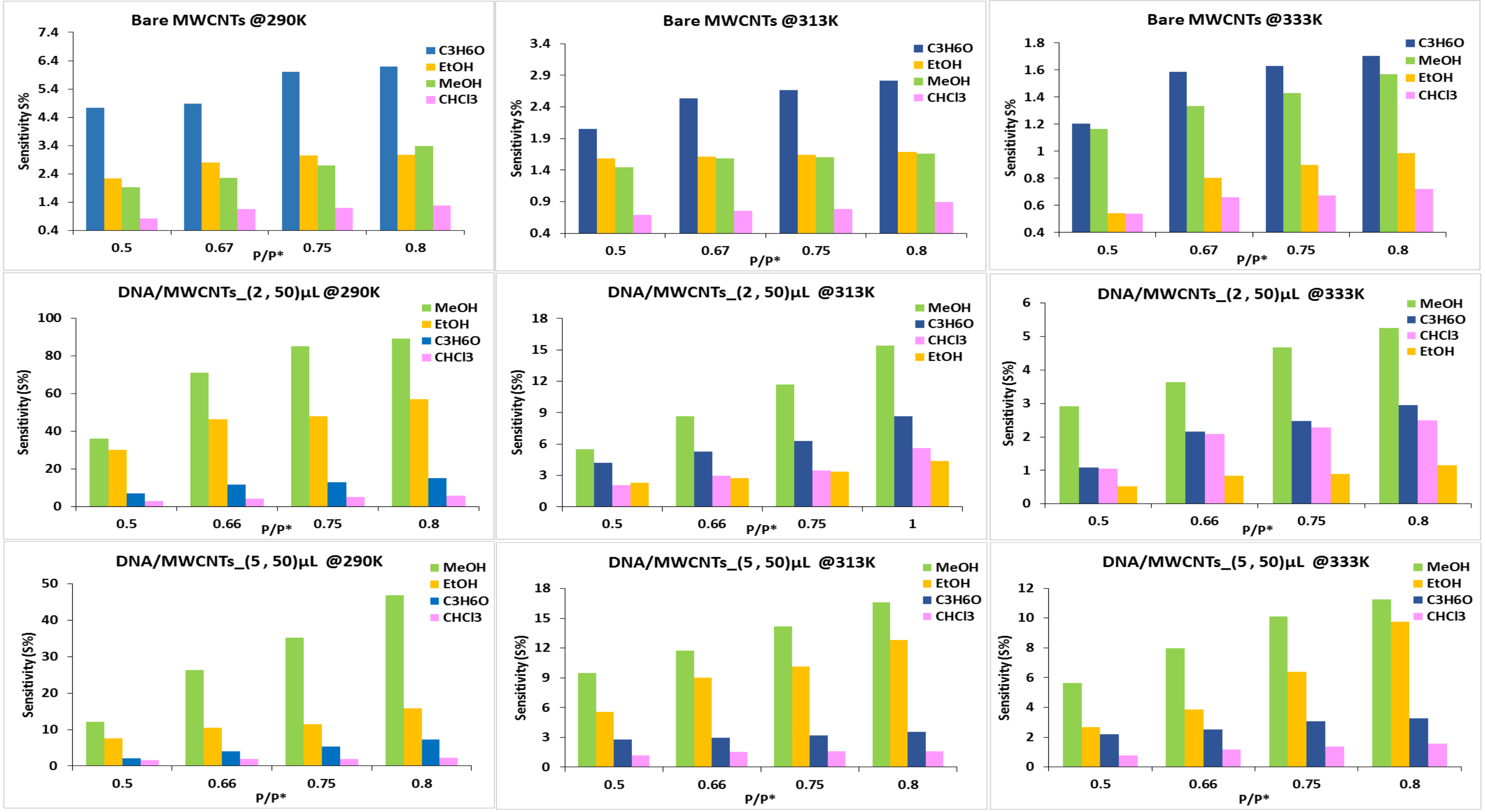

Figure 6-16 The change in the sensitivity of bare and hybrid MWCNTs at different ratio of MWCNTs:DNA for methanol, ethanol, acetone and chloroform at different temperatures

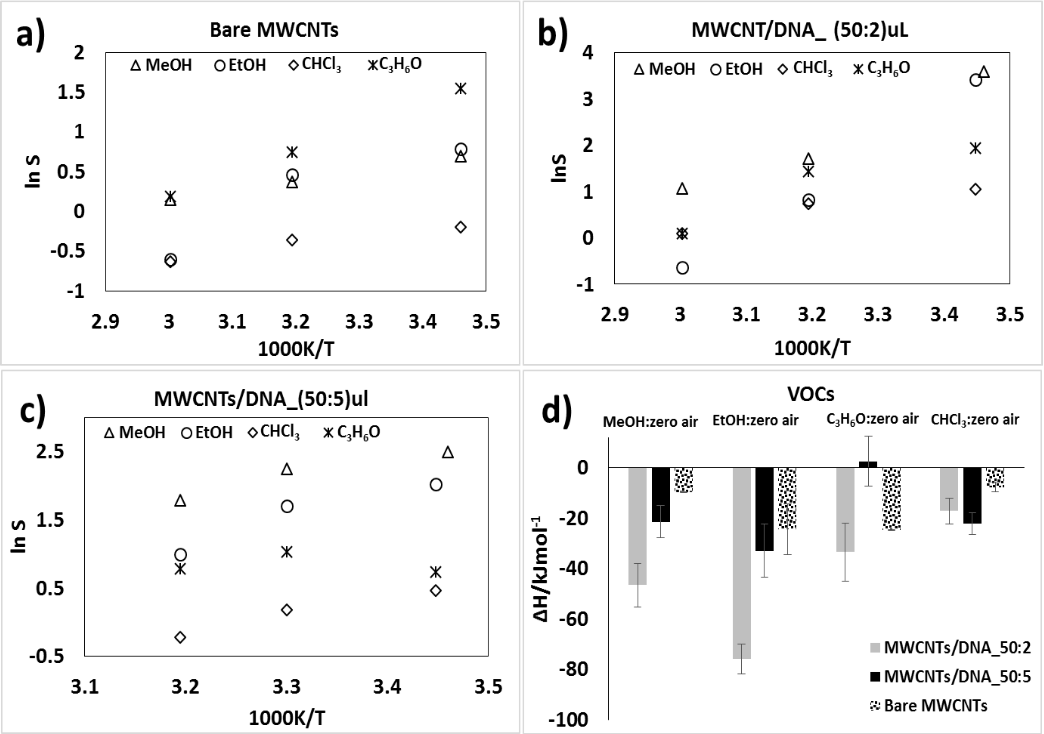

Figure 6-17 (a-c) show the change in LnS of bare MWCNTs and DNA-coated MWCNTs films at different temperatures, (d) plot of ΔH^{θ} of pristine MWCNTs and DNA@MWCNTs with different VOCs in $P= 0.5/P^{*}$.

DNA can enhance the sensitivity and selectivity of carbon nanotubes for VOCs and comparing these results with what have been obtained in chapter three of Ppy@MWCNTs, it can be recognized that DNA@MWCNTs are more selective to methanol in the gas phase than ethanol, acetone and chloroform, see figure (6-18). And from figure (6-18) it has been shown that Ppy/CNTs respond strongly to acetone than DNA/CNTs. The sensing mechanism can depend on the surface coverage and also DNA affects the binding between analyte and CNTs (absorbent layer).

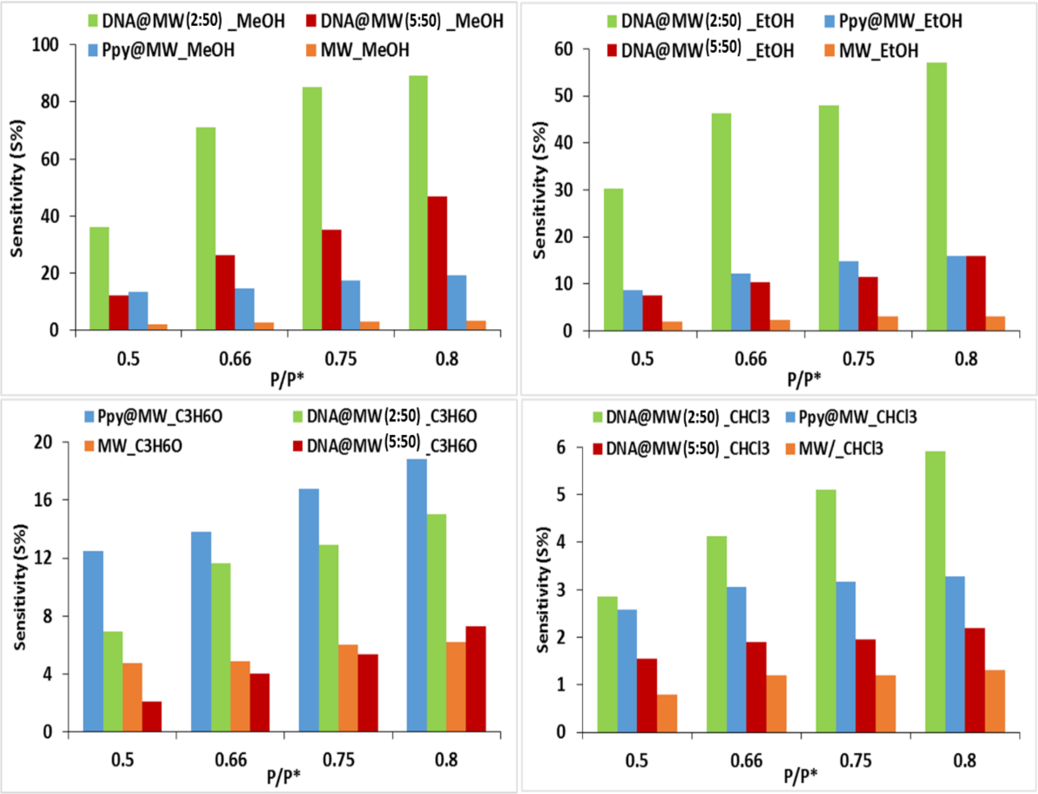

Figure 6-18 The change in the sensitivity of MWCNTs after coated by conductive polymer (polypyrrole) and DNA. DNA is more promising than polypyrrole to sens VOCs and more selective for methanol and ethanol than polypyrrole.

From figure (6-18) the ratio of DNA:CNTs (1:10) has a less effect than CNTs/DNA ratio (10:0.25) and CPs and larger than bare CNTs for ethanol and methanol.

6.3. Conclusions

Chemical sensors have been designed and based on MWCNTs decorated by dsDNA. DNA coated carbon nanotubes adsorb on the walls of CNTs and introduce tunnel barriers where CNTs cross. The electrical current of MWCNTs was decreased with increase of the ratio of DNA to CNTs, but the sensitivity of CNTs was enhanced. DNA can increase the sensitivity and the selectivity of the nanotubes for VOCs in the gas phase. DNA@MWCNTs become more sensitive for methanol than others VOCs and it has been found that the films sensitivity depended on the temperature according to the Van't Hoff equation and the films sensitivity were decreased with raising the temperature. It has been noted that $\varDelta H^{\Theta}$ was negative value for bare and hybrid nanotubes as seen in figure (3-40). $\varDelta_{vap}H^{\Theta}$ of the VOCs were obtained from the NIST webbook (https://webbook.nist.gov). and compared to the enthalpies estimated from the temperature dependence of the sensor. It was found that the experimental values for most of $\Delta \mathrm{H}^{\Theta}$ in this study were smaller than $\varDelta_{vap}H^{\Theta}$, for example, in chloroform case and as a gas phase $\varDelta_{vap}H^{\Theta} > |\varDelta_{ads}H^{\Theta}|$ for all CNTs:DNA ratios, and also acetone vapour has $\varDelta_{vap}H^{\Theta}(42\,\frac{\mathrm{kJ}}{\mathrm{mol}}\,\mathrm{at}\ 303\ \mathrm{K}) > |\varDelta_{ads}H^{\Theta}|$, while $|\varDelta_{ads}H^{\Theta}|$ equals 24 kJ mol^{-1} and 2.4 kJ mol^{-1} for bare CNTs and CNTs:DNA (lowest ratio), respectively and 33 kJ mol^{-1} for the lowest ratio of (CNTs:DNA). In contrast (CNTs:DNA) (50:5) has a very small $|\varDelta_{ads}H^{\Theta}|$ = 2.4 kJ mol^{-1} which means a very weak reaction between the analyte and the sensor material. On the other hand, $\varDelta_{vap}H^{\Theta}$ of EtOH at 303 K is 42.2 kJ mol^{-1} [157] while $|\varDelta_{ads}H^{\Theta}|$ for bare CNTs and CNTs:DNA (50:5) equal 23 kJ mol^{-1} and 33 kJ mol^{-1}, respectively, but for the lowest ratio of CNTs:DNA shows $|\varDelta_{ads}H^{\Theta}|\ (70\,\frac{kJ}{mol}) > \varDelta_{vap}H^{\Theta}(42.2\,\frac{kJ}{mol})$ which means a strong interaction between the analyte and the sensor material. In general $|\varDelta_{ads}H^{\Theta}| < \varDelta_{vap}H^{\Theta}$, which suggests the VOCs molecules were adsorbed by the sensor material and not simply condensed as a liquid. However when $|\varDelta_{ads}H^{\Theta}| = \varDelta_{vap}H^{\Theta}$ (in the case of acetone for the lowest ratio of CNTs:DNA) the process can be described in terms of the VOCs simply condensing as a liquid on the device.

Chapter Seven: Conclusions and future work

7.1. Conclusions

The aim of this chapter is to draw together the main conclusions from the thesis and to provide general perspective on the results. The aim of this study was to understand the sensitivity of bare and hybrid carbon nanotubes in two types: single-walled and multi-walled carbon nanotubes as VOCs, CO and ozone gas sensors. In general, networks comprising only CNTs (MWCNTs or SWCNTs) were found to show the highest conductivity (chapter three, section 3.1.3), however these bare CNT or pure CNT composites generally showed the smallest sensitivity to various analytes (chapter three, section 3.3). The sensitivity is the fractional change in current or resistance of the device in response to the analyte and was used because it normalizes for factors such as device size and the amount of material deposited. We observed that incorporation of conductive polymers (polypyrrole) into CNT composites changed the overall electrical behaviour from metal-like to semiconducting in the sense that the resistance decreased with increasing temperature. This behaviour is consistent with a network model of the composite in which conduction through the portion of polymer between CNT junctions is limiting the transport. Similarly, DNA-coated CNTs (chapter six) showed a transition from metal-like conduction behaviour to semiconductor-like conduction behaviour as the DNA: CNT ratio increased (chapter six, section 6.1.2.). The composites showed superior sensitivity to various analytes in almost all cases; this suggests that the origin of the resistance changes responsible for the sensing behaviour is at the resistive CNT/CNT junctions which are modified by the presence of semiconducting (polypyrrole) or insulating (DNA, BNNT) materials.

More specific conclusions for various aspects of the work are presented in four parts:

(1): Polypyrrole@CNTs as VOCs gas sensor, (2): BNNTs@CNTs as ozone gas sensor, (3): Polypyrrole@CNTs to detect carbon monoxide gas and (4): DNA@CNTs to detect VOCs.

(1)

The general results of coated CNTs by the conductive polymer Ppy are:

- Carbon nanotubes were successfully coated with polypyrrole using *in situ* chemical oxidative polymerization method.
- AFM and TEM images show the significant change in the diameters of the nanotubes after coating and poly pyrrole coated CNTs as shells.
- FTIR demonstrated peaks of polypyrrole in the spectrum of CNTs with a small shift in the peaks, which indicates chemical interaction between the conductive polymer and CNTs during the polymerisation process, while Raman peaks showed the G and D bands of carbon nanotubes and bands due to polypyrrole.
- I-V characteristics for two terminal nanotube devices showed a change in the electrical properties of carbon nanotubes after coating. The electrical conductance decreased after coateing. Impedance spectroscopy showed that the bare CNTs behave as

a simple real resistor, while the Ppy@CNTs have also an imaginary part of the impedance. Furthermore polypyrrole@CNTs showed a semiconductor-like behaviour as a function of temperature which can be interpreted in terms of a hopping mechanism, Arrhenius equation gave more details about the electrical properties of polypyrrole@CNTs (chapter three, section 3.1.3.)

- Pristine CNTs showed a weak sensitivity to volatile organic compounds VOCs for (methanol, ethanol, acetone and chloroform), but the film sensitivity was enhanced more than ten-fold after coating CNTs by polypyrrole. Acetone showed the highest response of the tested VOCs for SWCNTS/Ppy while $CHCl_3$ recorded the lowest response.
- As a gas sensor, CNTs and CNTs/Ppy demonstrated increasing in the electrical resistance when the VOC exposure and decreased after gas off with a reversible change. This suggests the mechanism does not involve a chemical reaction with the polymer.
- Generally, acetone showed a higher response than MeOH, EtOH and $CHCl_3$ 0.7% and 6 % for SWCNTs and MWCNTs respectively. Bare and hybrid CNTs have a fast response time (1-2) min and with recovery times between (1-4) min.
- The sensitivity of bare and hybrid carbon nanotubes decreased with increasing temperature and the temperature dependence is

consistent with the Van't Hoff equation and reversible adsorption of the analyte on the device.

- Bare CNTs show a linear change between the film sensitivity and the VOCs concentration with correlation coefficient between (0.91-0.99) for a small amount of the VOCs $P/P^* < 0.2$, in contract with CNTs/Ppy correlation coefficient between 0.79 to 0.95 for correlation coefficient, and 0.22 to 0.68 for chloroform. There was a nonlinear relation between the film sensitivity and the vapor concentrations.
- It was observed that decreasing the concentration of the conductive polymer below 1 M led to a discontinuous coverage of the nanotubes by polypyrrole and lower sensitivity.
- Laser treatment of bare CNTs led to increase the sensitivity of CNTs to chloroform vapour than MeOH, EtOH and C_3H_6O, Laser irradiation of CNTs therefore provides another useful means to alter the selectivity of CNTs sensors. Laser radiation also led to disorder in the structure of the CNTs.
- From observing the sensitivity of bare and hybrid CNTs for 30 min, it has been found that the change in the electrical resistance of the CNTs films was stable and reversible for all the VOCs. While observing CNTs/Ppy for 10 days found the sensitivity of the nanocomposite decreased after ten days.
- The main mechanism of electrons transport inside the CNTs and CNTs/Ppy depends on the variable range hopping (VRH) and tunnelling transport (TT) at junctions.

- In some sensing experiments of CNTs/Ppy as chloroform sensor, it has been shown swelling in the polypyrrole matrix and appeared to decrease the electrical resistance and an irreversible change.

(2)

The general results of BNNTs@CNTs films are:

- Electrical current of SWCNTs and MWCNTs was decreased after mixing with BNNTs and from I-V characteristics it has been shown that the linear plot between the current and the voltage without any evidence refers to a barrier between Pt/NT mixtures.
- Impedance spectroscopy demonstrated that there is only real part of the resistance before and after mixing BNNTs with CNTs unlike the case of polypyrrole/CNT composites.
- Raman spectroscopy shows a strong interaction between BNNTs and CNTs.
- In the sensing applications, bare SWCNTs and bare MWCNTs shows a fast response to the ozone gas with irreversible change and long recovery time depending on the gas concentration.
- Upon ozone exposure, the electrical current increased and decreased when the gas was switched off.
- The mixture of BNNTs CNTs increased the film sensitivity to the ozone with short recovery times.
- Bare and hybrid SWCNTs showed more sensitivity to the ozone molecules than pristine and hybrid MWCNTs.

- The sensitivity of bare and hybrid carbon nanotubes increased with increasing the temperature and it has been noted that the recovery times decreased.
- From the Van’t Hoff analysis of the sensitivity, and apparent enthalpy $\Delta H^{\theta} > 0$ was observed. A positive enthalpy is not consistent with an adsorption mechanism and along with the irreversibility this suggests instead the mechanism involves a chemical reaction and the temperature dependence reflects Arrhenius kinetics.
- Ozone depletes electrons from CNTs and increase the concentration of the holes as majority chargers in the nanotube network.
- XPS data show that exposure ozone gas on CNTs led to oxidation of the nanotubes, but greater effects are seen in BNNTs where oxidation of boron atoms happens.

(3)

The main conclusions of using CNTs as a carbon monoxide gas sensors are:

- Bare CNTs have a weak sensitivity to carbon monoxide gas.
- Coating CNTs by polypyrrole led to an increase the sensitivity.
- From observing the change in the electrical resistance, it has been shown that the electrical resistance decreased with gas exposure with irreversible change, with a fast response times.

- Bare SWCNTs more sensitive to the carbon monoxide gas than bare MWCNTs.
- The recovery times become slower after coating by polypyrrole, but no more than 5.5 min in SWCNTs/Ppy and >2.5 min for MWCNTs/Ppy.
- The sensitivity of bare and hybrid carbon nanotubes decreased with an increase the temperature, and from the Van't Hoff equation it was found that the interaction of carbon monoxide gas with surface of CNTs can be described as an exothermic adsorption reaction.

(4)

The last part in these conclusions are related to the coated MWCNTs by dsDNA as a VOCs gas sensors:

- DNA coated MWCNTs function as a VOC gas sensor.
- The electrical properties of MWCNTs have been changed after coating, the electrical conductance decreased after the coating process.
- The ratio of CNTs: DNA (10:1) represents the best ratio to obtain a good response to the VOCs vapour, while increasing the ratio beyond 10:1 led to devices insensitive to the VOCs.
- As a gas sensor, the sensitivity of MWCNTs increased after DNA coating.
- DNA@MWCNTs become more sensitive for methanol vapour than others VOCs (acetone, ethanol and chloroform).

- When the temperature > 293 K, the film sensitivity decreased and according to the Van's Hoff equation for the samples of $\Delta_{ads}H^{\Theta} \vee \Delta_{vap}H^{\Theta}$, the VOCs molecules were adsorbed by the sensor material and not simply condensed as a liquid and when $\Delta_{ads}H^{\Theta}\ Vs\ \Delta_{vap}H^{\Theta}$ (in acetone case for the lowest ratio of CNTs:DNA) can be described the VOCs molecules as simply condensed as a liquid.
- DNA@CNTs films are more promising than Ppy/CNTs to sense VOCs and more selective for ethanol and methanol than polypyrrole.

7.2. Limitations and future work

This thesis focused on using bare and hybrid carbon nanotube networks as gas and vapour sensors, and it has been found that the conductive polymer as polypyrrole, DNA and BNNTs enhanced the sensitivity of carbon nanotubes for volatile organic compounds, carbon monoxide and ozone gas. The coating and mixing process helped to change the electrical properties of CNTs to increase the sensitivity to gases and vapour.

Coating CNTs by DNA helped to increase the selectivity of CNTs to methanol over other VOCs, whereas polypyrrole/CNT composites showed selectivity for acetone. In previous works[185, 186], CNTs were used to detect ozone, however these devices suffered from long recovery times after removal of the ozone. In this thesis BNNTs@CNTs films was used in the first time to detect the ozone gas with reduced recovery time. Previous researchers used vacuum and the thermal treatment to obtain a recovery time of 30 min at best while in our study we obtained a lower recovery time (3-17) min –depending on the gas concentration- at room temperature without vacuum system. Generally, the mechanism of response for pristine and composite carbon nanotube devices was different and dependent on the types of the gas. We have observed evidence of mechanisms based on adsorption (VOC on Ppy/CNY and based on reaction ozone/CNTs). It has been noticed that during chloroform vapour detection there was a negative response and an irreversible change with the swelling in the polypyrrole@CNTs matrix. AFM imaging showed that there was an increase in the polypyrrole particles size which suggests a mechanism based on swelling and closing of gaps in the conduction pathway.

In summary, we find that modification of CNTs by incorporation of various insulating or lower conductivity materials improves their analytical sensitivity in a range of gas sensing devices. The bare CNTs are too conductive and too inert to show a strong response to analytes despite their high surface to volume ratio. However, the decrease in conductance upon making various composites is not a significant disadvantage to the production of sensing devices and also allows one to adjust the selectivity by careful choice of materials.

References

1. V. B. King, *Nanotechnology research advances*, Nova Science Publishers, New York, 2007.
2. E. Karl, PhD, Norwegian University of Science and Technology, 2012.
3. B. Yadav and K. Ritesh *IJNA*, 2008, **2**, 15-24.
4. M. Meyyappan, *Carbon nanotubes sciense and applications* CRC PRESS, Florida, USA, 2004.
5. A. H. Shah, in *Carbon Nanotubes: Current Progress of their Polymer Composite* INTECH, London, United Kingdom, 2016, pp. 459-494.
6. Valentin N. Popov and Philippe Lambin, *Carbon nanotubes* Springer, The Netherlands 2005.
7. K. Richard, F. , Lee, J. Barry , Cox and M. James , Hill, *Nanoscale*, 2010, **2**, 859-872.
8. T. Lin, V. Bajpai, T. Ji and L. Dai, *Aust. J. Chem.* , 2003, **56**, 635-651.
9. H. Peter, *Carbon Nanotubes and Related Structures: New Materials for the Twenty - first Century*, The Press Syndicate of the University of Cambridge The United Kingdom, 1999.
10. H. Peter, *Carbon Research*, 2018, **4**, 1-17.
11. A. Eatemadi, H. Daraee, H. Karimkhanloo, M. Kouhi, N. Zarghami, A. Akbarzadeh, M. Abasi, Y. Hanifehpour and S. W. Joo, *Nanoscale Research Letters*, 2014, **9**, 1-13.
12. G. Korotcenkov, *Handbook of Gas Sensor Materials : Properties, Advantages and Shortcomings for Applications*, Springer, New York, USA, 2014.
13. E. Radauscher, PhD thesis, Duke University, 2015.
14. C. H. Wong and M. Pumera, *PCCP*, 2013, **15**, 7755-7759.
15. V. B. King, *Nanotechnology*, Nova Science New York, 2007.
16. S. I. Rushfeldt, Master of Engineering, Massachusetts Institute Technology, 2004.
17. V. N. Popov, *Materials Science and Engineering R*, 2004, **43**, 61-102.
18. R. Saito, G. dresselhaus and M. Dresselhaus, *Physical properties of carbon nanotubes* Imperial Collage London London, UK, 2003.
19. A. Aqel, K. El-Nour, R. Ammar and A. Al-Warthan, *Arabian Journal of Chemistry*, 2012, **5**, 1-23.
20. N. Wang, Z. Tang, G. Li and J. Chen, *Nature*, 2000, **408**, 50-51.
21. S. Cai, H. B. Alexandra and W. YuHuang, *Nanoscale*, 2011, **3**, 503-518.
22. J. K. Streit, S. Lam, Y. Piao, A. R. Hight Walker, J. A. Fagan and M. Zheng, *Nanoscale*, 2017, **9**, 2531-2540.
23. C. Journet, W. K. Maser, P. Bernier , A. Loiseau, M. Lamyde , S. Lefrant, P. Deniard, R. Leek and J. E. Fischerk *Nature*, 1997, **388**, 756-758.

24. J. Seetharamappa, S. Yellappa and F. D'Souza, *Carbon Nanotubes: Next Generation of Electronic Materials*, USA, 2006.
25. P. Pandey and M. Dahiya, *IJPSRI*, 2016, **1**, 15-21.
26. P. M. Ajayan and T. W. Ebbesenz, *IOP science* 1997, **60**, 1025-1062.
27. Arc Discharge method, https://shellzero.wordpress.com/2012/05/14/arc-discharge-method/, (accessed May, 2018).
28. D. S. Bethune, C. H. Klang, M. S. de Vries, G. Gorman, R. Savoy, J. Vazques and R. Beyers, *Nature* 1993, **363**, 605-607.
29. A. Raunika, S. A. Raj, K. Jayakrishna and M. T. H. Sultan, *IOP Conference Series: Materials Science and Engineering*, 2017, **270**, 012027.
30. Z. Otto , S. Hideo , G. Bo , O. Soojin, F. Les and G. Yue, *Acc. Chem. Res*, 2002, **35**, 1045-1053.
31. S. Andrea , P. Caterina , C. Anita , G. Girolamo , V. Danilo and B. János , Nagy, *Materials* 2010, **3**, 3092-3140.
32. M. Kumar and Y. Ando, *Journal of Nanoscience and Nanotechnology*, 2010, **10**, 3739-3758.
33. F. Abdulrazzak, A. Abbas and F. Hussein, *Frontiers in Nanoscience and Nanotechnology*, 2017, **3**, 1-7.
34. C. Lan, P. Srisungsitthisunti, P. B. Amama, T. S. Fisher, X. Xu and R. G. Reifenberger, *Nanotechnology*, 2008, **19**, 125703.
35. T. Guo, P. Nikolaev, A. Thess, D. T. Colbert and R. E. Smalley, *chem Phys Lett*, 1995, **243**, 49-54.
36. S. Ilani and P. L. McEuen, *Annual Review of Condensed Matter Physics*, 2010, **1**, 1-25.
37. Y. Shaoning, PhD, The Nanyang Technological University, 2009.
38. B. Mahatme, T. Priyanka, P. Dongre, S. Nakhate, V. Mukhamale and A. Tabhane, *IJSR*, 2015, **2013**, 145-152.
39. R. Ravichandran, S. Sundarrajan, J. R. Venugopal, S. Mukherjee and S. Ramakrishna, *J R Soc Interface*, 2010, **7 Suppl 5**, S559–S579.
40. P. Pfluger, M. Krounbi, G. B. Street and G. Weiser, *Chemical Physics*, 1983, **78**, 3212-3218.
41. T. K. Das and S. Prusty, *Polymer-Plastics Technology and Engineering*, 2012, **51**, 1487-1500.
42. G. Inzelt, *Journal*, 2008.
43. M. Raicopol, A. Pruna and L. Pilan, *Chemistry*, 2013, **2013**, 1-8.
44. P. Chuang , Z. Shengwen , J. Daniel and Z. George , Chen, *Progress in Natural Science*, 2008, **18**, 777-188.
45. W. Lin-Xia , Xin-Gui L. and Y.-L. Y. . *Reactive & Functional Polymers*, 2001, **47**, 125-139.
46. V. Khomenkoa, E. Frackowiakb and F. B´eguina, *Elsvier*, 2005, **50**, 2499–2506.
47. S. Baytekin and Z. Kucukyavuz, *Macromol Symp*, 2010, **295**, 59-64.
48. M. Yu, B. Yakobson and R. Ruoff, *Phys. Chem. B* 2000, **104**, 8764-8767.
49. R. Meysam and H. Pascal, *Composites Science and Technology*, 2011, **72**, 72-84.

50. Y. Hu, O. Tan, W. Zhu and W. Cao, *Sensors for Chemical and Biological Applications*, CRC Press, Taylor & Francis Group, United States of America, 2010.
51. R. Saito, G. Dresselhaus and M. S. Dresselhaus, *Physical Properties of Carbon Nanotubes*, Imperioal Collage Press London, 1998.
52. V. K. Thakur, J. Yan, M.-F. Lin, C. Zhi, D. Golberg, Y. Bando, R. Sim and P. S. Lee, *Polymer Chemistry*, 2012, **3**, 962–969.
53. J. Wang, C. H. Lee, Y. Bando, D. Golberg and Y. K. Yap, 2009, DOI: 10.1007/978-1-4419-0086-9_2, 23-44.
54. K. S. Kim, M. J. Kim, C. Park, C. C. Fay, S.-H. Chu, C. T. Kingston and B. Simard, *Semiconductor Science and Technology*, 2017, **32**, 1-18.
55. S. Son, M. Taheri, E. Carpenter, V. G. Harris and M. E. McHenry, *Applied Physics*, 2002, **91**, 7589-7591.
56. C. H. Lee, S. Bhandari, B. Tiwari, N. Yapici, D. Zhang and Y. K. Yap, *Molecules*, 2016, **21**, 1-19.
57. K. H. Lee, H. J. Shin, J. Lee, I. Y. Lee, G. H. Kim, J. Y. Choi and S. W. Kim, *Nano Lett*, 2012, **12**, 714-718.
58. Y. Wang and J. T. W. Yeow, *Sensors*, 2009, **2009**, 1-24.
59. T. Zhang, S. Mubeen, N. V. Myung and M. A. Deshusses, *Nanotechnology*, 2008, **19**, 1-14.
60. M. Y. Faizah, A. Fakhru'l-Razi, R. M. Sidek and A. G. L. Abdullah, *IJET*, 2007, **4**, 106-113.
61. M. J. O'Connell, *Carbon Nanotubes: Properties and Applications*, CRC Press, Taylor and Francis Group, 2006.
62. F. F. Komarov and A. M. Mironov, *Physics and chemistry solid state* 2004, **5**, 411-429.
63. *Chemical Sensors: Simulation and Modeling Volume 5: Electrochemical Sensors*, Momentum Press, USA.
64. *Anal. Chem.*, 1987, **59**, 1091A-1098A.
65. Alphasens, http://www.alphasense.com/index.php/air/).
66. C. M. Zimmer, K. T. Kallis and F. J. Giebel, *J. Sens. Sens. Syst.*, 2015, **4**, 151-157.
67. C. Staii and A. T. Johnson, *Nano Lett*, 2005, **5**, 1774-1778.
68. A. Johnson, C. Staii, M. Chen, S. Khamis, R. Johnson, M. Klein and A. Gelperin, *Semiconductor Science and Technology*, 2006, **21**, S17-S21.
69. T. Someya, J. Small, P. Kim, C. Nuckolls and J. Yardley, *Nano letters* 2003, **3**, 877-881.
70. Z. Zanolli, R. Leghrib, A. Felten, J. J. Pireaux, E. Llobet and J. C. Charlier, *ACS Nano*, 2011, **5**, 4592-4599.
71. K. Umemura, *Nanomaterials*, 2015, **5**, 321-350.
72. J. Zhao, A. Buldum, J. Han and J. P. Lu, *Nanotechnology*, 2002, **13**, 195-200.
73. F. Wang, H. Gu and T. M. Swager, *Am. Chem. Soc.*, 2008, **130**, 5392-5393.
74. S.-J. Young and Z.-D. Lin, *ECS Journal of Solid State Science and Technology*, 2017, **6**, M130-M132.

75. M. Sanchez, R. Guirado and M. E. Rinc, *Mater. Sci. Mater. Electron.*, 2007, **18**, 1131 - 1136.
76. K. S. V. Santhanama, R. Sangoia and L. Fullerc, *Sensors and Actuators B: Chemical*, 2005, **106**, 766-771.
77. S. K. Verma, P. Kar, D. J. Yang and A. Choudhury, *Sensors and Actuators B: Chemical*, 2015, **219**, 199-208.
78. J. F. Feller, J. Lu, K. Zhang, B. Kumar, M. Castro, N. Gatt and H. J. Choi, *Journal of Materials Chemistry*, 2011, **21**, 4142.
79. P. G. Collins, K. Bradley, M. Ishigami and A. Zettl, *Sci.*, 2000, **287**, 1801-1804.
80. D. R. Kauffman and A. Star, *Angew Chem Int Ed Engl*, 2008, **47**, 6550-6570.
81. V. Derycke, R. Martel, J. Appenzeller and P. Avouris, *Applied Physics Letters*, 2002, **80**, 2773-2775.
82. A. Goldoni, R. Larciprete, L. Petaccia and S. Lizzit, *J. Am. Chem. Soc.* , 2003, **125**, 11329-11333.
83. *Phy rev lett.*, 2000, **85**, 1096-1099.
84. S. Peng and K. Cho, *Nanotechnology*, 2000, **11** 57-60.
85. D. C. Sorescu, K. D. Jordan and P. Avouris, *J. Phys. Chem. B*, 2001, **105**, 11227-11232.
86. S. M. Cho, Y. J. Kim, Y. S. Kim, Y. Yang and S. C. Ha, Vienna University of Technology, Vienna, Austria, 2004.
87. B. Philip, J. Abraham, A. Chandrasekhar and V. Varadan, *IOP science*, 2003, **12**, 935-939.
88. K. H. An, S. Y. Jeong, H. R. Hwang and Y. H. Lee, *Adv. Mater.* , 2004, **16**.
89. S. J. Young and Z. D. Lin, *Microsystem Technologies*, 2016, **24**, 55-58.
90. G. Zhang, H. Tai, G. Xie, Y. Jiang and Y. Zhou, *Science China Technological Sciences*, 2013, **56**, 2576-2580.
91. S. Gautam, D. Kumar, P. S. Alegaonkar, P. Jha, N. Jain and J. S. Rawat, *Integrated Ferroelectrics*, 2018, **186**, 65-70.
92. M. Al-Hinai, PhD thesis Newcastle upon Tyne, 2012.
93. R. Wilson and H. Bullen, *Introduction to scanning probe microscopy (SPM)*, Departmaent of Chemitry, Northern Kentucky University, USA, 2007.
94. R. Garcia, J. Tamayo, M. Calleja and F. Garcia, *Applied Physics A*, 1998, **66**, 309-312.
95. P. hansma, J. Cleveland, M. Radmacher, D. Walters, P. Hillner, M. Bezanilla, M. Fritz, D. Vie and H. Hansma, *Appl Phys Lett*, 1994, **65**, 1738-1740.
96. A. L. Weisenhorn, P. Maivald, H. J. Butt and P. K. Hansma, *Physical Review B*, 1992, **45**, 11226-11232.
97. R. D. Heidenreich, *Fundamentals of transmission electron microscopy*, Interscience Publishers, New York, USA, 1964.
98. R. F. Egerton, *Physical principles of electron microscopy an introduction to TEM, SEM, and AEM*, Springer USA, 2005.
99. B. Fultz and J. Howe, *Transmission Electron Microscopy and Diffractometry of Materials*, Springer, Germany and USA, 2008.

100. F. Logiurato, *Journal of Modern Physics*, 2014, **05**, 1-7.
101. P. E. Champness, *Electron diffraction in the transmission electron microscope*, Taylor & Francis Ltd London, United Kingdom, 2001.
102. Electron Nanoscopy Instrumentation Facility, http://go.unl.edu/m5ki, 2017).
103. E. Smith and G. Dent, *Modern Raman Spectroscopy: A Practical Approach*, John Wiley & Sons, Ltd, UK, 2005.
104. M. R. Witkowski, *American Pharmaceutical Review*, 2005, **5**, 1-5.
105. Raman Spectroscopy - A Tutorial http://www.kosi.com/na_en/products/raman-spectroscopy/raman-technical-resources/raman-tutorial.php, (accessed May, 2018).
106. S. Gong, Z. H. Zhu and Z. Li, *PCCP*, 2017, **19**, 5113-5120.
107. M. E. Orazem and B. Tribollet, *Electrochemical impedance spectroscopy*, Hoboken, N.J. : Wiley, 2008.
108. E. Barsoukov and J. R. Macdonald, *Impedance spectroscopy : theory, experiment, and applications.*, John Wiley & Sons, Inc., New Jersey, USA, 2005.
109. S. Fakirov, *Handbook of Condensation Thermoplastic Elastomers*, Wiley-VCH Verlag Gmbh & Co. KGaA Germany, 2005

.
110. J. C. Vickerman and I. Gilmore, *Surface Analysis : The Principal Techniques*, John Wiley & Sons Ltd., Chichester, UK, 2 edn., 2009.
111. M. Kaufman; and A. H. Seidman, *Handbook of electronics calculations for engineers and technicians*, McGraw-Hill New York 1979.
112. I. V. Zaporotskova, N. P. Boroznina, Y. N. Parkhomenko and L. V. Kozhitov, *Modern Electronic Materials*, 2016, **2**, 95-105.
113. J. M. Simmons, B. M. Nichols, S. E. Baker, Matthew S. Marcus, O. M. Castellini, C.-S. Lee, R. J. Hamers and M. A. Eriksson, *J. Phys. Chem.*, 2006, **110**, 7113-7118.
114. D. Roizard, in *Encyclopedia of Membranes*, Springer, Berlin, Heidelberg, 2016, pp. 1-3.
115. C. L. Yaws, P. K. Narasimhan and C. Gabbula, *Yaws' Handbook of Antoine Coefficients for Vapor Pressure*, Knovel, New york, USA, 2 edn., 2005.
116. J. Lim, V. G. Bairi and A. Fong, *Materials Chemistry and Physics*, 2017, **198**, 324-330.
117. T. Katayama, H. Araki and K. Yoshino, *Applied Physics*, 2002, **91**, 6675-6678.
118. S. Sze, *Semiconductor Devices Physics and Technology*, Wiley, New York, USA, 1985.
119. DoITPoMS, Metals: the Drude model of electrical conduction, https://www.doitpoms.ac.uk/tlplib/thermal_electrical/drude.php, 2017).
120. E. Y. Tsymbal, in *Introduction to Solid State Physics*, University of Nebraska, Lincoln., USA, 2017.
121. W. D. Zhang and W. H. Zhang, *Journal of Sensors*, 2009, **2009**, 1-16.

122. K. P. Yung, J. Wei, Z. F. Wang and B. K. Tay, presented in part at the 2nd IEEE International Nanoelectronics Conference (INEC 2008), Singapore, 2008.
123. J. Svensson and E. Campbell, *Journal of Applied Physics*, 2011, **110**, 1-16.
124. D. S. Maddison and T. L. Tansley, *Journal of Applied Physics*, 1992, **72**, 4677-4682.
125. Q. W. Li, Y. Li, X. F. Zhang, S. B. Chikkannanavar, Y. H. Zhao, A. M. Dangelewicz, L. X. Zheng, S. K. Doorn, Q. X. Jia, D. E. Peterson, P. N. Arendt and Y. T. Zhu, *Advanced Materials*, 2007, **19**, 3358-3363.
126. A. Oskouyi, U. Sundararaj and P. Mertiny, *Journal of Nanotechnology in Engineering and Medicine*, 2015, **5**, 1-6.
127. Y. Yakovlev, E. Lobko and Z. Gagolkina, presented in part at the 3rd International research and practice conference , nanotechnology and nanomaterials, Ivan Franko National University of Lviv, Ukraine, 2015.
128. S. Alghamdi, PhD thesis, Newcastle Upon Tyne University 2010.
129. M. J. O’Connell, *Carbon Nanotubes: Properties and Applications*, Taylor and Francis Group, United State, 2006.
130. B. Zhang, Y. Xu, Y. Zheng, L. Dai, M. Zhang, J. Yang, Y. Chen, X. Chen and J. Zhou, *Nanoscale Research Letters*, 2011, **6**, 1-9.
131. B. Omrane, PhD thesis, University of Victoria, 2009.
132. J. Zhou, H. Zhao, X. Mu, J. Chen, P. Zhang, Y. Wang, Y. He, Z. Zhang, X. Pan and E. Xie, *Nanoscale*, 2015, **7**, 14697-14706.
133. D. Huyen, N. Tung, T. Vinh and N. Thien, *Sensors*, 2012, **12**, 7965-7974.
134. H. Chen, M. R. Golder, F. Wang, R. Jasti and A. K. Swan, *Carbon*, 2014, **67**, 203-213.
135. M. J. L. Santos, A. G. Brolo and E. M. Girotto, *Electrochimica Acta*, 2007, **52**, 6141-6145.
136. H. J. Kharat, K. P. Kakde, P. A. Savale, K. Datta, P. Ghosh and M. D. Shirsat, *Polymers for Advanced Technologies*, 2007, **18**, 397-402.
137. B. Tian and G. Zerbi, *J. Chem. Phys.*, 1990, **92**, 3886-3891.
138. L. Hu, D. Hecht and G. Gruner, *Chem. Rev.* , 2010, **110**, 5790–5844.
139. R. Saito, M. Fujita, G. Dresselhaus and M. S. Dresselhaus, *Phys. Rev. B*, 1992, **46**, 1804-1811.
140. S. Brahim, S. Colbern, R. Gump, A. Moser and L. Grigorian, *Nanotechnology*, 2009, **20**, 1-8.
141. K. An, S. Jeong, H. Hwang and Y. Lee, *Chem Phys Lett* 2003, **16**, 1005-1009.
142. K. H. An, S. Y. Jeong, H. R. Hwang and Y. H. Lee, *Adv. Mater.*, 2004, **16**, 1005-1009.
143. P. Qi, O. Vermesh, M. Grecu, A. Javey, Q. Wang and H. Dai, *Nano Letter.*, 2003, **3**, 347-351.
144. G. Cao, *Nanostructures and Nanomaterials : synthesis, properties and applications*, Imperial Collage Press, London, 2004.

145. O. Varghese, P. Kichambre, D. Gong, K. Ong, E. Dickey and C. Grimes, *Elsevier, Sensors and Actuators B.*, 2001, **81**, 32-41.
146. J. Chung, K. H. Lee, J. Lee, D. Troya and G. C. Schatz, *Nanotechnology*, 2004, **15**, 1596-1602.
147. T. Ueda, S. Katsuki, K. Takahashi, H. A. Narges, T. Ikegami and F. Mitsugi, *Diamond and Related Materials*, 2008, **17**, 1586-1589.
148. Volatile Organic Compounds' Impact on Indoor Air Quality, United States Environmental Protection Agency, EPA.org, 2017).
149. N. B. o. S. Department of Commerce, *Journal*, 1967, 1-64.
150. S. Badhulika, N. V. Myung and A. Mulchandani, *Talanta*, 2014, **123**, 109-114.
151. K. Shi and I. Zhitomirsky, *ACS Appl. Mater. Interfaces* 2013, **5**, 13161-13170.
152. P. Poetschke, A. Bhattacharyya and A. Janke., *Compos. Interfaces*, 2003, **10**, 389–404.
153. J. L. Bahr and J. M. Tour, *Materials Chemistry*, 2002, **12**, 1952-1958.
154. A. Hirsch, *Angew. Chem. Int. Ed.*, 2002, **41**, 1853-1859.
155. S. Niyogi, M. Hamon, H. Hu, B. Zhao, P. Bhowmik, R. Sen, M. Itiks and R. Haddon, *Acc. Chem. Res.*, 2002, **35**, 1105-1113.
156. C. Li, E. T. Thostenson and T.-W. Chou, *Composites Science and Technology*, 2008, **68**, 1227-1249.
157. H. Gibbard and J. Creek, *Journal of Chemical and Engineering Data*, 1974, **19**, 308-310.
158. V. Majer and V. Svoboda, *Enthalpies of Vaporization of Organic Compounds: A Critical Review and Data Compilation* Blackwell Science 1985.
159. I. H. Hafez, in *Nanotechnology and Nanomaterials*, INTECH, 2016, DOI: 10.5772/63058

.

160. S. Cui, H. Pu, G. Lu, Z. Wen, E. C. Mattson, C. Hirschmugl, M. Gajdardziska-Josifovska, M. Weinert and J. Chen, *ACS Appl. Mater. Interfaces* 2012, **4**, 4898-4904.
161. W. T. Silfvast, *Laser fundamentals*, Cambridge University Press, Cambridge, England, 1996.
162. T. Ueda, S. Katsuki, N. H. Abhari, T. Ikegami, F. Mitsugi and T. Nakamiya, *Surface and Coatings Technology*, 2008, **202**, 5325-5328.
163. L. Wei, S. Zhu, H. Zhou, Z. Li, H. Yin, X. Bi, W. Jiang and Z. Chen, *Optik* 2018, **154**, 711-716.
164. P. Collins and P. Avouris, *Nanotubes for Electronics*, USA, 2000.
165. T. Nakamiya, T. Ueda, T. Ikegami, K. Ebihara and R. Tsuda, *Current Applied Physics*, 2008, **8**, 400-403.
166. Z. Lim, A. Lee, K. Lim, Y. Zhu and C. Sow, *J. Appl. Phys.*, 2010, **107**, 1-7.
167. J. Yotani, S. Uemura, T. Nagasako, H. Kurachi, H. Yamada, T. Ezaki, T. Maesoba, T. Nakao, M. Ito, T. Ishida and Y. Saito, *Jpn. J. Appl. Phys.*, 2004, **43**, L1459-L1462.

168. K. Lee and J. Kong, in *Carbon Nanotube Electronics*, Springer, USA, 2009, DOI: 10.1007/978-0-387-69285-2, ch. Chemical Sensing with SWNT FETs.
169. A. Zangwill, *Physics at Surfaces*, Cambridge University Press, United States of America 1988.
170. S. Santucci, S. Picozzi, F. Di Gregorio, L. Lozzi, C. Cantalini, L. Valentini, J. M. Kenny and B. Delley, *J. Chem. Phys.*, 2003, **119**, 10904-10910.
171. J. P. Novak, E. S. Snow, E. J. Houser, D. Park, J. L. Stepnowski and R. A. McGill, *Appl. Phys. Lett.*, 2003, **83**, 4026-4028.
172. J. Kong, N. Franklin, C. Zhou, M. Chapline, S. Peng, K. Cho and H. Dai, *Science*, 2000, **287**, 622-626.
173. A. Goldoni, L. Petaccia, S. Lizzit and R. Larciprete, *J. Phys.: Condens. Matter*, 2010, **22**, 1-8.
174. K. Bradley, M. Briman, A. Star and G. Gruner, *Nano letters*, 2004, **4**, 253-256.
175. L. Valentini, L. Lozzi, C. Cantalini, I. Armentano, J. M. Kenny, L. Ottaviano and S. Santucci, *Thin Solid Films*, 2003, **436**, 95-100.
176. Y. Park, K. Dong, J. Lee, J. Choi, G. Bae and B. Ju, *Sensors and Actuators B*, 2009, **140**, 407-411.
177. W. Han, H. Yu, C. Zhi, J. Wang, Z. Liu, T. Sekiguchi and Y. Bando, *Nano letters*, 2008, **8**, 491-494.
178. X. Chen and C. Ke, in *Boron Nitride Nanotubes in Nanomedicine* Elsevier, 2016, DOI: 10.1016/B978-0-323-38945-7.00012-2, pp. 183-199.
179. Boron Nitride Nanotubes: Properties, Synthesis and Applications, https://www.sigmaaldrich.com/, 2018).
180. F. W. Degrazia, V. C. B. Leitune, S. M. W. Samuel and F. M. Collares, *J Dent*, 2017, **62**, 85-90.
181. M. L. Y. Sin, G. C. T. Chow, G. M. K. Wong, W. J. Li, P. H. W. Leong and K. W. Wong, *IEEE Transactions on Nanotechnology*, 2007, **6**, 571-577.
182. A. A. Gonçalves, *Brazilian archives of biology technology*, 2009 , **52**, 1527-1539.
183. J. Zhang, H. Zou, Q. Qing, Y. Yang, Q. Li, Z. Liu, X. Guo and Z. Du, *J. Phys. Chem. B* 2003, **107**, 3712-3718.
184. S. Banerjee and S. S. Wong, *Nano Lett*, 2004, **4**, 1445-1450.
185. S. Picozz, L. Lozzi, S. Santucci, C. Cantalinib, C. Baratto, G. Sberveglier, I. Armentanod, J. M. Kennyd, L. Valentinid and B. Delley, *Proceedings of IEEE*, 2003, **1**, 436-439
186. J. M. Simmons, B. M. Nichols, S. E. Baker, M. S. Marcus, O. M. Castellini, C.-S. Lee, R. J. Hamers and M. A. Eriksson, *J. Phys. Chem. B*, 2006, **110**, 7113-7118.
187. J. Gao and Y. L. Loo, *PCCP*, 2014, **16**, 10861-10865.
188. S. Kang, J. Seo and S. Park, *Adv. Mater.Sci.Eng.*, 2015, **2015**, 1-9.
189. O. Byl, J. Liu and J. Yates, *Langmuir : the ACS journal of surfaces and colloids*, 2005, **21**, 4200-4204.

190. A. Narlikar and Y. Fu, *Oxford Handbook of Nanoscience and Technology: Frontiers and Advances*, Oxford University Press, Oxford, UK., 2009.
191. E. Chigo Anota, H. Hernández Cocoletzi and E. Rubio Rosas, *The European Physical Journal D*, 2011, **63**, 271-273.
192. D. Farmanzadeh and N. Askari Ardehjani, *Applied Surface Science*, 2018, **444**, 642-649.
193. H. Liu and C. H. Turner, *Journal of computational chemistry*, 2014, **35**, 1058-1063.
194. N. G. Tsierkezos and U. Ritter, *Journal of Experimental Nanoscience*, 2012, **9**, 421-431.
195. N. Kovtyukhova, T. Mallouk, L. Pan and E. Dickey, *J. AM. CHEM. SOC.*, 2003, **125**, 9761-9769.
196. W. L. Yim and Z. F. Liu, *Chem.Phys. Lett.*, 2004, **398**, 297-303.
197. W. Sun, U. Khaled, H. Tomita, Z. Li, K. Imasaka and J. Suehiro, *Jpn. J. Appl. Phys.*, 2010, **49**, 1-5.
198. M. Varga, T. Izak, V. Vretenar, H. Kozak, J. Holovsky, A. Artemenko, M. Hulman, V. Skakalova, D. S. Lee and A. Kromka, *Carbon*, 2017, **111**, 54-61.
199. T. I. T. Okpalugo, P. Papakonstantinou, H. Murphy, J. McLaughlin and N. M. D. Brown, *Carbon*, 2005, **43**, 153-161.
200. P. Zhou, W. Li, X. Zhu, Y. Li, X. Jin and J. Chen, *Journal of The Electrochemical Society*, 2016, **163**, D160-D166.
201. K. D. Grossman, T. S. Sakthivel, C. Dillier, E. L. Petersen and S. Seal, *RSC Adv.*, 2016, **6**, 89635-89641.
202. M. A. Abass, A. A. Syed, C. Gervais and G. Singh, *RSC Adv.*, 2017, **7**, 21576-21584.
203. S. M. Castanho and R. Moreno, *Cerâmica*, 1998, **44**, 141-145.
204. B. Zhong, L. Song, X. X. Huang, G. W. Wen and L. Xia, *Materials Research Bulletin*, 2011, **46**, 1521-1523.
205. C. E. Reeves, S. A. Penkett, S. Bauguitte, K. S. Law, M. J. Evans, B. J. Bandy, P. S. Monks, G. D. Edwards, G. Phillips, H. Barjat, J. Kent, K. Dewey, S. Schmitgen and D. Kley, *Geophysical Research: Atmospheres*, 2002, **107**, ACH 14-11-ACH 14-14.
206. M. Mittal and A. Kumar, *Sensors and Actuators B: Chemical*, 2014, **203**, 349-362.
207. D. Kim, P. V. Pikhitsa, H. Yang and M. Choi, *Nanotechnology*, 2011, **22**, 1-7.
208. J. Li, Y. Lu, Q. Ye, M. Cinke, J. Han and M. Meyyappan, *Nano Letters*, 2003, **3**, 929-933.
209. J. Yun, J. Kim, Y. Park, J. Song, D. Shin and C. Han, *Nanotechnology*, 2009, **20**, 1-5.
210. R. K. Frank Hennrich , Katharina Arnold , Jan Stu , Sergei Lebedkin , Thomas Koch , Thomas Schimme , Manfred Kappes, *J. Phys. Chem. B* 2007, **111**, 1932-1937.
211. R. Afrin and N. A. Shah, *Diamond and Related Materials*, 2015, **60**, 42-49.
212. I. V. Zaporotskova, N. P. Boroznina, Y. N. Parkhomenko and L. V. Kozhitov, *MoEM*, 2016, **2**, 95-105.

213. H. Eom, J. Jeong and J. Choi, *Environmental Health and Toxicology*, 2015, **30**, 1-8.
214. C. Matranga and B. Bockrath, *J. Phys. Chem.*, 2005, **109**, 4853-4864.
215. K. An, S. Jeong, H. R. Hwang and Y. H. Lee, *Adv. Mater.*, 2004, **16**, 1005-1009.
216. Q. Zhang, B. Piro, V. Noël, S. Reisberg and M. Pham, *Adv. Nat. Sci.: Nanosci. Nanotechnol.*, 2011, **1**, 1-8.
217. C. Zunijga, M. Rinaldil, S. Khamis, T. Jones, A. Johnson and G. Piazza, presented in part at the IEEE 22nd International Conference on Micro Electro Mechanical Systems Sorrento, Italy 2009.
218. Y. Liu, M. Chen, M. Mohebbi, M. L. Wang and M. R. Dokmeci, presented in part at the Solid-State Sensors, Actuators and Microsystems Conference (TRANSDUCERS), Beijing, China 2011.
219. M. Penza, G. Cassano, R. Rossi, M. Alvisi, A. Rizzo, M. A. Signore, T. Dikonimos, E. Serra and R. Giorgi, *Appl. Phys. Lett.*, 2007, **90**, 1-3.
220. M. Zheng, A. Jagota, E. D. Semke, B. A. Diner, R. S. McLean, S. R. Lustig, R. E. Richardson and N. G. Tassi, *Nat Mater*, 2003, **2**, 338-342.
221. R. C. Olby, *The path to the double helix : the discovery of DNA*, New York : Dover Publications, New York, USA, c1994.
222. The DNA molecule is shaped like a twisted ladder, http://www.dnaftb.org/19/bio-3.html, 2018).
223. J. D. Bernal, *Nature*, 1958, **182**, pp 154.
224. R. Tahvildari, PhD thesis, University of Otttaw, 2017.
225. N. Nakashima, Okuzono, S., Murakami, H., Nakai, T. , Yoshikawa, K. , *Chem. Lett.* , 2003, **32**, 456-457.
226. Y. Wanna, N. Srisukhumbowornchai, A. Tuantranont, A. Wisitsoraat, N. Thavarungkul and P. Singjai, *J. Nanosci. Nanotechnol.*, 2006, **6**, 3893-3896.
227. R. Wang, J. Sun, L. Gao and J. Zhang, *Materials Chemistry*, 2010, **20**, 6903-6909.
228. A. P. Alivisatos, Kai P. Johnsson, Xiaogang Peng, Troy E. Wilson , Colin J. Loweth , Marcel P. Bruchez Jr, Peter G. Schultz *Nature* 1996, **382**, 609-611.
229. C. A. Mirkin, R. L. Letsinger, R. C. Mucic and J. J. Storhoff, *Nature*, 1996, **382**, 607-609.
230. H. Ishida, *Characterization of composite materials*, Momentum Press., New York, USA, Materials characterization series 1st ed edn., 2010.
231. X. Huang, R. S. Mclean and M. Zheng, *Anal. Chem.*, 2005, **77**, 6225-6228.
232. M. E. Hughes, E. Brandin and J. A. Golovchenko, *Nano Lett*, 2007, **7**, 1191-1194.
233. V. H. Nguyen and J.-J. Shim, *Journal of Spectroscopy*, 2015, **2015**, 1-9.
234. P. D. Tam, N. Van Hieu, N. D. Chien, A. T. Le and M. Anh Tuan, *J Immunol Methods*, 2009, **350**, 118-124.

235. M. B. Pingang He *Langmuir : the ACS journal of surfaces and colloids*, 2005, **21**, 6086-6092.
236. M. Bradley, FTIR Sample Techniques: Attenuated Total Reflection (ATR), https://www.thermofisher.com/uk/en/home/industrial/spectroscopy-elemental-isotope-analysis/spectroscopy-elemental-isotope-analysis-learning-center/molecular-spectroscopy-information/ftir-information/ftir-sample-handling-techniques/ftir-sample-handling-techniques-attenuated-total-reflection-atr.html, (accessed 18 April 2018).
237. H. Dhillon, H. D. Wit and J. Dodson, Spectroscopy: CVD diamond attenuated-total-reflection prisms benefit FTIR spectroscopy, https://www.laserfocusworld.com/articles/print/volume-52/issue-10/features/spectroscopy-cvd-diamond-attenuated-total-reflection-prisms-benefit-ftir-spectroscopy.html, 2018).
238. S. Bhattarai, S. Aryal, R. Bahadur, N. Bhattarai, P. Hwang, H. Yi and H. Kim, *Materials Science and Engineering C*, 2008, **28**, 64–69.
239. F. F. C. Branca , V. Magazu , A. Mangione, *J. Phys. Chem.*, 2004, **108**, 3469-3473.
240. S. R. Ede, V. Mani, N. Kalaiselvi and S. Kundu, *New J.Chem.*, 2016, **40**, 6185-6199.
241. G. Dovbeshko, *Talanta*, 2000, **53**, 233-246.
242. A. A. Ouameur and H. A. Tajmir-Riahi, *J Biol Chem*, 2004, **279**, 42041-42054.
243. Y. Zhang, H. Ma, K. Zhang, S. Zhang and J. Wang, *Electrochimica Acta*, 2009, **54**, 2385-2391.
244. S. Alex and P. Dupuis, *Inorganica Chimica Acta.* , 1989, **157**, 271-281.
245. N. J. Kybert, M. B. Lerner, J. S. Yodh, G. Preti and A. T. Johnson, *ACS Nano*, 2013, **7**, 2800-2807.
246. S. M. Khamis, R. A. Jones, A. T. C. Johnson, G. Preti, J. Kwak and A. Gelperin, *AIP Advances*, 2012, **2**, 1-11.
247. K. Besteman, J. Lee, F. Wiertz, H. Heering and C. Dekker, *Nano Letters*, 2003, **3**, 727-730.
248. A. Star, T. R. Han, V. Joshi, J. Christophe and G. Gruner, *Adv. mater.*, 2004, **16**, 2049-2052.

Appendix

Supplemental Materials

Table S1: Ozone calibration

Absorbance at the 350 nm peak (A) for four tests	4.652
	5.451
	5.225
	5.939
Absorbance average (A)	5.209
Absorption coefficient (α) dm^3 mol^{-1} s^{-1}	2.60E+04
Pathway cell width d (cm)	1
Concentration of iodide in aliquot (C) C=A/(α d) in mol dm^{-3}	2.00E-04
KI volume (dm^3)	0.1
No. of moles of I_3^- (mol) = Volume x C	2.00E-05
No. of moles of O_3 (mol) = Volume x C	2.0035E-05
Time (min)	20
Flow rate (m^3 S^{-1})	2.0833E-06
Volume of air (m^3) = flow rate x time	0.0025
Ozone concentration = No. of moles of O_3 / Volume of air	0.00801385
Air concentration assuming ideal gas law = P T/R P= 101325 Pa, R=8.314 J K^{-1} mol^{-1} , T= 293 K	41.5947934 mol m^{-3}
Mole fraction ozone = O_3 Conc. / (Air Conc. + O_3 Conc.)	0.00019263
Mass fraction ozone = (O3 Conc. x Moleculare wight of O3) / (O3 Conc. x Molecular wight of O3 + Air Conc. x Molecular weight of air)	0.00031981 Uncertainty 29.57
Ozone (ppm) = 1000000 x Mass fraction ozone	320 ± 30
Note	***320*** ppm for ***100%*** UV tube illumination ***217.6*** ppm for ***68%*** UV tube illumination ***128*** ppm for ***40%*** UV tube illumination

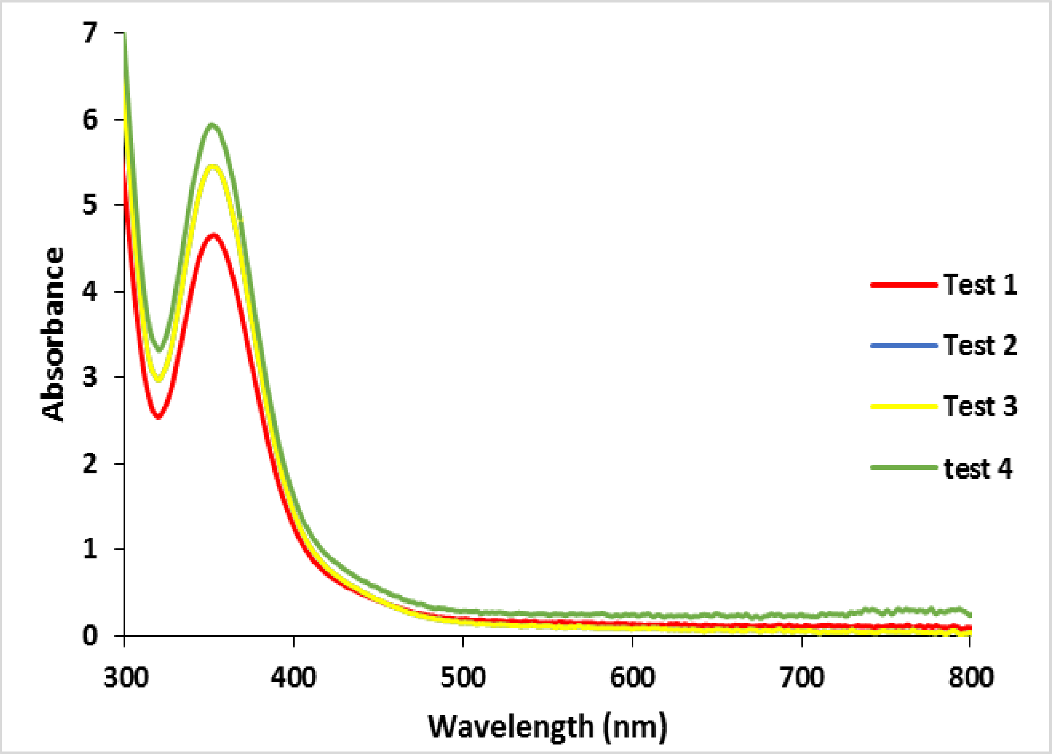

Figure S1: UV-vis plots of KI aqueous

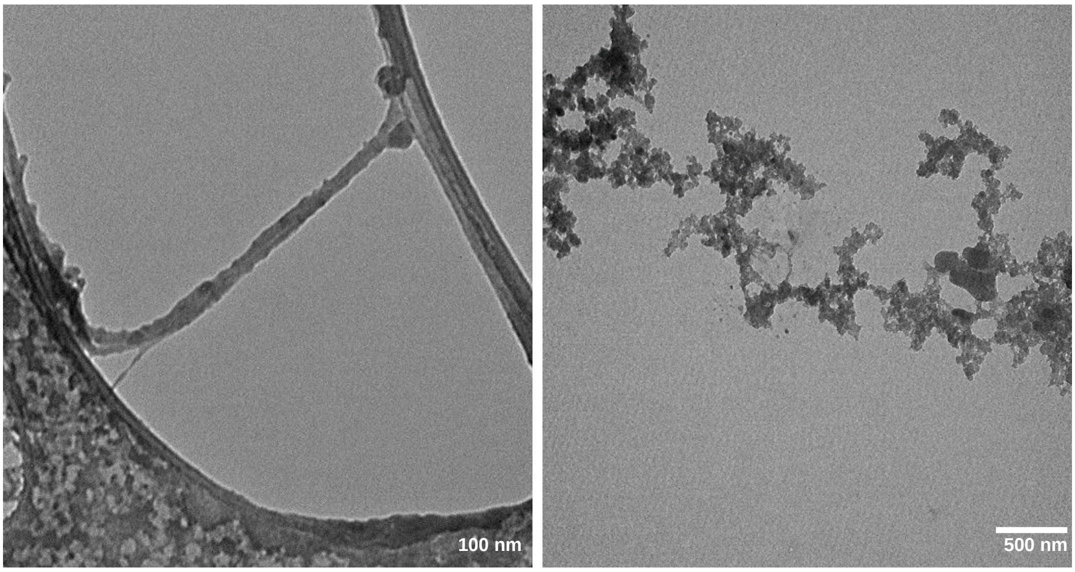

Figure S2: TEM images of SWCNTs/polypyrrole

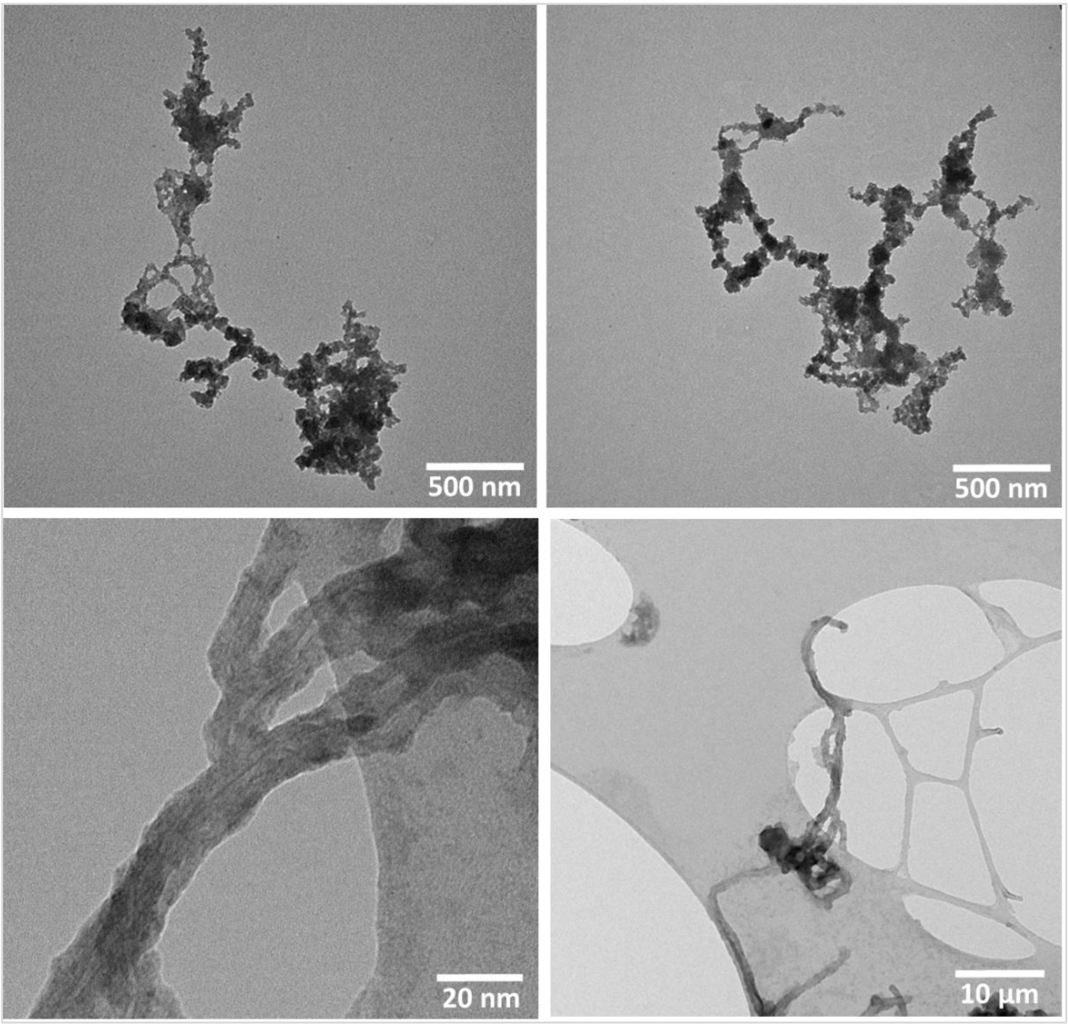

Figure S3: TEM images of MWCNTs/Polypyrrole

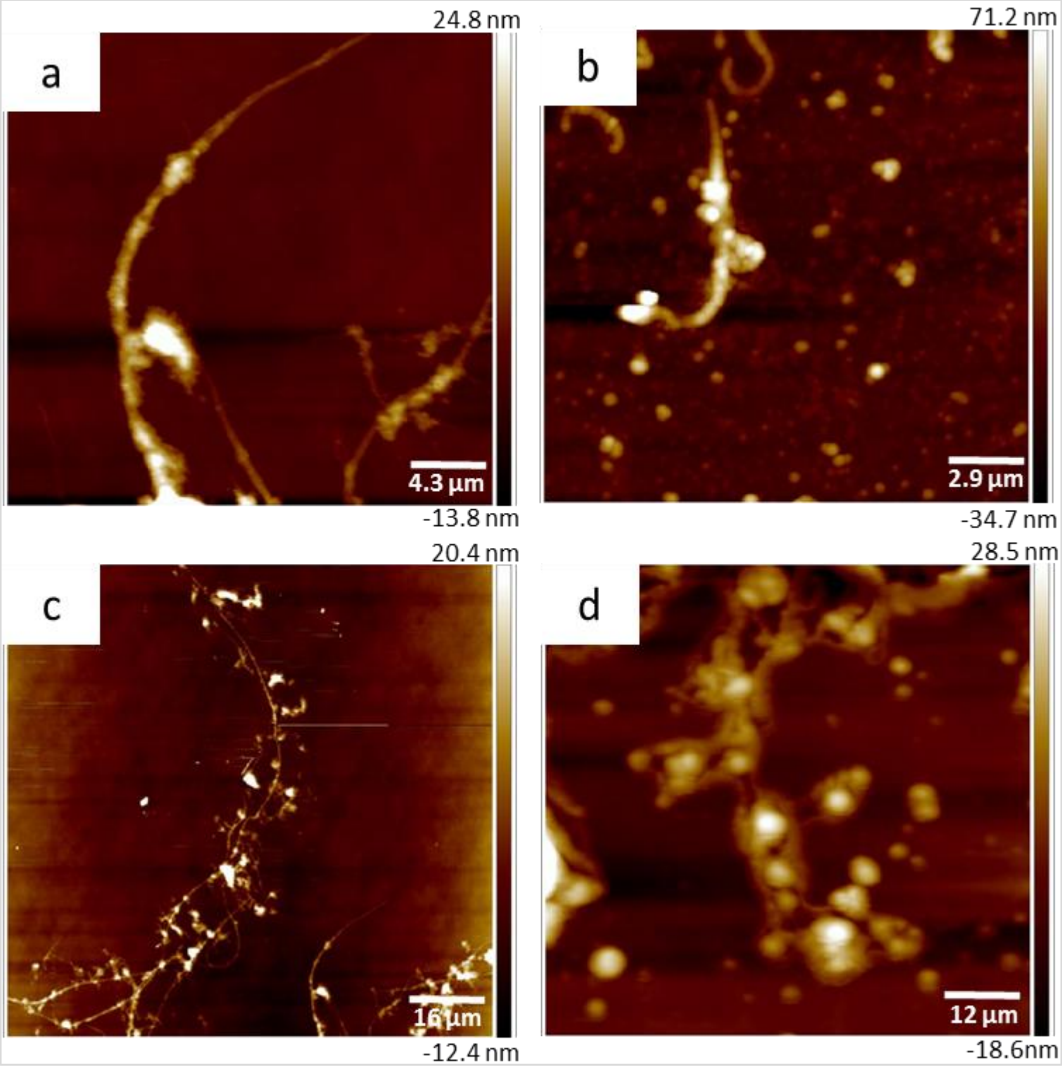

Figure S4: AFM images of (a&b) SWCNTs/Ppy, (c&d) MWCNTs/Ppy.

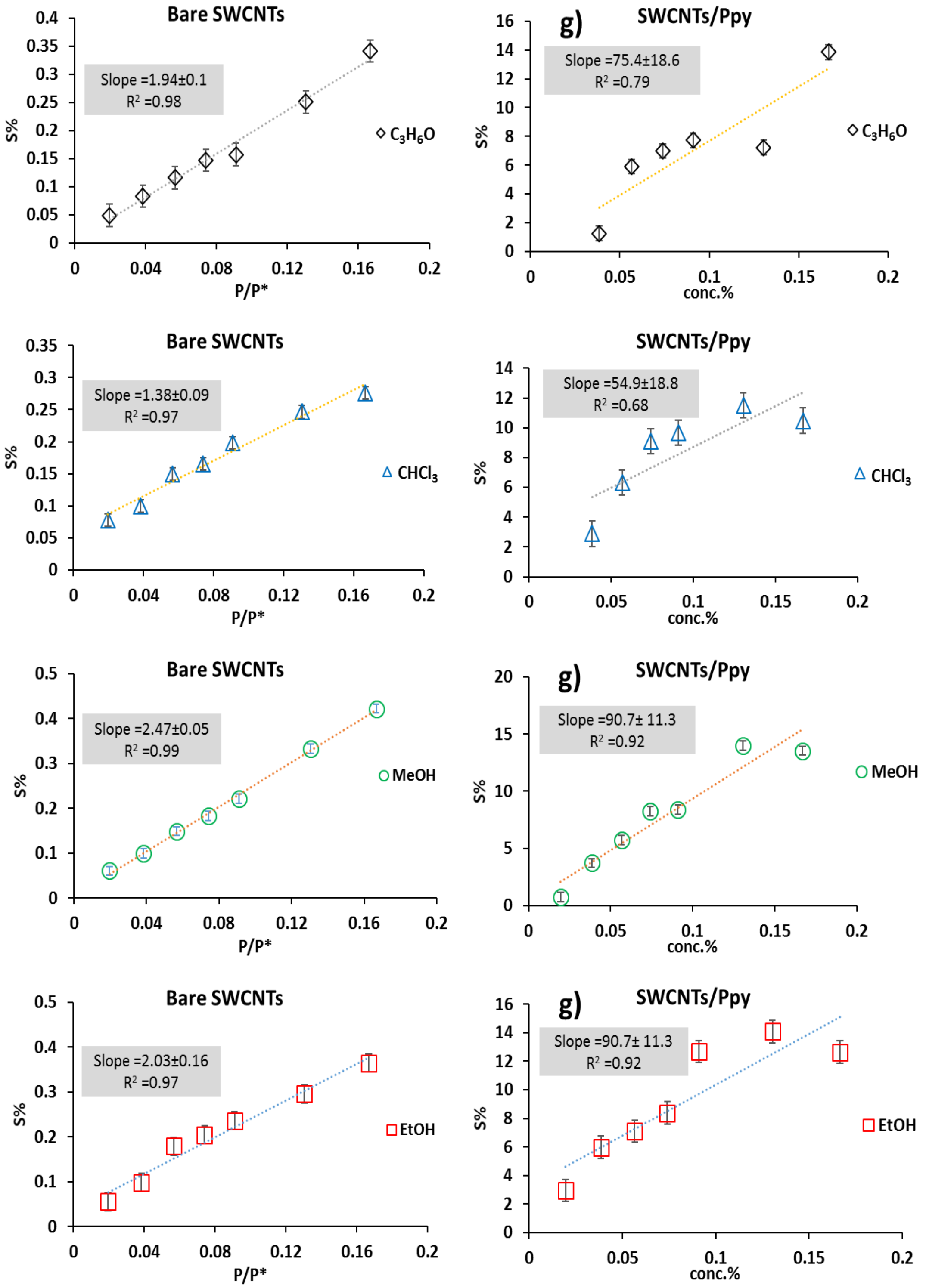

Figure S5: The variation of the sensing response of bare and hybrid SWCNTs towards different VOCs as a function of the vapour concentration.

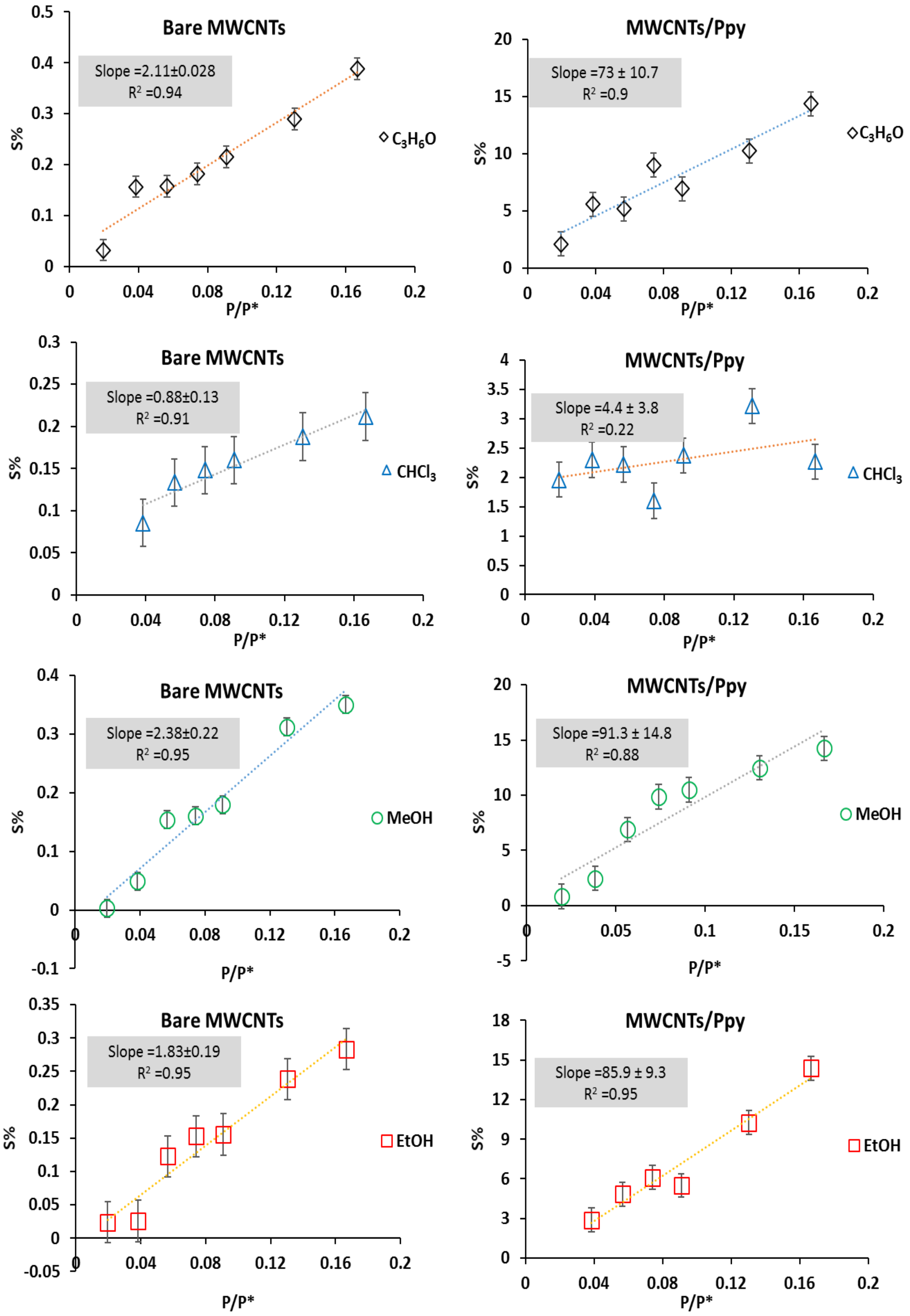

Figure S6: The variation of the sensing response of bare and hybrid MWCNTs towards different VOCs as a function of the vapour concentration.

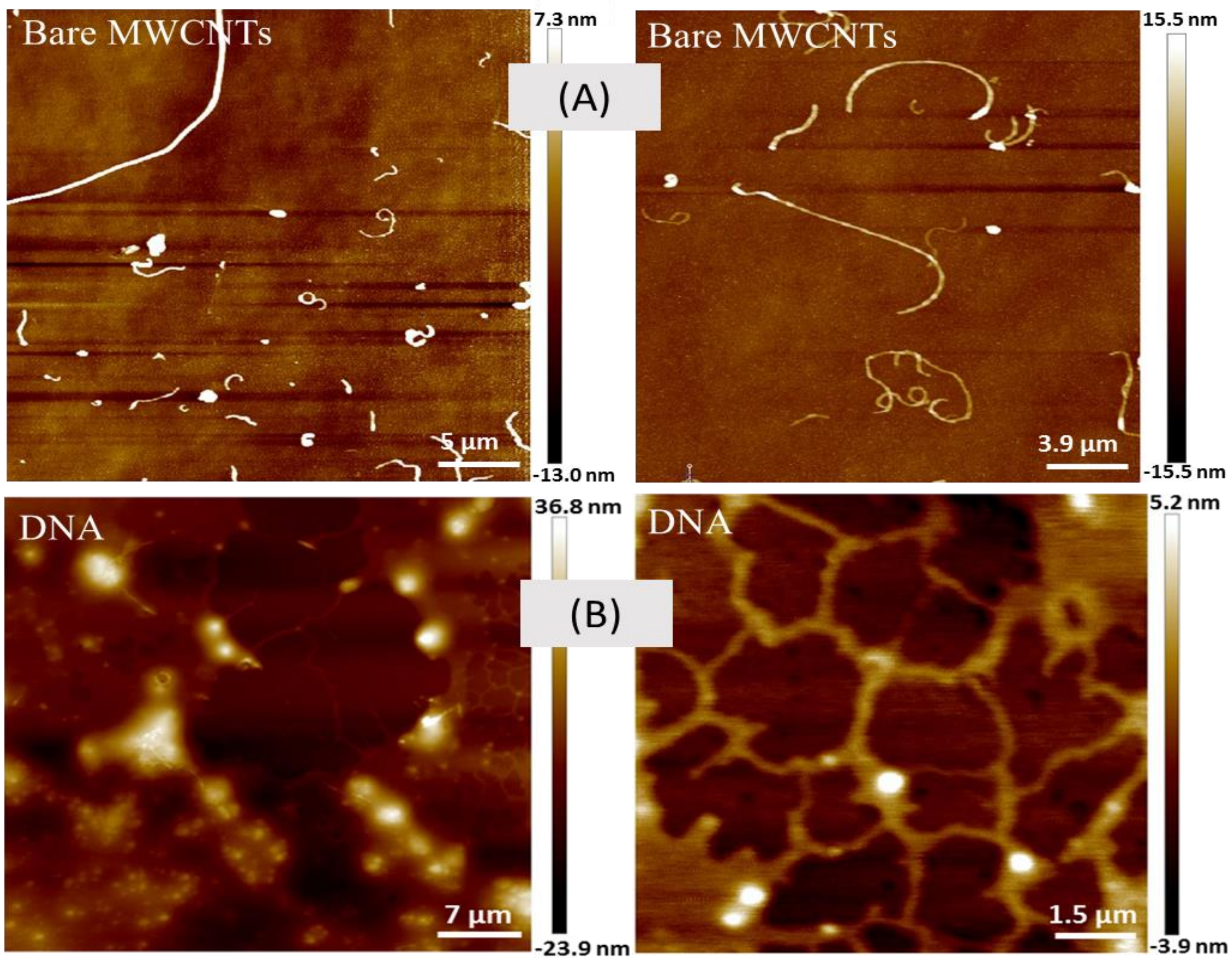

Figure S7: AFM images of (A) bare MWCNTs

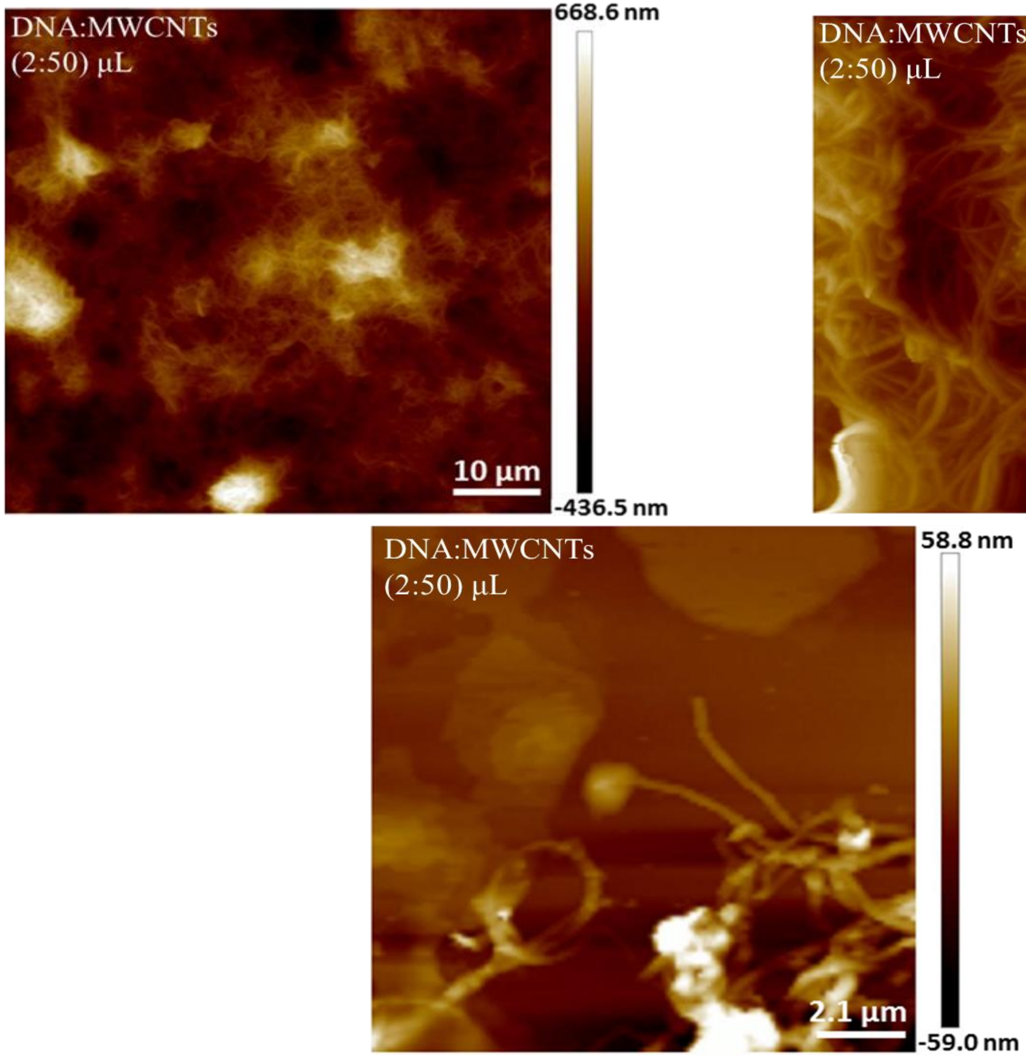

Figure S8: AFM images of DNA:CNTs (2:50) µL

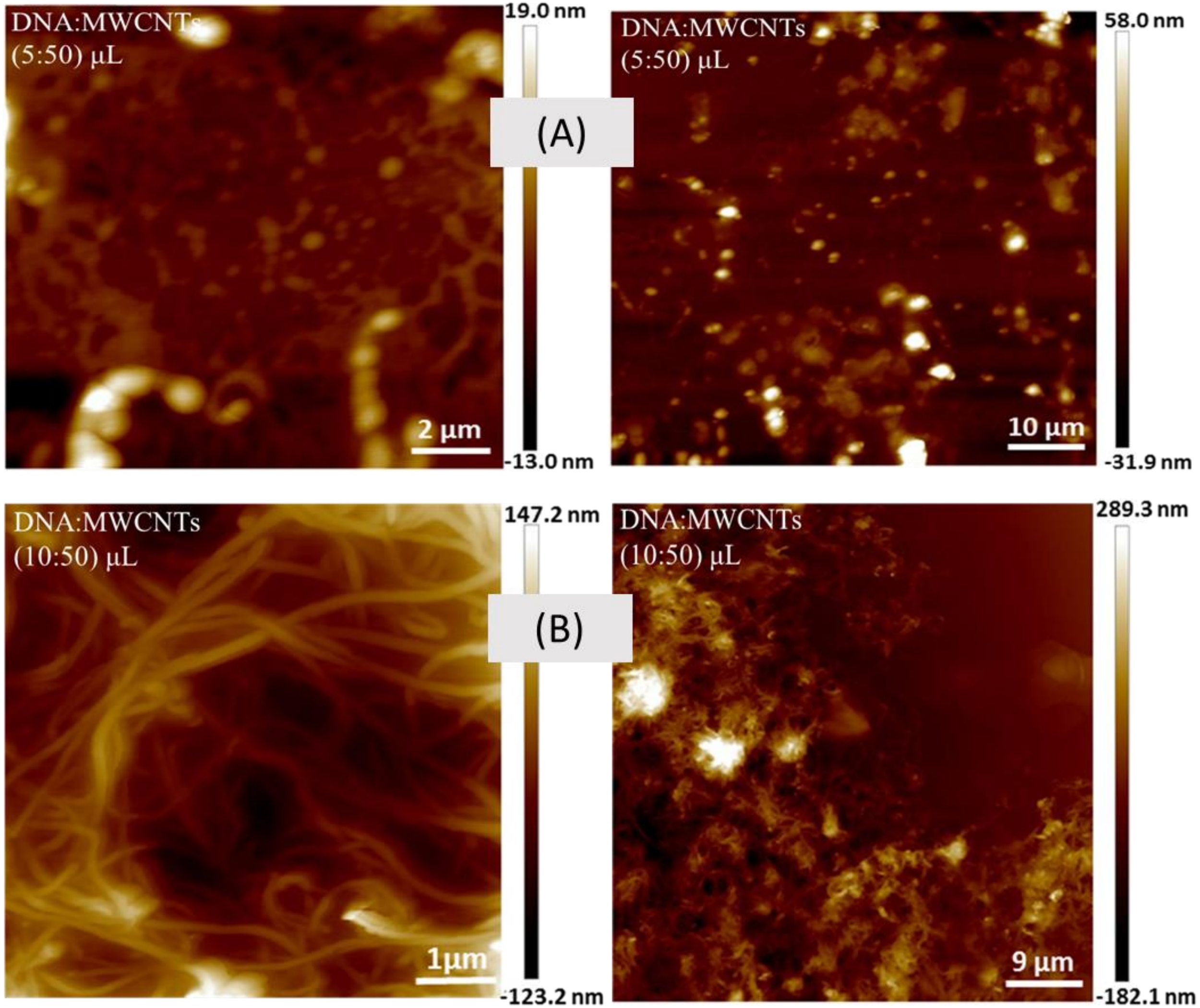

Figure S9: AFM images of DNA:MWCNTs: (A) (5:50)µL, (B) (10:50)µL

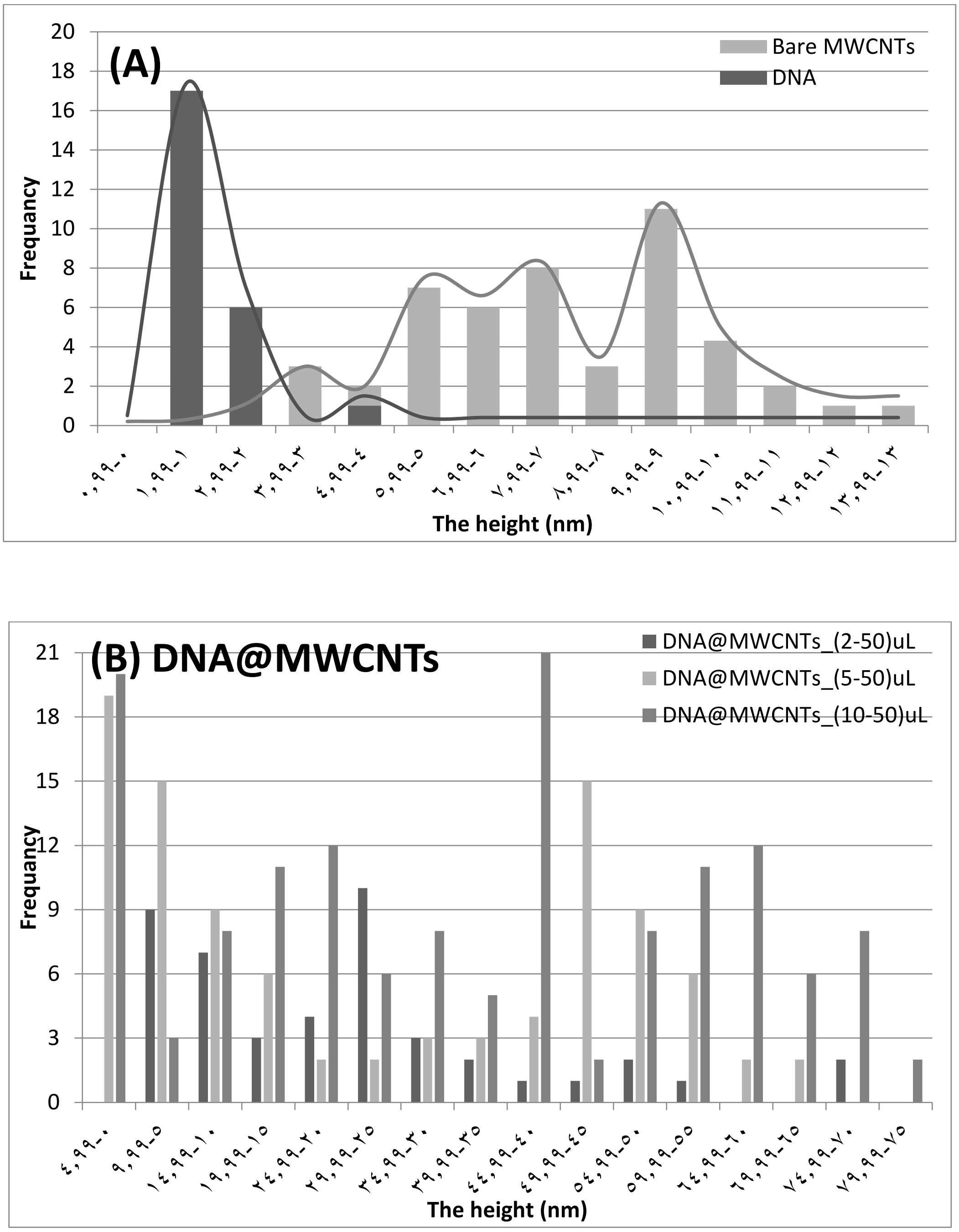

Figure S10: The histogram of (A) bare carbon nanotubes and pure DNA, (B) DNA@MWCNTs at different ratios.

Table S2: the calculations of the vapour pressure for acetone, ethanol, methanol and chloroform at different temperature with different concentration mixture (VOC:zero air).

@ 293K				
	$P_{vap} = 0.5 * P_{sat}$	$P_{vap} = 0.67 * P_{sat}$	$P_{vap} = 0.75 * P_{sat}$	$P_{vap} = 0.8 * P_{sat}$
C_3H_6O P_{sat} = 24603.8 Pa	12300	16500	18500	19700
EtOH P_{sat} = 5872 Pa	2940	3930	4400	4700
MeOH P_{sat} = 12996 Pa	6500	8710	9750	10400
$CHCl_3$ P_{sat} = 208205. 27 Pa	104000	139000	156000	167000
@ 303K				
	$P_{vap} = 0.5 * P_{sat}$	$P_{vap} = 0.67 * P_{sat}$	$P_{vap} = 0.75 * P_{sat}$	$P_{vap} = 0.8 * P_{sat}$
C_3H_6O P_{sat} = 37752 Pa	18900	25300	28300	30200
EtOH P_{sat} = 10469.7 Pa	5230	7010	7850	8380
MeOH P_{sat} = 21860.9 Pa	10900	14600	16400	17500
$CHCl_3$ P_{sat} = 31964 Pa	15900	21400	23973.0	25600
@ 313 K				
	$P_{vap} = 0.5 * P_{sat}$	$P_{vap} = 0.67 * P_{sat}$	$P_{vap} = 0.75 * P_{sat}$	$P_{vap} = 0.8 * P_{sat}$
C_3H_6O P_{sat} = 561866 Pa	281000	376000	421000	449000
EtOH P_{sat} = 17891.9 Pa	8900	12000	13400	14300
MeOH P_{sat} = 35430.3 Pa	17700	23700	26600	28300
$CHCl_3$ P_{sat} = 47581.6 Pa	23800	31900	35700	38100
@ 323 K				
	$P_{vap} = 0.5 * P_{sat}$	$P_{vap} = 0.67 * P_{sat}$	$P_{vap} = 0.75 * P_{sat}$	$P_{vap} = 0.8 * P_{sat}$
C_3H_6O P_{sat} = 81366 Pa	40700	54500	61000	65100
EtOH P_{sat} = 29439.43 Pa	14700	19700	22100	23600
MeOH P_{sat} = 55539 Pa	27800	37200	41700	44400
$CHCl_3$ P_{sat} = 68861.23 Pa	34400	46100	51600	55100
@ 333 K				
	$P_{vap} = 0.5 * P_{sat}$	$P_{vap} = 0.67 * P_{sat}$	$P_{vap} = 0.75 * P_{sat}$	$P_{vap} = 0.8 * P_{sat}$
C_3H_6O P_{sat} = 114963.2 Pa	57500	77000	86200	92000
EtOH P_{sat} = 46898.4 Pa	23400	46900	35200	37500
MeOH P_{sat} = 84999.8 Pa	42500	56900	63700	68000
$CHCl_3$ P_{sat} = 97167.8 Pa	48500	65100	72900	77700